UNIVERSITÀ
DEGLI STUDI
DI PADOVA

Sede Amministrativa: Università degli Studi di Padova

Dipartimento di Ingegneria Industriale

CORSO DI DOTTORATO DI RICERCA IN: INGEGNERIA INDUSTRIALE
CURRICOLO: INGEGNERIA DEI MATERIALI
CICLO XXXIV

EFFECTS OF MOLD SURFACE NANOTEXTURING ON POLYMER FLOW FOR INDUSTRIAL APPLICATIONS

Coordinatore: Ch.mo Prof. Paolo Sgarbossa
Supervisore: Ch.mo Prof. Giovanni Lucchetta
Co-Supervisore: Ch.mo Prof. Davide Masato

Dottorando: Leonardo Piccolo

Everyday things can tell secrets to people who are able to look at them and listen to them.

Sergio Endrigo

RINGRAZIAMENTI

Con questa tesi si conclude il mio Dottorato di ricerca in Ingegneria Industriale, un traguardo che raccoglie in sé un percorso personale e condiviso durato tre anni. È qui che voglio sostare a ricordare le persone che ho avuto la fortuna di trovare lungo questo tempo, senza le quali l'esito non sarebbe stato lo stesso.

Il primo ringraziamento è per i due supervisori che mi hanno seguito, il prof. Lucchetta e il prof. Masato, nei due luoghi dove ho fatto ricerca. Li ringrazio per aver alimentato il mio desiderio di fare ricerca, strutturandolo e concretizzandolo attraverso esperienze sempre nuove ed affascinanti. In sintonia con loro ringrazio il prof. Sorgato, che è sempre stato sicuro punto di riferimento.

Un grazie alle persone che mi hanno accompagnato durante il periodo all'University of Massachusetts Lowell. Ringrazio il prof. Johnston, il prof. Kazmer e il prof. Shen per avermi ospitato nelle loro aule e nei loro laboratori, facendomi vivere esperienze uniche. Un grazie a tutte persone che lì ho incontrato, tra cui Dario, Josh, Zibo, Michael, Kyle, Ye, Avia, Anshal, Dhanashree e Zhe.

Voglio ringraziare anche chi all'Università di Modena e Reggio Emilia mi ha fatto sentire benvenuto nel loro laboratorio, permettendomi di crescere nella ricerca sul laser; il prof. Orazi, Riccardo e Michele.

Un grazie ai miei colleghi che hanno condiviso con me il tempo trascorso al laboratorio Te.Si., tra cui Riccardo, Andrea, Elia, Riccardo, Filippo, Lucia, Rachele, e Federico.

I miei più profondi ringraziamenti vanno alla mia famiglia; i miei genitori, Pierluigi e Antonella, i miei fratelli, Stefano e Marco, e per Cecilia e Mattia, che sono sempre stati a mio fianco, porto sicuro per sostare e da cui proiettarsi in nuove esperienze.

Voglio ringraziare tutti i miei amici con cui ho condiviso questi tre anni, che sanno quanto gli voglia bene anche se qui non li cito.

Voglio concludere non ringraziando il Covid e ricordando come le persone che riecheggiano in questa pagina mi abbiano aiutato a trovare vie nuove per ottenere quello che era il proposito.

Grazie. *L. P.*

SOMMARIO

L'utilizzo di sorgenti laser ultraveloci per la micro e nano testurizzazione è uno tra i campi di ricerca più attivi e in costante crescita che può far progredire il settore dello stampaggio ad iniezione. L'integrazione della testurizzazione laser nello stampaggio può incrementare la sostenibilità tecnica e ambientale della produzione di massa di prodotti in plastica. Superfici stampo ingegnerizzate hanno effetti sulle prestazio-ni di riempimento della cavità e sulla topografia della parte stampata, riducendo il consumo di materiale specifico per il componente ed introducendo ulteriori funzionalità che possono offrire nuove risposte ai problemi ambientali, soprattutto quando combinate con polimeri sostenibili. La nuova applicazione della tecnologia laser allo stampaggio ha sollevato numerose opportunità e interrogativi. In questo contesto, la progettazione delle superfici degli stampi rappresenta la congiuntura strategica per potenziare le innovazioni di processo e le nuove funzionalità di prodotto.

In questo lavoro, la generazione di tessiture per indurre nuovi flussi polimerici nella cavità è stata studiata per ottenere flussi da requisiti energetici inferiori, progettando e realizzando tessiture per il processo dei polimeri. Micro e nano tessiture regolari, rivestimenti superficiali e la loro combinazione sono state introdotte sullo stampo ad iniezione per modificare le proprietà morfologiche, chimiche e termiche della superficie. Le campagne sperimentali mirano a caratterizzare gli effetti sul riempimento della cavità e sulle prestazioni di replicazione del processo. Gli studi sul riempimento si concentrano sui fenomeni che si verificano durante il flusso per ridurre la caduta di pressione in cavità. Gli studi sulla capacità di replicazione del polimero si concentrano sulle interazioni che avvengono in superficie per ottimizzare l'accuratezza nella replicazione.

Durante le indagini sperimentali sono state implementate avanzate apparecchiature di caratterizzazione e di monitoraggio del processo in linea. I risultati sperimentali dimostrano che le strutture dello stampo e i rivestimenti superficiali riducono la caduta di pressione in cavità. Calibrando un modello numerico e modellando un caso studio con il rivestimento dello stampo proposto, il risultato è stato tradotto in termini di riduzione dell'intensità del materiale, ottenendo una riduzione del volume del componente dell'8%. I risultati mostrano che, in relazione all'accuratezza nella replicazione, le parti in plastica possono essere funzionalizzate, aumentando l'angolo di contatto con l'acqua. Uno strumento di progettazione del processo per funzionalizzare parti in plastica è stato implementato con un modello multi-scala che prevede il grado di replicazione, composto da un

modello numerico che risolve il macro flusso in cavità e alimenta il modello analitico per il micro flusso del polimero nelle strutture, sviluppato in questo lavoro. Il modello multi-scala risulta sensibile alle variazioni del polimero e del processo, con un errore massimo dell'8%.

I risultati di questo lavoro possono aprire nuove opportunità e mercati per i settori della testurizzazione laser e dello stampaggio, fornendo strumenti di progettazione più consapevole di parti e stampi verso le richieste del mercato. Le tessiture indotte dai laser ultraveloci per applicazioni di stampaggio a iniezione possono introdurre nuove funzionalità su parti stampate ad iniezione come proprietà autopulenti. Il modello multi-scala ha fornito un contributo significativo alla comprensione dei fenomeni che controllano il processo di stampaggio a iniezione su scala micro e nanometrica, fornendo strumenti per la progettazione del processo e delle strutture sullo stampo. Gli sforzi verso la modellazione dell'effetto dei rivestimenti consentiranno una progettazione di parti in plastica più sostenibili, riducendo il consumo di materiale specifico.

ABSTRACT

Ultrafast laser micro and nanotexturing are among the most active and promising fields of research that have recently boomed and can advance the plastics manufacturing industry. The integration of laser texturing in thermoplastic injection molding can enable the technical and environmental sustainability of the mass manufacturing of plastics products. Engineered mold surfaces have effects on the cavity filling performances and the replicated topography of the part. Parts with a reduced material intensity that embed a wider number of functionalities may offer new technological answers to the environmental issues, especially when combined with sustainable polymers. The application of ultrafast laser technology to the injection molding market is new and there are a wide number of open points related to the technologies' integration. In this context, the design of mold surfaces represents the strategic juncture to boost processing innovations and new product functionalities.

In this work, the generation of novel engineered mold surfaces was studied to enable novel polymer flows in the cavity, characterized by lower energy requirements. Specific textures have been designed and manufactured to meet the polymer process requirements. Regular micro and nano surface textures, surface thin coatings, and the combination of textures and coatings are obtained and introduced into the injection mold to modify the morphological, chemical, and thermal properties of the surface. Experimental campaigns were carried out to characterize the effects of the modifications onto the cavity filling and the replication performances of the process. Filling studies focus on the flow phenomena happening during the filling phase and aim at reducing the pressure drop yielded by the polymer to completely fill the cavity. Replication studies focus on the interactions that affect the mold surface morphology replica and aim to optimize the replication fidelity.

In-line process monitoring and advanced characterization equipment have been implemented in the experimental investigations. The experimental results show that mold textures and surface coatings effectively reduce the pressure drop inside the mold cavity. The result has been translated in terms of material intensity reduction by calibrating a numerical model and modeling a case study with the proposed mold coating, obtaining a part volume reduction of 8%. The results of the experimental campaign on replication show that, depending on the replication grade of the mold micro- and nanostructures, the plastic parts can be functionalized, increasing the water contact angle. A process design tool for part functionalization was

implemented through a multi-scale model predicting the replication of the mold texture. A numerical model solves the macro flow in the cavity and feeds the proposed analytical model for the micro polymer flow into the structures. The multi-scale model is sensitive to the variations of the polymer and process, with a maximum error of 8%.

In general, the findings of this work can open new opportunities and markets for the laser texturing and injection molding sectors, providing tools for a more aware design of parts and molds towards the new market demands. Ultrafast laser-induced textures are specifically designed and manufactured for injection molding applications to introduce new functionalities as self-cleaning properties on injection molded parts in a cost-effective way. The multi-scale model resulted in a significant contribution to the understanding of the phenomena that control the injection molding process at the micro and nanoscale, providing tools for texture and process design. The efforts towards the modeling of the effect of coatings will allow for a more sustainable plastic part design, reducing their material intensity.

CONTENTS

I Literature Review

II Materials and Methods

III Laser texturing

IV Cavity filling

V Mold surface replication

VI Modeling

VII Conclusions

LIST OF FIGURES

LIST OF TABLES

Part I

LITERATURE REVIEW

1

OVERVIEW OF THE INJECTION MOLDING MANUFACTURING

Over the last century, plastic products and components have offered innovative solutions to society's permanently evolving needs. The high versatility and adaptability to always increasing applications fields match the fast innovation typical of such products. Plastics surely improve the quality of life of people across the globe, meeting functional and aesthetic demands, from drinking clean water to attractive LED car lighting systems. Plastics will continue shaping our future, however, we have to address the global changes relative to their negative impact on the environment, unlocking the full potential of these materials.

Plastic waste is unacceptable in any habitat. This is the plastics industry's top priority of all time. The global problem of plastic waste demands a global approach to the solution. The European guidelines stress the creation of strong relations between all stakeholders to develop, improve and reinforce circular management of plastic materials. Still today, most plastic materials are fossil-based. In the future, plastic production should decouple from fossil feedstock, introducing always higher amounts of alternative raw materials, like recycled plastics, chemically recycled polymers, and plastics produced by alternative feedstocks as bio-derived oils from responsibly sourced biomass. In addition to material management, there is also a need of addressing energy and emission savings. The plastic industry is still a poorly engineered industrial system, generating low-efficiency manufacturing processes, which grow into a crucial issue when applied to a large-scale process as polymer processing is.

Research in the field of plastics manufacturing processes has the responsibility to lead the engineering improvements of the technology, the plastic processes, and products. Increased technologic culture will result in higher global competitiveness triggering technological and economical growth, conjugated to a reduction of the environmental impact of the products and the process. New fit for purpose and resource-efficient products will be developed. New workforce will be needed to sustain this process, increasing the availability of higher-quality jobs and ultimately increasing the prosperity of the society we live in.

1.1 THE EU PLASTICS MARKET

Since the 1950s, the importance of the plastic market has been rapidly growing and still is getting more and more important in the world. In 2004, the global plastics production was reported 225 million tons [1] and, despite the restrictions applied by several states, increased by 143 million tons in 15 years, to 368 million tons produced in 2019 (cf. Figure 1.1 (a)). Due to the severe EU regulations, plastic production in Europe is slightly decreasing over the last three years. The result of such politics is shifting plastics production and manufacturing out of the European borders. Indeed, as the plastic worldwide production increases by 64% in 15 years (cf. Figure 1.1 (b)), the plastic imports from extra-UE countries have increased by 33% from 2014 to 2019 and the European plastic production share has contracted from 27% to 16% in 15 years. A lot has still to be done to effectively reducing and regulating the number of plastics and plastics products being used in Europe and worldwide.

The tremendous growth that the plastic market has experienced closely correlates with the difficulties that the world is facing in reducing and finding new alternatives to polymers. These new challenges arise from strong drivers that pertain to plastics.

- Many types of polymers have been developed to face effectively a large variety of specific functionalities.
- Polymers are often characterized by high specific material properties which favored replacements of conventional materials.
- Polymers are characterized by ease of processability, reducing the equipment and processing costs, thus facilitating both the technological growth and development of polymer processing technologies.
- Being easy to form, polymers can be successfully employed in net-shape or near-net-shape processes even if the part geometry has a certain level of complexity, satisfying close geometrical and aesthetic requirements.

The plastics manufacturing industry is mainly driven by three segments: (i) the packaging industry, (ii) the building and construction industry, and (iii) the automotive industry. The first two market segments are way dominating the plastic consumption, with overall consumption of 60% of the plastic produced in Europe in 2019 (cf. Figure 1.2). Different from the first two sectors, which mainly produce goods characterized by low-added value, the automotive sector exploits plastics for costly applications.

By selecting the most appropriate resin type, plastics could meet the needs of a large variety of markets. Consequently, the resin selection typically is firstly related to the market value of the good to be

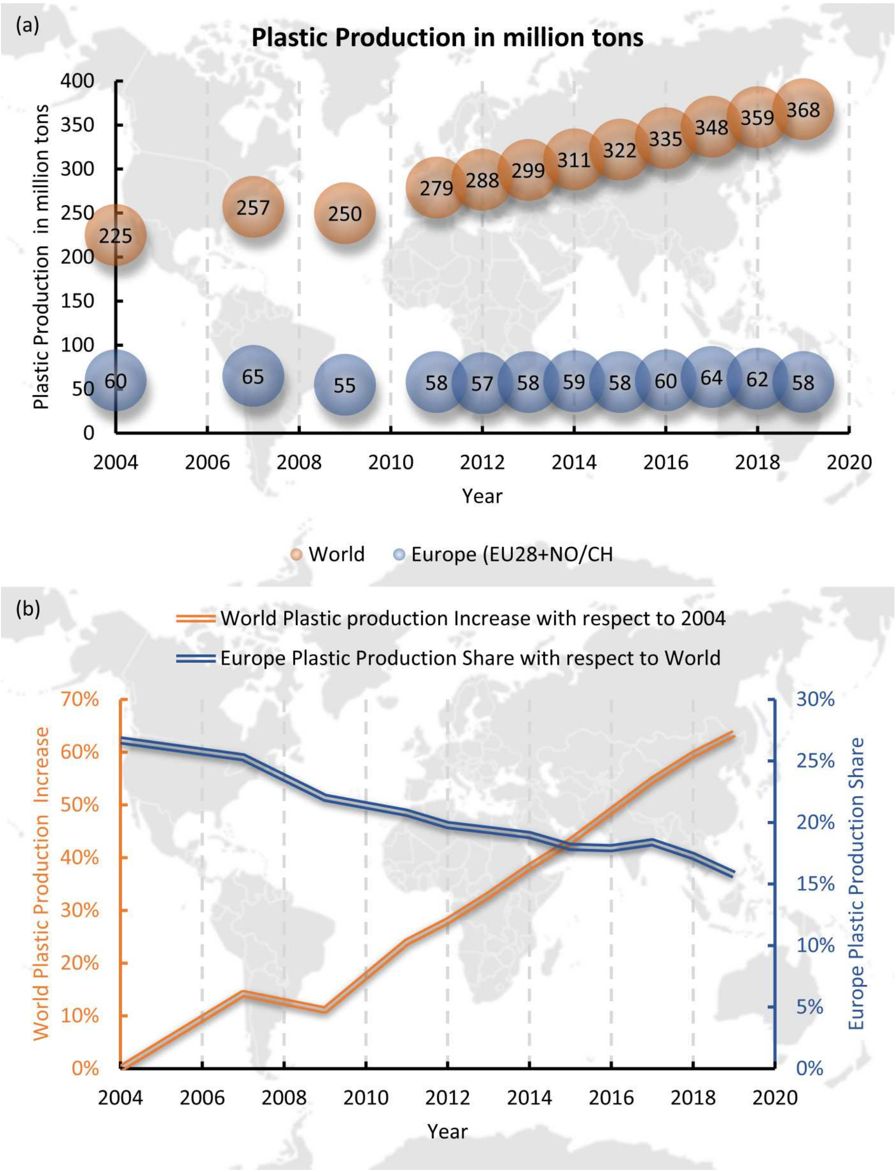

Figure 1.1: Global plastics production in million tons as reported by the last Plastics Europe Surveys (a) and World plastic production increase and the European share of the overall production (b) [1] [2] [3] [4]

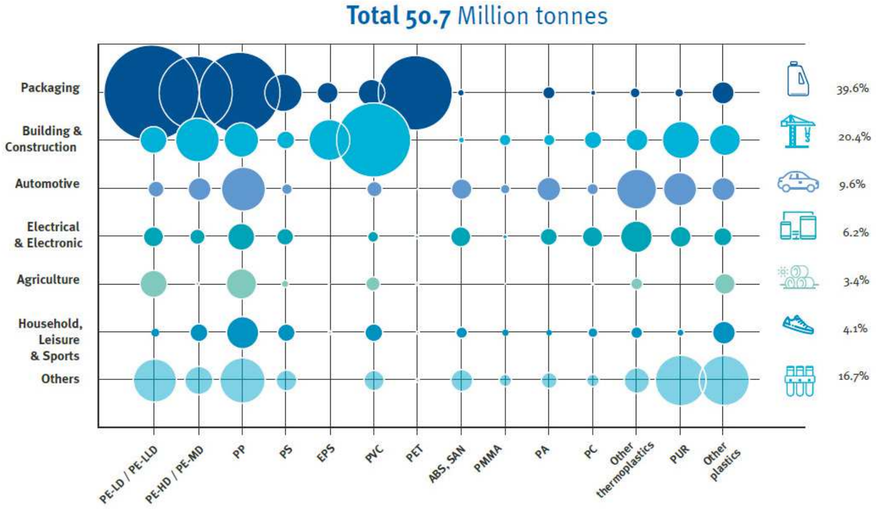

Figure 1.2: Plastics demand by segment and polymer type in 2019 [4]

produced. *'Commodity plastics'* are resins that are widely employed for low-cost products, that are typical of the packaging, the constructions and buildings, and the agriculture sector. To those resins belong the major production share. *Commodity plastics* are:

- *Polyethylene (PE)*: used for the major part in the packaging and building and constructions sectors.
- *Polypropylene (PP)*: an incredibly versatile resin, widely exploited in almost all market sectors. PP is the most utilized resin reaching almost 20% of the total resin demand in Europe in 2019 [4].
- *Polyvinyl Chloride (PVC)*: Largely used in the building and construction sector for pipes and electrical housings due to its thermal and mechanical properties.
- *Polystyrene (PS)*: Mainly used in the packaging industry due to its high transparency.
- *Polyethylene Terephthalate (PET)*: Used almost exclusively in the packaging industry for water and drinks bottles, due to its high transparency and high mechanical properties.

1.1.1 Environmental impact

The plastic market enormous growth and the increasing number of practical applications fulfilled by polymers had arose several environmental issues. The main problem linked to plastic production is the product end-of-life management. It is possible to observe that the major issue linked to plastic waste emerges by the much higher development speed of the plastic manufacturing sector in contrast to the plastic waste collecting sector. The European Union is indeed pushing the plastics world to be circular. The circular economy of plastics' first objective is the continuous increase of the amount of plastic post-consumer waste collected and sent to a disposal treatment. To address the environmental issue, this first objective is needed for the effectiveness of the following ones. Three are the main waste treatments for plastic products:

- *Recycling*: It is the preferred treatment for plastic post-consumer waste and comprises mechanical and chemical recycling.
- *Energy recovery*: The treatment converts the high energy content of plastic waste into electricity, synthetic gas, and fuels.
- $Landfill$: it is the to-be-minimized treatment, as it does not close the circular management of the material. Several European countries are applying restrictions to the amount of plastic waste sent to landfills.

Zero landfilling is needed to achieve the circular economy of plastics. Over the last 12 years, the European countries strongly improve the end-of-life management of plastic products, simultaneously increasing the amount of collected plastic post-consumer waste and the number of plastics sent to circular treatments (cf. Figure 1.3). Mechanical recycling of post-consumer plastic products is today's most favored end-of-life treatment, as it closes the feedstock circularity within the short cycle. It typically comprises 5 steps: (*i*) collection, (*ii*) first sorting, (*iii*) shredding, (*iv*) washing, (*v*) second sorting, and (*vi*) extrusion for ready-to-use material for manufacture new products.

1.1.2 Outlooks

In the last three years in Europe, we can observe a decline in plastics production. The Covid-19 impact on the plastics market caused a big drop in primary material production, which will not be recovered before 2022. Post-consumer recycled plastics are finding more and more applications in the market. The building and construction sector is the most receptive one, handling almost half of the total recycled volume of plastics (cf. Figure 1.4). A lot has still to be done for other sectors, as the automotive, and the packaging ones.

In this context, the development of more sustainable plastics and new sustainable plastics manufacturing technologies is important in order to aim at reducing the environmental impact of the whole sector. The plastics engineering production technologies have a crucial role in these processes, aiming at designing new manufacturing solutions for lighter products, enhanced recycling approaches, and new processing solutions for sustainable and bio-derived plastics feedstocks.

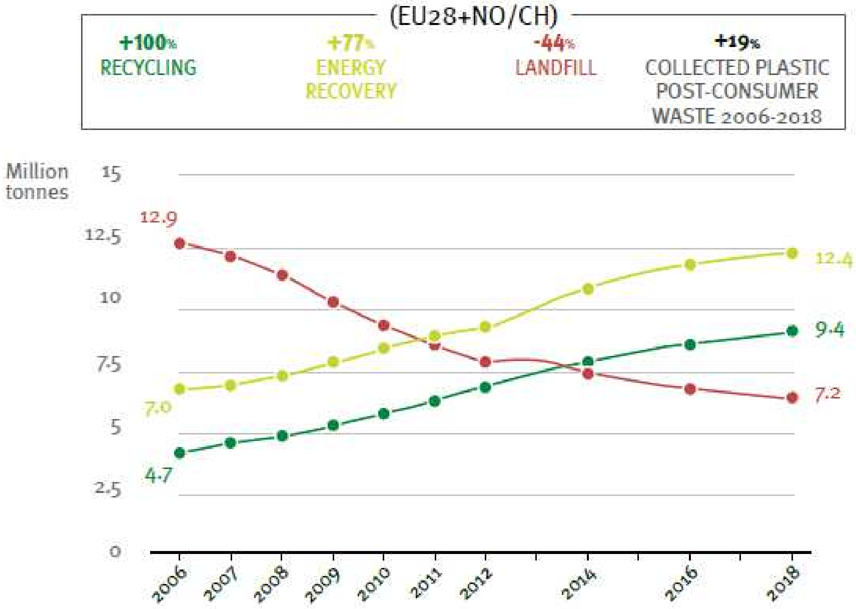

Figure 1.3: 2006-2018 evolution of plastic post-consumer waste treatment [4]

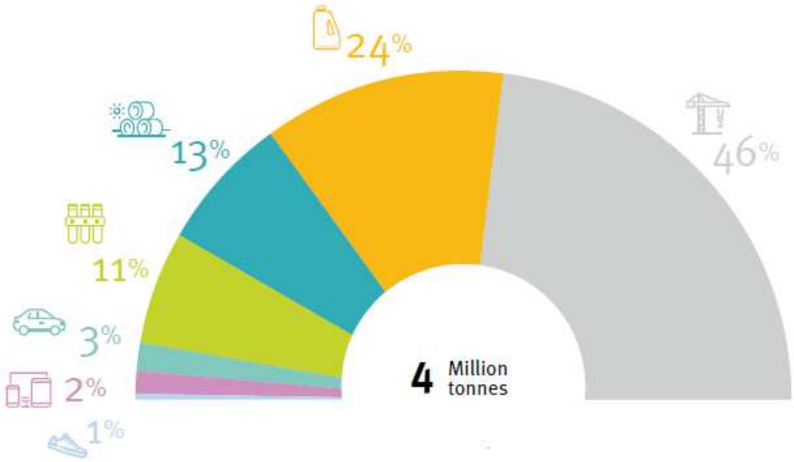

Figure 1.4: Plastic recyclates used in new products in Europe in 2018 [4]

1.2 INJECTION MOLDING

Nowadays, more than a third of the world's produced plastic products are manufactured with the use of injection molding [5]. The major strengths of the process can be individuated in the capability of manufacturing complex parts within a short cycle time, thus being highly suited for mass production applications [6]. Furthermore, the process is flexible to the employed resin and has an intrinsic high reliability. The injection molding process includes four major stages. Firstly, the reciprocating metering screw and the cylinder melt the polymer pellets exploiting the simultaneous mechanical and thermal action of the screw and the hot cylinder. Then, the polymer melt is injected into the colder metal mold. The third and fourth stages consist of cooling the molded part down into the mold and finally ejecting the final cold part.

Each of those stages presents its peculiar aspects, through which engineers and designers can elaborate to improve the final outcome of the part, in terms of part functionality, aesthetic quality, cost, and environmental impact [5]. Following these ambitions, the proper design of the features of the process will improve the following:

- Achievement of the desired shape and features of the part.
- Optimization of the outcome of the part surfaces.
- Establishment of process repeatability, control, and stability.
- Minimization of the material volume for the desired functionality.

Among the various ways to address the previous ambitions, this work puts the attention into two categories of injection molding products, linked to the part characteristics:

- Micro injection molding.
- Thin wall injection molding.

1.2.1 Machines and processing steps

Injection molding is a thermal and mechanical process of transferring the raw resins (which are in the form of pellets) into a part. Following the path of a single plastic pellet, it is possible to describe the thermal and mechanical evolutions through the process.

- *Drying*: The resin is firstly conditioned to get the most appropriate pellets environment for molding. Typically, in this stage, the pellets are dried from the moisture that can be present on their surface or even inside the pellet volume.

- *Plasticizing*: As the pellets got the required conditions it is melted and plasticized inside the plasticizing cylinder (barrel). The energy required for melting is mainly delivered to the resin by the screw, which shears the pellets increasing their temperature through viscous dissipations and friction. The cylinder's heating element's role is mainly setting and maintaining the desired temperature, to improve the consistency of the process.

- *Injection*: The screw movement accumulates the molten plastic on the front of the screw, ready to be injected. Once the mold is closed, the melt gets pressurized by the screw and is injected into the mold cavity.

- *Packing and cooling*: At the switchover point, the machine applies the packing pressure, in order to compensate for the polymer shrinking. Thus, as it gets inside the cold mold cavity, the melt immediately starts to cool down and shrink.

- *Ejection*: As the plastic inside the mold cavity has sufficiently solidified, the machine opens the mold and the ejectors demold the part.

The above-mentioned process is a typical injection molding process, which is carried out inside an injection molding machine. It is possible to individuate three different units that compose an injection molding machine:

- *The metering unit*: the major task of this unit is melting and plasticizing the resin, fed into the front of the screw, inject it into the cavity and maintain the holding pressure through the packing phase.

- *The clamping unit*: its role is to control the mold opening and closing, and tightly hold the two haves of the mold during mold closing to avoid flash formation.

- *The mold*: the mold is the heart of the injection molding machine, its cost can easily be higher than the cost of all the other parts of an injection molding machine together. The functions are to distribute the melt into the cavity, give the part its shape, and cooling it.

- *The auxiliaries*: To successfully operate an injection molding machine, auxiliaries are always required. Depending on the application, different auxiliaries have to be considered, but typically the machines need a drying unit for polymer conditioning before processing and a thermoregulator to control the mold temperature.

1.2.2 Micro injection molding

The miniaturization of parts is an escapable step for the evolution of technologies, where more functions would be integrated into a lower space. The miniaturization goal has continuously pushed the technologies to a lower scale, trying to match the mass-production goals to small components. From the 1980s microsystem technologies have grown in importance and nowadays play a central role in the market [7]. Micro injection molding can be considered as miniaturization of the injection molding process and aims at meeting the low-cost mass-production identity of injection molding to the request of small components and tight tolerances. Moreover, a large variety of polymers can be processed through micro injection molding to obtain the required application-related properties. In this context, micro injection molding can be assessed as a key enabling technology, with the capacity of producing micro components at a low cost.

Micro injection molding can be defined as the modification of the injection molding technology to produce micro parts. In this sense, the definition of what injection molding is can be translated into the definition of what a micro-molded product is. A micro molded product can be defined as [8]:

- Parts possessing weight in the range of few milligrams.
- Parts that show features with dimensions in the micrometer range.
- Parts possessing micrometer dimensional tolerances, which have not a dimension limit.

1.2.2.1 *Downscaling injection molding*

The micro injection molding process raises new processing challenges with respect to conventional injection molding. The small features that have to be replicated typically require higher forces and pressures which need to be tightly controlled. To accomplish these major requirements, the equipment typically includes a modified metering unit, where the plasticization and the injection are separated (cf. Figure 1.5). The plasticization takes place in a dedicated functional part of the machine, where the screw melts and ultimately delivers the melt into an intermediate hot chamber. An injection plunger (which can be as small as 5 mm in diameter) is exploited to inject and dose the desired volume of material in the cavity. By splitting the plasticization and injection phases, it is possible to overcome the limitation on the screw diameters (typically min 12 mm). In such a way the injection system can suitably answer the processing requirements of micro injection molding:

- Accurate melt dosing of small volumes.

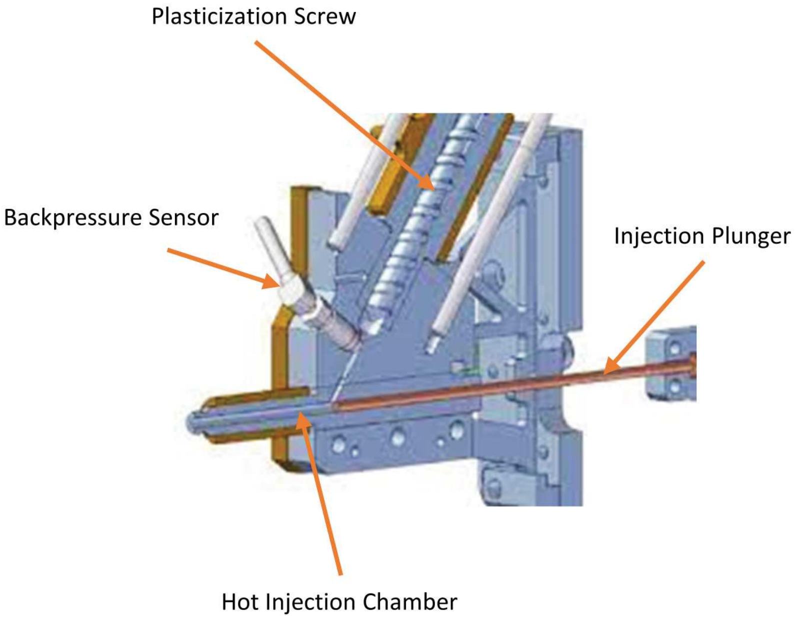

Figure 1.5: Typical modified metering unit for microinjection molding applications.

- Precise high-speed injection.
- Resistant to high injection pressures.

1.2.2.2 *Applications*

A broad range of micro molded parts are already in the market, and many are going to arise in the future. Micro injection molding is one of the most promising technology for high volume production of micro components with high dimensional accuracy and replication fidelity. Those capabilities, combined with the wide variety of processable thermoplastic polymers, opens the possibility of producing high-volume and low-cost parts for many diverse stakeholders. Markets in which microparts are already applied are:

- Medical technology (e.g. micro-fluidic devices with micro-channels hearing aids, implants, devices for DNA analysis, bio-MEMS, tissue scaffolds, vascular clamp).
- Micro-structured micro-parts (lab on the chip, data carrier, self-cleaning surfaces, sensor disk structure).
- Sensors (e.g. airbag sensors, sensor disk, bio-sensors).

- Automotive (e.g. micro-switch, sensors, ABS-Systems).
- Computer (e.g. head of an ink-jet printer).
- Telecommunication (e.g. mobile phone, SIM card connector).
- Micro-equipment (e.g. valve technology).
- Glass fiber conductors (ferrules, connectors).
- Connectors (e.g. plug connectors, couplers).
- Electronics micro parts on circuit boards.
- Sensors (e.g. airbag sensors, sensor disk, bio-sensors).
- Micro-mechanics (e.g. micro-motor, rotor, micro-gears, microswitch, locking lever, catch wheel, operating pins, sleeve).
- Optics (e.g. lenses, displays).
- Precise suppliers.
- Watches (e.g. gear wheels, latches, micro-transmissions).
- Patterned adhesives.
- Special materials (e.g. PIM (MIM/CIM), PTFE).
- Institutes, Universities (e.g. material, technology for research).

The miniaturization trend has been reinforced by the successful realization of micro components, and now new parts with sub-micro and nano features are in the process to enter the market. New technological challenges are set, both regarding the microinjection molding process and mold-making technologies.

1.2.3 Thin wall injection molding

The product's environmental impact reduction is now one of the most demanding objectives during product design, especially in the packaging and automotive sectors. Two are the strategies that are commonly applied in those sectors, the reduction of the amount of material per functionality and the substitution of the product material with a more *green* one, which may be recycled or simply more sustainable (e.g. bioderived polymers). Often, the two strategies are applied together to multiply the effectiveness of the engineering solution.

In this context, thin-wall injection molding is a specialized application of the process which focuses on the production of thin and light parts. The definition of a thin wall refers to the nominal thickness and surface area of the part (they have to be less than 1 mm and at least

50 cm^2, respectively), thus to the flow/thickness ratio (typically above 100) [9]. In general, the major benefits of thin-wall injection molding are linked to the reduction of the part volume, which translates into:

- *Reduced material consumption*: less material hat to be employed, leading to a decrease of material costs and environmental impact.
- *Faster cycle times*: thinner parts cool quicker, triggering a faster process which reduces production costs and energy consumption.
- *Reduced weight*: when considering parts that travel a lot during their use phase, lighter parts become less energy-intensive (typical for products of the packaging and automotive industry).

Thus, thin wall injection molding can be considered an environmentally oriented modification of the conventional injection molding process.

1.2.3.1 Issues

The part nominal thickness is the leading parameter that determines the manufacturability of a plastic part. Indeed, despite all the efforts towards miniaturization, the thickness of an injection molded plastic part is often constrained by the manufacturing technology, oversizing the thickness required for the product functionality. The thin wall has been recognized as a major manufacturing constraint [10]. The difficulty lies in the fast cooling of a thin section during cavity filling. As the polymer melt is pushed into the cold cavity, a frozen layer immediately develops in contact with the mold. This layer (called the skin layer) has an increased effect as the cavity thickness is reduced, leading to incomplete replication of the cavity or even short shots. Moreover, the stabilization of the process becomes hard to develop, as the processing window shrinks. For these reasons, highly skilled technicians are typically required to manage the process effectively. A reduced cavity thickness mainly leads to:

- *Faster cooling of the melt*: the amount of heat carried by the melt is lower, triggering fast freezing which may cause short shots or incomplete replication. In addition to that, polymer cooling is much more sensitive to mold temperature, thus well-designed cooling systems are needed to achieve good parts.
- *Increased resistance to the melt flow*: higher injection pressures are required to fill small sections, ultimately increasing the pressures and forces acting on the mold tool, which has to be designed accordingly.

- *Reduced processing window*: the fast freezing of the melt and the high resistance to the melt flow narrows the processing window down, requiring highly skilled technicians and more sophisticated technologies.

The processing issues are even more severe when the two environmentally friendly strategies (i.e. material volume reduction and selection of recycled or bio-derived materials). Indeed, often those polymers suffer from other issues as fast degradation or increased viscosity [11]. More sophisticated processing and technologies are then required to accurately run those materials.

1.2.3.2 Applications

The economic (i.e. lower material and processing costs) and environmental (i.e. reduced material and energy intensity of the product) convenience in producing thin-walled parts are attracting more and more stakeholders to the manufacturing technology. Above all, the industrial sector that dominates are:

- Food packaging
- Medical
- Automotive
- Computing equipment
- Electronics
- Mobile telecommunications

An iconic application of the thin wall injection molding for packaging is certainly the polyethylene terephthalate (PET) bottle. The thickness of the (to be blown) preform is set by processing constraints. Both fast melt cooling and high-injection pressure constraints apply to this application. Indeed, the mass-production characteristic of the product pushes molders to set low mold temperatures (even lower than 15°C) which brings to filling issues. In addition, huge molds with many cavities (it is not strange to find molds with 56 cavities) highly increase the required injection pressure.

In bio-medical applications, thin wall designs often coincide with the presence of micro and even mano features of the part surface. A typical example is the lab-on-a-chip devices, which integrate several functionalities into a single plastic part. The functionalities are mainly activated by the surface topography, which alters the part response to liquids and micro-organisms.

1.2.4 State of the art of micro- and thin wall injection molding

Considering the context described in this chapter, micro-and thin wall injection molding has shown the potential to mass-produce complex and environmentally optimized plastic parts and can be considered as key enabling technologies. However, the market and the increasing strictness of international environmental regulations are setting new goals. Following this trend, the market is requiring always thinner and more complex parts, arising severe technological issues.

Sub-micro and nano part features are now required to match the functional and aesthetic requirements of new high-tech products, pushing to the limit on one side the mold making technologies, and on the other side the replication technologies. The material ablation techniques employed for the conventional injection molding are not suitable for features on the microscale (and even smaller) [7]. New technologies have to be explored, aiming at achieving the desired topography at a competitive cost.

The injection molding of such innovative parts and features triggers new challenges. In particular, the filling phase [12], the replication effectiveness [13] and the part ejection [14] are critical steps for the positive outcome of the process. The understanding of the physical mechanisms involved in the process steps and the processing constraints for the production is essential to improve both the design and manufacturing stages.

2 CAVITY FILLING

Nowadays, it is difficult to imagine a world without plastics. However, its increasing use has been leading to enormous burdens for environmental sustainability. The massive commercial growth of plastic components has not been accompanied by the efficient development of the plastics manufacturing industry. This has been leading to the ‘demise‘ of manufacturing in developed countries due to industrial inefficiencies and low global competitiveness [15]. According to the European waste management hierarchy, which indicates an order of preference for action to reduce and manage waste, preventing plastic waste generation is the most effective way to reduce the environmental impact of plastics [16]. Waste prevention (or minimization) includes a series of processes and practices that aim to reduce or eliminate the amount of harmful and persistent waste generated. Waste minimization supports efforts to promote a more sustainable society [17]. Plastic waste minimization involves redesigning products and processes as well as changing societal patterns of consumption and production.

Plastic parts are widely produced by injection molding, which is the most cost-effective manufacturing technology for mass production of complex geometries. Injection-molded parts are designed to maintain a uniform thickness because it will allow for the most balanced flow of the plastic through the mold cavity and the uniform cooling and shrinkage of the part. The decision to establish a nominal wall thickness is dictated by the functional performance requirements of the part, considering the mechanical and physical properties of the selected plastic. For example, refrigerator drawers can be molded using polypropylene (PP), which has a flexural modulus of 1600 MPa, or a compound of PP filled with 30% by weight of talc, which has a flexural modulus of 3300 MPa. Due to the significant difference in mechanical properties, a drawer made of PP and designed with a wall thickness of 2 mm has the equivalent bending stiffness of a 1.6 mm thick drawer made of PP filled with 30% talc. Plastic waste minimization through product redesign can be achieved by exploiting the higher mechanical properties of compounds, engineering plastics, and high molecular weight polymers compared to commodity plastics. The reduction of the main wall thickness generally results in a smaller part volume and, therefore, in lower material intensity. Injection molding a thinner wall part also results in a shorter cycle time, decreasing the economic and environmental burdens related to the

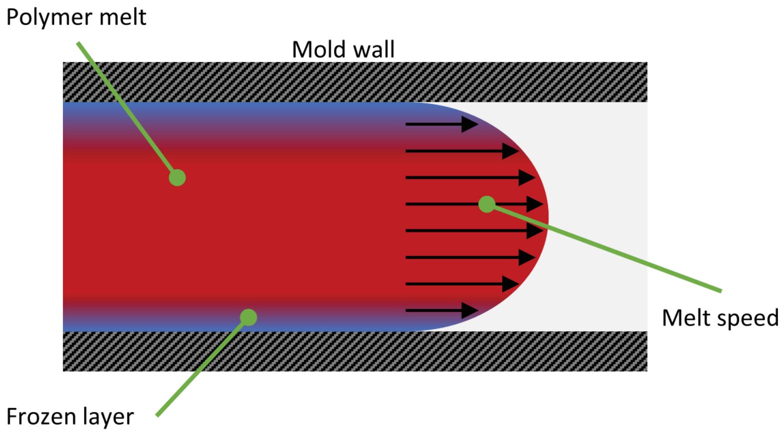

Figure 2.1: Fountain flow of polymer melt.

process [18]. However, the filling of narrower cavities requires higher injection pressure, thus limiting the manufacturing capabilities [19].

2.1 IN-CAVITY FLOW MECHANISMS

2.1.1 Fountain flow

In conventional injection molding, the hot polymer melt is pushed inside the cold cavity to allow for polymer solidification in a short time. Therefore, the mold temperature is set below (frequently it is set well below) the freezing temperature of the selected resin. Hence, when the polymer melt enters the cavity, during the injection phase, the outer skin in contact with the wall freezes. The core remains in a fluid state and it moves forward towards the melt front area and out to the wall surface (c.f. Figure 2.1). This is known as the *fountain flow* and is characterized by a so-called *skin – core* morphology. The skin formed along the surface of the main cavity generates two major effects:

- *Reduced flow section*: the skin formation along the cavity wall reduces the flow section of the moving melt, increasing the pressure requirement;

- *Hesitation effect*: the skin formation opposes the filling of features placed on the surface, reducing the effect of the packing pressure [20].

2.1.2 Heat Transfer Coefficient

The heat convection between the filling polymer and the mold is generally described using the Heat Transfer Coefficient (HTC). The HTC is defined as the ratio between the heat flux and the temperature difference, which acts as the driving force of the heat flux.

$$HTC = \frac{q}{\Delta T} \tag{2.1}$$

Where:

- q is the heat flux (W/m^2);
- HTC is the heat transfer coefficient W/(m^2°C);
- $\Delta\ T$ is difference in temperature between the mold surface and the polymer melt.

The HTC changes along the molding cycle, being higher during the injection phase and progressively lowering its value. Typical values for the HTC range between 2000 and 5000 W/(m^2°C). A physical explanation of the phenomena can be qualitatively addressed through the molding phases:

- In the filling phase, high cavity pressures, and high melt speed promote a high HTC;
- In the packing phase, the cavity pressure is still high, but the melt has no or very limited speed, causing a reduction in HTC;
- In the cooling stage, the holding pressure is released, and the part shrinks, eventually forming an air gap between the yet solidified polymer and the mold.

2.1.3 Polymer flow in thin-wall cavities

Thin-wall injection molding is characterized by the high flow length-to-thickness ratio, which requires high injection pressure to drive the Poiseuille flow and achieve complete replication of the mold geometry [9]. A smaller cavity thickness can cause shear rates to be an order of magnitude higher than those experienced in conventional injection molding [21, 22]. Indeed, shear stress and shear rate are inversely proportional to cavity dimension:

$$\tau, \eta \propto \frac{1}{h} \tag{2.2}$$

The flow of polymer melts in cavities with reduced dimensions are characterized by different filling behavior compared to conventional cavities [23, 24]. For instance, viscosity was found to increase as cavity size decreases to micrometers [25]. In order to reduce polymer flow resistance, possible solutions involve the adjustment and optimization of critical process parameters - such as the temperature of the mold and injection speed [26] - and of the mold and gate design [27].

2.2 SOLUTIONS FOR REDUCING POLYMER FLOW RESISTANCE

The reduction of the polymer flow resistance brings to several processing advantages:

- The reduction of the required injection pressure to fill the cavity, lowering both the requirements for the injection molding machine and the forces acting on the mold tool.
- The reduction of the pressure gradient along the cavity during the filling phase.
- The reduction of the shear stresses of the injected melt along the fill path.

In the literature, several authors have been focusing on strategies to reduce the melt flow resistance by optimizing the most impactful process parameters [26]. By increasing the process thermal boundary condition (i.e. the mold temperature) it is possible to control and ultimately delay the development of the skin layer. The skin layer of frozen polymer effectively reduces the flow area of the injected melt. This has been achieved through rapid heat cycle molding (RCHM) (also known as Variotherm), which consists of rapid heating of the mold temperature before injection and subsequent fast cooling of the tool to allow for freezing of the polymer and ejection of the part. The approach is capable of heating the mold above the glass temperature of the polymer, avoiding the formation of the skin layer [28, 29]. The benefits that the RHCM technology offers are not only linked to the drag reduction but comprises also better surface quality and a more uniform packing of the part. Despite those advantages, RCHM is characterized by high initial investments for the fabrication of the tool, and it significantly increases the cycle time and energy consumption, increasing the processing costs [30].

One alternative to RCHM is high-speed injection molding. The technology requires a high initial investment for the mold tool and complex process optimization. The fast melt injection counteracts the skin layer formation to allow for the complete filling of the cavity. The typical application of the technology is thin wall cavities that suffer from short shots. High speed injection molding typically does not reduce the injection pressure but is exploited to fill cavities that the conventional process is not able to fill.

Following the thermal concept of RCHM, one other melt flow drag reduction strategy uses insulating mold coatings to delaying the heat transfer between the hot polymer and the melt. This technology, known as 'passive variotherm', delaying the polymer freezing during the injection phase, reduces the skin layer thickness and the cross-section freezing and ultimately the melt resistance [31]. Similar to the RCHM, improvements in the superficial characteristics have been found for ABS components produced using TiN and PTFE-coated molds [32]. The reduction of the melt flow resistance associated with the thermal insulation effect of the ceramic mold surface coatings can be described by modifying the HTC between the melt and the mold. However, few investigations are still present in the literature, especially when considering the rheology of the polymer melt and the contribution of the processing conditions on the HTC value.

2.3 WALL SLIP

Polymer resistance builds up during cavity filling as a result of the stresses which form due to shear. The polymer in contact with the mold is generally assumed as perfectly adhered to the mold surface. The no-slip boundary condition is typical in fluid systems. However, polymer melts slip over solid surfaces when the shear stress exceeds a certain threshold [33]. Understanding the wall slip phenomenon is of primary importance in determining the polymer behavior during polymer (typically high-speed) manufacturing processes [34].

An interface rheological law was proposed by Brochard and de Gennes, describing the wall slip phenomenon in terms of an extrapolation length called *slippage length b* [35]:

$$u_s = b\left[\frac{du}{dy}\right]_{y=0} = b\dot{\gamma_w} = \left[\frac{b}{\eta}\right]\sigma_w \tag{2.3}$$

where u_s is the slip velocity, $\dot{\gamma_w}$ is the shear rate at the wall (i.e. the slope of the velocity profile at the interface, cf. Figure 2.2) and η is the viscosity of the melt at $\dot{\gamma_w}$.

2.3.1 Macromolecular interactions during flow

Considering a polymer melt flowing in contact with a solid surface, a certain level of diffusion between the atoms of the polymer inside the solid wall is present. It is generally assumed that this phenomenon only involves few atoms of the long macromolecular polymer chains. The diffused atoms create attachment sites for the polymer macromolecules to the wall [36].

The polymer molecules that are attached (or adsorbed) to the solid wall are connected to those of the bulk of the flowing melt through

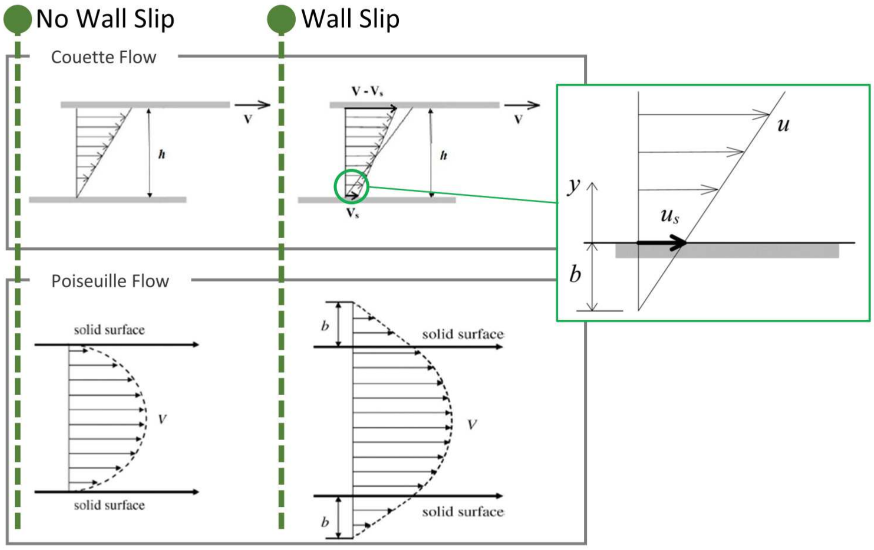

Figure 2.2: Speed profile for a polymer melt subjected to Couette and Poiseuille flows in no-wall slip and wall slip conditions.

entanglements with the neighbor ones. Considering the interaction of the polymer macromolecules at the solid-melt interface, it is possible to categorize three types of wall slip phenomena (c.f. Figure 2.3) [33]:

i. *Weak slip regime*: under relatively low shear regimes, the adsorption sites fail and detachment/desorption of the macromolecular chains from the wall occurs, leading to weak slip. In this flow regime, small deviations from a no-slip boundary condition can be detected.

ii. *Stick-slip regime* – under intermediate shear stresses, partial disentanglement and subsequent re-linking of the bulk macromolecular chains from chains adsorbed at the wall leads to the onset of periodic oscillations in slip velocity and shear stresses.

iii. *Strong slip regime* - under strong flow conditions the macromolecular chains adsorbed at the wall orientate along the flow direction, causing a sudden disentanglement and impeding the relinking of the polymer molecules. Thus, the mechanism of slip is a relative motion of the chains in the bulk over those in the monolayer of polymer chains adsorbed at the wall [37]. In such conditions, the velocity profile of the polymer melt flow approaches that of a plug flow.

Wall slip is a complex phenomenon which depends on several parameters linked to the physical conditions in which the process is carried out and the properties of the processed polymer and the solid surface. The most important parameters affecting wall slip are:

- The processing temperatures [38];

- The pressure and shear imposed by the process [39];
- The surface energy and the topography of the solid wall [40];
- The molecular weight and stiffness of the polymer chains [41, 42].

2.3.2 Wall slip in injection molding

Despite the relatively large research efforts, the vast majority of the investigations on wall slip were performed under isothermal conditions. The intrinsic high non-isothermal conditions of the injection molding process put severe complications on the modeling and understanding of the mechanisms of the wall slip. Despite these considerations, often the wall slip phenomenon is evocated for thin-wall injection molding applications [43].

Open-flow silt die cavities were exploited to evaluate the reduction of the apparent viscosity due to wall slip for processing conditions that want to approach those of injection molding [44, 45]. Ebrahimi et al. studied the wall slip in a slit die for different solid surface topographies and surfaces energies [46]. However, the experiments were always carried out in isothermal conditions, keeping the mold (or die) temperature equal to those of the polymer melt, which does not apply to injection molding. More recently, wall slip on non-isothermal conditions was experimentally studied with polystyrene using coated mold cavities. Correlations with the wetting behavior of the wall and the wall slip velocities were found, with a negative correlation between the two [47]. A numerical model was calibrated on the experimental results of wall slip in non-isothermal molding conditions using patterned mold surfaces [48]. The results show that the presence of certain patterns can increase the slip velocity. However, those experiments were carried out using ultra-thin cavity thicknesses, which can be hardly translated in industrial applications.

2.4 MOLD COATINGS

Polymer resistance to flow results from the shear stresses that the melt is experiencing during the injection. Assuming a no-wall slip condition, the shear rates are only determined by the polymer flow rate and the cavity geometry. In thin-wall applications, the polymer resistance can invalidate the outcome, causing short shots, inhomogeneous packing, and low mold replication. Shear stresses can be lowered by increasing the temperature on the polymer, especially in the volumes affected by high shear rates (i.e. close to the mold surface). The use of insulating coating can be seen as a modification of RHCM

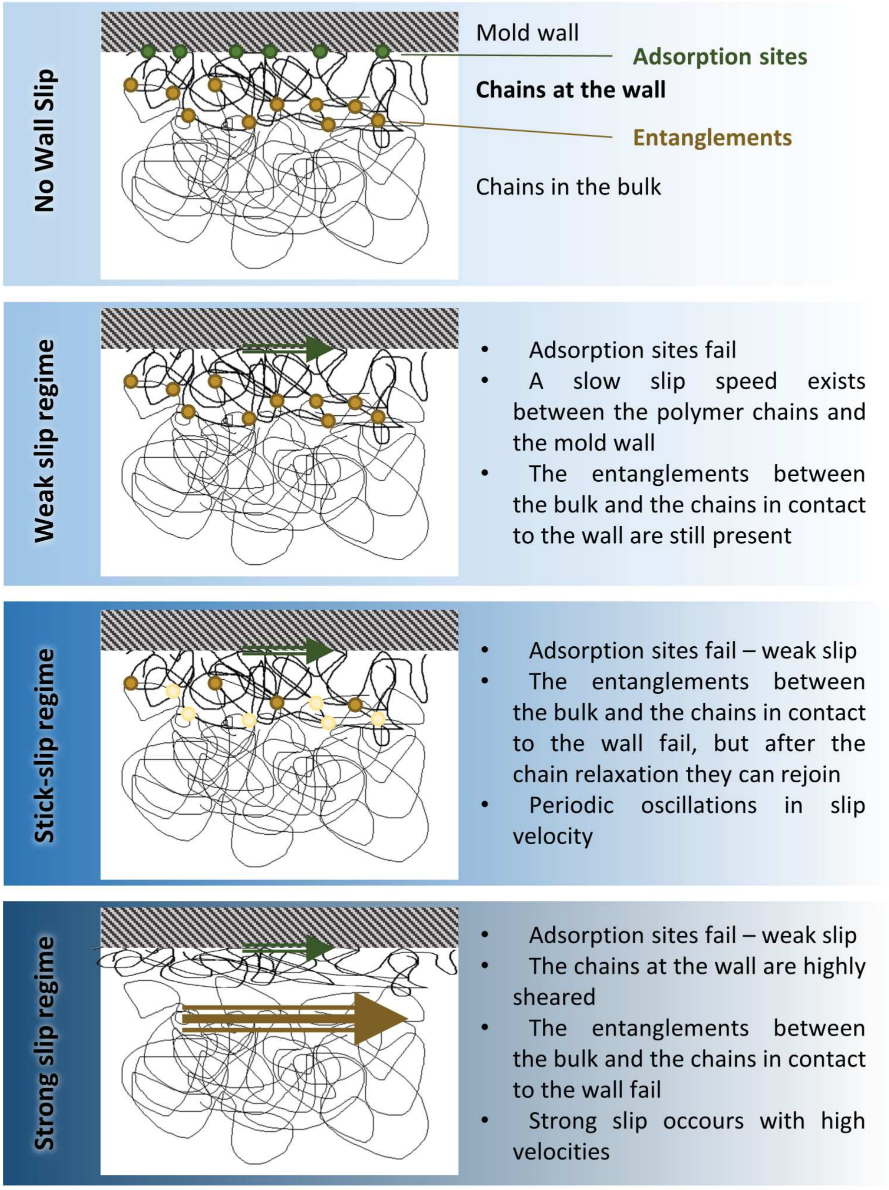

- Adsorption sites fail
- A slow slip speed exists between the polymer chains and the mold wall
- The entanglements between the bulk and the chains in contact to the wall are still present

- Adsorption sites fail – weak slip
- The entanglements between the bulk and the chains in contact to the wall fail, but after the chain relaxation they can rejoin
- Periodic oscillations in slip velocity

- Adsorption sites fail – weak slip
- The chains at the wall are highly sheared
- The entanglements between the bulk and the chains in contact to the wall fail
- Strong slip occours with high velocities

Figure 2.3: Wall Slip regimes and the interactions between the mold wall, the chains at the wall, and the chains in the bulk.

(cf. section 2.2) and is known as 'passive variotherm' [31]. The technology is passive as no further energy consumption is required. The insulating coating acts delaying the heat transfer between the polymer melt and the mold surface. The thermal delay effect is limited to the filling phase.

ABS components molded into a TiN (i.e. titanium nitride) and PTFE (i.e. polytetrafluoroethylene) coated mold showed enhanced surface characteristics [32]. Other researchers demonstrate how mold surface coatings modify the interfacial tension between polymer and mold, affecting the friction during the injection phase [29]. Therefore, mold surface coatings improve the thermal and tribological properties of the polymer-mold interface, unaffecting the resin properties. Moreover, the process-related benefit, namely the reduction of the melt flow resistance, could be translated into an improvement of the processability of the part or could have an impact on the thickness of the cavity. Indeed, by lowering the polymer resistance to flow, it is possible to fill narrower cavities at the same injection pressure, enabling material savings. Concluding, mold coatings can both improve the mold tribological and thermal properties, extending the mold life and enabling the processing of thinner parts.

2.4.1 Skin layer reduction

During injection, the hot polymer melt develops the so-called fountain flow [49]. The melt layer that touches the cold mold quickly cools down steel and freezes creating the *skin layer*. The frozen polymer layer buildup on the mold walls progressively reduces the flow section, increasing the melt resistance to flow and ultimately triggering part defects as short shots. The mold surface coatings act delaying the heat transfer at the fluid/solid interface, by reducing the HTC (cf. subsection 2.1.2). Therefore, the amount of heat drawn by the mold walls is lower, reducing the skin layer thickness and maintaining a more open flow section. In Figure 2.4 the effect of mold coatings on polymer flow is schematized. The reduced section of the uncoated setup causes a steeper melt speed profile, which origin higher shear rates and stresses.

2.4.2 Shear induced-crystallization

The outcome of the molded part and the process derive largely from the nature of the selected resin. When considering semi-crystalline polymers such as polypropylene (PP), polyethylene (PET), or polyamide (PA), the crystallization phenomena that occur during molding have to be considered [50]. The crystals' nucleation and growth kinetics is a function of material, process, and thermal variables. As the molten polymer enters the cold cavity, it experiences a complex non-

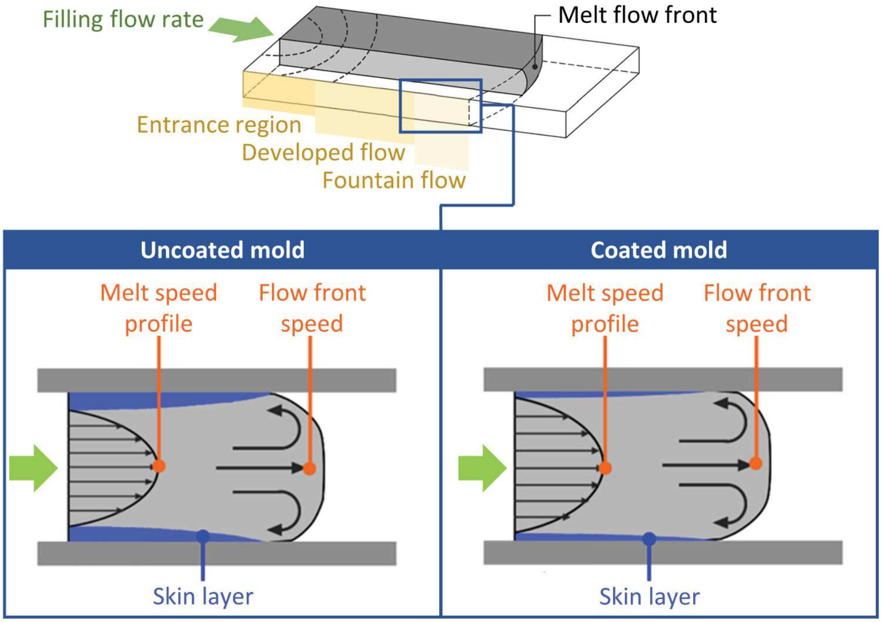

Figure 2.4: Schematics of the effects of mold surface coatings on the skin layer thickness growth and cavity velocity profiles.

isothermal shearing flow, which ultimately affects the crystallization phenomena [51]. The crystallization behavior may influence the viscosity and therefore the process dynamics more than a decrease in temperature [52].

Polymer crystallization kinetics was deeply investigated for resins subjected to cooling or shear. During injection molding, the two phenomena occur simultaneously, increasing the complexity of the macromolecules' behavior. Polymer crystallization rate (with respect to cooling) is extensively studied, in order to engineer optimized resins for easier processing or improved product qualities [50]. Crystallization rate studies are typically carried out in static and slow cooling conditions, to successfully control and describe the physical process mechanisms.

The crystallization thermodynamic barrier for the crystal formation decreases by applying deformation [53]. The phenomenon is known as flow-induced crystallization (FIC) or shear-induced crystallization (SIC). Parallel plate [54], rotational [55], and channel flow [56] geometries have been extensively exploited to study the crystallization dynamics under shear in the literature. However, those studies are typically carried out in isothermal or slowly cooling systems.

A glass fiber was used to generate shear onto an isothermal polymer volume [57]. The molecular structure of the polymers was found relevant in the crystal formation process. Crystals' growth rate was studied by Duplay et al. [58] as a function of the molecular weight of the resin. The growth rate was observed to increase when the polymer is subjected to shear. A 10-fold increase in growth speed was found as a function of the molecular structure. In particular, an increasing the average molecular weight of the macromolecules results in a higher crystal growth rate. D'Haese et al. [59] found that an increase in the shear rate stretches and orients the macromolecules for quicker nucleation. Interestingly, the trend was observed only at low and high shear rates. In between, a plateau was found. Farah and Bertas [60] studied the shear-induced crystallization of isotactic polypropylene exploiting a rotational rheometer and a slit die finding that there is a sudden steep increase in shear stress, which is correlated to melt crystallization. The time between the starting of external input and the crystallization onset (i.e. induction time) was found dependent on polymer and environmental variables and, in particular, on the shear rate and temperature of the melt [50]. The induction of FIC was found to be triggered by a certain level of strain accumulated by the polymer melt [61]. Interestingly, the threshold strain was found to increase for increasing shear rates. Scelsi et al. [62] experimentally validated a numerical model of the FIC and propose that the nucleation begins when a critical value of specific work is undergone by the polymer. Beyond the strain levels, the temperature has a primary role in FIC. Derakhshandeh et al. [61] found that temperature controls the decrease of the thermodynamic barrier for crystal formation. Indeed, the results show that a few degrees of temperature variation alter the induction times by an order of magnitude.

Polymer crystallization during cooling or shear has been explored thoughtfully. Generally, crystallization is facilitated when an increase in strain and strain rate or decrease of temperature is found. However, the typical non-isothermal shearing flow conditions of the injection molding process are still far from the studied conditions. New approaches for investigating the nucleation and growth of the crystals are required for a better understanding of the viscosity evolution in the cavity. In this context, the filling phase is of particular interest since steep changes in viscosity would alter the cavity pressure distribution and ultimately the part quality.

3 REPLICATION

In the last decade, submicron-structured surfaces have attracted considerable attention in the medical, automotive, aerospace, and mechanical industries. The modification of the surface morphology can improve the surface properties, adding value to the product. In the medical field, such structures are applied to tissue engineering, antimicrobial surfaces, and other functional devices.

Recent advances in regenerative medicine and tissue engineering often depend on the use of temporary scaffolds made of biocompatible and resorbable polymers to drive and optimize tissue growth [63]. A range of synthetic bio-based polymers has been developed for this purpose [64]. Among these, polylactic acid (PLA) and its copolymers are the most widely utilized. In the automotive, aerospace, and mechanical industry applications of micron and submicron-structured surfaces comprehend self-cleaning surfaces [65, 66], optical gratings [67], anti-icing surfaces [68, 69], and friction reduction [70, 71]. Similar textures have also been applied to injection molding tools, specifically to cavity vents [72] and surfaces [73].

3.1 IN-CAVITY REPLICATION MECHANISMS

One of the most cost-effective technology for the mass-production of plastic parts featuring submicron-structured surfaces is to replicate a master geometry by microinjection molding [74]. Polymer replication at the submicron scale is challenging since the injected molten polymer tends to hesitate and solidify at the entrance of the submicron features [10]. The replication quality is influenced mainly by mold temperature, melt temperature [75], injection velocity [76], and packing pressure [77]. Replication of the submicron mold structures occurs either during the filling phase or the packing phase of microinjection molding [78]. The replication phenomenon is mainly controlled by the temperature of the outermost layer of the melt, which ultimately controls the polymer local viscosity.

3.2 FILLING PHASE REPLICATION

Replication of the submicron mold structures occurs in the filling phase when relatively low mold temperatures are set. Low mold temperatures allow for fast cooling and ejection of the part, thus shortening the cooling time and ultimately the process impact on the part cost. At low mold temperatures, the outermost layer of the polymer melt in the vicinity of the structures solidifies (or vitrifies) in less than a millisecond [79].

3.2.1 Role of injection speed

During the filling phase, the maximum cavity pressure is reached at the very end of the injection stroke, when the flow front reaches the end of the cavity. The sharp increase in pressure can drive more material into the mold micro structures [76]. By increasing the injection speed, it is possible to achieve a faster filling of the cavity that promotes:

- Higher increase of the cavity pressure at the end of fill;
- Faster filling translates in less time for the polymer in contact with the mold to freeze before the cavity pressure increase.
- Higher shear rates at the wall which promotes lower polymer viscosities;
- Higher temperature of the polymer in contact with the mold, thanks to shear heating effects.

The scheme proposed in Figure 3.1 compares the conventional injection speed and high injection speed pressure and temperature profiles along with the filling phase. Thanks to high injection speed, the melt in contact with the mold has less time to cool down, thus its temperature is higher. Moreover, the increase in cavity pressure along the filling flow further promotes the filling of the microcavities. At the end of fill, the sharp increase in cavity pressure is more pronounced for high injection speed. The higher local temperature and pressure at the end of fill promote a high replication of mold microstructures.

Increasing the injection speed requires special tools to provide adequate mold strength and cavity venting. Common issues are linked to flash formation, burn marks on the part, and overpacking. Moreover, the complete replication throughout the whole part's surface is hard to achieve when the part is long. Indeed, the time required for cavity filling may still be too long for replicating the mold structures close to the gate, which typically suffer from the hesitation effect.

3.2.2 Role of cavity thickness

The part geometry can influence the melt filling and in particular the replication of surface structures, by directly affecting the pressure profile in the macro cavity. In particular, the cavity thickness, which is much larger compared to the microfeatures, changes the

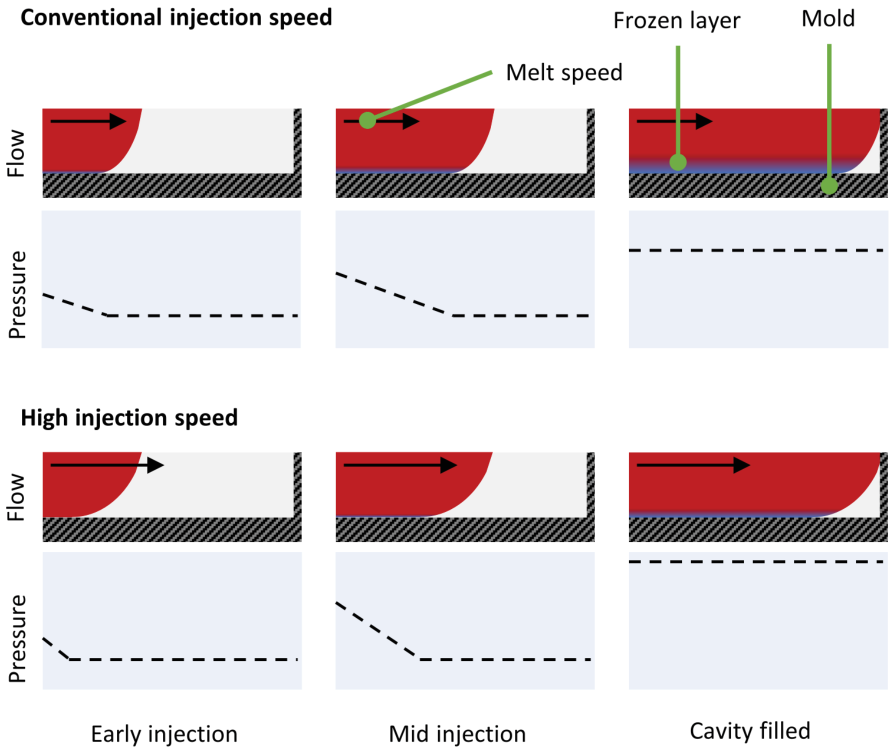

Figure 3.1: Comparison of the cavity filling profiles between conventional and high-speed injection.

evolution of the cavity pressure generated during the injection phase [80]. Moreover, cavity thickness is critical because it determines the cavity filling time for a given injection speed [81]. A decrease in part thickness could enhance the filling of micro-features by decreasing the filling time and increasing the shear rates at wall. This affects the local temperature of the melt in contact with the mold, counteracting the rapid cooling [82]. However, some authors indicated that the reduction of part thickness declines the filling capability of the melt [83]. The reduction of the part thickness causes a severe increase in required pressure to fill the cavity, eventually leading to short shots and premature freezing of the flow section. Due to rheological reasons, it was suggested that injection molded parts with a sufficient replication quality need a minimum thickness of approximately 2 mm [84]. To obtain sufficient replication, careful considerations of the value of the thickness of the main flow region should take into account both aspects of the problem [85].

3.2.3 Role of mold venting

The forced evacuation of the air from the cavity has been exploited in micro injection molding to remove the air pockets trapped in the micro features. The air pockets can resist the approaching melt front causing incomplete replication of the mold surface features. Vacuum venting of the mold consists of removing the air trapped inside the cavity just after mold closing. The application of the technology on increasing polymer replication has reported controversial results. Positive results [86, 87] and irrelevant or even negative results [88, 89] have been addressed to forced air evacuation of the cavity.

The positive results of removing the air inside the microcavities are counteracted by the decrease of the mold surface temperature during the vacuum process. Indeed, positive results have been reported for high mold temperatures, thus compensating for the mold surface cooling before injection. Moreover, interactions between the effect of the effectiveness of the vacuum venting and the viscosity and wetting properties of the selected resin are reported [90]. By comparing cyclic olefin copolymer and low-viscosity polystyrene the authors found that the polymer viscosity sensibility to temperature around the glass transition temperature positively affects the effectiveness of the vacuum venting. High wetting properties were found to positively correlate to the application of air evacuation as well.

3.2.4 Role of mold/polymer wettability

Wetting is the ability of a liquid to maintain contact with a solid surface, resulting from the intermolecular interactions when they are brought together [91]. The microinjection molding process, especially when considering replication of small mold features, can be considered as a wetting process. The injected hot melt interfacial effects over the cold mold have been already found critical as the mold structures approach the micro-size [92]. Therefore, the wetting behavior of the polymer melt at the mold interface contributes to the filling of submicron structures, especially in the very first milliseconds, before the formation of a frozen layer. Matschuk and Larsen [93] reported improved nanostructure replication using fluorocarbon films. Mosaddegh and Angstadt [94] reported the importance of interfacial wetting by showing differences in the filling behavior of submicron silicon structures for three different polymers.

Mold surface coatings can be used to modify polymer/mold wetting interactions [95], and improve the replication of high aspect ratio nanostructures [96] up to 20:1 [97]. In particular, when replicating micro-features by injection molding, high wetting properties facilitate the flow of the melt polymer into the micro-features. High wetting is the condition in which the fluid easily spreads over the surface, showing low contact angles. Indeed, mold surface coatings modify the thermal and rheological [47] interactions at the interface with the melt polymer during filling reducing the flow resistance. The surface coatings can contribute also to the demolding of small structures, an anti-adhesion treatment was used to minimize the risk of failure of high-aspect-ratio nanopillars [98].

3.3 PACKING PHASE REPLICATION

Replication of micro and sub-micro surface structures can be achieved also during the packing phase. The high pressure held during packing can drive additional material into the submicron structures [81]. The pressure present inside the cavity has to overcome the local forces inhibiting the polymer flow inside the small cavities. Therefore there is the need of increasing the mold temperature near or above the glass transition temperature of the resing during filling and packing. In such a way, the reduced mold/polymer thermal gradient inhibits the skin layer formation and lowers the local forces. To allow for ejection of the part, the resin preset inside the cavity has to be cooled down well below the transition temperature. Therefore, fast control and variation of the mold temperature are needed to perform the injection at high temperatures. Zhang et al. [99] reduced the mold/polymer thermal gradient exploiting the RHCM approach, which consists of rapid heating of the mold during the filling phase, and rapid cooling before ejection. Kim et al. [100] produced nanoscale polymer gratings using induction heating of the mold surface.

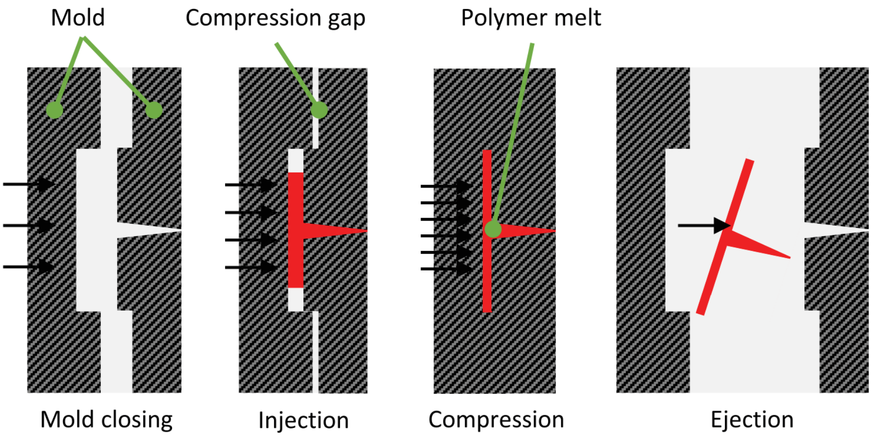

Figure 3.2: Processing steps of the micro injection compression molding.

3.3.1 Injection-compression molding

Injection compression molding is a variant of the injection molding process (microinjection compression molding is the one for micro injection molding). Different from the conventional process, during injection, the mold is kept slightly open. The mold closing is performed as a certain shot volume has already been pushed into the cavity. In this way, the pressure inside the cavity reaches high and uniform values. The process is often exploited for molding optical components, allowing a reduction of the differential packing of the part. A uniform replication grade can in theory be achieved even for relatively large parts, as the pressure at mold closing should reach higher and constant distribution throughout the cavity [101]. High replication grades of sub-micrometric features have been achieved using this process [102]. However, microinjection compression molding requires specific tooling and highly-trained operators, as the processing variables grow in number.

The quality of structure replication is indeed not only controlled by the parameters affecting it for the conventional process. It was reposted how the replication is affected by different selections of compression parameters [103]. The compression stroke, delay, and speed have to be controlled closely [104]. As for the conventional process, the process parameters have to be selected to optimize the thermal and rheological conditions of the polymer close to the mold wall. High compression strokes [105] and long compression delays [106] negatively affect the replication. These results have been correlated to the thermal condition of the skin layer. Indeed, both high compression strokes and long delays lengthen the time before compression, allowing the thickening of the skin layer. The following compression phase is found to be insufficient to drive the material into the micro features. Conversely, quick injection and fast mold closing were found to positively affect the replication grade [107]. The effectiveness of the compression phase was also found dependent on the viscosity of the flash formed around the cavity, which allowed the growth of the cavity pressure [108].

3.4 REPLICATION MODELING

When considering micro- and nano-scale polymer replication, the flow of the melt is characterized by the onset of scaling issues that are still hindering the modeling efforts [24]. Analytical, numerical, and combined models have been proposed for polymer replication to overcome the difficulties linked to the down-sizing of the mold features. Approaching the micro and nanoscale a more robust description of the input data has to be considered, especially with respect to the description of the structure geometry, the polymer properties, and the nature of the interaction happening at such a small scale.

Zhiltsova et al. [43] reported that rheological models do not predict well the polymer properties at a small scale, affecting the accuracy of numerical models. Lin et al. [88] develop an analytical model implementing the strong assumption that the micro-cavities fill only during the packing phase. Different authors suggested the use of multi-scale models, to decouple the macro filling from the micro filling. In those types of models, the analysis of the macro-cavity defines the boundary conditions for the micro- or nano-scale polymer flow [109]. Kim and Turng [110] proposed the use of a two-step numerical model to overcome the limitations linked to the small mesh size required for simulating microflow. Recently, Loaldi et al. [111] exploited the same approach and demonstrated that their numerical multiscale approach well predicts injection pressure and filling time for different case studies.

Scaling the polymer flow down to the microscale enhances the contribution of interactions that are typically neglected in conventional injection molding simulations. Yao and Kim [112] observed that the relative contribution of the surface tension at the melt front should be taken into consideration when the wall thickness of the part decreases. The contribution of the surface tension was implemented by Rytka et al. [113] by modifying the linear momentum equation with the addition of a capillary force.

Overall, the proposed models well predict the polymer flow behavior but also present some strong limitations for the analysis of submicron-scale systems. A comprehensive characterization of the polymer properties at the microscale flow conditions is still lacking. Indeed, current polymer micro-scale replication models lack accuracy, and they do not provide a comprehensive description of polymer/-mold interface interactions.

4 ULTRAFAST LASER TEXTURING

The broad range of properties that characterize polymers has made texturing a significant segment of the plastics industry. Surface texturing has been widely used in the plastic injection molding industry to functionalize plastic parts. The value of a textured plastic part can be very high thanks to its added functionalities. Consumer products with surface textures are widespread, and they offer the user a wide array of looks and feels. The surface texture design and the feeling associated with it profoundly influence the customer quality perception. Texturing of plastic parts finds applications for both consumer and high-end engineering products. The functionalities introduced by surface texturing range from simple aesthetics (e.g., rigid plastic packaging) to advanced biomedical applications (e.g., scaffolds for tissue engineering). More recently, texturing has been used to functionalize injection molds to improve both the process's filling and ejection phases.

4.1 LASER WORKING PRINCIPLE

Ultrafast laser texturing exploits electromagnetic energy to melt and vaporize the material on the surface, creating a texture. LASER (Light Amplification by Stimulated Emission of Radiation) generates a monochromatic and coherent light beam (i.e., light waves with the same wavelength and phase). The laser beam usually has low divergence (i.e., it can travel for long distances), thus focusing on small spots with high irradiance.

4.1.1 Stimulated emission of light

Under specific conditions, as hypothesized by Einstein, light energy with a defined frequency can stimulate an atom's electrons to emit light, which has the same characteristics as the stimulating light [114]. As an atom is hit by light with the right frequency (photon) or heat (phonon) with a specific energy value, it gets excited (i.e., it goes to a higher energy level). The phenomenon of atom excitation is called absorption. On the other hand, the movement to a lower energy level is called emission. However, the atom does not remain excited; thus, the energy is absorbed end emitted by the atom electrons, which can occupy defined energy levels. These energy levels are fixed for each

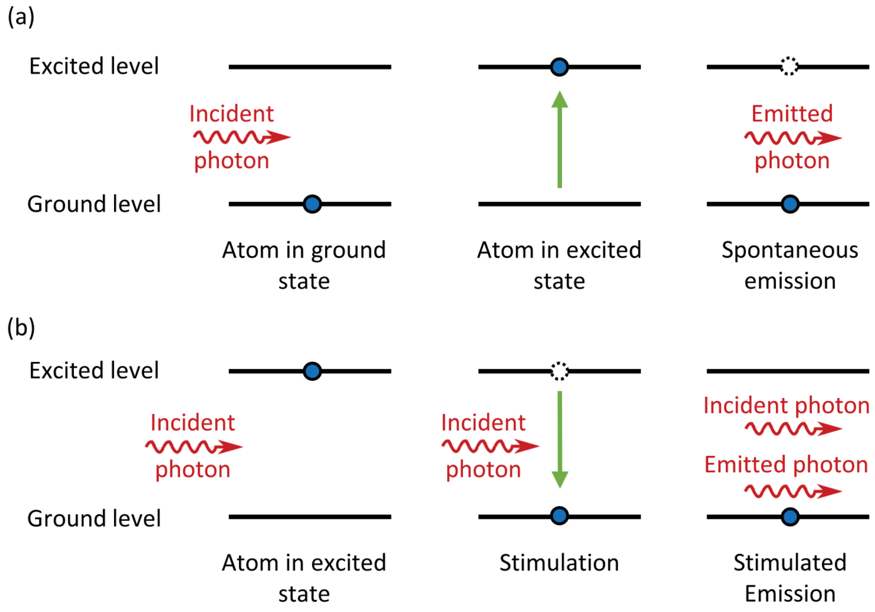

Figure 4.1: (a) Spontaneous emission of light, and (b) stimulated emission of light.

atom; therefore, each particle can generate just a specific wavelength. This process is called spontaneous emission (Figure 4.1 (a)): the generated light has a random phase and direction, but a fixed wavelength. Lasers exploit one slightly different process called stimulated emission (Figure 4.1 (b)).

4.1.2 Optical amplifiers

In stimulated emission, the emission is stimulated by an incident photon, and the atom is already in the excited state. These excited atoms belong to the so-called gain medium. The gain medium is the heart of the laser and consists of a material of controlled purity, size, concentration, and shape. The atoms of the gain medium are continuously excited by an external energy source, causing a population inversion (i.e., when the number of excited atoms exceeds the one on lower energy levels). When a photon hits an excited atom, one other photon is emitted with the same wavelength, phase, and direction. This stimulated emission is the working principle of the optical amplifiers. The gain medium is set between two mirrors placed at a resonance frequency for the particular laser wavelength utilized (i.e., at a multiple of the wavelength). One of the two mirrors is fully reflective (high reflector), the other (the output coupler) allows some light to go through (Figure 4.2). The light confined in the system maintains the amplification process through stimulated emission. On the other hand, the light that goes out from the system generates a laser beam

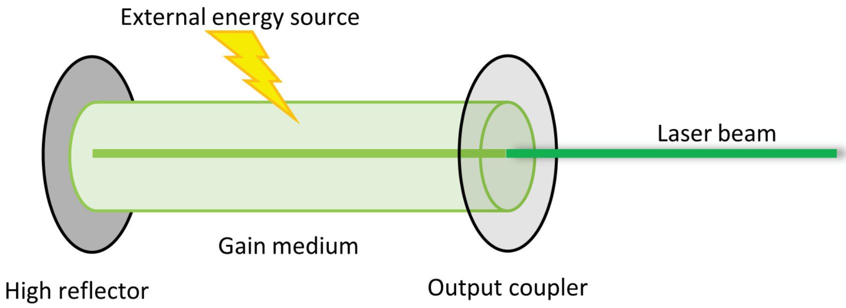

Figure 4.2: Scheme of a resonator system for the generation of a laser beam.

with photons that have the same wavelength and phase. With these properties, the beam can easily be focused in tiny spots to obtain incredibly high intensities [115].

The wavelength of commonly used laser systems is between 0.2 and 11 μm (Ruby = 0.7 μm, Nd:YAG = 1.0 μm, CO = 2.7 μm, CO2 = 10.6 μm, and Ti:Sapphire = 0.78 μm). Depending on the gain medium being used, two types of lasers can be found: solid-state lasers and gas lasers. Typically gas lasers can reach higher powers. Indeed, industrial lasers can also be divided into continuous-wave lasers and pulsed lasers. Continuous-wave lasers are used for welding or surface hardening, which requires an uninterrupted supply of energy for a full thermal process. Pulsed lasers are preferable for machining purposes because the controlled pulse energy can enhance the MRR containing the extension of the Heat-Affected Zone (HAZ). Shorter pulse durations lead to smaller HAZ, but typically lasers with short pulse duration are substantially more expensive.

4.2 LASER TEXTURING TECHNOLOGY

4.2.1 Laser Writing

Laser writing uses the entire laser beam spot size to ablate and texture the surface of the workpiece. The light irradiation is focused on the metal surface, melting and vaporizing the metal in controlled areas. The heat generated by the laser beam creates a Heat-Affected Zone (HAZ), which could have micro-cracks or nano-bubbles, depending on the processing parameters. The minimum texture size that can be machined depends on the laser beam divergence, which is a function of the laser light quality. For some applications, a laser spot diameter – and consequently feature dimensions – of some tens of micrometers can be machined [116]. In a laser writing process, either the laser source or the workpiece can be moved using a CNC system to texture a complex surface. However, the maximum surface area that can be textured is limited by moving the system over a large area. Moreover, for complex three-dimensional geometries, texturing might not be possible for areas that are not optically accessible, or for areas on which the laser beam cannot be properly focused.

Fibre laser systems exploit a glass fiber to deliver the laser light from the resonant chamber to the optical head. This laser allows for smaller and more compact laser equipment, which guarantees increased flexibility for moving the optical head around the workpiece. When using a fiber laser, the workpiece is set in the moving stage to increase the machining degrees of freedom. The laser beam's high stability and flexible configuration allow texturing of complex geometries with good accuracy and precision. High-aspect ratio dimples (i.e., blind holes) are the most common texture machined by laser writing. However, many different textures can be produced, with the main limitation being the minimum laser spot size. The texturing speed is limited by the need to ablate individual features using the laser beam directly.

4.2.2 Trough mask laser texturing

Through mask laser texturing guarantees higher productivity than direct writing by interposing a mask between the laser beam and the focus region. Along the laser path, the irradiance (power per unit area), or the fluence (energy for units of area), is weaker than in the focus area; thus, the mask is not damaged by the laser. The beam is homogenized before hitting the mask to flatten the laser beam's Gaussian energy profile, allowing for homogenous texturing (Figure 4.3). The laser beam's low divergence allows for accurate projection of the shapes of the mask onto the workpiece surface. Texturing is obtained by selective irradiation of the workpiece surface, which results in selective ablation [117].

Pattern characterized by various shapes can be engraved with this technique. However, limitations on the minimum size achievable should be taken into consideration. Indeed, the minimum size of the structures has to be higher than the laser light wavelength to avoid diffraction effects. In general, features as big as few microns can be machined using through mask laser texturing.

4.2.3 Ultrafast Laser Texturing

Ultrafast texturing is a recent development in laser technologies, which has many peculiarities and allows machining of different textures. Ultrafast lasers are pulsed lasers characterized by a duration that goes from few nanoseconds to femtoseconds and frequency ranging between one to several hundreds of kHz. Ultrafast laser systems are characterized by low power characteristics (i.e., units of Watts); how-

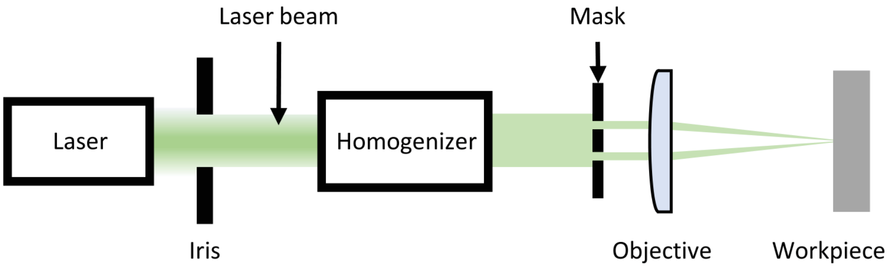

Figure 4.3: Working principle of through mask laser texturing.

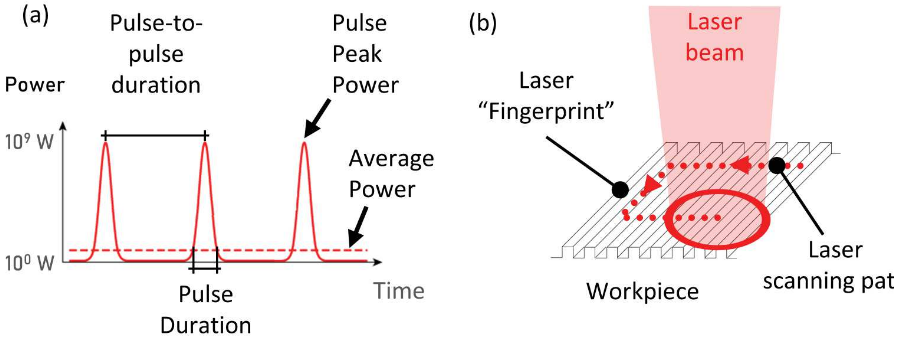

Figure 4.4: (a) Pulsing power typical shape, and (b) representation of the ultrafast texturing process.

ever, the use of high power light pulses allows for high values of pulse energies being focused on the workpiece surface. In general, pulse powers exceed the gigawatts range (Figure 4.4 (a)).

The extremely powerful pulses have a complex interaction with the workpiece surface that results in various types of textures [118]. The high power ablates the material, which absorbs most of the energy delivered to the surface, limiting the HAZ dimension. Indeed, a thin layer (approximately 1 micron) of the bulk material is affected by the texturing process.

Ultrafast laser texturing exploits the complex interaction between the light pulse and the workpiece surface to machine textures with features that can be much smaller than the laser spot size and even smaller than the laser light wavelength [119]. The laser pulsing on the workpiece leaves a fingerprint of its nature in the form of a texture (Figure 4.4 (b)). The ablation mechanism involves the interference between the laser wavelength and the surface-associated wave. Ultrafast texturing is a complex phenomenon that occurs for a narrow range of laser fluence. The ablation threshold is specific for each material and should be controlled and identified for the designed optical setup. The texturing process is affected by the characteristics of the beam and the process parameters. The textures' main characteristics that can be controlled are features dimensions, shape, pitch distance, directionality, and regularity. Typical sizes of the structures range from several tens of nanometers to hundreds of microns. The structures' size is strongly linked to the energy delivered to the surface (i.e., fluence) and the light wavelength. In particular, shorter wavelengths typically lead to smaller textures. The pitch and directionality of the pattern are controlled by the polarization and the wavelength of the laser beam. Good homogeneity of the texture can be obtained by optimizing the surface scanning parameters [120].

4.2.4 Direct Laser Interface Patterning

Direct Laser Interference Patterning (DLIP) exploits two or more laser beams to create an interference pattern on the workpiece surface, which ablates the workpiece surface, creating a texture. The development of small optical heads offers the possibility to process planar surfaces and complex three-dimensional products. The primary beam is split into two or more beams using beam splitters. Each generated beam is then sized and shaped to achieve the desired intensity (Figure 4.5). DLIP does not require deep focusing on the workpiece since the energy is sharpened in the desired areas by the interference field. The number of the interfering laser beams and its intercepting angle determines the shape and the spatial period of the intensity distribution pattern on the workpiece. The interference field results in high-temperature gradients, which ablate the material producing a surface pattern.

DLIP can produce tiny textures, which can have the size of the laser beam wavelength. A large variety of pattern geometries can be engraved by tailoring the interference pattern as a function of the number of beams and their properties (e.g., polarization, intensity). With the use of ultrafast laser, hierarchical patterns can be machined with high control over the pitch. Hierarchical patterns are textures that present two or more patterns one over the other. The laser beam interference field machines the structures with the bigger pitch. Patterns with smaller pitches are obtained exploiting the phenomena discussed for the ultrafast laser patterning [121].

4.3 TEXTURING TECHNOLOGIES COMPARISON

Many techniques have been developed to address the texturing needs of a large variety of stakeholders. Mechanical machining, electrochemical etching, thermo-electric, and additive processes have been applied in different fields due to their unique advantages. The selection of the most appropriate texturing process depends on the application and requires combining different engineering skills in mate-

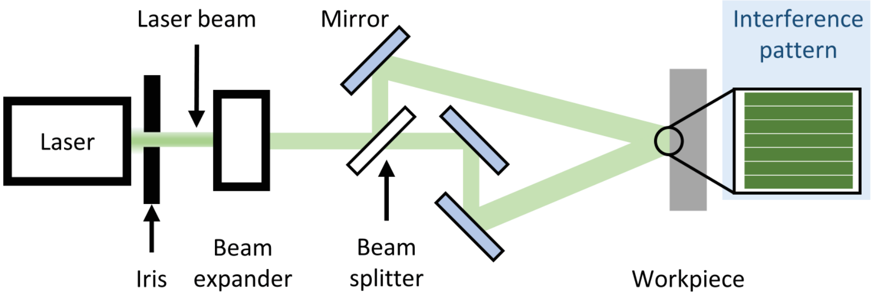

Figure 4.5: Schematic diagram of the DLIP process setup.

rials, manufacturing processes, product design, quality control, and more. Texturing of a plastic product affects the customer perception, and thus changes its market value.

Depending on the primary working principle, texturing processes can be classified as mechanical, thermo-electric, electro-chemical, and additive. Each one of these processes can be further divided into processes that exploit a mask to work on the surface selectively, or processes that concentrate the energy on a small spot of the surface (cf. Figure 4.6).

- *Mechanical machining technologies* involve physical contact between the tool and the workpiece to remove material from the surface. Downsizing milling technologies is tricky but possible. This particular process (also called micro-milling) can machine complex textures, but at a very low rate. Considerable improvements are achieved by employing a diamond tool or by vibrating the tool at ultrasonic frequencies. Besides micro-milling, one other crucial texturing technology that exploits mechanical energy to machine the surface is abrasive jet machining. Typically, the workpiece surface is masked, and many variations of the process capabilities can be obtained depending on the size and type of abrasive particles used and the type of fluid that carries the abrasive.

- *Chemical and electrochemical technologies* are often exploited to etch texture on steels. Chemical etching uses a particular chemical to etch the unmasked parts of the workpiece surface. This process is widely used for texturing big surfaces but can only obtain low aspect ratio structures (i.e., it is difficult to etch deep textures accurately). Electrochemical etching is suitable for both masked and unmasked texturing, depending on the particular application. Typically, the electrodes employed for masked electrochemical etching are larger and have much simpler geometries than those for the unmasked process, which may directly present the texture to transfer it to the workpiece. Micro electric

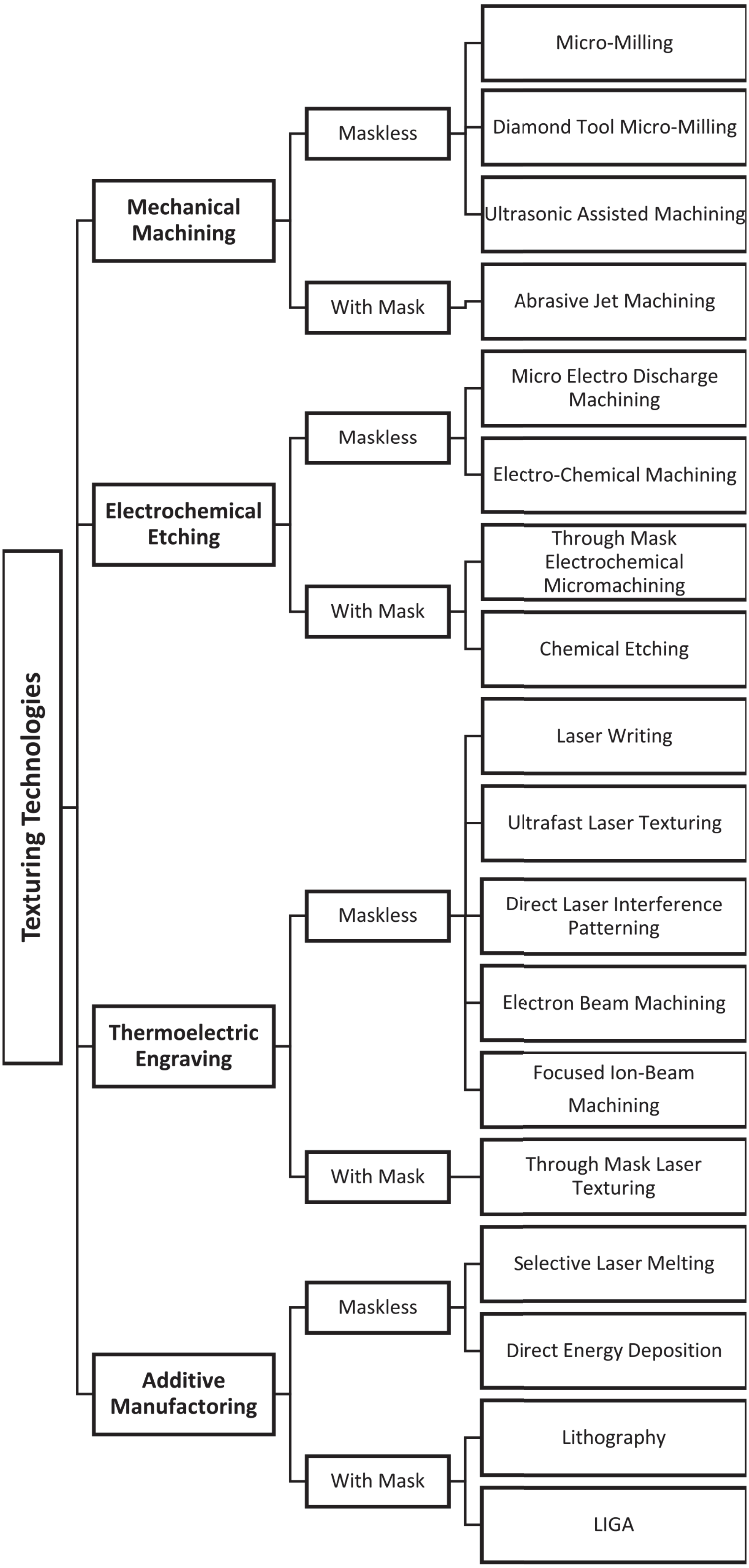

Figure 4.6: Classification of the texturing processes.

discharge machining (μEDM) engraves the surface by applying a voltage between the workpiece and the tool and shooting a spark. A texture can either be obtained by moving a simple tool along the surface or exploiting a larger textured tool. A large variety of tool shapes is employed to machine diverse textures.

- *Thermoelectric engraving processes* exploit thermal energy to ablate the texture by melting or vaporizing the workpiece surface material. The thermal energy can be delivered to the surface by different energy vectors. Laser techniques exploit a laser source's monochromatic and coherent light to heat the surface material quickly and ablate it. The laser light's unique properties allow the selective irradiation of a surface portion by interposing a mask between the light source and the workpiece. Furthermore, the laser light can be focused onto the surface to achieve high irradiances at the light spot. The spot is then quickly scanned along the surface to achieve the desired texture. Laser writing exploits this principle to engrave an enormous variety of patterns. The introduction of ultrafast pulsed lasers enabled the development of the other two processes, namely ultrafast laser texturing and direct laser interference patterning (DLIP). These processes are capable of engraving much smaller textures (compared to laser writing) by exploiting the actual laser light properties such as wavelength and polarization and, in the case of DLIP, by creating a sort of virtual mask with the induced interference pattern. Electron beam machining (EBM) and focused ion beam machining (FIBM) exploit a high energy flux of electrons or ions to remove material from the workpiece. EBM and FIBM are between the most accurate processes and can machine incredibly small features, but they turn to be slow and expensive.

- *Additive technologies* can be divided into lithography technologies and 3D printing technologies. The first typically exploits masks while the latter does not. Lithography was first developed for materials and electronics applications, but it was transported into a metal application. The pattern transcription is typically done by selective irradiation of a resist material. Lithography is typically exploited in mask production to enable all the other mask-assisted texturing processes. However, there are some exceptions as the LIGA technique in which lithography is followed by electroplating to build textured mold inserts. 3D printing techniques for texturing exploit a laser beam's thermal energy to melt stainless steel powders together. In selective laser melting (SLM), a laser beam scans in certain areas the powder bed to build, layer by layer, 3D structures. Direct energy deposition (DED) exploits a powder jet that delivers particles onto the surface where a laser beam heats them and melts them. The first process is way more precise than the latter, but it can only be done on flat surfaces.

4.3.1 Texture geometric parameters

The most critical parameter to consider when selecting texturing technologies is the dimensions of the surface features. Different scale features within the texture result in a wide range of diverse functionalities. Depending on the desired product properties, texture dimensions can range from millimeters (10^{-3} m) to nanometers (10^{-9} m). The successful manufacturing of textures at different scales requires considering different technologies. In fact, not all texturing technologies can be used to manufacture a specific scale texture. However, each technology is characterized by its dimensional range.

Textures are also divided into random and patterns. The former refers to surface features that are not regularly disposed over the product surface. The latter defines textures that have specific features orientation, location, and reciprocal distance. The ability to generate an accurate pattern rather than random structures is a specific characteristic of the different texturing technologies. The characterization methods for the two types are also different. The topography of random textures is well characterized using surface roughness values. Instead, regular patterns require more accurate and broad characterization, which might require the quality analysis of individual features. In general, patterns tend to be bigger than random textures because of the need for regularity and the more stringent quality criteria.

Different geometrical parameters can be defined to describe a texture. The most important are:

- The spatial pitch of the pattern, i.e., the distance between consecutive features.

- The features cross-section geometry, such as their diameter or their width.

- The feature height or depth, i.e., the distance from the substrate to the top or bottom of the features.

- The aspect ratio, i.e., the ratio between the feature height or depth and its width.

Among all dimensional parameters, the aspect ratio of the texture is the most significant when considering the manufacturing of a textured plastic product. For most applications, aspect ratio correlates with surface functionality, thus being crucial for selecting and comparing texturing technologies. The aspect ratio is one of the most

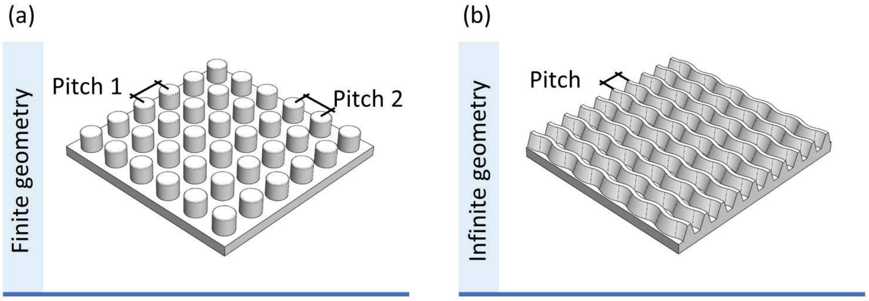

Figure 4.7: Schematic of (a) finite geometries pattern, and (b) infinite geometries pattern.

critical texturing characteristics and constitutes a manufacturing constraint in applying the specific texturing technology to a broader range of applications [74].

4.3.1.1 Pattern geometries

The feature geometries can be divided into two main categories: finite and infinite geometries. Finite geometries are defined by distinct features that all have dimensions in the same order of magnitude. Examples are distinct pillars, holes, bumps, and more (Figure 4.7 (a)). Infinite geometries are texture features characterized by a dimension being substantially larger than the others (Figure 4.7 (b)).

Some texturing technologies can allow the manufacturing of hierarchical surface features. Hierarchical textures are characterized by overlapping two textures, one on the other (Figure 4.8) [122]. This type of texture allows different product functionalities due to the presence of features at different scales. Typically, the larger and smaller features have dimensions in different order of magnitude.

The functionality of a textured surface is inherently linked to its quality. Quality criteria for textures include features, shape, dimensional, and positioning accuracy. Shape accuracy is typically limited by the presence of burrs, undercuts, and recasts. Even if such defects do not compromise the texture, they may trigger undesired optical effects which affects the aesthetic outcome of the surface.

4.3.2 Mechanical machining technologies

4.3.2.1 Feature dimensions

Micro-milling technologies are used to machine 3-dimensional textures with features that may be as small as 10 microns, and an aspect ratio of 3÷4 [123]. The CNC control guarantees high shape consistency (i.e., the capability to produce the same shape) across the texture. However, the shape accuracy (i.e., the capability of producing

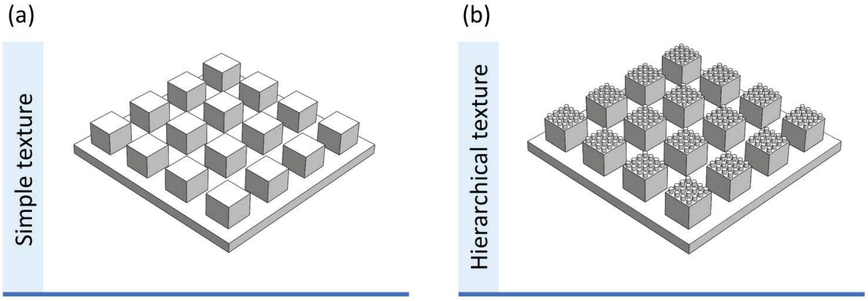

Figure 4.8: Schematic of (a) a texture with structures of the same order of magnitude, and (b) of a hierarchical texture.

the desired shape) is affected by the material grain size and the presence of burrs. The latter being very difficult to remove at the microscale. Machining of smaller grain size steel showed much higher shape accuracies [124]. Process modifications, such as diamond tool micro-milling or ultrasonic-assisted machining, were introduced to limit burrs formation.

In the AJM process, the mask defines the minimum feature dimension, typically in the order of 100 micrometers. The mask material has to be tough enough to withstand the erosion of the abrasive jet. Aspect ratios for this process are usually low (around 0.5). The shape accuracy can be enhanced by choosing different abrasive particles. The size, the shape, and the material hardness of the abrasive have a substantial effect on the shape accuracy [125]. Smaller particles with few sharp edges and relatively low hardness can produce better textures.

4.3.2.2 Geometrical flexibility

In mechanical machining technologies, the tool movements are CNC controlled along multiple axes. Thus, the equipment is highly flexible and can be used to texture complex surfaces. However, milling-based technologies are limited by the length-to-diameter ratio of the cutting tool [123, 126]. Abrasive jet machining is more flexible when texturing hard-to-approach areas, as the jet can be optimized to travel a longer distance on the workpiece [125]. However, the generation of regular patterns requires a mask, limiting the ability to work on complex free-form surfaces. In comparison, abrasive jet machining can be used to obtain random textures on complex products.

4.3.2.3 Process related material modifications

Textures obtained with mechanical machining processes are characterized by residual stresses, affecting the texture strength and wear resistance. The tool contacts create these defects as a result of the ablation and material removal. Textures can be micro-milled on a wide range of materials, and the quality is mainly affected by the grain size. The edge radius of cutting tools can be as small as the grain size, and machining instabilities can occur [127]. Hence, for high-accuracy applications, materials with finer grain sizes are preferred. Similar phenomena are also crucial in abrasive jet machining, in which the particle size, shape, and hardness are selected to avoid the inclusion of particles inside the workpiece [126].

4.3.3 Electrochemical etching technologies

4.3.3.1 *Feature dimensions*

A large variety of structures shapes can be obtained using μEDM with dimensions down to tenths of microns. The aspect ratio is mainly constrained by the flushing efficiency [128], and the maximum values are about 2. Indeed, flushing is increasingly challenging for a higher aspect ratio, and the adequate electrical conditions for the spark may not be reached. Flushing can also affect the stability of slender electrodes when the flushing velocity is increased. The feature shape accuracy is mainly linked to the spark crater and tool wear, which can be minimized by reducing the spark energy. Tool wear is avoided in ECMM (Electro Chemical Micro Machining), resulting in higher texture consistency. The machinable features and aspect ratios are comparable to μEDM for the conventional process, and they depend on process parameters like voltage and electrolyte purity. Ultrasound-assisted ECMM was introduced to push the feature dimensions down to 1 μm and the aspect ratio to 3 [129]. The tool vibration enhances the electrolyte flushing and heat removal.

Masked processes as TMECM (Through Mask Electrochemical Machining) or chemical etching are used to manufacture 2.5-dimensional textures. The achievable aspect ratio is about 1, but textures with lower aspect ratios are usually machined with these processes [130]. The electrolyte or the etchant are flushed over the surface to maintain a homogenous material ablation and obtain better structure consistency throughout the entire surface. In both processes, etching can create undesired undercuts by removing material under the mask. Hence, larger masks are used to consider this effect.

4.3.3.2 *Geometrical flexibility*

The use of a mask introduces geometrical limitations for electro-chemical etching processes, such as chemical etching and through mask electrochemical machining. Mask-less technologies, such as micro electrodischarge machining and electro-chemical micromachining, can be used for more complex geometries [129]. These processes can exploit either simple shape tools or pre-patterned ones to texture different workpiece geometries [71]. In this case, the effective flush of the debris from the working area is crucial, which defines the limits for geometrical complexity.

4.3.3.3 *Process related material modifications*

Electro-chemical etching techniques result in stress-free textures. However, selecting the appropriate etchant for a specific substrate material is crucial to avoid chemical damage to the workpiece surface. Chemical modifications of the exposed surface are evident even after rinsing, but they are a concern only for specific applications (e.g., clean room tools). The chemical modifications of the surface are minor with ECMM. However, if the presence of inclusions characterizes the metal substrate, those can affect the resulting properties.

In the EDM process, the texture is generated by thermal phenomena, such as localized melting and vaporization. Thermal stresses on a superficial layer characterize textures obtained with this technology. However, structure and crystallinity can be modified further down in the workpiece, thus defining the Heat-Affected Zone (HAZ) [131]. Thermo-electric processes are always characterized by the presence of a HAZ on the textured surface.

4.3.4 Thermoelectric engraving technologies

4.3.4.1 *Feature dimensions*

Laser-based technologies generate different features based on how the beam light is delivered and focused on the surface. In laser writing, a large variety of features as small as 20 μm can be obtained, with an aspect ratio up to 3 [116]. The interference phenomena that characterize ultrafast laser texturing and DLIP result in smaller feature dimensions, down to 100 nanometers. For these technologies, the texture dimensions depend on the light properties (i.e., wavelength) and process conditions (i.e., irradiance and scanning speed). The upper limit on feature size is around 100 μm for ultrafast laser texturing, and 500 μm for DLIP [121]. The shapes obtained with these technologies are limited due to the tight correlation with laser light properties, such as polarization and wavelength. Ultrafast laser texturing and DLIP can be used to generate hierarchical textures. The primary shape defects of laser-based texturing technologies are recasts around the engraved area and thermal micro-cracks. As a consequence, texture consistency and shape accuracy are the main challenges.

When a mask is used for laser texturing, the minimum feature dimension is constrained by the diffraction effects when the laser light crosses the mask. Features dimensions as small as 5 μm can be engraved with aspect ratios smaller than 0.5. The texture consistency along the surface is typically high, but the shape accuracy is limited by recast and thermal micro-cracks. High-energy beam techniques are used to generate three-dimensional structures with small dimensions (i.e., down to 100 nm for FIBM [132]) with an aspect ratio not bigger than 1. The machined features are typically accurate and precise.

4.3.4.2 *Geometrical flexibility*

Laser-based thermo-electric engraving technologies allow good geometrical flexibility. Laser writing is the most flexible technology since the optical head is mounted on a 5-axis CNC machine. When using an ultrafast pulsed laser, issues related to the beam handling reduce the flexibility for ULT and DLIP. These technologies cannot exploit CNC machines because of the high pulse power. Hence, they use mirror systems to re-direct the laser beam to specific surface locations. However, the need to deliver an unchanged laser beam to the workpiece surface makes this approach complex and limited. Indeed, ultrafast pulsed laser technologies exploit the laser beam's lightwave characteristics, not just its thermal energy. Similarly, high-energy beam machining techniques (i.e., EBM and FIBM) require advanced equipment to handle the beam, limiting the workpiece dimension and allowing texturing of 2D surfaces only [130].

4.3.4.3 *Process related material modifications*

Laser-based texturing technologies typically show thermal micro-cracks and recasts. The fast cooling of the melted material over the surface that is not ablated produces the micro-cracks. The condensation of vaporized material over the surface produces the recasts. Pulsed lasers were specifically introduced to reduce the HAZ and enhance machining accuracy. Ultrafast pulsed laser processing is defined as a 'cold process' because the HAZ can be neglected [118]. However, surface oxidation can be a problem with these technologies. The HAZ is also minimal for high-energy beam machining, but EBM and FIBM are executed in a vacuum environment to avoid oxidation.

4.3.5 Additive technologies

4.3.5.1 *Feature dimensions*

A wide range of three-dimensional surface features with dimensions as small as 100 μm can be manufactured using additive manufacturing technologies. DED's working principle makes the achievable features bigger and less accurate than those that can be obtained using SLM. SLM offers the possibility of achieving higher aspect ratios (i.e., up to 4 for SLM, and up to 2 for DED). The minimum feature dimensions and the shape accuracy are affected by the powder particle dimensions, which are typically not smaller than a few tens of microns [133]. Typical defects are the bridging between different surface features, balling, non-evacuated powders, or internal voids.

Lithographic techniques manufacture 2.5-dimensional features with high aspect ratios, with dimensions as small as few nanometers [134]. Simple 3-dimensional features can be manufactured using the LIGA technique. However, features cannot be smaller than 500 nm. These techniques result in textures characterized by high consistency and accuracy.

4.3.5.2 *Geometrical flexibility*

Lithography and LIGA technologies allow texturing of planar surfaces only. Additive manufacturing texturing technologies have higher flexibility. For example, DED nozzles are often mounted on multi-axis CNC machines [135]. However, substantial limitations should be considered for concave geometries' texturing, due to the dimensions of the nozzle and the short powder jet length. The SLM process allows texturing of free-form surfaces only when the product and the texture are realized in the same process. However, the processing times can be very long. Conversely, if SLM is used to texture an existing product, only planar surfaces are allowed, but the texturing time is significantly shorter.

4.3.5.3 *Process related material modifications*

Additive manufacturing texturing can only be carried out with materials that are not prone to oxidation, such as stainless steel [133]. The oxidizing of the powders ultimately compromise the texturing process. Residual thermal stresses, micro-cracks, and internal porosities are the most common defects for this process. Porosities, inclusions, and residual stresses are common in the LIGA process because of the electroplating with nickel.

4.3.6 State of the art of texturing technologies

The different texturing technologies presented are here summarized in the feature size - texturing speed plot (c.f. Figure 4.9). The plot quickly assesses the capabilities of each technique. The most interesting technology should be flexible to the feature size (i.e. the cloud should horizontally cover the whole plot) and should be fast (i.e. the cloud should be at the top of the plot). The main trend that can be captured is a decrease of the texturing speed as the main feature dimensions decrease.

Laser-induced periodic surface structures (LIPPS) creation through ultrafast laser texturing is a single-process step that has gained remarkable attention in the last decades, developing into a scientific evergreen. From 1982 more than 1100 peer-reviewed papers have been published and the trend is constantly growing [136]. The research is dynamic both for the development of new powerful laser systems and for the more precise control of the light beam for new applications. New developments are likely to quickly arise from the research. In addition to that, the laser writing process can be carried out within the same setup as ultrafast laser texturing. Historically, the main limitation was the limited power of ultrafast lasers, which limits the material removal rate. Nowadays, powerful ultrafast laser systems are available in the market and can be exploited for both laser writing and ultrafast laser texturing. In such a way, it is possible to merge the two clouds in Figure 4.9.

The obtained cloud demonstrates outstanding flexibility to the feature size, with an unmatched texturing speed. However, the texturing speed is still low for texturing applications for the mass manufacturing market. The texturing cost is nowadays only acceptable for high-level parts for niche markets. In this context, coupling a replication process with the laser texturing of the master may be an ideal application for laser texturing technologies. In this work, the process chain involving laser texturing of the mold and replication of the laser structures is studied taking into account the challenges and opportunities of both technologies.

4.4 APPLICATIONS OF TEXTURING IN INJECTION MOLDING

Texturing finds different applications in injection molding technologies, ranging from plastic products to mold functionalization. Textures have been used to improve both the appearance and the functionality of plastic products, allowing significant opportunities for plastic manufacturers. The increased availability of texturing technologies has opened up opportunities for mold surface functionalization. The generation of micro- and nano-scale features on tool surfaces has improved both the filling and ejection in plastic injection molding.

4.4.1 Aestetic texturing

A plastic product's aesthetic appearance can be modified with the addition of textures in the sub-millimeter on the micro-scale range. Smaller features, not visible by the human eye, are typically used for other applications. The texture design process is often based on creativity and marketing. Examples range from the interior surfaces of different vehicles to PET soda bottles. However, these surfaces' applications are limitless and have been successfully implemented in automotive, electronics, packaging, and more industries [137].

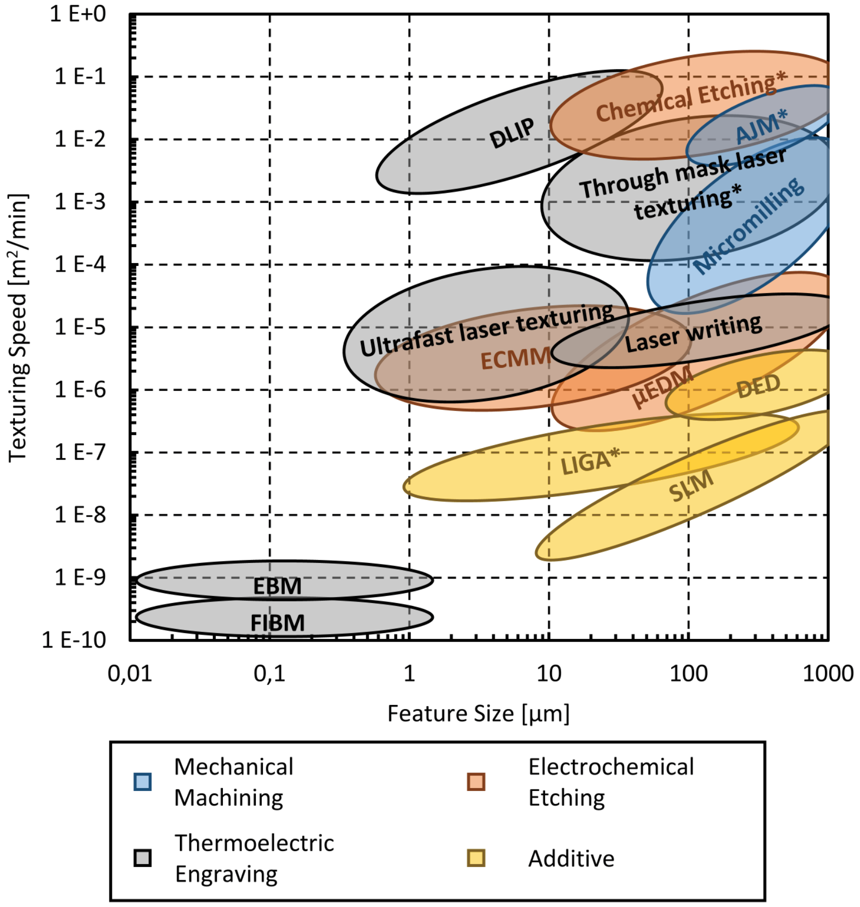

Figure 4.9: Feature size and texturing speed capabilities of surface texturing technologies. Multi-step technologies are indicated with a star (*).

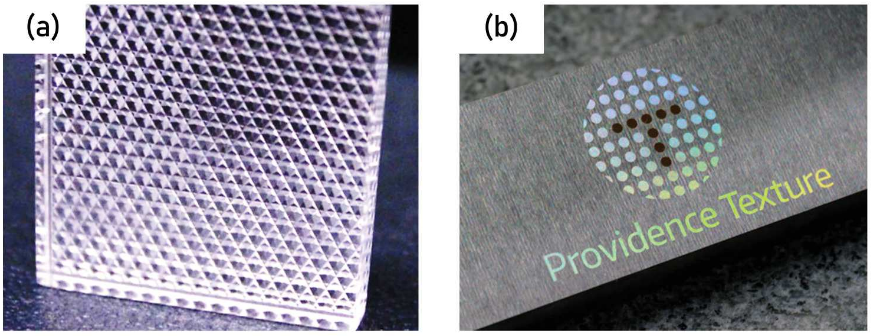

Figure 4.10: (a) Micro-lens array and (b) branding with an iridescent texture.

Precise texturing can introduce specific optical properties to the part. Optics applications require replicating mold textures using transparent polymers, allowing the manufacturing of different optical components. Examples of micro- and nano-textured optical components (cf. Figure 4.10 (a)) include lenses, diffractive optical elements, diffraction gratings, blazed gratings, slanted gratings, diffractive diffusers, optical diffusers, beam splitters. In the automotive and electronics industry, semiconductors for illumination and sensing systems led to the development of micro-lenses, which are used as diffractive elements.

Branding with appealing logos or artistic textures is widely used for both consumer and high-end products. By engraving a brand name, serial number, or other legal marks on a product, a company not only reinforces its brand image but also protects its name (cf. Figure 4.10 (b)). Counterfeiting can be a challenge to a company's ability to protect its name and brand identity. An engraved serial number or a complex geometry on a mold ensures a level of security for the company [138]. Moreover, engravings are used to report information regarding the polymer grade, recyclability, and end-of-life strategies.

Submicron scale patterns create light diffraction effects when their pitches dimension is close to the visible light wavelength (i.e., 380-740 nm). Depending on the size and orientation of the structures and the angle of orientation of the incident light, different shiny shades of colors are visible throughout the entire visible spectrum (cf. Figure 4.10 (b)) [118, 139]. Homogenous textures with long ripples are required to show structural colors, and they may be alternated by smooth areas to increase the shiny effect [138].

4.4.2 Part functionalization

Textures with micro- and nano-scale features are used to modify and control a surface's wetting properties. The most famous example of the effect of texturing on surface wettability is found in nature on

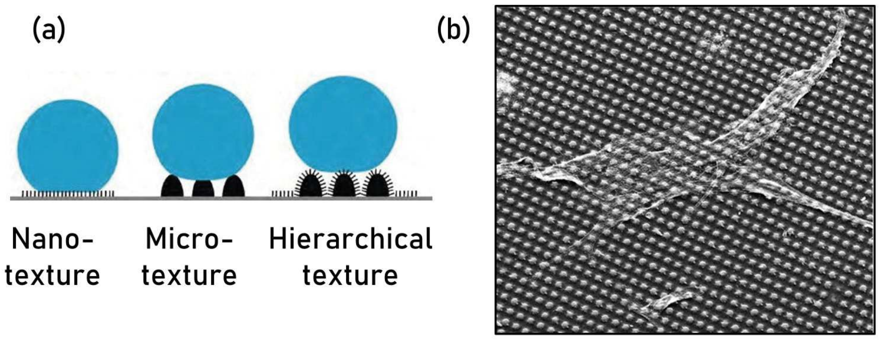

Figure 4.11: (a) scheme of the wetting performance of textures based on the magnitude and geometry of the pattern, (b) micro-scale pillars that improve cell growth [143].

lotus leaves, which easily repel water. Engineering applications that exploit this phenomenon include hydrophobic, hydrophilic, icephobic, anti-fogging, self-cleaning, anti-fouling, and more functional surfaces [140]. Oleophobicity (i.e., the ability of a surface to repel oils) and amphiphobicity (i.e., the surface's ability to repel both water and oil) of the surface can also be controlled and enhanced using texturing. Hierarchical textures are commonly exploited to obtain high performances in terms of wetting properties (cf. Figure 4.11 (a)). It should be noted that the polymer-texture interaction is also significant in these applications because the effect of patterning the surface is that of enhancing the intrinsic surface properties of the polymer. Typically, polymers show a low wetting with water that can be further improved, obtaining a more hydrophobic behavior (i.e., reducing its surface energy) [141]. Moreover, the polymer rheological and thermal properties influence the ability to achieve complete replication when using a specific polymer processing technology [142]. The topography modification can also significantly impact the biological response of the surface (cf. Figure 4.11 (b)). Textured surfaces have been used to improve the interrelation between implants (e.g., pins, screws, rods, clips, etc.) and the surrounding tissue. Other examples include scaffolds for tissues and cell engineering, microfluidic devices, organ-on-chip, and surgical tools.

4.4.3 Mold functionalization

The tool surface represents the boundary that controls the polymer/-tool interactions. Modifications of tool topography can be used to control the polymer replication, achieving significant processing benefits. Different strategies have been used to achieve that, particularly surface modification using coatings [144] and surface texturing [73]. The most significant benefits of surface engineering were observed for the filling of the micro- or nano-scale features and the ejection of the replicated texture from the tool.

Micro- and nano-scale texturing can affect the filling flow by changing the thermal boundary condition at the polymer/mold interface [145]. The air pockets trapped in the troughs in the texture have low thermal conductivity, thus they delay the heat transfer to the mold and keep the polymer warmer during filling. However, this effect is relevant only for thin-wall plastic parts, an experimental threshold at 150 μm was identified [146, 147]. Moreover, the wall slip phenomenon can be facilitated by reducing the interactions between the melt and the mold [46].

The effect of surface roughness during part ejection has been widely studied and exploited [148]. The force required to separate a plastic part from the mold generally increases with a rougher surface. However, highly polished tool surfaces also lead to high forces due to the vacuum generated at the interface. The optimization of the mold topography through texturing has been demonstrated as an effective solution to solve demolding issues [149].

4.5 STATE OF THE ART OF ULTRAFAST LASER TEXTURING FOR INJECTION MOLDING APPLICATIONS

Ultrafast laser texturing is a fast and inexpensive alternative to other micro-and nano-technologies available in the market (cf. section 4.3). From the first observation by Birnbaum in 1965 [150], the research and industrial stakeholders' interest is always increasing as the technology is improving and boosting new applications. This is based on the high levels of robustness and simplicity of the single-step characteristic of the process. The obtainable types of surface structures and functionalities depend on the irradiation conditions and the materials involved in the process. Therefore, different feature sizes and shapes can be obtained by tweaking inputs as the laser light pulse characteristics and energy, the laser wavelength, the polarization direction, and the texturing procedure and environment. This section describes strategies for obtaining various textures geometries on steel using ultrafast laser sources.

4.5.1 LIPSS formation

The spatial periods and arrangement of the quasi-periodic ridges show a strong dependence on the light properties and on the processing conditions:

- Laser light wavelength [151]

- Laser light polarization [152]
- energy delivered per area [153]
- beam incidence angle [142]

The LIPSS formation has been studied in relation to those parameters, but a complete understanding of the phenomena taking place at the interface is still missing [154]. In the literature, four ablation mechanisms have been proposed:

- *Spallation*: happens when the material fails due to tensile stresses arose by sudden changes in volume and pressure after irradiation [155].
- *Phase explosion*: refers to a metastable liquid reaching the massive nucleation thermodynamic point, which occurs suddenly breaking the liquid down into droplets and gas [156].
- *Fragmentation*: refers to the process of desegregation of the superficial material due to the strain caused by the relaxation of the thermoelastic stresses [157].
- *Vaporization*: happens when the whole surface layer is completely atomized as the deposited energy gets higher than the cohesive energy of the target material [158].

LIPSS are generally classified into two types, depending on the spatial period of their pattern. (i) Low spatial frequency LIPSS (LSFL) are structures with a period comprised between λ (laser wavelength) and $\lambda/2$. (ii) High spatial frequency LIPSS (HSFL) have a lower period, below $\lambda/2$ [118]. The first is aligned perpendicular to the laser light polarization, hence they are orthogonal to the electric field vector [159]. The latter is instead parallel to the laser light polarization, and it appears only for ultrashort (i.e. pico or femtosecond) laser pulses [160]. The two types of surface structures differ by the formation mechanism.

LSFL and/or HSFL can be generated by modifying the laser fluence (i.e. energy delivered per unit area) deposited over the surface [160]. The formation of LSFL has been attributed to the interference between the Surface Plasmons Polaritons (SPPs) and the incident laser light [161] [19]. The formation mechanism of HSFL is still controversial. Recent approaches attribute the HSFL formation to the interference between the incident laser light and the scattered radiation [162].

4.5.2 LIPSS pitch

The LIPSS pitch can be modified by changing the laser setup or the scanning strategy. Moreover, by controlling the laser spot motion on the steel surface and the light fluence (i.e., energy delivered on a specific area) it is possible to optimize the regularity of the structures. The pitch between consecutive structures is strongly linked to the wavelength of the laser light. In particular, the studies report that the pitch is typically slightly smaller than the laser wavelength [118]). For a Transverse Magnetic (TM) wave, it can be found that the period of the structures is [163, 164]:

$$\Lambda \leq \frac{\lambda}{n(1 \pm sin\theta)} \tag{4.1}$$

Where Λ is the LIPSS pitch, λ is the laser light wavelength, n is the refractive index of the medium through the irradiation is performed, and θ is the incidence angle of the laser beam over the working surface. Materials irradiation is typically carried out perpendicularly and in air environment, which has a refractive index close to 1. In these conditions, the obtained pitch turns out close to the laser wavelength.

- *Laser wavelength (λ).* The most direct way to affect the pitch of the induced structures is by setting the desired laser wavelength. However, tunable laser systems are more expensive than single wavelength ones. Moreover, the frequency splitting typically limits the output power and only a few more wavelengths can be provided. The surface structures are impressed over the steel surface if the lifetime of the wave of molten material is lower than the lifetime of the melt pool left by the pulse [165]. Despite those drawbacks, the modification of the beam frequency is often exploited as it is controllable. Figure 4.12 shows linear ripples obtained on polished steel using infrared and green laser light. The effect of the different wavelengths is clear. A periodicity (Λ_{IR}) of 980 nm is found for the infrared irradiation (λ_{IR} = 1064 nm) (cf. Figure 4.12 (a)). The pitch divides approximately to a half (Λ_{GR} = 460 nm) with the green beam (λ_{GR} = 532 nm) (cf. Figure 4.12 (b)).

- *Irradiation environment (n).* The properties of the LIPSS pattern are influenced by the environment around the irradiated surface. The refraction index role on the LIPSS pitch can be followed by other impacts as thermal effects. The vast majority of the works irradiates silicon through different liquids such as water, oil, and acetone, showing modified periodicities [166–168]. The effect of the irradiation environment does not show a difference in the obtained LIPSS when variating the substrate material between metals and dielectrics [164]. By irradiating steel underwater, the liquid refraction index impact is evident. Figure 4.13 shows how the regular ripples pattern obtained in air (Figure 4.13 (a)) gets shrunk and disturbed by the presence of water (Figure 4.13 (b)).

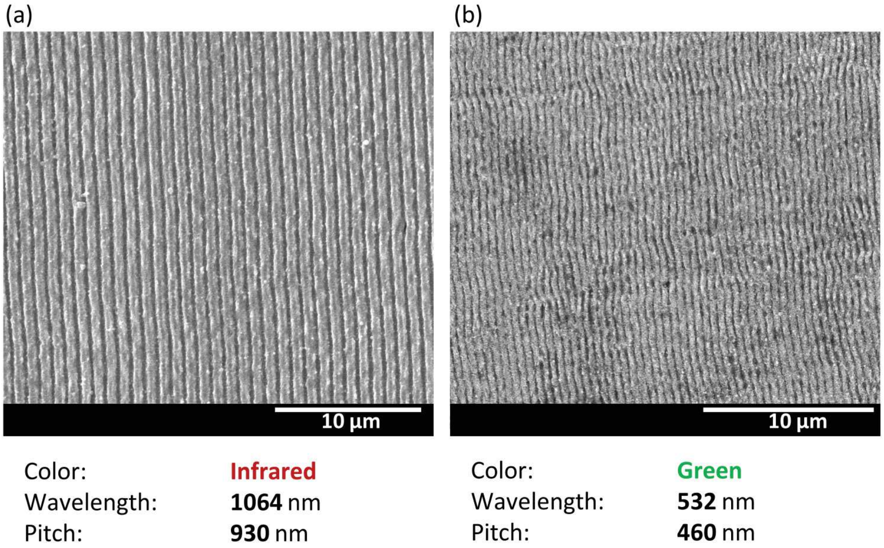

Figure 4.12: Linear ripples obtained through laser irradiation at different wavelengths: (a) infrared irradiation, (b) green irradiation.

Beam Incident Angle °	First Periodicity nm	Second Periodicity nm	Reference
0	800 ± 80		Figure 4.14 (a)
10	930 ± 90	670 ± 50	Figure 4.14 (b)
20	1060 ± 110	570 ± 80	Figure 4.14 (c)
30	1530 ± 250	550 ± 70	Figure 4.14 (d)

Table 4.1: Periodicities obtained for the laser irradiation at different beam incident angles.

- *Light beam incidence angle (θ).* The periodicity of the LIPSS can be also varied by introducing an angle between the laser beam and the working surface. The laser Beam Incident Angle (BIA) controls the energy interference pattern between the incident wave and the one excited over the surface (i.e. surface electromagnetic wave) [142]. Tilting the laser beam, the pattern shows structures with two periods, one representing the solution with the positive sinus (i.e. the lower period) and the latter the negative solution (i.e. the higher period). Figure 4.14 shows a steel surface irradiated with different BIAs. Normal incidence is the most common case and a regular pattern with a single 800 nm pitch can be seen. As the incidence angle increases, the two pattern periodicities deviate to higher or lower values from the first normal one (cf. Table 4.1).

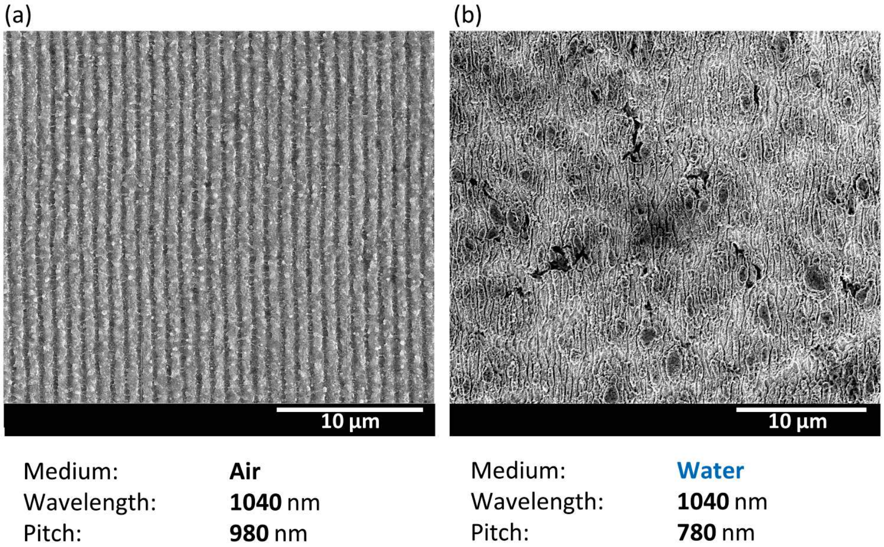

Figure 4.13: Linear ripples obtained through laser irradiation in different environments: (a) through-air irradiation, (b) through-water irradiation.

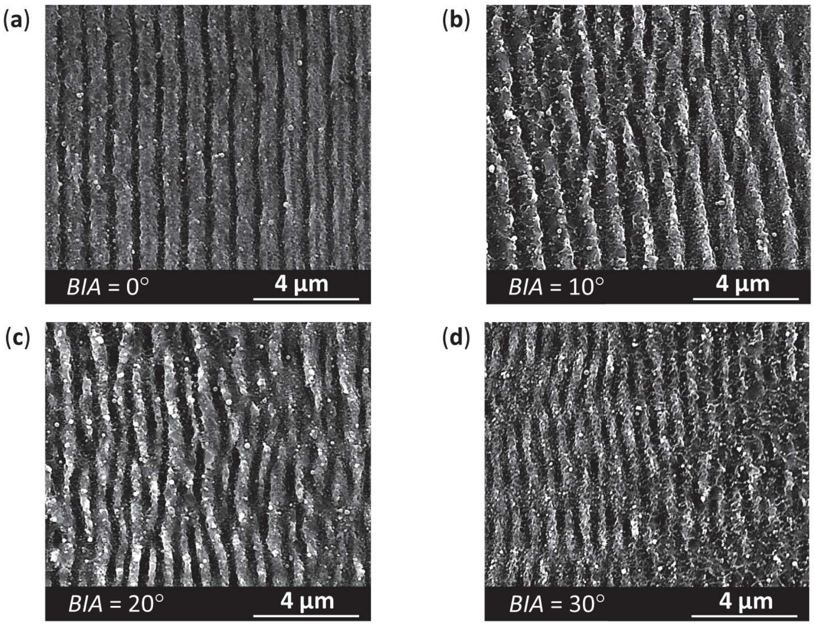

Figure 4.14: Linear ripples obtained through laser irradiation at different laser beam inclinations: (a) BIA = 0°, (b) BIA = 10°, (c) BIA = 20°, (d) BIA = 30°.

4.5.3 LIPSS geometry

Similar to what was previously discussed for the pattern periodicities, the geometry of the surface structures shows a large dependence on the laser light properties. The major contributions to the structure's shape can be related to three factors.

4.5.3.1 *The accumulated fluence*

As the pulsed laser light is scanned over the target surface, the subsequent pulses may overlap in a certain area. The pulse overlapping is controlled through the repetition rate of the laser source, which may also be tunable, and through the scanning velocity. In addition to this first source of overlapping, there is also lateral overlapping. An area is typically patterned scanning multiple lines one next to the other and introducing a certain overlap. In Figure 4.15 it is reported a scheme of a laser patterning strategy. The scheme is not to scale for clarity, but it shows the pulse step size (L) and the lateral step size (H), which control the pulse and the lateral overlap respectively.

The surface structures shapes are sensible to the number of pulses that the surface receives [169]. Therefore, the structure geometry is sensible to the sum of the energies delivered by each hitting pulse, showing a sort of memory effect. The parameter which is commonly used in the literature to count for this effect is the accumulated fluence [170]. The fluence is the energetic parameter that is used to describe the light deposition, and it is expressed in energy above area dimensions. Therefore, the accumulated fluence (Φ) is:

$$\Phi = \phi \cdot N \tag{4.2}$$

Where ϕ is the fluence and N is the number of superimposed laser pulses:

$$N = \frac{\pi \omega_0^2}{H \cdot L} \tag{4.3}$$

$$\phi = \frac{P}{\pi \omega_0^2 f} \tag{4.4}$$

Where ${\omega_0}^2$ is the laser spot radius, P is the average power of the laser, and f is the pulse repetition rate. Figure 4.16 shows LIPSS patterns obtained at different accumulated fluences. The laser spot diameter is 12 μm. The right balance between the scanning and energy parameters is needed to achieve the most regular texture (cf. Figure 4.16 (d)). Excessive values of fluence cause a distortion of the pattern (cf. Figure 4.16 (b) with Figure 4.16 (a)). Following the same ratio, an excessive density of pulses also causes an increase in accumulated fluence and a distortion of the pattern (cf. Figure 4.16 (c) with Figure 4.16 (d)).

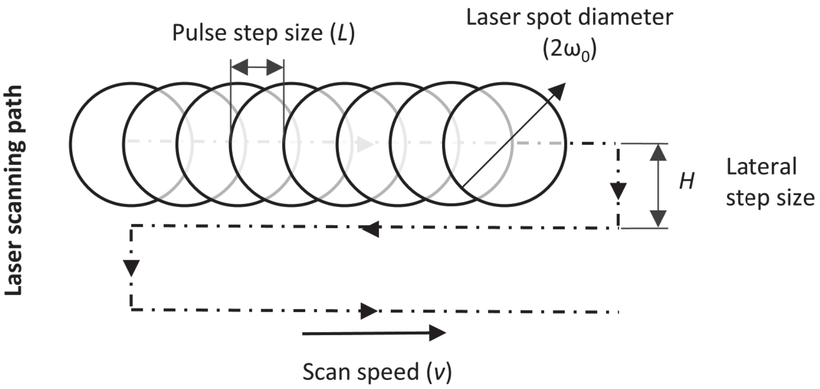

Figure 4.15: Laser scanning path for surface patterning, the consecutive pulses are schematized as circles. (Dimensions are not to scale for clarity)

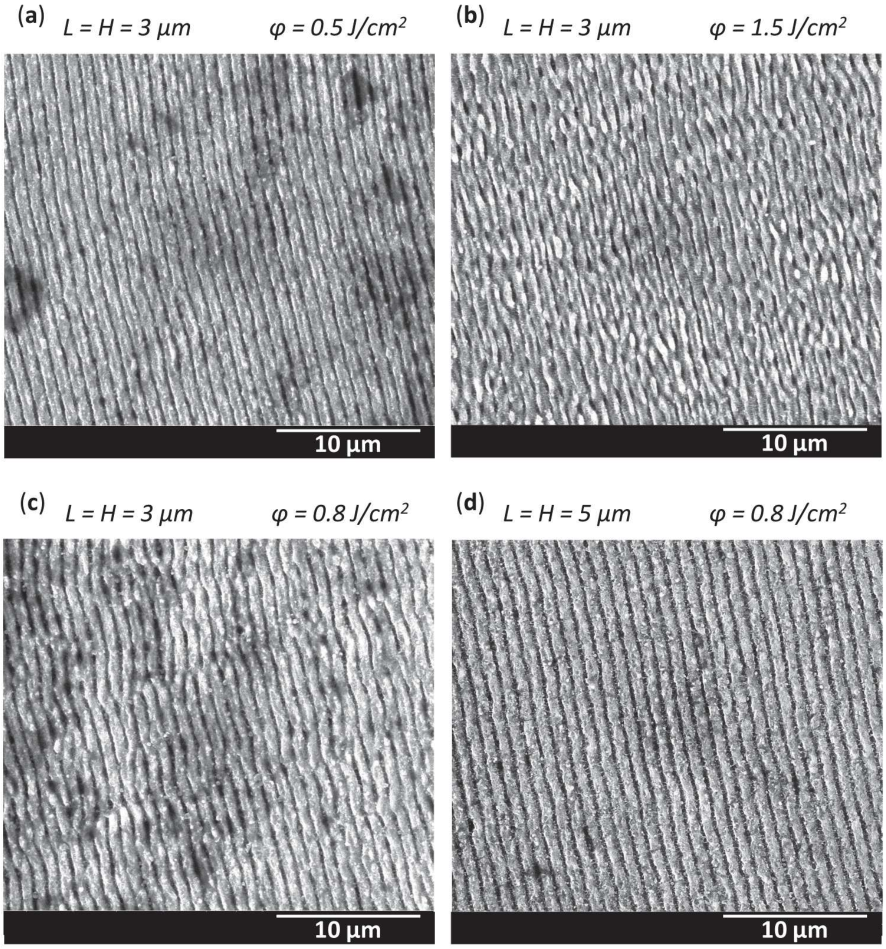

Figure 4.16: LIPSS textures obtained at different accumulated fluences modifying the scanning method and the laser fluence on the surface.

4.5.3.2 *The light polarization*

.

LIPSS induced over materials surfaces impress the laser light properties over the surface. The polarization of the laser light has a dominant effect on the structure shapes and orientation. By modifying the polarization through surface processing, it is possible to directly tailor the micro and nano- surface structures [171]. Linear polarization creates long parallel ripples (cf. Figure 4.16 (d)), aligned perpendicularly to the polarization direction (known as LSFL – cf. subsection 4.5.2). Nanodots, hexagonal, and triangular structures have been found through laser irradiation with circularly polarized light [160, 172]. Elliptical, radial, and azimuthal polarization have been exploited to obtain complex ripples arrangements as spirals and concentric circles. However, such complex structures may be damaged by pulse overlapping [159].

4.5.3.3 *The irradiation environment*

. The irradiation environment has a fundamental role in the thermal behavior of the melt induced by the pulses. The comparison presented in Figure 4.13 already shows a fundamental effect of the surrounding fluid onto the surface structures geometries.

During the selective ablation of the surface, the removed material forms a plasma plume (i.e. a cloud of vapor and atom and ions gas) over the exposed material. The plume behavior, size, and temperature depend on the laser fluence [173] and on the nature of the surrounding environment, [160]. When irradiating the surface at low fluences, the plasma plume has low energy and experiences small displacements from the ablated spot. In such conditions, the surrounding fluid can play a major role in the recast process of the vapor in the vicinity of the surface. Figure 4.17 show the effect of through water laser irradiation on steel, compared to conventional air irradiation. The schemes at the top translate the concept of plume displacement after material irradiation, highlighting the smaller height reached by the water-immersed cloud. The water irradiation forms unique crystal-like lamellae exhibiting thicknesses below 100 nm (Figure 4.17 (b).

4.5.4 Hierarchical

Hierarchical textures show outstanding performances in wetting applications (cf. subsection 4.4.2). For manufacturing purposes, two contrasting needs have to be addressed. Fast (and inexpensive) hierarchical surface texturing requires a minimum number of processing steps to obtain the outcome. On the other hand, precise (and more performant) hierarchical texturing requires more steps. By opti-

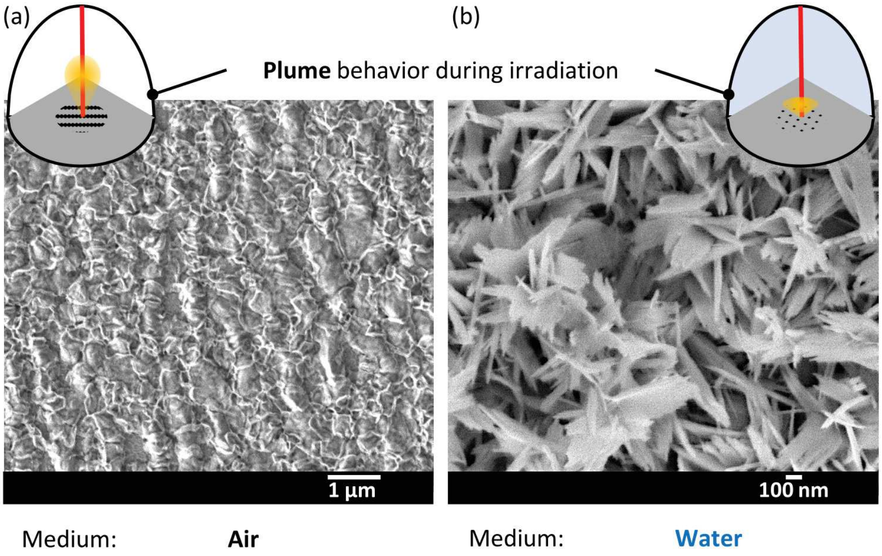

Figure 4.17: LIPSS textures obtained at low fluence in air and water environment. On the top, schemes of the plasma plume displacement picture the laser beam (red) hitting the steel surface (grey).

mizing the processing conditions, it is possible to obtain hierarchical textures through both approaches.

4.5.4.1 One-step hierarchical textures

By increasing the amount of laser energy deposited onto the surface, it is possible to generate hierarchical textures [174]. The two textures are generated on the microlevel (typically with pitches higher than 10 μm) and on the nanoscale (down to pitches of some hundreds of nanometers). In Figure 4.18 (a) an example of a hierarchical texture obtained in one-step is proposed. The first texture is constituted by a pillar pattern. The latter one comprises LIPSS generated over the pillars. The one-step fabrication method is quick, but the texture geometries, pattern pitches, and features depths that can be generated are limited and are both linked to the properties of the light and of the process. Therefore, it is tricky to obtain two regular patterns, as the process optimization for the regularity of one level pattern weakens the other's one.

4.5.4.2 Multiple-step hierarchical textures

The other approach to obtain hierarchical textures has the advantage of controlling the structuring of the two textures separately. The micro-texture is generated first, as the process is characterized by high energy levels and will erase whatever small feature present on the surface. In terms of process classification, the first step can be considered a laser writing technique (cf. subsection 4.2.1). The small

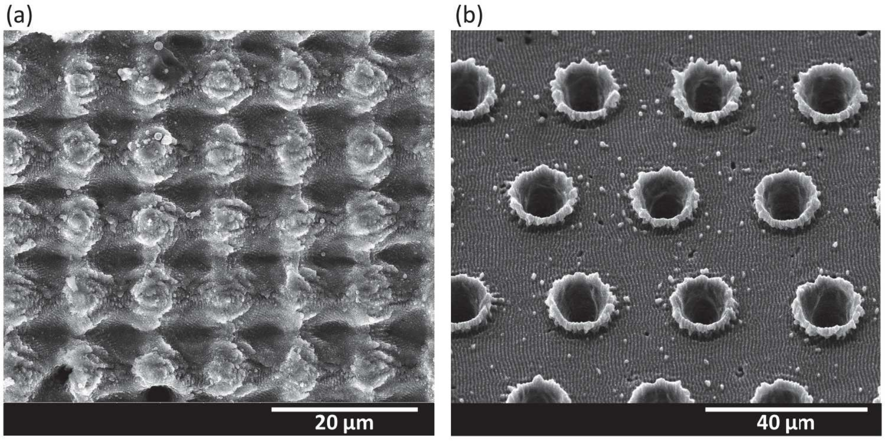

Figure 4.18: Example of hierarchical textures obtained in (a) one-step and (b) multiple-step laser processing.

texture is then created over the micro-texture [175]. The multi-step approach has the advantage of optimizing each step, for precise surface structuring. In Figure 4.18 (b) an example of a hierarchical texture obtained in multiple-step is proposed. The laser writing technique used in this case is laser drilling of a pattern of deep holes. Next, linear ripples were obtained over the top surface. More than two steps may be required when the first laser writing process forms large quantities of recasts (it is the case of picosecond laser writing). Between the two steps for texture formation, a laser-polishing step can be added to prepare the surface for LIPSS formation.

Part II

MATERIALS AND METHODS

5 ULTRAFAST LASER TEXTURING

Mold surfaces are realized employing a wide variety of machining processes, among with (cf. section 4.3) milling and electro-discharge machining are the most common. Each machining process has its peculiar effect on surface finish, being a result of the exploited physical mechanism. As the cavity dimensions shrink, either for thin-wall injection molding or in micro injection molding applications, the effects of the surface properties can gain importance and cannot be neglected. In this work, ultrafast laser-based technologies were exploited to modify the mold surface, generating periodic textures. The effects of such surfaces were investigated onto different aspects of the injection molding process, namely the filling flow and the replication process.

5.1 PICOSECOND LASER SYSTEM

The ultrafast laser texturing process has been thoughtfully studied to widen the structuring capabilities in terms of achievable geometries and the regularity of the patterns (cf. section 4.5). The laser utilized for the experiments is an Atlantic IR5-GR2-UV1 picosecond laser source, produced by Ekspla. The laser source emits on three different wavelengths 10 ps laser pulses. The fundamental laser beam, which has a wavelength of 1064 nm, is frequency-doubled and frequency-tripled by inserting non-linear crystals. The beam output specifications, as stated by the producer of the laser source, are provided in Table 5.1. The laser source computer control allows for the managing of the emitted laser wavelength, the beam power, and the pulse repetition rate.

The emitted laser beams are treated and carried over the working area using three distinct optical paths to optimize the beam handling. In Figure 5.1 a simplified example of the optical path is provided. The laser beam emitted by the laser source is expanded through a beam expander and delivered to the Galvo scanner through mirrors and an optical polarizer (cf. Figure 5.2). The 2-axis Galvanometer scanner (SUPERSCAN V-15 Raylase) is characterized by a digital encoder technology, which achieves high positioning resolution, minimal drift, and low noise to obtain sharp corners. The 2-axis deflection unit is fully computer-controlled. In Figure 5.3 (a) a schematic of the working principle of the unit is provided. After the controlled deflections onto the two motor-controlled mirrors, the laser beam passes through

Parameter		**Value**	**Unit**
Wavelength	IR	1064	nm
	GR	532	nm
	UV	355	nm
Pulse repetition rate (range)		100 – 1000	kHz
Maximal average output power at lowest pulse repetition rate	IR	> 3	W
	GR	> 1.8	W
	UV	> 1.0	W
Pulse energy at lowest pulse repetition rate	IR	30	μJ
	GR	> 18	μJ
	UV	8	μJ
Pulse contrast	IR	$> 100 : 1$	
	GR	$> 1000 : 1$	
	UV	$> 1000 : 1$	
Pulse energy stability	IR	< 0.8	%
	GR	< 1.5	%
	UV	< 1.5	%
Pulse duration		10 ± 3	ps
Polarization		Linear, vertical 100:1	
M^2		<1.3	
Beam circularity (far field)		>0.85	
Beam divergence	IR	< 2.0	mrad
	GR	< 1.5	mrad
	UV	< 1.5	mrad
Beam diameter (1/e^2) at 50 cm distance from laser aperture	IR	1.4 ± 0.2	mm
	GR	1.2 ± 0.2	mm
	UV	1.1 ± 0.2	mm

Table 5.1: Beam output specification of the Atlantic IR5-GR2-UV1 laser source as stated by the producer, Ekspla.

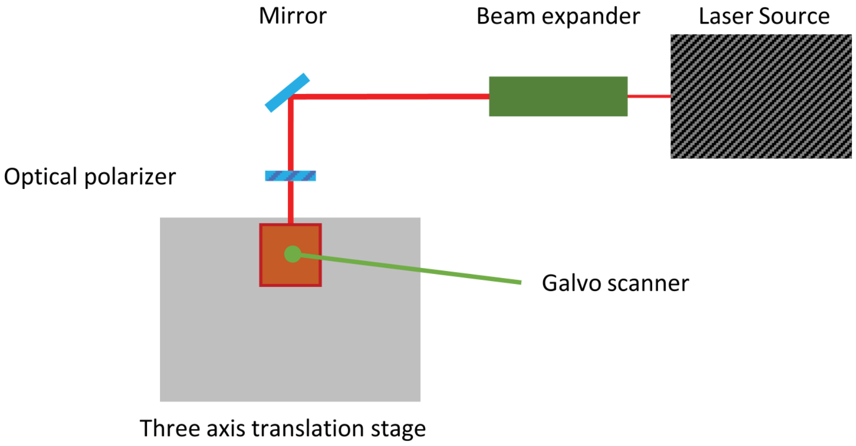

Figure 5.1: Simplified schematic showing the utilized optical path for the texturing experiments.

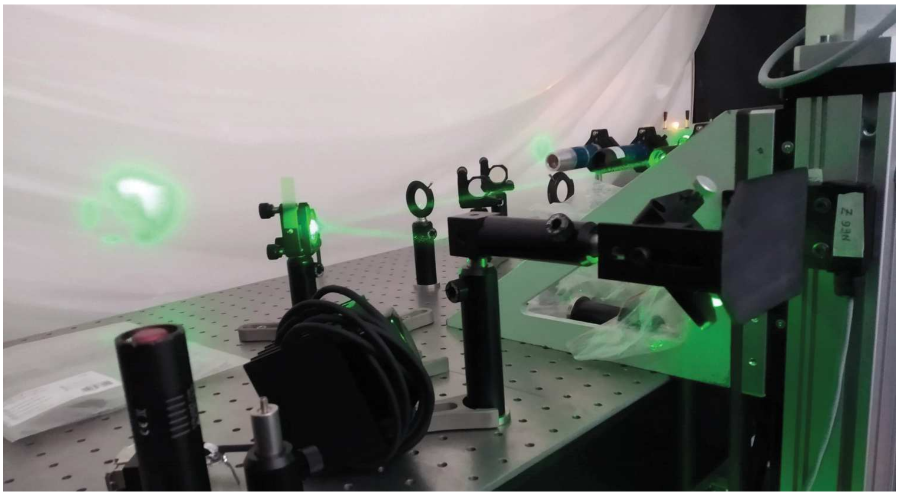

Figure 5.2: Green (wavelength 532 nm) laser beam directed from the beam expander to the Galvanometer sacnner.

an f-theta objective, which focuses the light over the working area. The focal length of the f-theta objective is 80 mm, 74 mm, and 137 mm for the IR, GR, and UV wavelengths respectively. The computer-controlled Galvanometer scanners are exploited to precisely move the laser spot over the surface. The optical system has the capability of moving the light spot at velocities up to 3 m/s with repeatability below 1 µm. A computer-controlled three-axis translation stage was exploited to precisely locate the mold inserts on the focal plane of the laser. The laser light power emitted by the laser has been measured through a power meter (Gentec-EO MAESTRO Single Channel Laser Power equipped with a XLP12-3S-H2-D0 sensor) cf. Figure 5.3 (b).

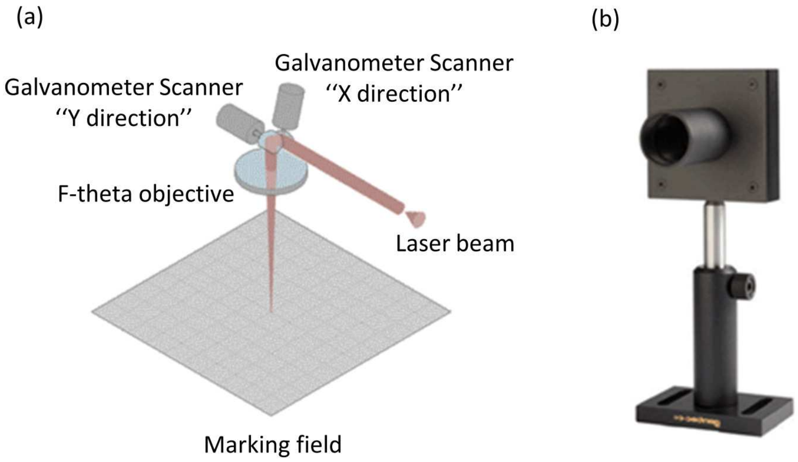

Figure 5.3: (a) Schematic representation of the working principle of the utilized Galvanometer sacnner. (b) Laser power meter exploited during the laser texturing experiments.

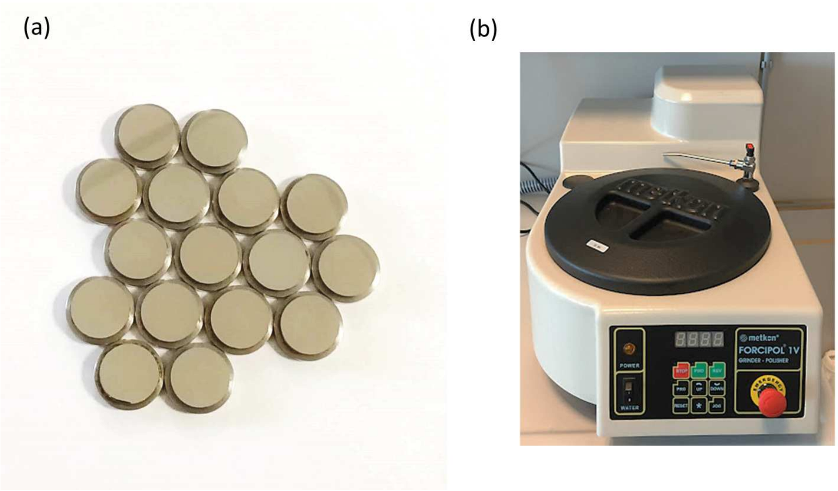

Figure 5.4: Mirror polished H11 steel samples for the ultrafast laser texturing operations.

5.2 SAMPLES AND INSERTS PREPARATION

The objective of the study regarding ultrafast laser processing is to achieve highly controlled and regular surface structures on mold steel. The roughness level of the surface irradiated by the pulsed light has shown an influence on the achieved textures, leading to undesired pattern defects and inaccuracies. The presence of random asperities over the surface scatters the laser light, modifying the local energy distribution and locally orientating the direction of the induced surface structures. With the aim of reducing the noise associated with the pre-existing surface roughness, all the testing samples and the mold inserts were mirror-polished to a value of Sa lower than 50 nm (cf. Figure 5.4 (a)). The polishing operations were carried out using a grinder - polisher (FORCIPOL 1V, Metkon Figure 5.4 (b)). The obtained surface finish is evaluated through interferometric optical microscopy (cf. section 7.1).

The samples utilized for the optimization of the laser-induced texture outcome and the injection mold inserts are constitutes by the same steels, namely stainless steel and common mold steel for injection molding applications. The first is Stavax ®(X40CrV14) and the latter is H11 (X37CrMoV5-1).

5.3 SCANNING AND ENERGY DEPOSITION METHODS

The mechanism of LIPSS formation is strongly dependent on the design of the surface scanning and the amount of energy delivered to the working material. A parameter that is often exploited to control the total amount of energy delivered per unit area is the accumulated fluence (cf. subsubsection 4.5.3.1). The experimental campaign explores a wide range of accumulated fluences by tailoring both energetical (i.e. settings of the laser source) and scanning (i.e. settings of the Galanometers scanners) parameters. The laser pulse energy and repetition rate were changed through the experiments. The scanning velocity, pulse step size, and lateral step size were varied to achieve a wide range of of superimposed pulses number over the working surface.

6 INJECTION MOLDING SETUP

In this work, the objective of injection molding part is characterizing the filling and the replication phenomena occurring in the mold cavity varying the mold surface properties. These experimental investigations require dedicated experimental setups and an accurate and precise injection molding machine. The experimental approach does take into account the application-driven characteristic of the study and the accurate understanding of the occurring phenomena. Therefore, the designed mold cavities are designed to represent the typical feature of the industrial products and minimize the cavity complexity to distinguish the effects of the mold surface. Moreover, the identification of simple mold designs facilitates the numerical and analytical description of the polymer flow.

6.1 INJECTION MOLDING MACHINE

The state-of-the-art micro injection molding machine (Wittmann Battenfeld, MicroPower 15) used for the experiments is characterized by the separation of the metering (14 mm plasticizing screw) and injection (5 mm injection plunger) units (cf. Figure 6.1). The clamping unit is characterized by a maximum closing force of 150 kN. The machine can reach a maximum injection speed of 750 mm/s and a maximum injection pressure of 2700 bar. The main characteristics of the micro-injection molding machine are reported in Table 6.1. The machine is controlled through the *Unilog B6* control unit, which also allows for the evaluation of the quality of the process by plotting actual value graphs cycle by cycle.

6.1.1 Injection molding auxiliaries

Injection molding auxiliaries were exploited to maintain and control the process within the desired tolerances. In particular, during the experimental investigations, a polymer pellets dryer (Moretto X Dry Air) was used to conditionate the resins before molding (cf. Figure 6.2 (a)). The double chamber technology allows for high drying reliability. The dryer can maintain temperatures as high as 180 °C.

The mold temperature control was achieved using a thermoregulator (Wittmann Battenfeld Tempro plus D Micro 100) (cf. Figure 6.2 (b)). The water temperature controller is equipped with powerful

Properties	**Unit**	**Value**
Clamping unit		
Clamping force	kN	150
Opening stroke / Opening force	mm/kN	100/15
Ejector stroke / Ejector force	mm/kN	40/5
Injection unit		
Dosing screw diameter	mm	14
Dosing screw stroke	mm	9
Screw L/D ratio		20
Injection plunger diameter	mm	5
Max injection volume	cm^3	1.4
Specific injection pressure	bar	$2,500$
Max. screw speed	min^{-1}	200
Max. plasticizing rate	g/s	1.7
Max. screw torque	Nm	90
Nozzle stroke b / Contact force	mm/kN	230/40
Injection speed	mm/s	750
Injection rate into air	cm^3/s	38
Barrel heating power, nozzle inc.	kW	2.45
Drive		
Electrical power supply	kVA	9

Table 6.1: Wittmann Battenfeld Micropower 15t technical data sheet.

Figure 6.1: Micro injection molding machined utilized through the experimental campaign.

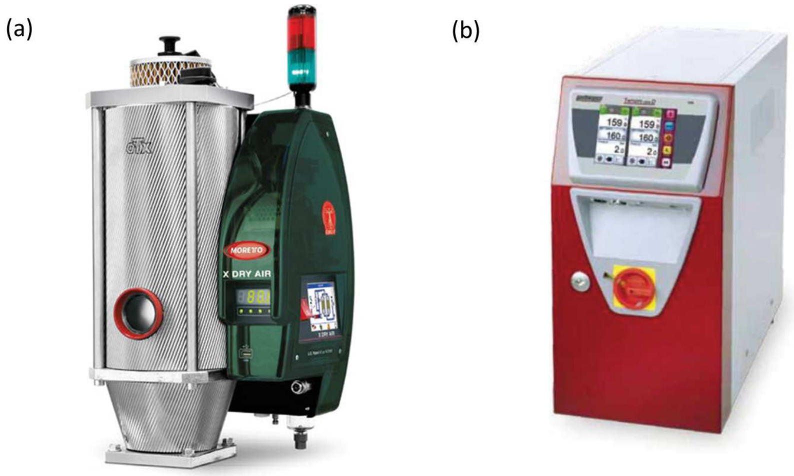

Figure 6.2: Auxiliaries utilized during the experimental campaign: (a) polymer pellets dryer and (b) water temperature controller for mold conditioning.

pumps (the pressures can go up to 5 bar with flow rates up to 30 l/min) and a sensible microprocessor controller with an accuracy of 0.2 °C.

6.2 CAVITY DESIGN

Different mold setups were exploited to study the effect of surface modifications on filling flow and on replication. The mold assembly was based on a Hasco K-standard modular system; several centering elements and coupling units were introduced to guarantee the accurate coupling of the two mold halves upon closing. For all the mold assembly, the temperature was set using an external thermoregulator (cf. subsection 6.1.1) pumping water into a hexagonal cooling circuit and two electrical cartridge heaters for each mold side. The diameter of the heaters is 6.5 mm. The mold temperature was controlled using a single thermocouple placed just below the insert in each of the mold fixed and moving halves.

6.2.1 Filling characterization setup

The analysis of the surface engineering effects on the polymer filling flow was carried out using a slit die open-flow channel. The mold is specifically designed to allow for the fast mounting of inserts to test their different surface properties on both fix and moving plates (cf. Figure 6.3). The length of the rectangular cavity is 50.5 mm, the width is 6 mm and the thicknesses can be easily changed thanks to the intermediate mold plate. Through the experiments, five differ-

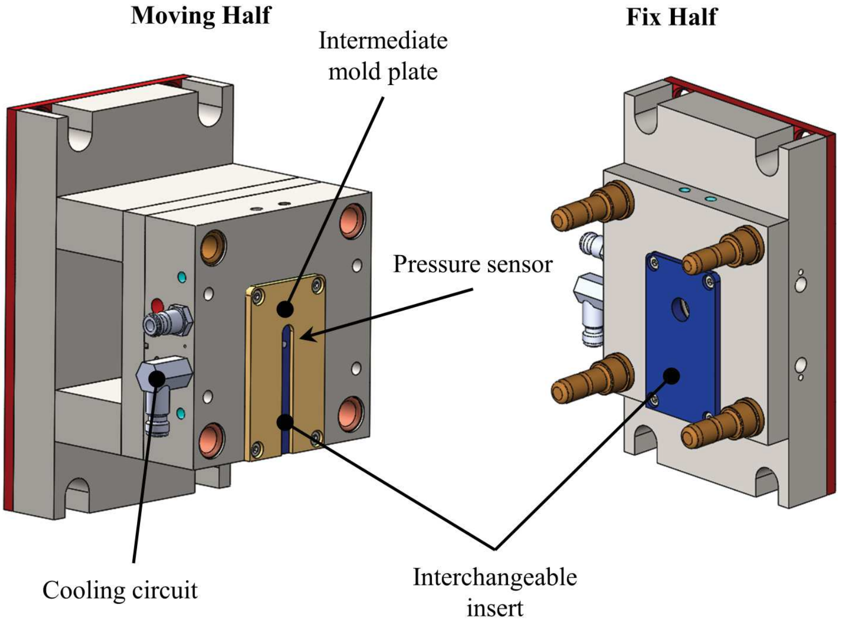

Figure 6.3: Design of the mold inserts for the moving and fixed halves.

ent intermediate mold plates characterized by different thicknesses were exploited to modify the cavity geometries. The considered slit die thicknesses, depending on the particular surface functionality explored, are 1, 1.5, 1.9, 2.1, and 2.5 mm.

The design of the moving half comprises a pressure transducer to monitor the cavity pressure. The sensor is flush-mounted at a distance of 42.5 mm from the end of the cavity. The mold temperature is set and controlled using two different thermocouples placed close to the mold cavity. The cooling channels are hexagonally arranged below the interchangeable inserts to perform a uniform cooling of the mold halves. The layout of the channels is symmetrical in the fix and moving halves and it is presented in Figure 6.4.

The open-flow slit die mold cavity has been designed to study the phenomena occurring during the filling phase of the injection molding cycle. By having different thickness intermediate mold plates, it is possible to characterize the polymer flow at a broad range of flow regimes. In other words, such a design allows for the study of flows characterized by very different shear rates. By having an open cavity, it is possible to separate between the cavity filling flow and the free flow of the polymer out of the mold. The distinction is executed through the analysis of the acquired pressure signal.

6.2.1.1 Cavity pressure measurement

The moving half of the mold is equipped with a piezoelectric pressure sensor (Kistler typer 5039 A). The signal from the sensor is collected by a Kistler CoMo control unit, which can collect the data from differ-

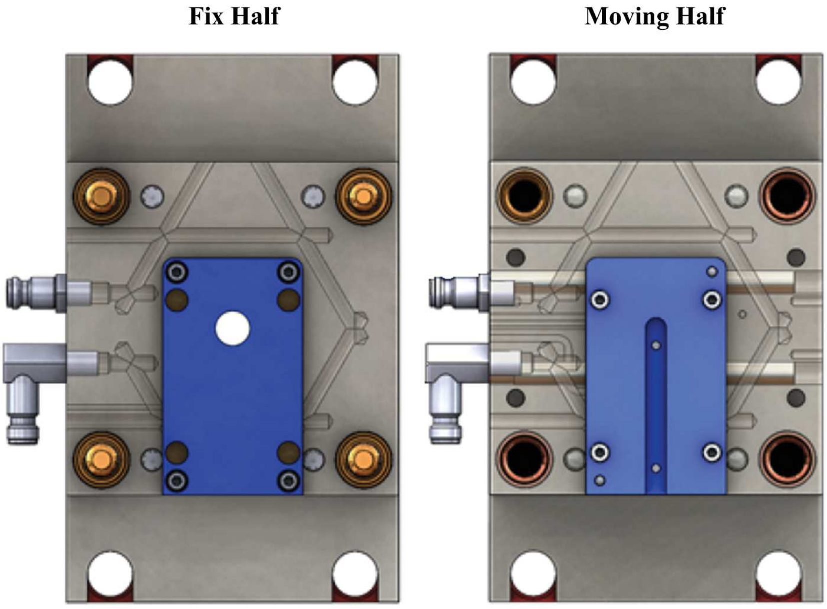

Figure 6.4: Arrangement of the cooling channels on the fix and moving halves of the mold.

ent channels and automatically organizes the data for data processing. The typical pressure curve (cf. Figure 6.5) exhibits a first quasi-linear pressure growth, which characterizes the filling of the cavity, and a plateau region, which characterizes the polymer flow through the slit die on open atmosphere. The pressure signals were acquired after process stabilization (after 15 molding cycles) and 10 signals were collected for each molding condition (cf. Figure 6.6 (a)). The acquired pressure signals were then processed in MS Excel to align them at the beginning of the injection phase. The alignment of the signals allows for the precise evaluation of the replicability of the pressure measurement. In Figure 6.6 (b) the standard deviation between the molding cycles plot shows the tool used during the experimental campaign to evaluate the quality of the data.

6.2.2 Replication characterization setup

The plastic part designed for the replication studies is a disc with a diameter of 18 mm and a depth of 1.5 mm (cf. Figure 6.7 (a)). The cavity was machined in the B-plate of the Hasco modular mold assembly at the end of a 7 mm long semi-cylindrical cold runner. Interchangeable cylindrical mold inserts were designed to study different surface properties and facilitate the polishing and laser structuring phases (cf. Figure 6.7 (b)). The mold insert carrier was designed to mount cylindrical inserts with the different surface properties object of the works (cf. Figure 6.8 (a)). Part ejection was achieved through three

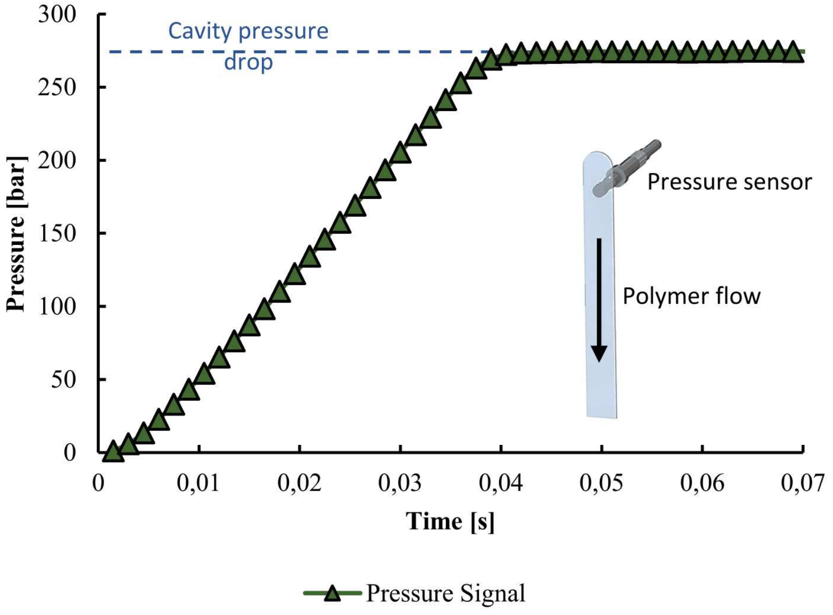

Figure 6.5: Example of an acquired pressure signal. The dashed line represents the cavity pressure drop between the sensor and the end of the open flow slit die.

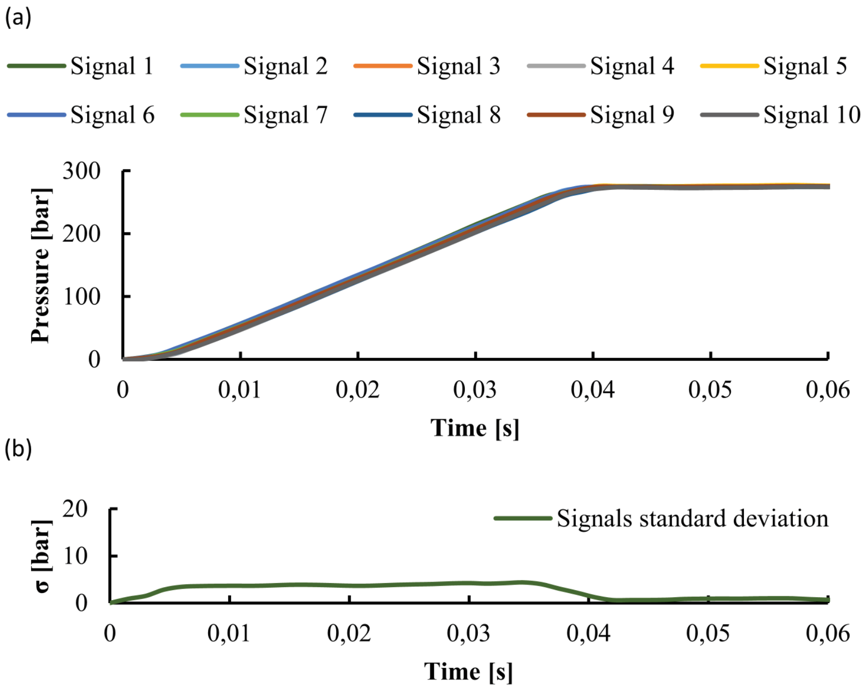

Figure 6.6: (a) Example of the pressure data obtained with 10 repeated measures for one molding condition. From the comparison of the pressure signals it is possible to calculate the mean and the standard deviation (b) of the pressure for each time step.

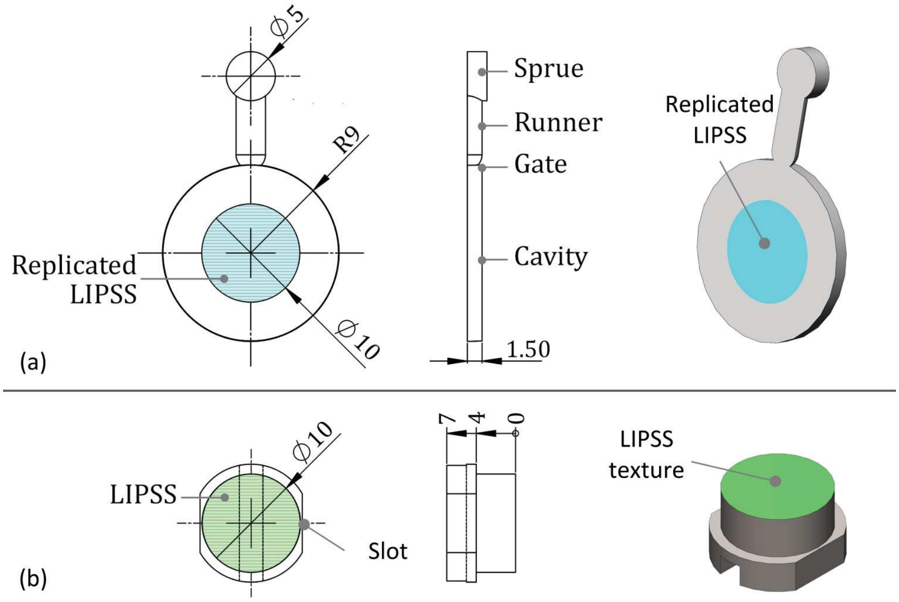

Figure 6.7: Design of (a) the molded part and of (b) the mold insert.

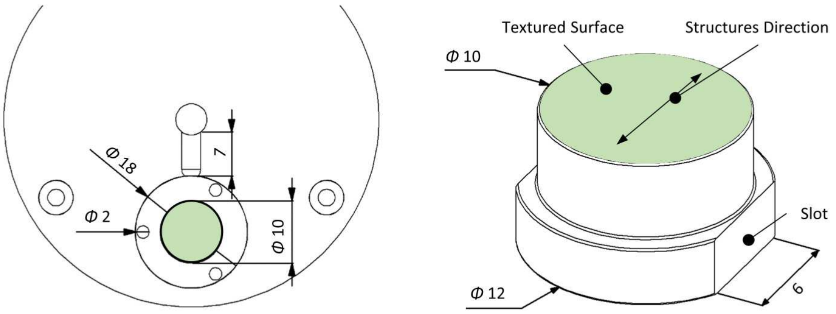

(a)

(b)

Figure 6.8: (a) Design of the mold cavity. (b) Design of the textured insert and alignment features. (All dimensions are in millimeters).

ejector pins uniformly distributed at the part circumference (i.e. at 120° distance). The cylindrical inserts bases were machined to obtain a reference for the alignment of the LIPSS texture (cf. Figure 6.8 (b)). The ripples on the mold surface were orthogonally aligned to the polymer flow direction, to perform the injection molding trials on the worst conditions for replication.

During the experiments, the mold temperature was widely varied, even above the glass transition temperature of the selected resin. Therefore, the mold temperature was set and controlled using a rapid heat cycle molding unit. The heating phase was carried out through electrical cartridges and the cooling one through water pumping on the hexagonally arranged cooling channels. To ensure the stability of the process, 20 molding cycles were performed before the first part was collected. For each condition, 15 parts were sampled.

6.3 MOLD INSERTS COATING

Mold surface coatings are commonly used in industrial applications to improve hardness and wear resistance, ultimately improving the mold life. Ceramic mold surface coatings were exploited in this work to passively modify the thermal boundary condition between the melt and the mold (cf. section 2.4). The aim of the work is to characterize the insulative and chemical effect of the coating on the polymer flow, on the replication of the structure, and on the structure of the very first layer of the molded plastic part.

Coating selection was carried out considering the target mold surface which has to be treated. In particular, micro and nanotextured surfaces coating need to be carried out taking into account possible structure clogging due to the coating deposition. For those reasons, the coatings selected for the studies that comprise smooth surfaces differ from the others.

6.3.1 Coating of smooth surfaces

The work focuses on the correlations between the surface coating and the substrate steel, considering the effects of the substrate thermal conductivity change. Four different mold inserts were selected according to their tribology, hardness, and thermal properties. Two different substrate steels were selected: (i) Stavax ®steel (X40CrV14) and (ii) H11 steel (X37CrMoV5-1). The steels were employed in the experimental campaign in the uncoated form and coated with (i) chromium nitride (CrN) and (ii) diamond-like carbon (DLC) respectively. The coatings were deposited over the steel substrates by Plasma Assisted – Chemical Vapor Deposition (PA-CVD). The achieved thickness is 2.0 $\pm$ 0.5 μm. The lifetime of the selected coatings does not constitute an issue since they are designed to increase surface hardness and thus wear resistance of mold surface.

6.3.2 Coating of textured surfaces

The geometry of the surface structures induced by ultrafast laser processing have dimensions ranging from few hundreds of nanometers to few microns. To avoid major texture geometric modifications, the coating process needs to form extremely thin ceramic layers. Therefore, the selected coating process was ALD. A 10 nm layer of Al2O3 was deposited over the mold structures. The deposition process was carried out at a temperature of 180°C, performing 100 cycles, using argon to purge after each cycle.

6.4 INJECTION MOLDING POLYMERS

Different types of polymer materials have been used during the experimental investigations of this work. The different resins were selected according to the specific aim of each work, considering the industrial application related to the work objective. Filling and replication phenomena are highly affected by the polymer rheological properties. Therefore, the rheological characterization of the resin and control of the polymer conditions are essential for comparing the properties of different polymers in a wide range of shearing conditions and for a deep understanding of the injection molding results and an effective injection molding process modeling.

6.4.1 Rheological characterization setup

The rheological characterization of the polymers utilized in this study was carried out using a rotational rheometer (Ta Instruments, ARES) and two capillary rheometer (Ceast, Rheo 2500 and Dynisco, LCR 7000). The rheometers allows for the determination of the dependence of the polymer viscosity to shear at a given temperature. By performing the tests at different temperatures, it is possible to characterize the viscosity dependence to the temperature.

The rotational and the capillary rheometers material information are complementary in the sense that the first allows for the measurement of the material properties at low shears (typically between 0.1 to 100 s^{-1}) and the latter is well suited for higher shears (between 50 to 5000 s^{-1}). The rotational measurements were carried out with a cone and plate setup, using 25 mm diameter discs. The capillary measurements were carried out exploiting two different dies to perform the Bagley correction. To substitute the hypothesis of Newtonian fluid, the Rabinowitch correction was applied to the raw data.

The corrected rheological data were exploited to fit the Cross-WLF (William-Landel-Ferry) model. The model is commonly coded in the simulation software to describe the polymer viscosity behavior. The Cross model describes the dependence of polymer melt viscosity on the shear rate:

$$\eta(\dot{\gamma}) = \frac{\eta_0}{1 + \left(\frac{\eta_0}{\tau^*}\dot{\gamma}\right)^{1-n}} \tag{6.1}$$

where $\eta(\dot{\gamma})$ is the the viscosity as a function of the shear rate, and η_0, τ^*, n are coefficients.

The WLF model describes the effect of the temperature onto the polymer viscosity:

$$\eta_0 = D_1 \exp\left(\frac{-A_1(T - T^*)}{A_2 + (T - T^*)}\right) \tag{6.2}$$

$$T^* = D_2 + D_3 \cdot P \tag{6.3}$$

$$A_2 = \tilde{A}_2 + D_3 \cdot P \tag{6.4}$$

where D_1, D_2, D_3, A_1 and $\tilde{A}_2$ are constants to be determined, while T^* is a reference temperature and P is the polymer pressure.

6.4.2 Thermal characterization setup

The thermal properties of polymers that are taken under consideration in this work are mainly correlated to the melting, solidification, and crystallization phenomena. Differential scanning calorimetry (DSC – TA instruments, Discovery DSC) was exploited to achieve the characterization of the polymer thermal properties. The resulting heat flow curve has been exploited to characterize the no-flow temperature (NFT). The NFT is one important parameter used by simulation software in combination with the Cross-WLF model to describe the local polymer properties during the non-isothermal shearing flow of the melt inside the mold cavity.

6.4.3 Polymer wetting characterization setup

The wetting properties of the different polymers over coated and uncoated mold surfaces were characterized to model the effect of coatings on replication. The contact angle between the molten polymer and coated and uncoated smooth mold inserts was measured using a drop shape analyzer (Kruss, DSA100), which was equipped with a high-temperature syringe dosing unit (Kruss, TC21) and measuring cell (Kruss, TC3213). The tests were performed for all polymers at the injection molding melt temperature selected for the resins.

The drop shape was analyzed using the software developed by the Kruss company and integrated with the instrument.

6.4.4 Polymer selection

6.4.4.1 Filling characterization

The characterization of the filling flow inside the open flow mold cavity was carried out using a commercial PET (Cepsa, PET SR08). Table 6.2 reports the main polymer properties. PET is a widespread polymer due to its use for plastic bottles, which are low-cost applications. Cost reasons push the process to adopt extremely low thickness cavities at severe thermal conditions. Therefore, particular attention is given to this polymer and its processability. Before the injection

Property	Unit	Test Method	PET
Density	g/cm^3	ISO 1183-2:2004	1.33
Melt Flow Index (200 °C – 5 kg)	g/10min	ISO 1133-1:2011	6
T_g (10 °C/min)	°C	ISO 11357-2:2013	80

Table 6.2: Main properties of PET.

Polymer	Structure	Density g/cm^3	Melt Flow Rate g/10 min
PS	Amorphous	1.05	12 (200°C – 5.0 kg)
PMMA	Amorphous	1.18	21 (230°C – 3.8 kg)
PS	Crystalline	0.90	35 (230°C – 5.0 kg)
PS	Crystalline	1.24	14 (220°C – 5.0 kg)
PS	Crystalline	1.49	11 (190°C – 5.0 kg)

Table 6.3: Main properties of the polymers selected for the replication studies.

molding experiments, a drying cycle at 180 °C for 8 hours was performed, with a dew point of -45 °C.

6.4.4.2 Replication characterization

A variety of polymer materials were exploited to study the effects of the mold surface engineering and of the injection molding process on the replication of micro and nanostructures. Both common petrol-based polymers and biopolymers are considered in the study. The mail polymer properties are summarized in Table 6.3.

- Polystyrene (PS) – Total Petrochemicals & Refining
- Poly-methyl methacrylate (PMMA) – Polycasa Acryl G55
- Isotactic polypropylene (PP) – Pro-fax 702 LyondellBasell
- Polylactic acid (PLA) – Ingeo NW3052D, Natureworks
- Polylactic acid and polybutylene adipate terephthalate blend (PBAT-PLA) – M-Vera BF MV GP1025 Biofed

Before either the injection molding or the rheological experiments, the polymers were dried at 80°C for 4h using the dryer described in subsection 6.1.1.

7 SURFACE CHARACTERIZATION

The surface generated either through on the mold or by replication on the plastic part was thoroughly characterized using different characterization techniques and instrumentations. Both laser-textured and coated insert surfaces were inspected to extract information for the modeling phase.

7.1 OPTICAL PROFILOMETRY

Optical profilometry has been exploited to assess the overall properties of the surface. While the coated smooth inserts can be effectively characterized by this technique, optical imaging cannot inspect surface features that are around the small micro scale. The 3D optical profiler (Sensofar, Plu Neox) was exploited in both the interferometric and confocal mode, depending on the surface properties of the measuring sample. In Table 7.1 the main properties of the 3D optical profiler (shown in Figure 7.1) are reported.

7.1.1 Roughness measurements

Roughness measurements were performed basically with two objectives. The first is to measure the obtained surface roughness after polishing operations. The latter is characterizing the roughness of the surface which will be interested in the polymer contact. The surface roughness was measured in three different locations along the area relative to the cavity (cf. Figure 7.2). The measurements were performed on uncoated smooth and coated smooth inserts. Depending on the surface reflectivity, the roughness measurements were per-

	5X	20X	100X
Numerical aperture	0.13	0.45	0.90
Maximum slope (deg.)	7	21	51
Field of view (μm)	3378 x 2826	636 x 477	127 x 95
Spatial sampling (μm)	1.38	0.83	0.17
Optical resolution (μm)	1.08	0.31	0.15

Table 7.1: Main characteristics of the 3D optical profiler.

Figure 7.1: Sensofar Plu Neox 3D optical profiler used during surface inspection.

formed both in confocal mode with the 20X objective and in interferometric mode with the 5X objective.

7.1.2 Texture measurements

Optical profilometry was also exploited to characterize the micro-sized pitch of the hierarchical texture. As previously said, the characterization of smaller features required different approaches. However, the confocal measurements offer a relatively fast characterization of the 3D structure of the big pattern. those morphological measurements were performed in confocal mode, using the 100X objective. The 3D profiler allows for the selection of the inspection light. It is possible to select red (characterized by a central wavelength of 630 nm), green (530 nm), blue (460 nm), and white light. Although the producer suggests using the green one for the vast majority of the measurements, in this case, the blue one has been used. As it is stated in the product descriptions, the shorter the wavelength the higher the optical resolution. In Figure 7.3 an example of the acquired and reconstructed 3D morphology is presented.

7.2 SCANNING ELECTRON MICROSCOPY

Scanning electron microscopy (SEM – Quanta FEI 400 and JEOL, 7401F FESEM) allows for the fast inspection of the treated surfaces. 2D measurements and only qualitative information of the mold topography are obtainable. Therefore, the SEM characterization has been widely

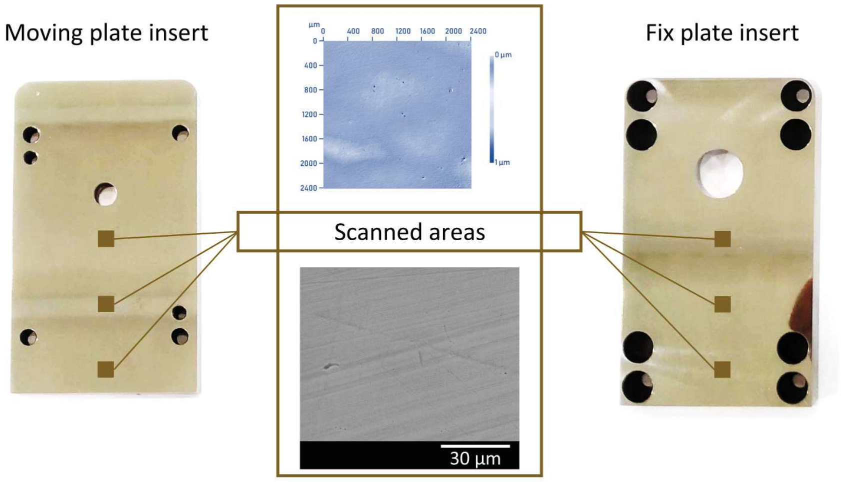

Figure 7.2: Schematic of the measured areas on the mold inserts and sample topography acquired for a sampling area.

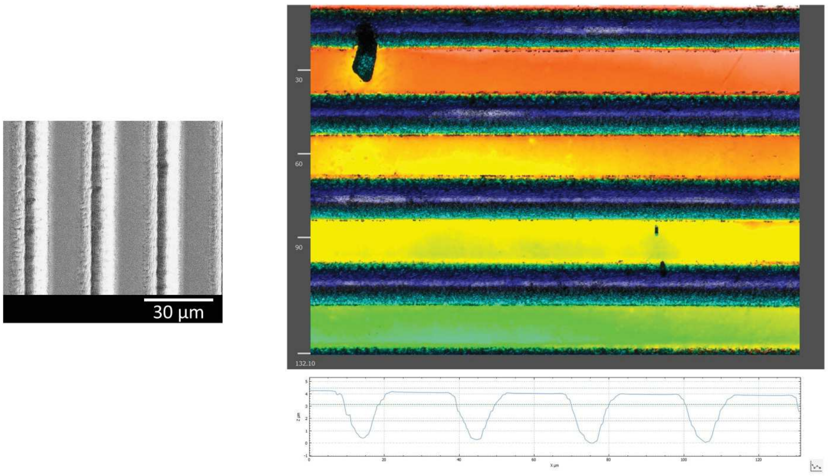

Figure 7.3: Example of an acquired 3D morphology of a laser-induced microtexture.

exploited to assess the geometrical properties along the surface. The measurements were carried out using a secondary and back-scattered electron detector (ETD) and with an acceleration voltage of 20 kV and a spot size of 4 */mum*.

The structure periodicity was carried out using 2D Fast Fourier Transform (2D FFT) analysis of the entire measured surface. The main peaks of the spectrum can be correlated to surface periodicities [176]. Two parameters were considered to describe the pattern quality, (i) regularity (R), and (ii) homogeneity.

7.2.1 Pattern regularity

Pattern regularity refers to the uniformity of the pitch distance between consecutive structures. This parameter was evaluated from the 2D FFT analysis of the topographies acquired using AFM. The regularity is represented by the standard deviation of the normal distribution associated with the peak of the considered ripple periodicity. Since the pitch variation was within the direction of the ripples, a horizontal profile of the 2D FFT analysis was extracted (cf. Figure 7.4). The regularity of the pattern was evaluated considering the ratio between the standard deviation (σ) of the normal distribution associated with each pitch (Λ) present along with the pattern and the pitch itself:

$$R = 1 - \sum_{i=1}^{n} \frac{2\sigma_i}{\Lambda_i} \tag{7.1}$$

7.2.2 Pattern homogeneity

The homogeneity of the texture was analyzed considering the ripple dispersion angle γ (i.e., the angle deviation of the ripples from the straight parallel configuration). This dispersion angle can be adequately described considering the angle γ that encloses the areal 2D FFT peak dispersion of the ripple frequency (cf. Figure 7.5).

7.3 ATOMIC FORCE MICROSCOPY

Atomic force microscopy (AFM - Veeco Digital Instruments and PSIA, XE-100) was exploited to acquire 3D point clouds describing the micro and nano morphology of the textured surfaces and of the replicated parts. The AFM setup is described in Table 7.2. The measurements were performed in non-contact tapping mode onto 20 x 20 μm and 10 x 10 μm areas were acquired. The scan direction was orientated perpendicularly to the mold or part structures to obtain the highest contrast. Both the forward and backward signal that is given

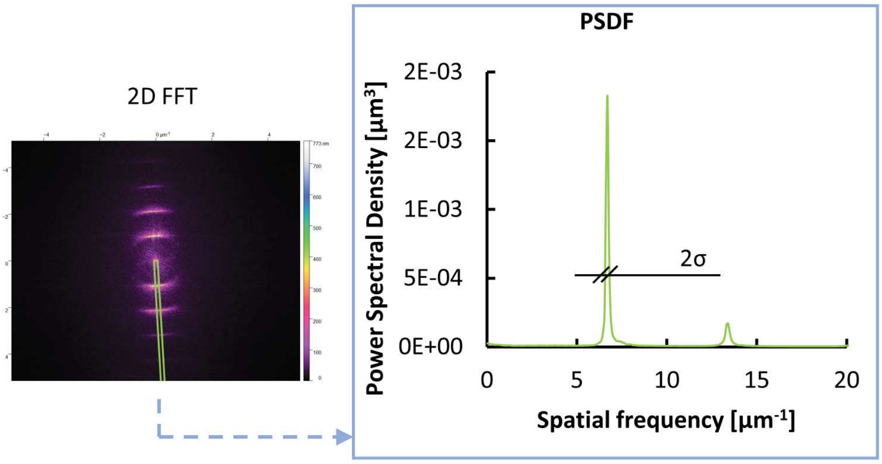

Figure 7.4: Example of a 2D FFT extraction from an SEM micrograph of a laser-induced pattern and Full Width at Half Maximum (FWHM) evaluation by the horizontal profile extracted from the 2D representative 2D FFT micrographs describing the dispersion angle.

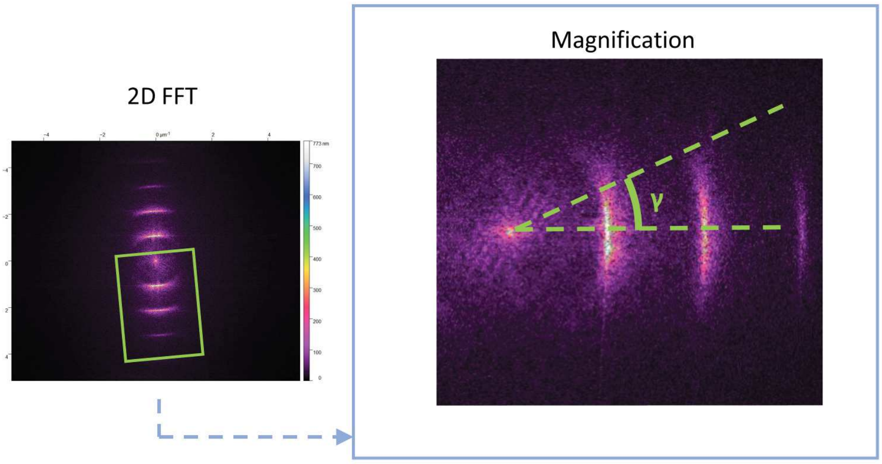

Figure 7.5: Example and magnification of a 2D FFT extracted form a SEM micrograph describing the dispersion angle.

Property	**Insert**	**Part**	**Units**
Tip material	Silicon	Gold	
Tip curvature radius	6	10	nm
Cantilever length	180	125	μm
Cantilever width	18	30	μm
Cantilever thickness	0.6	3	μm
Force constant	0.05	1.45	N/m
Resonant frequency	22	87	kHz

Table 7.2: AFM measuring setup for the texture topography of the mold and of the replicated plastic parts.

by the tip was exploited to reconstruct the surface. The scanning was performed in the high voltage mode, with a resolution lower than 0.15 nm. The line width was 0.078 μm.

The AFM measurements were carried out onto mold inserts and molded parts of the works on replication (cf. subsection 6.2.2). The topography was evaluated in three locations along the symmetry axis of the polymer flow inside the cavity. By defining such locations, it is possible to study the effect of the flow length on the replication effectiveness.

The definition of robust texture parameters is especially critical for femtosecond laser ablation, in which the ablating beam size is significantly larger than the generated LIPSS. The quantitative analysis of the acquired point clouds was carried out from the Abbott-Firestone curves according to standard DS/EN ISO 25178-2 [177]. The material ratio curve describes the increase of the material portion of the surface with increasing roughness depth. For each topography, the core surface roughness Sk was determined from the representation of the curve. The use of Sk allows the description of the surface roughness yielded by the submicron surface texture in the mold. The use of an area parameter that considers material height distribution meets the objective of having a reliable way of characterizing a texture whose dimensions are not directly correlated to tooling size.

The obtained AFM points clouds were all subjected to the same image processing steps. The image processing was carried out using the software *Gwyddion*.

- The tool *scar removal* was exploited to eventually eliminate artifacts of the acquired point clouds.
- The tool *level data* was used to remove sample tilting effects.
- The Abbott-Finestone curve was then obtained from the processed data cloud.

7.4 WETTING CHARACTERIZATION

The wetting properties of the textured plastic surface were evaluated through sessile contact angle measurements and benchmarked against those of a smooth plastic surface. The equipment used for the measurements consisted of (cf. Figure 7.6 (a)):

- Horizontally aligned stage
- Motor-driven micrometer syringe (UMP3) with a needle diameter of 0.21 mm
- Two background illumination sources (LED Pholox)
- Two cameras (MANTA G-146) with a telecentric 2X lens (VS-TC2-110)

The measurements were carried out using water droplets with a total drop volume of 500 nL.

The contact angle was measured along two directions at 90° to account for the effect of ripple directionality on the drop shape (cf. Figure 7.6 (b)). The acquired images were elaborated by fitting the shape of each droplet to calculate the contact angle, as shown in Figure 7.6 (c). a custom LabVIEW program fits the high contrast pictures boundaries on the drop and calculates the angle. The green box marks the area of the picture considered by the LabVIEW algorithm. The wetting characterization was performed on three parts made with each polymer for each combination of processing parameters. On each plastic part, six water droplets were deposited and their contact angles acquired. This allowed for the acquisition of 36 contact angle measurements per experimental condition.

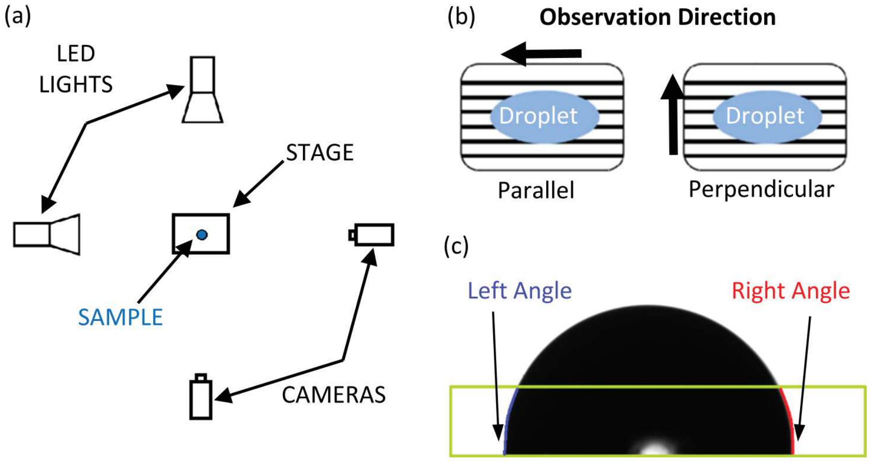

Figure 7.6: (a) double cameras layout for the wetting tests. (b) Droplet behavior over anisotropic surfaces and observation direction nomenclature for the water droplets angles measurement on the textures surface. (c) Estimation of the contact angles through the fitting of the droplet shape. The green square defines the searching area for the software.

Part III

LASER TEXTURING

8 HIERARCHICAL LIPSS

Outstanding wetting properties can be achieved by inducing hierarchical textures over surfaces (cf. subsection 4.5.4). Ultrafast laser texturing can be exploited to achieve such textures over a wide range of materials. Hierarchical textures can be obtained either by a one-step process or a multiple-step approach. In this work, a more precise approach was followed, even if it requires more processing time. The high cost typical of injection molding tools supports this choice. Therefore, the cost related to the longer processing time may not have a great impact. On the other hand, the multi-step process ensures control over both the pattern sizes and higher structure definition and regularity.

Given the three wavelengths available from the picosecond laser sources, the study focuses on the infrared and the green ones. The UV laser beam has not been exploited for the tests because it suffers from some drawbacks.

- The UV is the third harmonics of the laser source and it has the least power, which correlates to a substantially lower material removal rate.

- The wavelength is too short to induce LIPSS on steel. This effect is dependent on the complex phenomena occurring during and just after the pulse stroke over the surface. In brief, the duration of the surface plasmons induced by the laser pulse on the working surface lasts for a certain amount of time, which is dependent on the laser wavelength. The lower the wavelength, the lower the surface plasmons duration. UV light surface plasmons may last less than the duration of the melt induced on the first layer of material. Therefore, the ripples have already faint out and no structure can be achieved onto the surface.

The infrared light was exploited to obtain LIPSS. Being the longer wavelength, it produces the most regular structures. The green light was exploited to achieve both the microstructures and nano LIPSS. The second harmonics was selected for the micro structuring process since it allows for a tighter focusing and more narrow and precise microstructures. Table 8.1 schematizes the way the different laser beams were used.

Wavelength	UV	GR	IR
Microstructuring	No	Yes	No
LIPSS	No	Yes	Yes

Table 8.1: Utilized wavelengths for each fabrication phase.

8.1 EXPERIMENTAL APPROACH

The laser parameters optimization towards hierarchical structuring did consider the properties of the laser source, the characteristics of the optical path, and the possibilities given by the Galvanoscanners. The hierarchical texture process study consists of the following steps.

- First, a characterization of the laser properties was carried out. The laser power was measured for a wide range of power attenuation to characterize the effect of the automatic power selector. The laser pulses of the GR and IR light were separated over the surface to obtain single ablated spot and directly measure the effective laser spot on the steel. The ablated spots were measured using SEM.

- Second, the GR light was exploited to achieve regular and deep trenches. A DoE (Design of Experiments) was designed to study the effect of the laser process parameters and maximize the trench depth and the trench regularity. In parallel, the same laser beam was used to optimize the polishing step, required to remove the burrs left by the previous micro texturing step.

- Third, two DoEs were designed for both the GR and IR light for LIPSS induction. The objective of this study was to maximize the structure regularity and processing speed.

- The last step consists of superimposing the selected processing steps and create the hierarchical structure onto the injection molding inserts.

8.2 LASER BEAM CHARACTERIZATION

The preliminary characterization results described in this section have been attained to gain more meaningful and quantitative design tools for the laser parameters optimization DoEs. Indeed, the laser power and the geometrical properties of the laser spot at focus are two fundamental inputs for the calculation of the laser fluence and the accumulated fluence (cf. subsubsection 4.5.3.1).

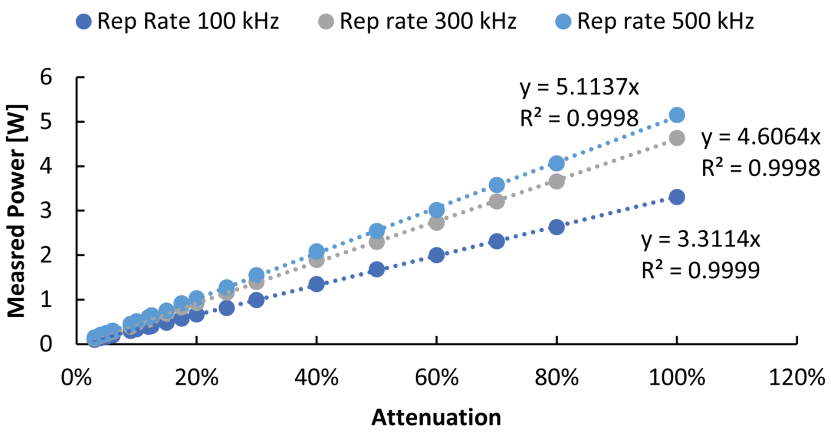

Figure 8.1: First harmonics laser power trend for different attenuations and repetition rates.

8.2.1 Laser power

The laser source controlling system allows for the regulation of the emitted power through the attenuation factor, which is a parameter of the control software. Due to the intrinsic non-linear phenomena occurring during laser stimulation, the attenuation factor may have a non-obvious effect on the emitted laser power. Therefore, a preliminary characterization of the emitted laser power for different laser repetition rates was carried out. The laser power was measured at the end of the optical path, in order to characterize the actual light power that strikes over the working piece. The result of the power characterization (cf. Table 8.2) shows that the emitted laser power is higher for higher repetition rates (i.e. 500 kHz). The response of the laser power of the IR beam against the variation of the attenuation is highly linear (cf. Figure 8.1).

The GR beam shows much less regularity than the first harmonics. The effect is linked to the crystal that splits the wavelength. In Figure 8.2 an example of the trend of the power emitted by the second harmonics is presented.

In order to account for the sensed nonlinearities, the laser power was always characterized before each texturing experiment.

8.2.2 Laser spot diameter

The characterization of the engraving laser spot diameter onto the steel surface was carried out for the first and the second laser harmonics. Before the experimental trials, the sample was accurately placed on the focal plane. The objective of the characterization is to identify the spot area irradiated by the pulse to calculate the actual laser fluence. Moreover, by having the size of the spot diameter at

Selected Attenuation	Rep Rate 100 kHz [W]	Rep Rate 300 kHz [W]	Rep Rate 500 kHz [W]
3%	0.09	0.13	0.15
4%	0.13	0.19	0.21
5%	0.16	0.23	0.25
6%	0.19	0.27	0.30
9%	0.29	0.39	0.46
10%	0.33	0.47	0.52
12%	0.39	0.55	0.61
13%	0.41	0.59	0.65
15%	0.49	0.68	0.75
18%	0.57	0.83	0.92
20%	0.67	0.93	1.03
25%	0.81	1.16	1.28
30%	0.99	1.40	1.55
40%	1.35	1.90	2.09
50%	1.68	2.30	2.54
60%	2.00	2.73	3.01
70%	2.32	3.21	3.58
80%	2.63	3.66	4.06
100%	3.31	4.64	5.15

Table 8.2: Laser powers for the IR laser beam at three different laser repetition rates.

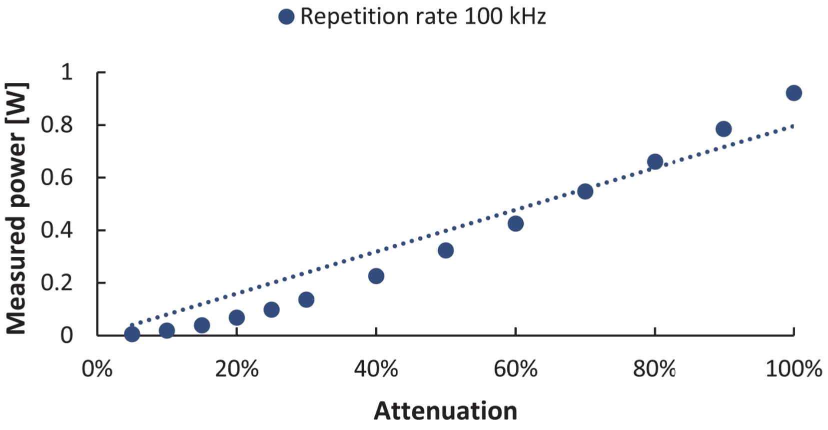

Figure 8.2: Second harmonics laser power trend at 100 kHz.

focus, it is possible to have a quantitative design tool to determine the scanning parameters (i.e. the lateral step size and the pulse step).

The single spots were separated by using high pulse step and lateral step sizes. A lateral step and a pulse step of 30 μm was used. A scanning speed of 1.5 m/s and a repetition rate of 50 kHz was selected to achieve the desired pulse step. For each wavelength, 12 energy levels were selected. The SEM micrographs in Figure 8.3 show how the engraved spot area increases for increasing laser powers. The effect is linked to the quasi-gaussian irradiance (i.e. specific amount of power) distribution of the laser pulse. By measuring the spot diameters at various laser powers, it is possible to estimate the laser spot diameter. The results of the spot diameter measurements are reported in Table 8.4 for the first harmonic and Table 8.3 for the second harmonic.

8.2.2.1 Calculation of the spot radius

Gaussian distribution was assumed for the laser irradiance. The laser spot diameter was found to fit the fluence distribution and the measured engraved diameters. When the laser pulse hits the surface, it only engraves the areas that have a fluence higher than the threshold one. Therefore, the fluence at the engraved diameter is the threshold one. Since the experiments were performed at the same height (i.e. with the sample on the focal plane), the spot diameter is always the same. During the experiments, only the pulse energy was changed. Thus, the Gaussian distributions for increasing pulse energies show larger integrals and a higher peak (cf. Figure 8.4).

The Gaussian distribution of fluences is:

$$F(x) = F_0 \cdot e^{-\frac{2 \cdot x^2}{w_0^2}} \tag{8.1}$$

$$F_0 = \frac{2 \cdot PE}{\pi \cdot w_0^2} \tag{8.2}$$

Where $F(x)$ is the fluence level at a certain distance from the laser beam axis (x), F_0 is the peak fluence, PE is the pulse energy and w_0 is the spot radius at 1/e intensity. The Gaussian distribution of fluences encounters the threshold fluence (that is unique) at an increasing distance from the beam center for increasing pulse energies. The property was exploited to calculate the beam radius (w_0).

A spot radius of 6 and 4.5 μm was found for the IR and GR laser beams, respectively.

8.2.3 Calculation of the accumulated fluence

In the introduction, a simple formula for the calculation of the laser accumulated fluence was introduced (cf. subsubsection 4.5.3.1). The

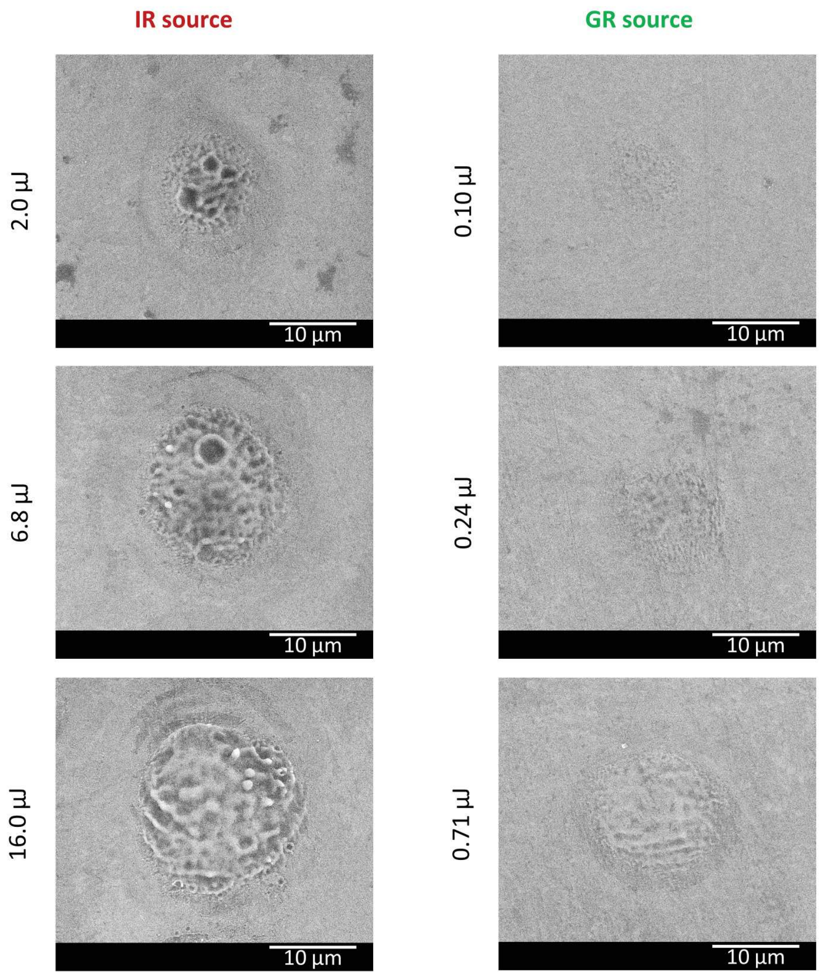

Figure 8.3: SEM micrographs of the single spots engraved by the IR and GR laser beams. The pulse energy is reported on the left of each picture.

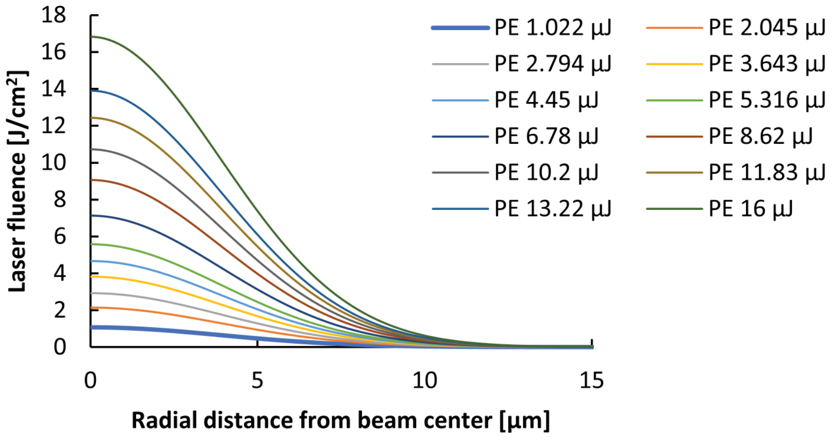

Figure 8.4: Gaussina distribution of the laser fluence for increasing pulse energies.

Attenuation	Power *mW*	Pulse energy *μJ*	Engraved Diameter *μm*
5%	1.3	0.004	-
10%	4.9	0.016	-
15%	9.0	0.030	-
20%	14.9	0.050	4.5
25%	21.6	0.072	6
30%	30.0	0.100	6.7
40%	46.7	0.156	8.2
50%	71.8	0.239	9
60%	96.7	0.322	9.5
70%	125.3	0.418	10
80%	152.7	0.509	11
100%	212.3	0.708	11.5

Table 8.3: Energy levels and spot diameter measurement results for the single spot irradiation using the GR beam.

Attenuation	Power *mW*	Pulse energy *μJ*	Engraved Diameter *μm*
5%	102	1.0	9.5
10%	205	2.0	11
15%	279	2.8	12
20%	364	3.6	13
25%	445	4.5	14
30%	532	5.3	15
40%	678	6.8	16.5
50%	862	8.6	17.5
60%	1020	10.2	18
70%	1183	11.8	18
80%	1322	13.2	18.5
100%	1600	16.0	20

Table 8.4: Energy levels and spot diameter measurement results for the single spot irradiation using the IR beam.

relation has the advantage of being simple, but it neglects the effect of the gaussian distribution of the laser energy. Coming back to the concept of accumulated fluence, it accounts for the whole amount of laser energy that hits a certain area. Therefore, it actually accounts for the sum of the Gaussian distributed fluences along and perpendicularly to the scanning direction. The model for the calculation of the accumulated fluence distribution first calculates the fluence accumulation along the scanning direction, then it considers the perpendicular direction (along with the hatch).

In Figure 8.5, the calculated distribution of the accumulated fluence is compared to the relative patterns. The laser and scanning process parameters relative to the three presented configurations are presented in Table 8.5. The gray and black gaussian curves represent the accumulated fluence along the scan direction, the orange ones represent the total distribution of the accumulated fluence. In the figure, the first accumulation phenomena are omitted, since the plot is similar to those presenting the total accumulated fluence distribution. However, it has to be noted that the peak fluences of the gray and black curves are higher than the peak fluence of the laser pulse. This is the result of the first accumulation along the scan direction.

Comparing the SEM micrographs and the corresponding accumulated fluence plot it is possible to capture the effect of the specific energy onto the LIPSS formation (cf. Figure 8.5).

- Constant accumulated fluence is necessary for homogeneous LIPSS creation on the irradiated surface. The SEM micrograph reported in Setup 2 highlights a pattern showing a horizontal and vertical pitch of 10 μm. The pattern is linked to the fluctuation of the accumulated fluence, which is calculated on the corresponding plot.

- Single-pulse irradiation does not show any linear structure (i.e. ripple), even if at the center of the spot a decent fluence has been obtained. A central role in the formation of regular ripples may be played by the pulse superimposition. Indeed, single pulse irradiation does not show ripples, while Setup 2 shows ripples only in a certain area, which may be interpreted as the areas where pulse superimposition occurs. Setup 1 confirms this hypothesis, showing a regular ripples pattern as a consequence of omnipresent pulse overlapping.

Similar conclusions can be drawn using the GR laser source (cf. Figure 8.6 and Table 8.5). It is interesting to see the effect of the smaller spot diameter on the pulse step dimension that brings to an even accumulated fluence distribution. At 5 x 5 μm irradiation, the IR pattern has already achieved homogeneous structures, whilst the GR one still shows important discontinuities. Indeed, for this setup,

Property	Setup 1	Setup 2	Setup 3	Unit
Wavelength		1064		nm
Spot diameter		12		μm
Power	0.194	0.485	0.491	W
Peak fluence	1.93	4.82	4.88	J/cm^2
Pulse step	5	10	30	μm
Hatch distance	5	10	30	μm
Accumulated fluence scan direction MAX	2.91	4.86	4.88	J/cm^2
Accumulated fluence MAX	4.37	4.89	4.88	J/cm^2
Accumulated fluence MIN	4.37	2.42	0	J/cm^2

Table 8.5: Selected laser and scanning process parameters for the three configurations of Figure 8.5.

Property	Setup 1	Setup 2	Setup 3	Unit
Wavelength		532		nm
Spot diameter		9		μm
Power	57.2	226	323	mW
Peak fluence	0.60	3.60	5.20	J/cm^2
Pulse step	2	5	30	μm
Hatch distance	2	5	30	μm
Accumulated fluence scan direction MAX	1.69	4.21	5.20	J/cm^2
Accumulated fluence MAX	4.77	4.92	5.20	J/cm^2
Accumulated fluence MIN	4.77	4.57	0	J/cm^2

Table 8.6: Selected laser and scanning process parameters for the three configurations of Figure 8.6.

both the IR and GR irradiations induce regular structures when the accumulated fluence reaches a stable value around 5 J/cm^2.

The model for the prediction of the accumulated fluence has shown the capabilities of predicting the final texture outcome. Therefore, the model has been exploited to determine the energetical and scanning levels for the following DoEs.

8.3 MICROSTRUCTURING OPTIMIZATION

GR light was exploited to achieve a linear parallel pattern of trenches. A DoE was designed to study the effect of the laser process parameters and maximize the trench depth and the trench regularity. The material removal rate is dependent on the amount of energy delivered onto the surface. A 3 factors 3x3x4 levels full factorial DoE was set (cf.

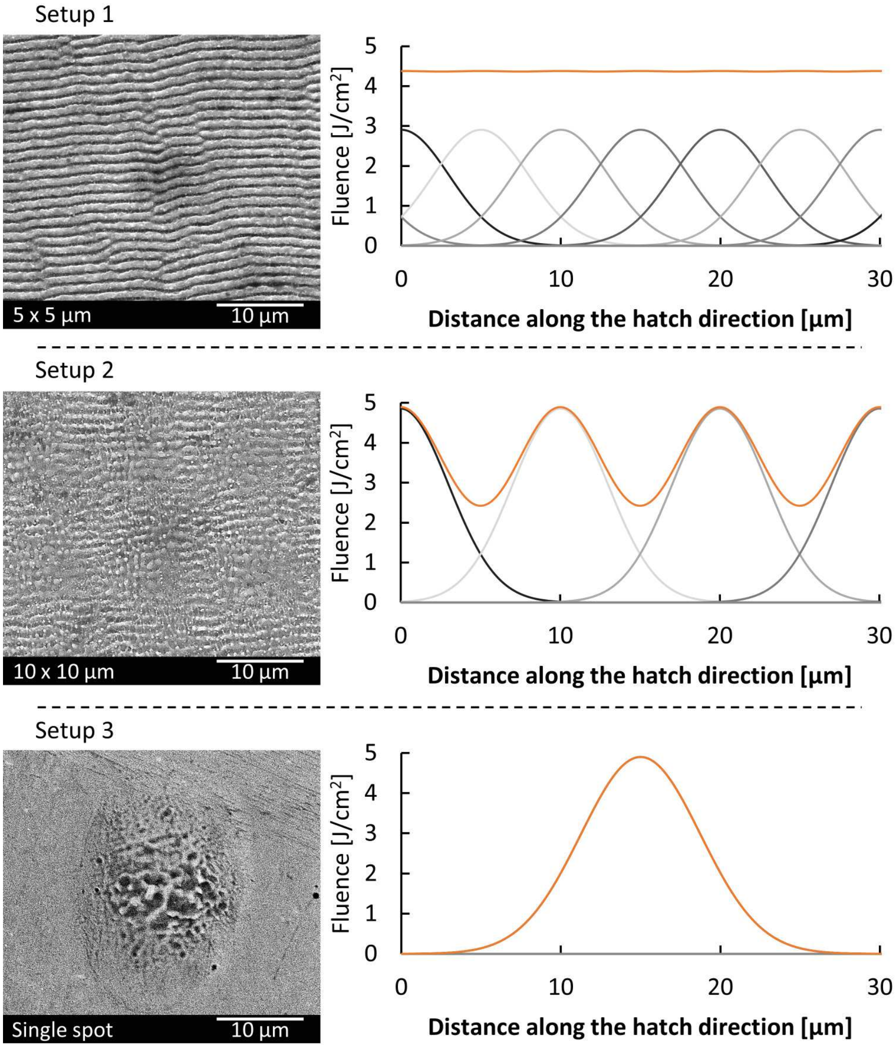

Figure 8.5: Effect of the scanning parameters on the achieved surface structures and modeling of the accumulated fluence. The three irradiations were performed with the IR beam. The three setups share a similar level of maximum accumulated fluence. The black curves represent the fluence accumulated along the scanning direction, the orange curve represents the total accumulated fluence.

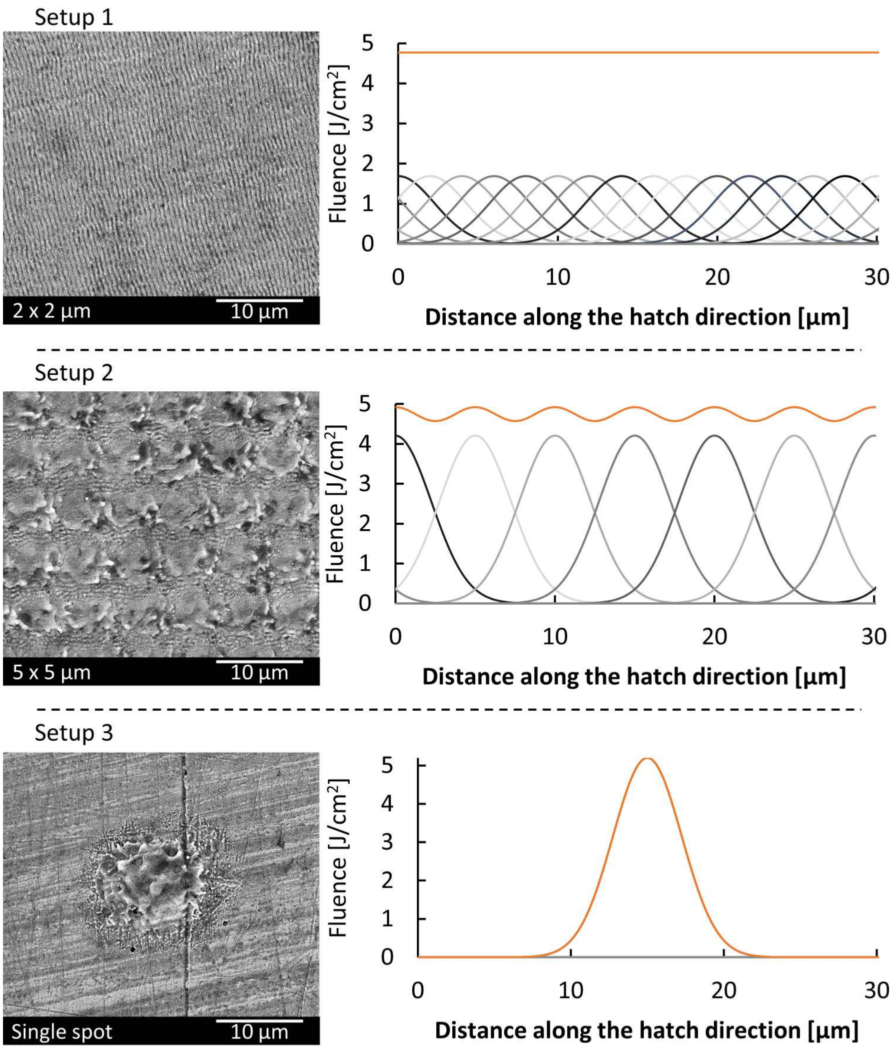

Figure 8.6: Effect of the scanning parameters on the achieved surface structures and modeling of the accumulated fluence. The three irradiations were performed with the GR beam. The three setups share a similar level of maximum accumulated fluence. The black curves represent the fluence accumulated along the scanning direction, the orange curve represents the total accumulated fluence.

Factors	Level 1	Level 2	Level 3	Level 4	Unit
Repetition rate	100	200	250		*kHz*
Scan N	30	60	90		
Scan velocity	500	1500	2500	3500	*mm/s*

Table 8.7: DoE table for the experimental campaign for the optimization of the microstructures.

Table 8.7). The pulse repetition rate, scan number, and scan velocity were varied through the experiments. Therefore, the pulse step size and the laser power varied through the experiments (cf. Table 8.8).

8.3.1 Accumulated energy

Different from the patterning operations, the microstructure that is the object of the study does not require overlapping in two directions. Thus, the accumulated fluence parameter, which shows a close correlation to the achieved patterns, is less suited to describe this process. Instead, the calculation of the accumulated energy (E) is proposed.

$$E = PE \cdot N \cdot \frac{\pi w_0}{PS} \tag{8.3}$$

Where PE is the pulse energy, N is the scan number (i.e. number of times the laser scans the same trench), w_0 is the laser spot radius, and PS is the pulse step.

8.3.2 Microstructures optimization

The analysis of the obtained microstructures was carried out by SEM and confocal profilometry. Interestingly, some runs show an array of deep holes on the bottom of the ablated trenches. The obtained textures were divided into three different classes of microstructures (cf. Figure 8.8).

- Textures that do not show the presence of the holes (1).
- Textures that show the holes on the bottom of the trench (3).
- Transition textures, which show only some sited where the holes are forming (2).

The formation mechanism of the holes is not completely clear. The induction of the holes is random, as can be seen by the overview micrograph of the class 2 microstructure (cf. Figure 8.8). The phenomenon seems to be independent of the pulse step, thus the holes cannot be regarded as the marks left by the laser pulses. Indeed, the

Rep. Rate	Scan N	Scan Speed	Pulse step	Laser Power	Fluence	Pulse Energy	Acc. Energy	Micro structure
kHz		mm/s	μm	W	J/cm^2	μJ	μJ	
100	30	500	5	1.37	21.5	13.7	581	1
100	30	1500	15	1.37	21.5	13.7	194	3
100	30	2500	25	1.37	21.5	13.7	116	3
100	30	3500	35	1.28	20.1	12.8	78	3
100	60	500	5	1.37	21.5	13.7	1162	1
100	60	1500	15	1.37	21.5	13.7	387	3
100	60	2500	25	1.37	21.5	13.7	232	3
100	60	3500	35	1.28	20.1	12.8	155	3
100	90	500	5	1.37	21.5	13.7	1743	1
100	90	1500	15	1.37	21.5	13.7	581	1
100	90	2500	25	1.37	21.5	13.7	349	2
100	90	3500	35	1.28	20.1	12.8	233	3
200	30	500	2.5	1.34	10.5	6.7	568	2
200	30	1500	7.5	1.34	10.5	6.7	189	3
200	30	2500	12.5	1.34	10.5	6.7	114	3
200	30	3500	17.5	1.28	10.1	6.4	78	3
200	60	500	2.5	1.34	10.5	6.7	1137	1
200	60	1500	7.5	1.34	10.5	6.7	379	3
200	60	2500	12.5	1.34	10.5	6.7	227	3
200	60	3500	17.5	1.28	10.1	6.4	155	3
200	90	500	2.5	1.34	10.5	6.7	1705	1
200	90	1500	7.5	1.34	10.5	6.7	568	2

Table 8.8: Laser and scanning parameters for the microstructuring DoE.

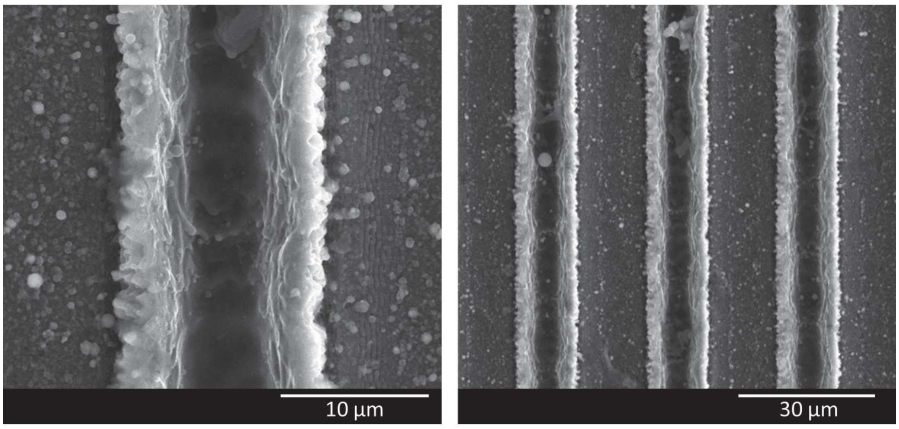

Figure 8.7: SEM micrographs of the selected microstructure.

Rep. Rate	Scan N	Scan Speed	Pulse step	Laser Power	Fluence	Pulse Energy	Acc. Energy
kHz		*mm/s*	*µm*	*W*	J/cm^2	*µJ*	*µJ*
100	60	1500	15	1.37	21.5	13.7	387

Table 8.9: Laser and scanning parameters for selected microstructure.

spacing between the holes is just below 10 microns, regardless of the pulse step of the scanning operation.

Instead, a close correlation with the accumulated energy can be found. The boxplot showed in Figure 8.9 readily demonstrates the effect of the accumulated energy onto the formation of the holes. The purpose of this work is to achieve a regular trench geometry. Therefore, the presence of holes needs to be avoided.

The selected microstructure is reported in Figure 8.7. The laser patterning was characterized by accumulated energy of 387 μJ. The complete set of process parameters is reported in Table 8.9. The selected microstructure presents a medium depth of about 8 μm Figure 8.10. The walls of the trenches have inclinations ranging between 20 and 25 degrees with respect to the normal at the surface. This effect is linked to partial light reflection at the trench walls.

8.4 POLISHING OPTIMIZATION

The polishing operations were carried out using the GR light. The DoE for the polishing operations was designed to reduce the steel deposits over the surface. A 3 factors 3x3x4 levels full factorial DoE was set (cf. Table 8.11). The laser fluence, scan number, and scan

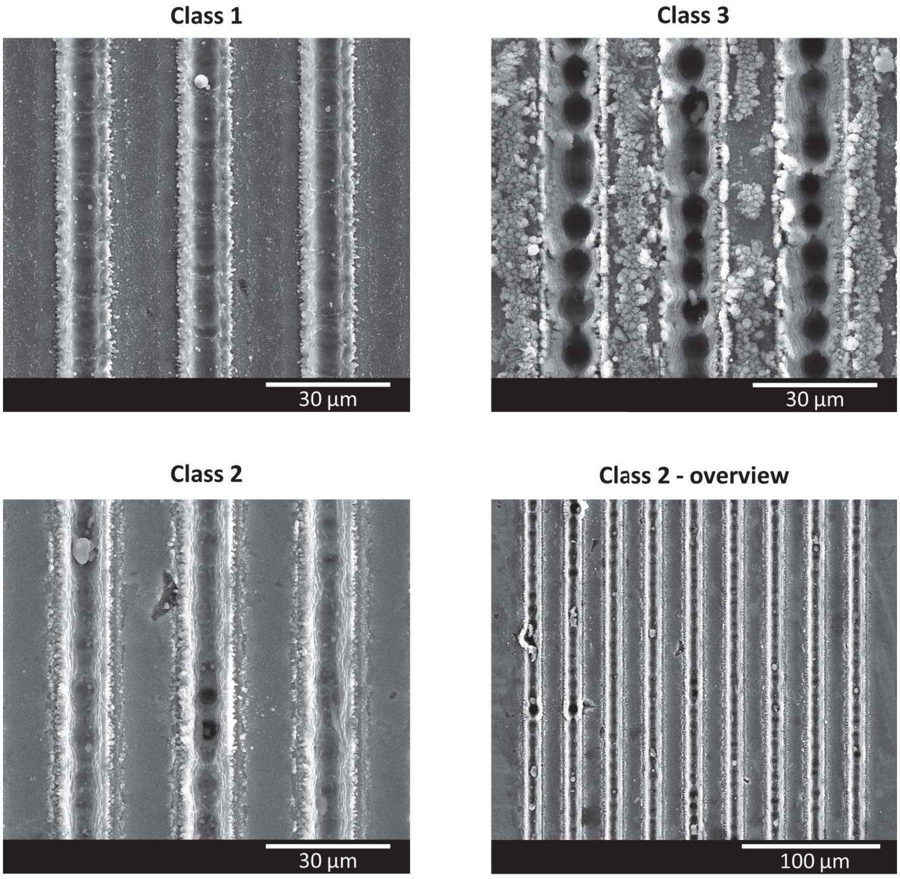

Figure 8.8: SEM micrographs of the three classes of microstructures achieved during the experiments. An overview of the transition textures is reported to further display the random induction of the holes phenomenon.

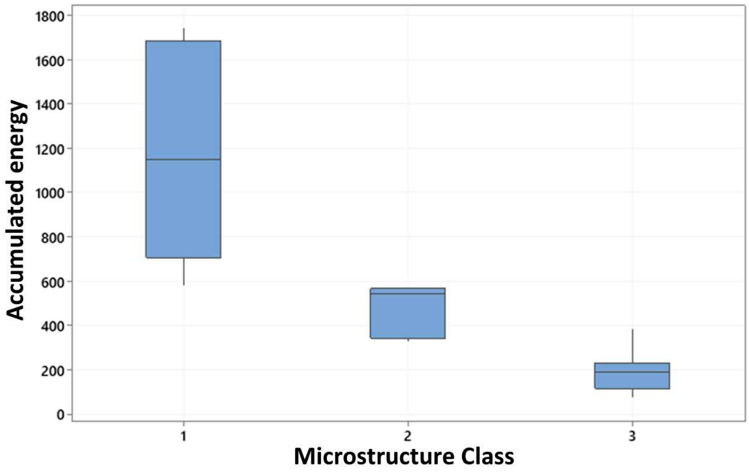

Figure 8.9: Boxplot showing the effect of the accumulated energy onto the holes phenomenon induction.

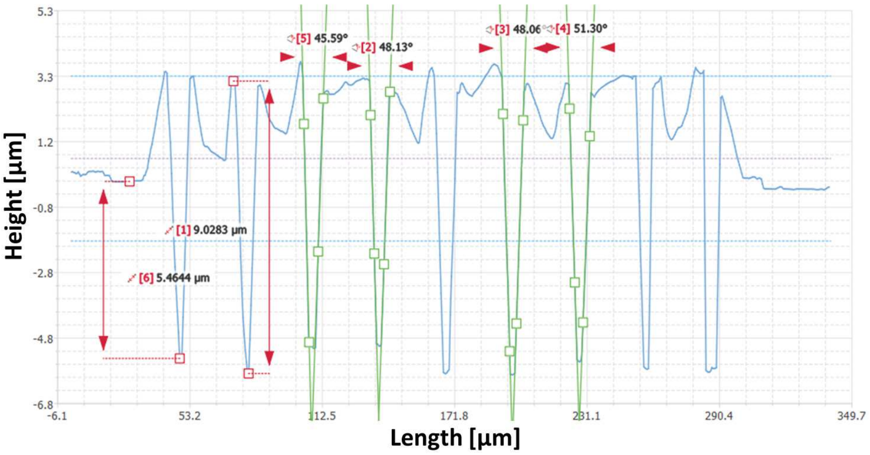

Figure 8.10: Profile of the laser-machined trenches for the selected process parameters. Depth and wall inclination measurements are reported in the profile.

velocity were varied through the experiments. Therefore, the pulse step size and the laser power varied, but a high pulse repetition rate (1 MHz) was kept constant (cf. Table 8.12). The high pulse repetition rate allows for the fast deposition of low-energy pulses, with the aim of interacting with just the first layer of material.

The steel surface for the polishing operations was previously micro-structured using a process parameters set (cf. Table 8.10) that leads to a significant amount of burrs and recasts over the non-etched surface. The different runs of the DoE were carried out on 1 x 1 mm squares over the micro-structured surface.

Figure 8.11 gives an overview of the polishing result obtained through the DoE. The top left side picture shows the status of the surface prior to the polishing operations. On the top right and bottom right side of the figure, there are two examples of a too soft and a too deep process respectively. A soft process just modifies the deposits' surface, inducing various nanostructures (cf. Figure 8.12 (a)), but it is not able to smoothen out the surface. Contrarily, a too-deep polishing process ablates a relatively thick layer of steel, reducing the height of the previously machined trenches. (cf. Figure 8.12 (b)) shows the boundary of the 1 x 1 square polished using the deep polishing process. The SEM micrograph cannot give a quantitative assessment of the ablated depth, but the difference in the shape of the holes suggests that the ablated material layer is consistent. The chosen process parameters for the polishing operations outcome are reported as the bottom left SEM micrograph in Figure 8.11. A decent amount of deposit smoothening has been achieved and the trench dept seems to be essentially conserved.

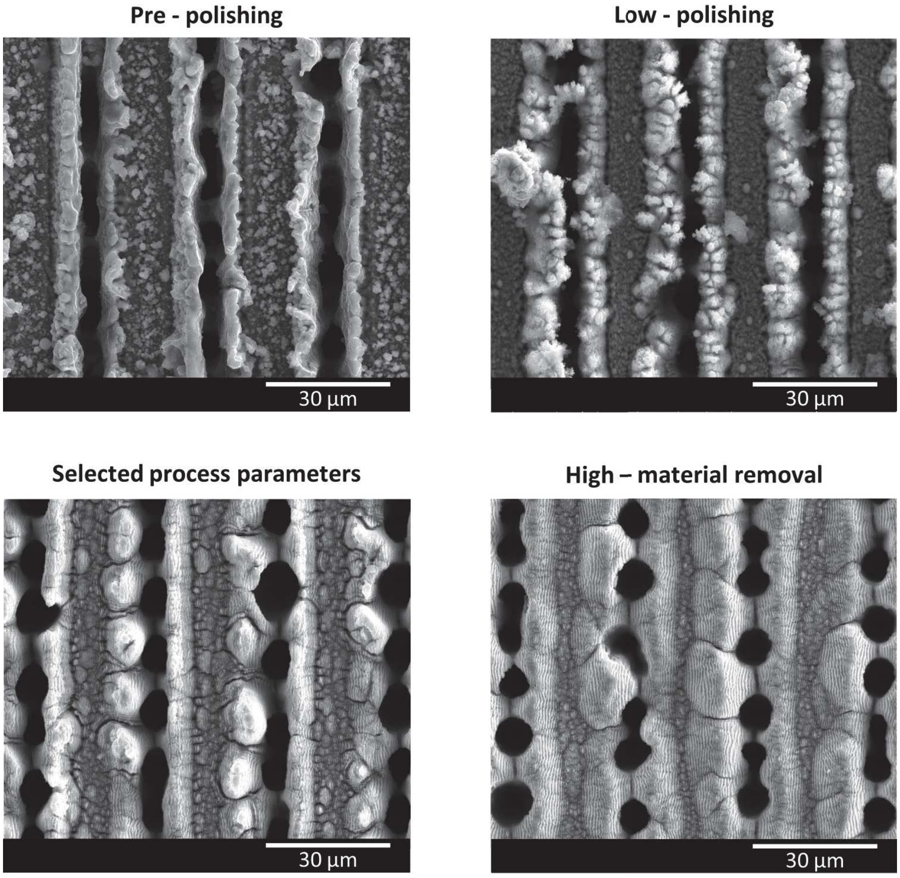

Figure 8.11: SEM micrographs for the polishing process. On the top left, the pre-polishing surface is shown. On the top and bottom right, two examples of respectively a too soft and a too deep process are shown. The bottom left SEM micrograph reports the result of the chosen process parameters.

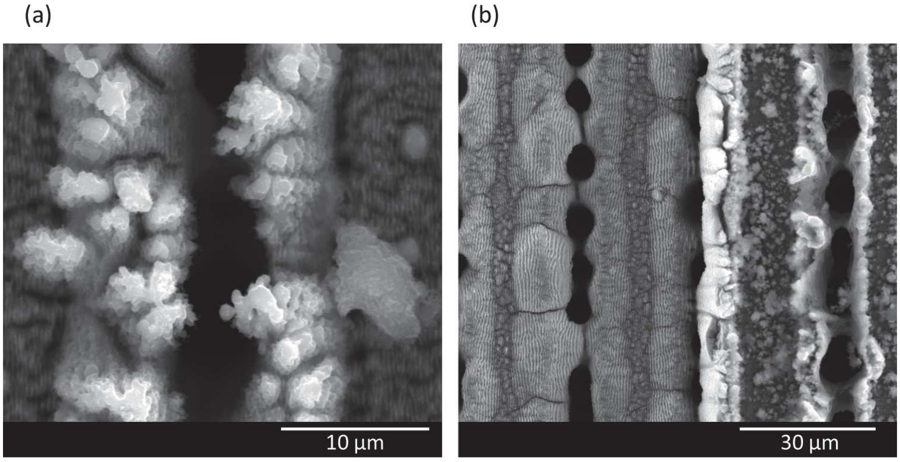

Figure 8.12: SEM micrographs of the nanostructures obtained through soft polishing (a) and through deep polishing (b).

Rep. Rate *kHz*	**Scan N**	**Scan Speed** *mm/s*	**Pulse step** *μm*	**Laser Power** *W*	**Fluence** J/cm^2	**Pulse Energy** *μJ*	**Acc. Energy** *μJ*
100	90	500	5	1.37	21.5	13.7	1743

Table 8.10: Laser and scanning parameters for selected microstructure.

Factors	Level 1	Level 2	Level 3	Level 4	Unit
Scan N	1	5	20		
Fluence	0.1	0.2	0.3	0.4	*μJ*
Scan Speed	1000	2000	3000		*mm/s*

Table 8.11: DoE table for the experimental campaign for the optimization of the polishing operations.

8.5 NANOSTRUCTURING OPTIMIZATION

According to the first laser beam and accumulated fluence effects characterization (cf. section 8.2), two distinct DoEs were set for the IR and GR irradiation. The objective of this work is the optimization of the LIPSS pattern geometry, regularity, and homogeneity. The laser and scanning process parameters were varied through the experiments.

8.5.1 GR nanostructuring DoE

The DoE for GR LIPSS optimization was designed as a 3 factors 2x4x3 levels full factorial DoE (cf. Table 8.14). The laser repetition rate, fluence, and pulse step were varied through the experiments. Therefore, the scanning speed size and the laser power varied (cf. Table 8.15). The scanning operations were always kept *squared*, which refers to the selection of an equal lateral step and pulse step to obtain an even distribution of the accumulated fluence through the surface.

The comparison of the surface structures obtained at different laser repetition rates does not show fundamental differences. Therefore, the processing at 300 kHz was preferred since it achieves higher patterning speeds. The reciprocal effect of fluence and pulse and lateral steps are linked to the accumulated fluence reflects here on the ripple shape homogeneity and regularity. The parameters which bring to the best LIPSS pattern are summarized in Table 8.16.

Rep. Rate *MHz*	**Scan N**	**Scan Speed** *mm/s*	**Pulse step** *μm*	**Laser Power** *W*	**Fluence** J/cm^2	**Pulse Energy** *μJ*
1	1	1000	1	0.064	0.1	0.064
1	1	2000	2	0.064	0.1	0.064
1	1	3000	3	0.064	0.1	0.064
1	1	1000	1	0.127	0.2	0.127
1	1	2000	2	0.127	0.2	0.127
1	1	3000	3	0.127	0.2	0.127
1	1	1000	1	0.191	0.3	0.191
1	1	2000	2	0.191	0.3	0.191
1	1	3000	3	0.191	0.3	0.191
1	1	1000	1	0.254	0.4	0.254
1	1	2000	2	0.254	0.4	0.254
1	1	3000	3	0.254	0.4	0.254
1	5	1000	1	0.064	0.1	0.064
1	5	2000	2	0.064	0.1	0.064
1	5	3000	3	0.064	0.1	0.064
1	5	1000	1	0.127	0.2	0.127
1	5	2000	2	0.127	0.2	0.127
1	5	3000	3	0.127	0.2	0.127
1	5	1000	1	0.191	0.3	0.191
1	5	2000	2	0.191	0.3	0.191
1	5	3000	3	0.191	0.3	0.191
1	5	1000	1	0.254	0.4	0.254
1	5	2000	2	0.254	0.4	0.254
1	5	3000	3	0.254	0.4	0.254
1	20	1000	1	0.064	0.1	0.064
1	20	2000	2	0.064	0.1	0.064
1	20	3000	3	0.064	0.1	0.064
1	20	1000	1	0.127	0.2	0.127
1	20	2000	2	0.127	0.2	0.127
1	20	3000	3	0.127	0.2	0.127
1	20	1000	1	0.191	0.3	0.191
1	20	2000	2	0.191	0.3	0.191
1	20	3000	3	0.191	0.3	0.191
1	20	1000	1	0.254	0.4	0.254
1	20	2000	2	0.254	0.4	0.254
1	20	3000	3	0.254	0.4	0.254

Table 8.12: Laser and scanning parameters for the polishing DoE.

8.5.1.1 SEM characterization

Figure 8.13 reports the SEM micrographs of the best LIPSS pattern obtained with the IR laser beam (at the center of the figure) and two non-optimal patterns obtained at lower (top of the figure) and higher (bottom of the figure) energy levels. Next to each SEM micrograph, a magnification is proposed to further detail the structure's shape. As a result of the first study on the accumulated fluence distribution, the totality of the achieved patterns show a flat accumulated energy deposition and thus the LIPSS do not show any defect derived from accumulated energy instabilities. However, low-energy levels show faint structures that eventually disappear and divide (cf. Figure 8.13 (a)). On the other hand, high-energy irradiation shows ripples deformations and breakage (cf. Figure 8.13 (c)). The selected pattern has long, straight, and uninterrupted ripples (cf. Figure 8.13 (b)). On all the showed textures, the long vertical ripples are covered by small horizontal features. Such LIPSS are called high spatial frequency LIPSS (HSFL), in contrast to the vertical low spatial frequency LIPSS (LSFL). The presence of HSFL is particularly evident on the magnifications but is not the object of this study.

8.5.1.2 2D FFT elaboration

To quantitively evaluate the achieved patterns the 2D Fast Fourier Transform of the SEM micrograph was carried out and the peaks of the spectrum were studied (cf. section 7.2). The 2D FFT images and spectra are reported in Figure 8.14. The ripple deformation and breakage translate in Figure 8.14 (c) in a horizontal and vertical widening of the peaks, respectively. Figure 8.14 (a) presents peaks that are only stretched vertically, due to the presence of several features along the faint ripples. Figure 8.14 (b) is relative to the best pattern and presents sharply defined peaks. Table 8.14 reports the calculated values of the measured periodicities (i.e. the structure pitch), the homogeneities, and the regularities. According to what can be seen by the SEM micrographs and the 2D FFT characterization, the quantitative evaluation confirms that the selected pattern is the most regular. The measured peak, according to the literature on LIPSS, is slightly smaller than the laser wavelength.

8.5.2 GR nanostructuring DoE

Similar to the optimization using the largest wavelength, the DoE for GR LIPSS optimization was designed as 3 factors 2x4x3 levels full factorial (cf. Table 8.18). The laser repetition rate, fluence, and pulse step were varied through the experiments (cf. Table 8.19). The scanning operations were kept *squared* also for the GR trials.

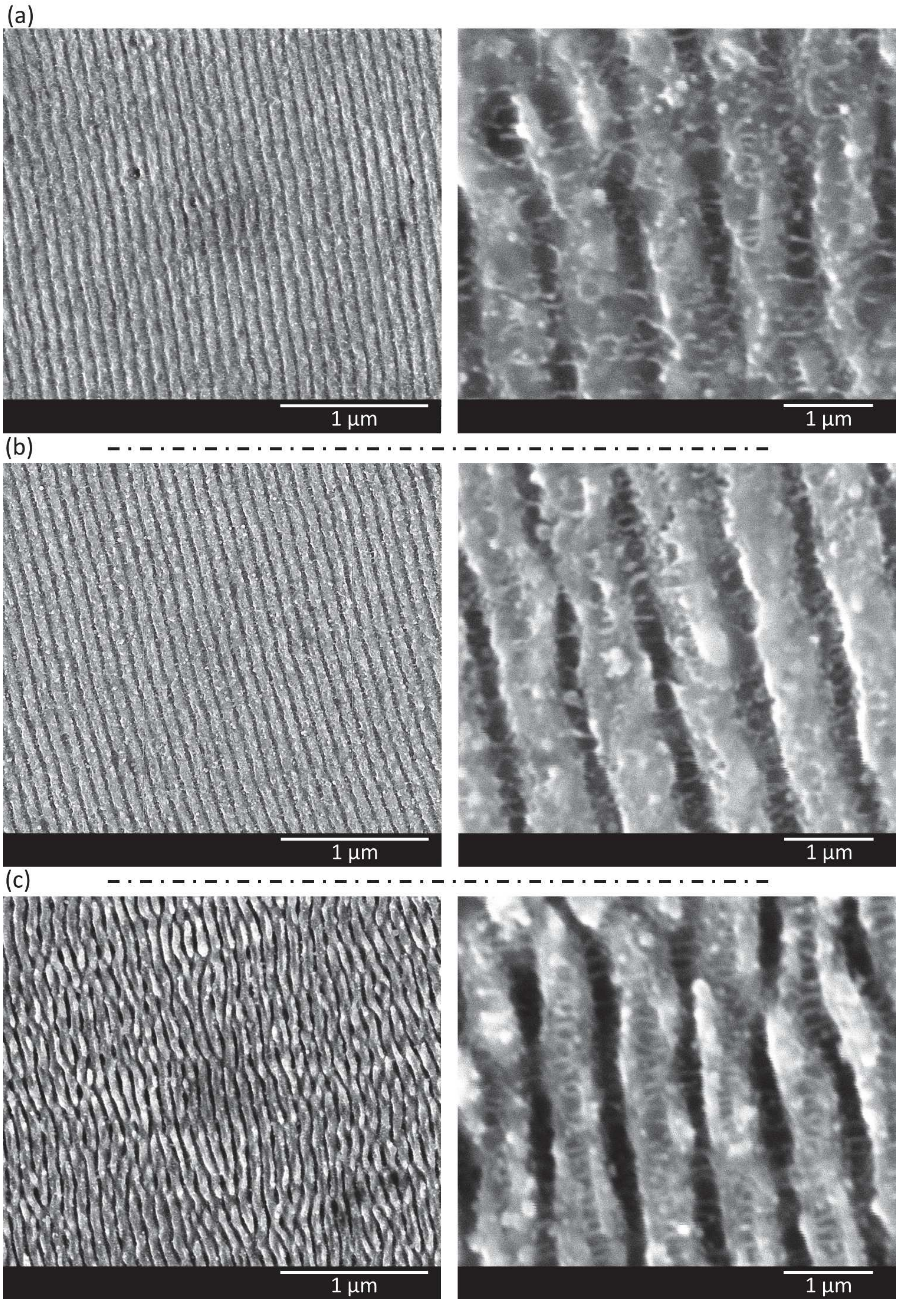

Figure 8.13: SEM micrographs IR beam induced LIPSS patterns. At the figure center (b) the selected texture is showed. Above and below the selected pattern, an example of a low-energy texture (a) and a high-energy texture (c) is proposed. Each SEM micrograph is accompanied by a magnification to better assess the structure shape.

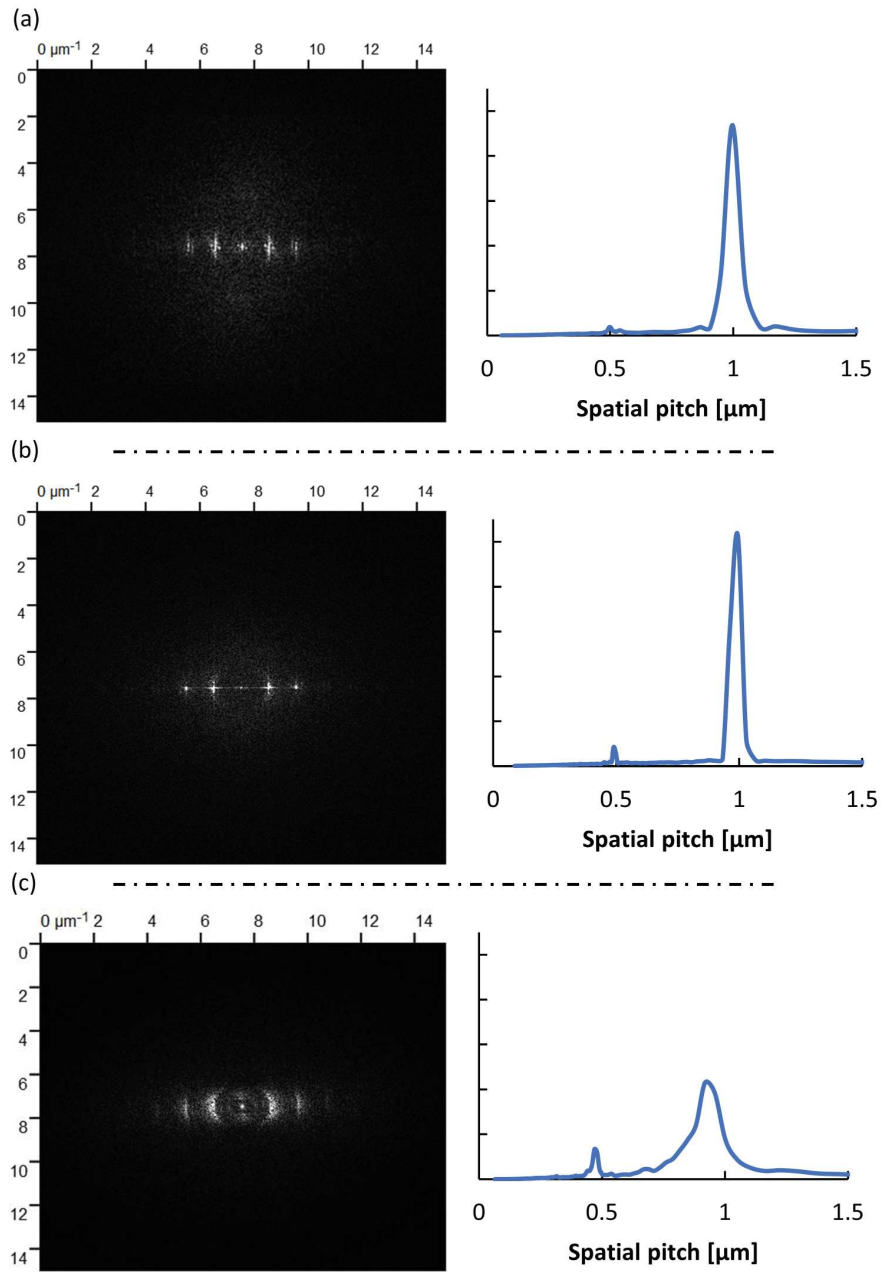

Figure 8.14: 2D Fast Fourier Transform and spectrum of the chosen SEM micrographs (cf. Figure 8.13). At the figure center (b) the elaboration of the selected texture SEM image is showed. Above and below the selected pattern elaboration, the 2D FFT and the spectrum of a low-energy texture (a) and a high-energy texture (c) are proposed.

Pattern	Parameter	Value	Error	Unit
Low	Pitch	1000	35	nm
	R	7%		
	γ	16	1	deg
Optimum	Pitch	1000	25	nm
	R	5%		
	γ	10	1	deg
High	Pitch	950	80	nm
	R	17%		
	γ	25	1.5	deg

Table 8.13: Pitch, regularity, and homogeneity results for the three patterns presented in Figure 8.13.

Factors	Level 1	Level 2	Level 3	Level 4	Unit
Repetition rate	100	300			kHz
Fluence	0.5	1	1.5	2	μJ
Pulse step	4	5	6		μm

Table 8.14: DoE table for the experimental campaign for the nanostructuring operations with the IR laser beam.

Rep. Rate *kHz*	**Pulse step** μm	**Scan Speed** mm/s	**Lateral Step** μm	**Laser Power** W	**Fluence** J/cm^2	**Pulse Energy** μJ
100	4	400	4	0.057	0.5	0.57
100	5	500	5	0.057	0.5	0.57
100	6	600	6	0.057	0.5	0.57
100	4	400	4	0.113	1	1.13
100	5	500	5	0.113	1	1.13
100	6	600	6	0.113	1	1.13
100	4	400	4	0.170	1.5	1.70
100	5	500	5	0.170	1.5	1.70
100	6	600	6	0.170	1.5	1.70
100	4	400	4	0.226	2	2.26
100	5	500	5	0.226	2	2.26
100	6	600	6	0.226	2	2.26
300	4	1200	4	0.170	0.5	0.57
300	5	1500	5	0.170	0.5	0.57
300	6	1800	6	0.170	0.5	0.57
300	4	1200	4	0.339	1	1.13
300	5	1500	5	0.339	1	1.13
300	6	1800	6	0.339	1	1.13
300	4	1200	4	0.509	1.5	1.70
300	5	1500	5	0.509	1.5	1.70
300	6	1800	6	0.509	1.5	1.70
300	4	1200	4	0.679	2	2.26
300	5	1500	5	0.679	2	2.26
300	6	1800	6	0.679	2	2.26

Table 8.15: Laser and scanning parameters for the IR beam nanostructuring DoE.

Rep. Rate *kHz*	**Pulse step** μm	**Scan Speed** mm/s	**Lateral Step** μm	**Laser Power** W	**Fluence** J/cm^2	**Pulse Energy** μJ
300	4	1200	4	0.339	1	1.13

Table 8.16: Selected laser and scanning parameters for the IR nanostructuring.

The comparison of the surface structures obtained at different laser repetition rates does not show fundamental differences. Therefore, the processing at 300 kHz was preferred since it achieves higher patterning speeds. The reciprocal effect of fluence and pulse and lateral steps are linked to the accumulated fluence reflects here on the ripple shape homogeneity and regularity. The parameters which bring to the best LIPSS pattern are summarized in Table 8.20. Different from what was experienced with the IR beam, the processing window (i.e. the extent of laser process parameters that brings to regular LIPSS) is substantially smaller.

8.5.2.1 SEM characterization

Figure 8.15 reports the SEM micrographs of the best LIPSS pattern obtained with the GR laser beam (at the center of the figure) and two non-optimal patterns obtained at lower (top of the figure) and higher (bottom of the figure) energy levels. Next to each SEM micrograph, a magnification is proposed to further detail the structure's shape. As a result of the first study on the accumulated fluence distribution, the totality of the achieved patterns show a flat accumulated energy deposition and thus the LIPSS do not show any defect derived from accumulated energy instabilities. However, low-energy levels show nanobubble covered faint structures (cf. Figure 8.15 (a)). Similar of the IR irradiation, high-energy irradiation correlates with ripples deformations and breakage (cf. Figure 8.15 (c)). The selected pattern has long, straight, and uninterrupted ripples (cf. Figure 8.15 (b)). Different from what arose from the irradiation with the larger wavelength, the textures do not present HSFL.

8.5.2.2 2D FFT elaboration

The 2D Fast Fourier Transform of the SEM micrograph was carried out to quantitively evaluate the achieved patterns and the peaks of the spectrum were studied (cf. section 7.2). The 2D FFT images and spectra are reported in Figure 8.16. The phenomenologies are analogous to the ones described earlier for the IR irradiation. Nanobubble presence translates in Figure 8.16 (a) in a widening of the peaks. Figure 8.16 (c) presents peaks that are clearer than the low energy ones, but still quite dispersed. Figure 8.16 (b) is relative to the best pattern and presents sharply defined peaks. It is interesting to note that for GR irradiation only the most regular patterns show the second-order peak on the 2D FFT (i.e. the peak at a double spatial frequency than the principal one). The second peak indicates the tendency of the ripples to be a square wave, thus gives more information to the structure shape. IR structures are more likely to show the second peak (cf. Figure 8.14).

Pattern	Parameter	Value	Error	Unit
Low	Pitch	480	35	nm
	R	7%		
	γ	18	2	deg
Optimum	Pitch	470	30	nm
	R	6%		
	γ	11	1	deg
High	Pitch	460	35	nm
	R	8%		
	γ	25	1.5	deg

Table 8.17: Pitch, regularity, and homogeneity results for the three patterns presented in Figure 8.15.

Factors	Level 1	Level 2	Level 3	Level 4	Unit
Repetition rate	100	300			kHz
Fluence	0.2	0.3	0.4	0.5	μJ
Pulse step	1	2	3		μm

Table 8.18: DoE table for the experimental campaign for the nanostructuring operations with the GR laser beam.

Table 8.17 reports the calculated values of the measured periodicities (i.e. the structure pitch), the homogeneities, and the regularities for GR irradiation. According to what can be seen by the SEM micrographs and the 2D FFT characterization, the quantitative evaluation confirms that the selected pattern is the most regular. The measured peak, according to the literature on LIPSS, is again slightly smaller than the laser wavelength.

8.6 HIERARCHICAL TEXTURES

Finally, all the processing step parameters have been found and optimized. Therefore, hierarchical textures are engraved on steel just by performing the micro structuring, polishing, and nanostructuring steps consecutively. The global objective of the work was to characterize the effects of hierarchical textures on the polymer flow in injection molding. Hence, the hierarchical textures were obtained directly onto the mold inserts (cf. subsection 6.2.1).

To study the effects of the different-sized textures, six surfaces were created.

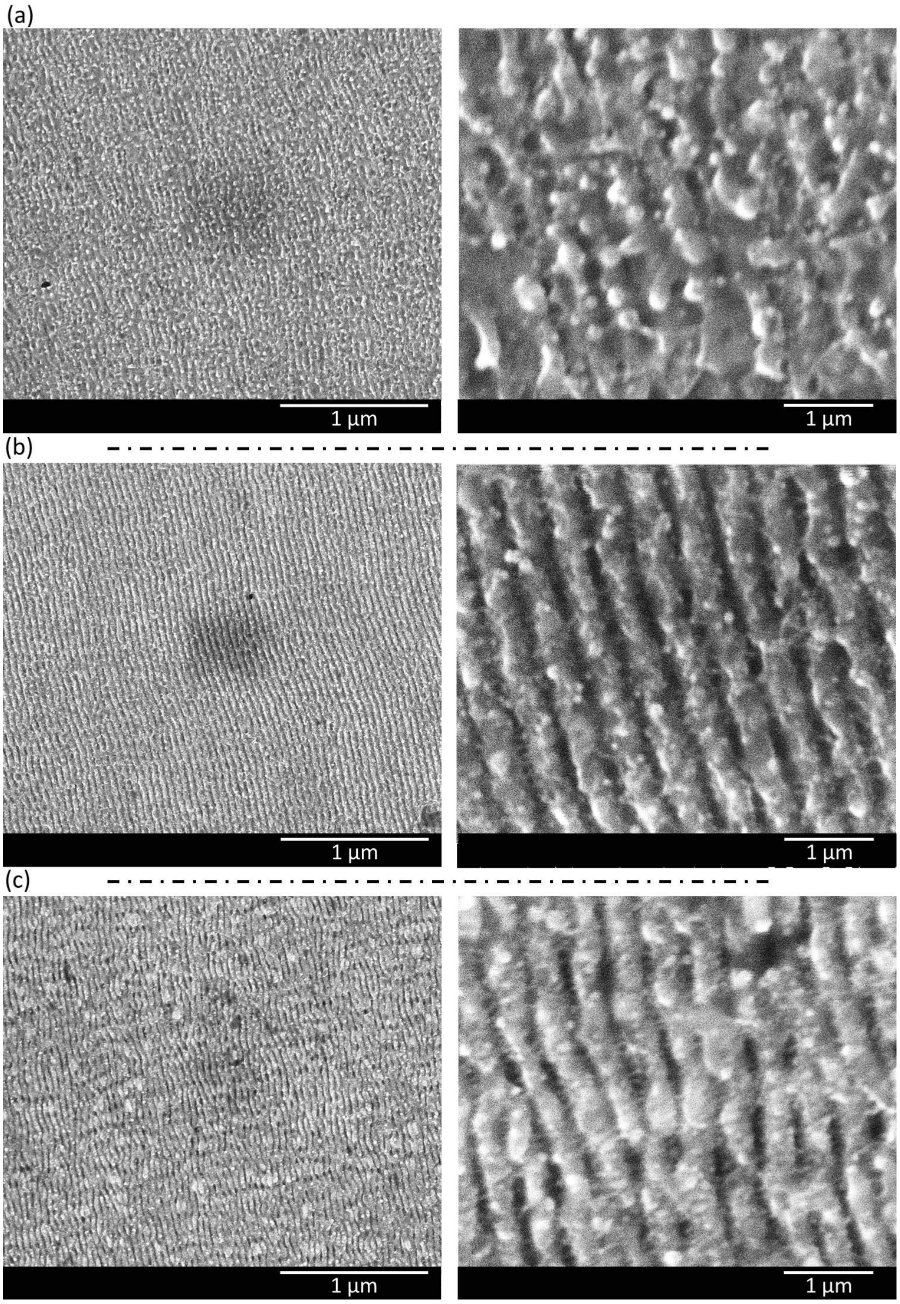

Figure 8.15: SEM micrographs GR beam induced LIPSS patterns. At the figure center (b) the selected texture is showed. Above and below the selected pattern, an example of a low-energy texture (a) and a high-energy texture (c) is proposed. Each SEM micrograph is accompanied by a magnification to better assess the structure shape.

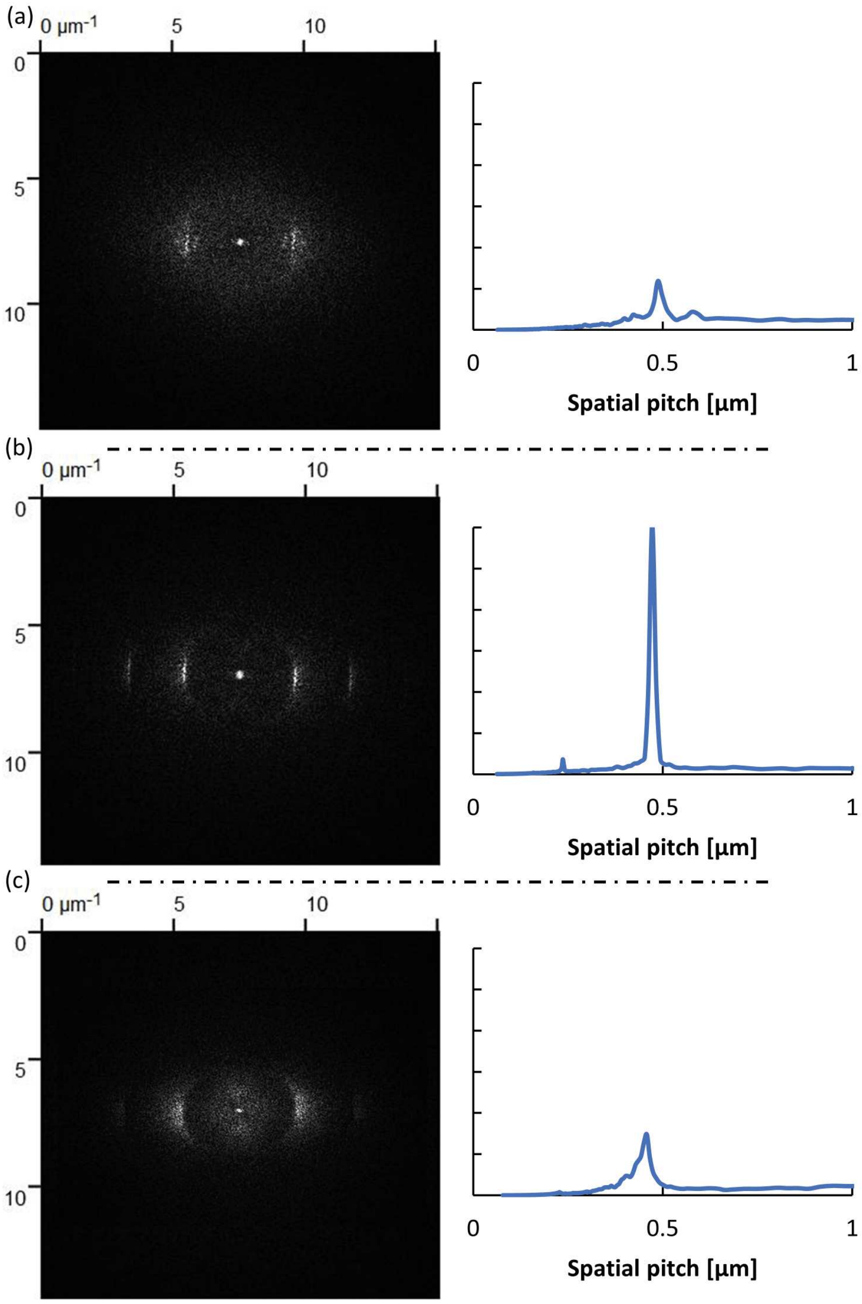

Figure 8.16: 2D Fast Fourier Transform and spectrum of the chosen SEM micrographs (cf. Figure 8.15). At the figure center (b) the elaboration of the selected texture SEM image is showed. Above and below the selected pattern elaboration, the 2D FFT and the spectrum of a low-energy texture (a) and a high-energy texture (c) are proposed.

Rep. Rate *kHz*	**Pulse step** *μm*	**Scan Speed** *mm/s*	**Lateral Step** *μm*	**Laser Power** *W*	**Fluence** J/cm^2	**Pulse Energy** *μJ*
100	1	100	1	0.013	0.2	0.13
100	2	200	2	0.013	0.2	0.13
100	3	300	3	0.013	0.2	0.13
100	1	100	1	0.019	0.3	0.19
100	2	200	2	0.019	0.3	0.19
100	3	300	3	0.019	0.3	0.19
100	1	100	1	0.025	0.4	0.25
100	2	200	2	0.025	0.4	0.25
100	3	300	3	0.025	0.4	0.25
100	1	100	1	0.032	0.5	0.32
100	2	200	2	0.032	0.5	0.32
100	3	300	3	0.032	0.5	0.32
300	1	300	1	0.038	0.2	0.13
300	2	600	2	0.038	0.2	0.13
300	3	900	3	0.038	0.2	0.13
300	1	300	1	0.057	0.3	0.19
300	2	600	2	0.057	0.3	0.19
300	3	900	3	0.057	0.3	0.19
300	1	300	1	0.076	0.4	0.25
300	2	600	2	0.076	0.4	0.25
300	3	900	3	0.076	0.4	0.25
300	1	300	1	0.095	0.5	0.32
300	2	600	2	0.095	0.5	0.32
300	3	900	3	0.095	0.5	0.32

Table 8.19: Laser and scanning parameters for the GR beam nanostructuring DoE.

Rep. Rate *kHz*	**Pulse step** *μm*	**Scan Speed** *mm/s*	**Lateral Step** *μm*	**Laser Power** *W*	**Fluence** J/cm^2	**Pulse Energy** *μJ*
300	2	600	2	0.057	0.3	0.19

Table 8.20: Selected laser and scanning parameters for the GR nanostructuring.

- A IR induced LIPSS pattern (cf. Figure 8.17 (a)).
- A GR induced LIPSS pattern (cf. Figure 8.17 (b)).
- A hierarchical texture composed by microstructure + IR induced LIPSS pattern (cf. Figure 8.17 (c)).
- A hierarchical texture composed by microstructure + GR induced LIPSS pattern (cf. Figure 8.17 (d)).
- An only microstructured texture (cf. Figure 8.17 (e)).
- A smooth surface for comparison (cf. Figure 8.17 (f)).

The SEM micrographs of the hierarchical textures reported in Figure 8.17 show that the IR LIPSS are more stable and can reach a decent level of regularity also over microstructures. In contrast, GR LIPSS are less marked.

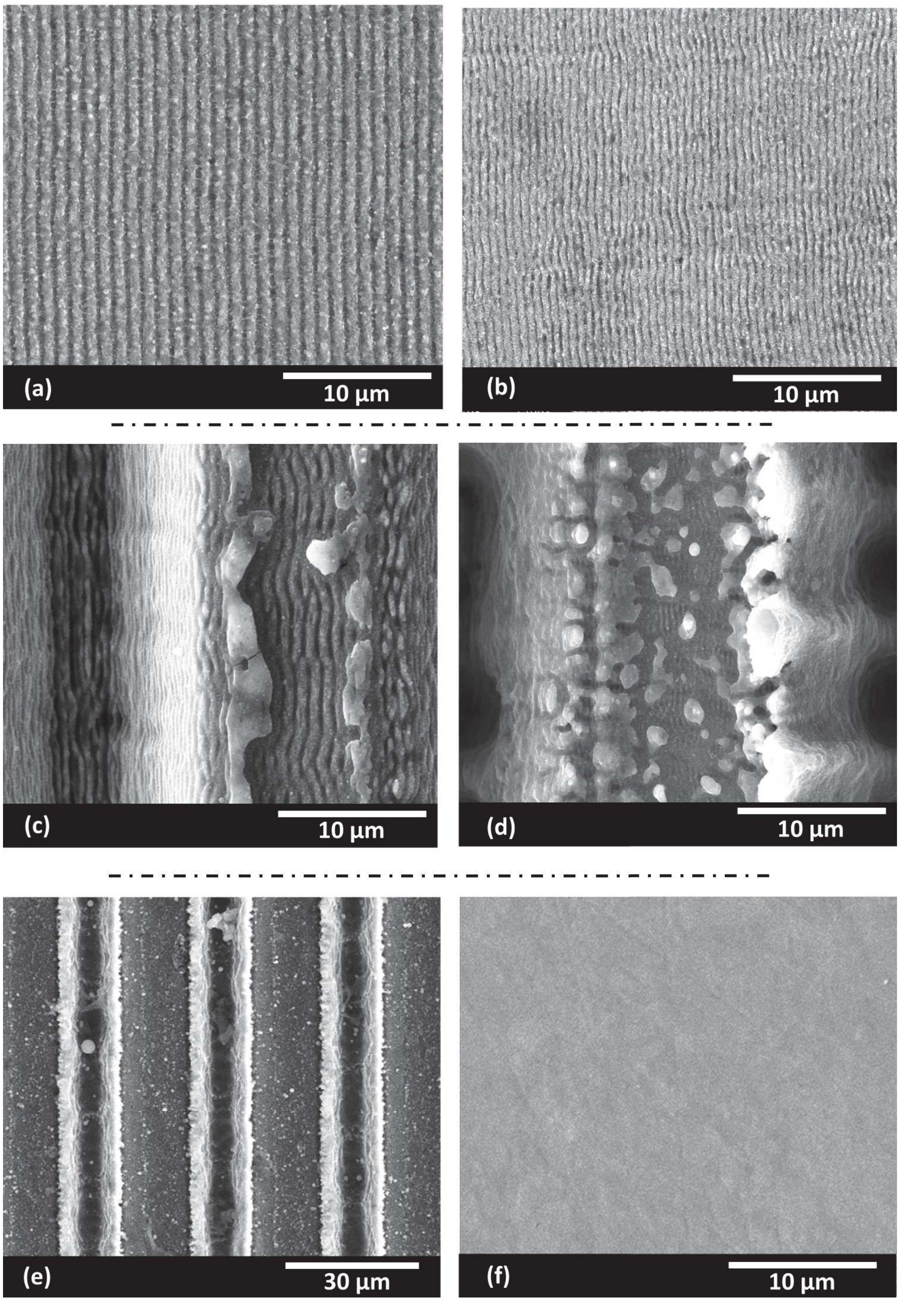

Figure 8.17: SEM micrographs of the mols insert generated surfaces: (a) IR beam induced LIPSS, (b) GR beam induced LIPSS, (c) hierarchical texture of microstructures and IR LIPSS, (d) hierarchical texture of microstructures and GR LIPSS, (e) only microstructures, and (f) smooth surface used for comparison.

Part IV

CAVITY FILLING

9 THERMAL BOUNDARY CONDITIONS EFFECTS ON FILL

In injection molding, factors as the reduced thickness of the part, the high viscosity of the thermoplastic polymers, and the low mold temperatures require elevated injection pressures to completely fill the mold cavity. The complex shearing and non-isothermal flow (cf. fountain flow subsection 2.1.1) determinates the building up of the pressure drop inside the mold, which ultimately determinates the injection pressure.

As discussed in section 2.2, several process modifications have been proposed to favor the polymer flow. Generally, the proposed solutions act on the thermal boundary condition, activating tools to increase the mold surface temperature and delay skin formation.

In this work, the effect of the thermal boundary conditions on filling flow is studied exploiting a semi-crystalline PET (cf. subsection 6.4.4). The thermal phenomena and the effects of the shear-induced crystallization (cf. subsection 2.4.2) are experimentally studied in the typical non-isothermal shearing flow condition of the injection molding process. The thermal boundary conditions at the polymer-wall interface were varied by exploiting two different substrate stainless steels and introducing two ceramic mold coatings. The polymer flow is studied exploiting an open-flow cavity mold. The SIC was studied by analyzing the pressure evolution in the cavity during the polymer injection.

9.1 EXPERIMENTAL APPROACH

The effects of the thermal boundary conditions on the polymer melt flow into the open cavity was studied by selecting different combinations of injection molding parameters. A full factorial DoE was set varying the mold insert properties, the mold cavity thickness, and the injection velocity. Table 9.1 3 reports the levels for each factor considered in the study. In total, 2x2x3x6 molding conditions are examined, for a total of 720 collected signals.

The effects of the different thermal boundary conditions were carried out by analyzing the whole pressure signal obtained with the sensor. The molding cycle was stabilized performing 20 cycles before the first data collection and sampling one pressure curve every three injections. For each molding condition, 10 cycles were collected. From the signals obtained by these repeated measures, it was possible to create a master curve, computing the arithmetical mean (cf.

Factor	Level 1	Level 2	Level 3	Level 4	Level 5	Level 6	Unit
Mold steel	Stavax	H11					
Coating	Coated	Uncoated					
Thickness	1.9	2.1	2.5				mm
Injection Speed	100	200	300	400	500	600	mm/s

Table 9.1: Mold inserts and injection molding parameters for the experimental DoE.

subsection 6.2.1). That was possible thanks to the high repeatability of the injection process.

9.2 INJECTION MOLDING RESULTS

The injection molding experimental results indicate that the different mold inserts affect the polymer flow in the open slit die. The results of the molding experiments were analyzed in terms of resulting pressure drop using the analysis of variance (ANOVA). The pressure drop is defined as the pressure sensed at the sensor location when the polymer starts to flow out of the mold, which is the point of separation between the filling flow of the cavity and the free flow out of the mold (cf. subsection 6.2.1).

In Table 9.2 the results for the single factors and the second-order interactions are reported. The ANOVA test is performed on the cavity pressure drop results. In this work, we selected a significance level of 5 %. All the single factors have statistically significant interaction with the selected response variable. Therefore, all the selected factors have a proven influence on the pressure drop. The significance of the cavity thickness and the injection velocity on the pressure drop is obvious since the factors were selected to study the behavior of the different mold setups at various molding conditions. Conversely, the significance of the insert steel type and the coating material is interesting. The mold steel and the coating presence affect the pressure drop in the cavity.

Figure 9.1 reports the main effects plot for the factors steel substrate and coating presence. The substrate plot shows that the Stavax steel and the presence of the coating improve the filling performance. The effect linked to the steel substrate can be interpreted as a result of a different thermal conductivity of the steel. The presence of the coating has a slightly higher effect with respect to the substrate. The mold coating plot shows that the coating presence improves the polymer flow inside the mold cavity, reducing the pressure required by

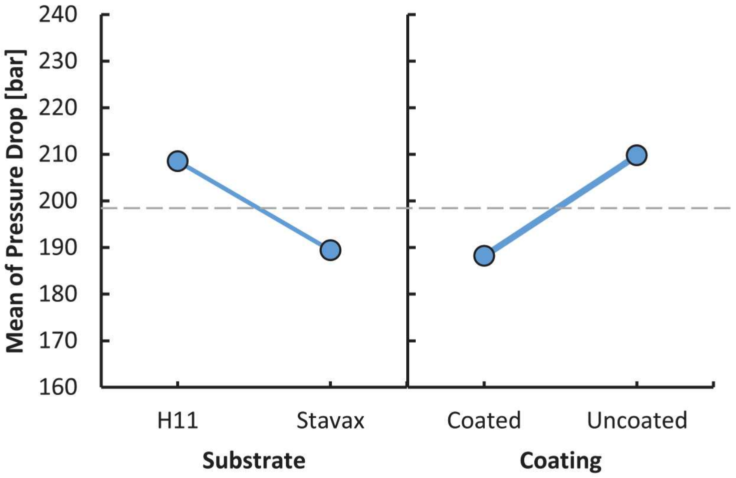

Figure 9.1: Main effects plot for the insert-related factors.

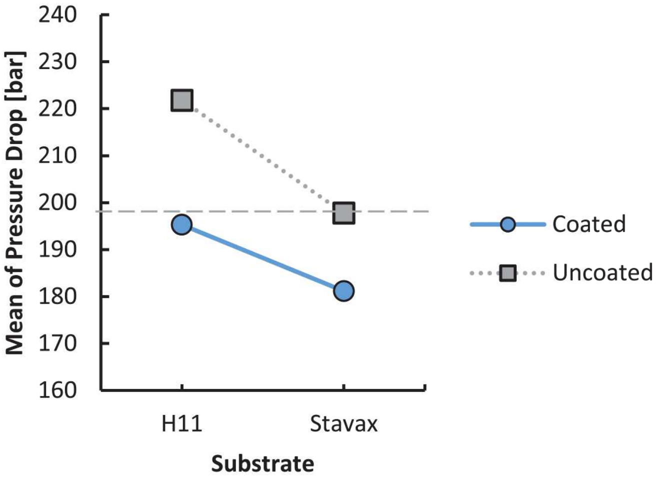

Figure 9.2: Interaction plot of the insert-related factors.

the melt to exit the mold. The thin ceramic layer may alter the thermal boundary conditions at the melt/mold interface, delaying the thermal transfer.

To better assess the effect of these two factors, in Figure 9.2 the interaction plot is presented. The plot describes how the coating presence improves the filling performance for both the selected steels. Therefore, the delaying effect of the coating adds to the effect of the steel. From a statistical point of view, the commented interaction is significant, with a P-Value lower than 5 % (cf. Table 9.2). The CrN coating over the Stavax substrate is the best performing setup in terms of pressure drop, whilst the DLC coating over the H11 steel is the best performing coating in terms of pressure reduction with respect to the uncoated solution.

Source	DF	Adj SS	Adj MS	F-Value	P-Value
Substrate	1	6574	6574	129	0.000
Coating	1	8378	8378	165	0.000
Thickness	2	217160	108580	2142	0.000
Injection Speed	5	87671	17534	345	0.000
Substrate * Coating	1	442	442	8.71	0.005
Substrate * Thickness	2	378	189	3.73	0.033
Substrate * Injection Speed	5	2528	506	9.98	0.000
Coating * Thickness	2	1756	878	17.32	0.000
Coating * Injection Speed	5	63	13	0.25	0.938
Thickness * Injection Speed	10	807	81	1.59	0.148

Table 9.2: ANOVA results for the experimental DoE.

9.2.1 Thermal boundary effect at varying processing conditions

In this section, the thermal boundary conditions' variations effects on flow are discussed considering the different used processing conditions. The effect of the coating on the pressure drop can be better addressed by comparing the solutions characterized by the same substrate. Therefore, the results are presented as a percentual drop decrease of the coated solution against the respective uncoated one. The coating acts as a thermal resistance in correspondence with the mold boundary, decreasing the pressure drop inside the mold cavity.

Figure 9.3 shows the percentual pressure drop decrease against the cavity thickness. At thickness 1.9 mm the two coatings have the same performance but as the thickness increases, the CrN effect fades away. Conversely, the effect of the DLC coating is stable.

Figure 9.4 shows the percentual pressure drop decrease against the injection speed. The trends for both the coatings are roughly flat. The effect of the injection speed on the performance of the coating is not as strong as the cavity thickness is. For increasing injection speeds, the polymer melt experiences more shear causing greater pressure drops. A stressed flow may trigger thermal phenomena (e.g. shear heating) that can generate a certain amount of heat near the mold surface. Such conditions can reduce the effect of thermal resistance at the surface. Therefore, the effect of the coating can show a decrease in intensity for increasing injection speeds. Since the trends are stable, the eventual presence of shear heating effects does not affect the pressure results. This conclusion is further confirmed by the high P-Value of the interaction between the coating presence and the injection speed (cf. Table 9.2).

The major effect of reducing the thickness is the increase of the shear strain and shear stress in the cavity, and ultimately of the pressure drop inside the cavity. The higher the pressure inside the cavity, the more the polymer is pressed to the mold, decreasing the thermal resistance between the polymer and the mold. An additional insulative layer will cause more visible effects when the polymer is in the best conditions for heat transfer, pressed to the cavity surface. Therefore, the performance of the coating should be more visible for lower thicknesses.

Moreover, the polymer flow is less sensitive to the cooling capability of the mold when the thickness is high. Indeed, the higher the thickness, the greater the heat introduced by convection is in the cavity. This effect adds to the effect of the pressure, increasing the influence of the coating for lower thicknesses.

From the results, it is possible to note that the DLC-coated solution performs better even when the cavity thickness is high (cf. Figure 9.3). Hence, we can note that the DLC-coated solution shows a lower sensibility to the pressure and heat introduced in the cavity.

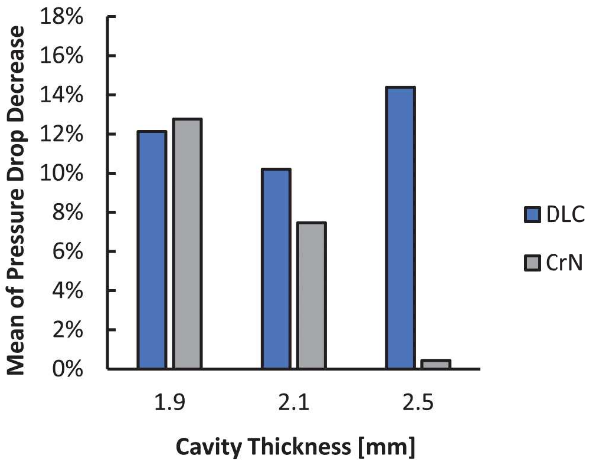

Figure 9.3: Percentual pressure drop decrease with respect to the uncoated solution against the cavity thickness.

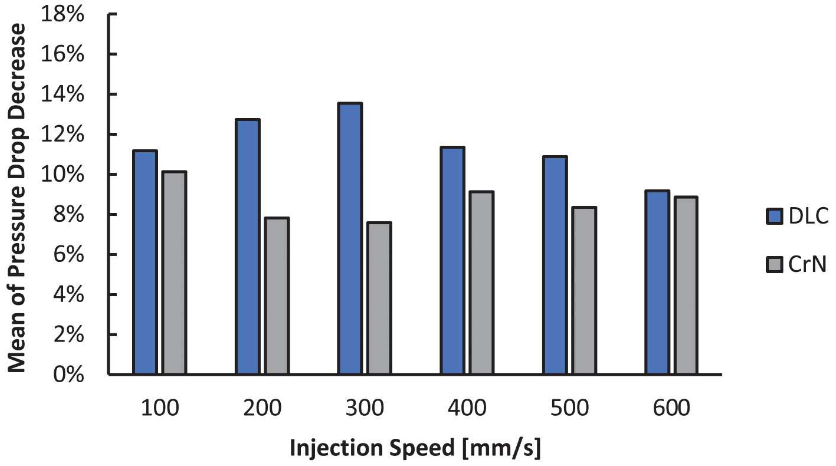

Figure 9.4: Percentual pressure drop decrease with respect to the uncoated solution against the injection speed.

9.2.2 Pressure drop evolution

An in-depth study of the effect of the coating presence effect at different flow conditions can be done by comparing the flow curves reported in Figure 9.5. As a first observation of the experimental results reported on the plot, it has to be noted that the coating presence is never causing a higher pressure drop. Therefore, the coating presence does not negatively affect the polymer flow. All the experimental points follow the major effects discussed above against both the injection speed and cavity thickness.

The difference between the uncoated flow curves (connected by solid lines) and the coated ones (connected by dotted lines) measures the coating performance. Figure 9.5 (a) shows that the effect of the DLC coating is constant throughout the different thicknesses. Indeed, the DLC flow curves are almost always shifted below the uncoated solution. On the other hand, the CrN results show a shifted trend only for high pressures (which means low cavity thickness and high injection velocity) and no coating impact for low pressures (cf. Figure 9.5 (b)).

A threshold pressure can be individuated for the two coatings. The dashed green line marks the pressure level at which the coating starts to have an effect on the polymer flow. The threshold pressure is always referred with respect to the standard flow in the uncoated solution. The DLC coating shows a threshold pressure of about 110 bar in the study condition (cf. Figure 9.5 (a)). The threshold for the CrN coating stays at about 170 bar (cf. Figure 9.5 (b)).

The pressure threshold has not to be intended as a property of the coatings since it is surely dependent on the position of the pressure sensor, the cavity geometry, and the molding conditions. The threshold has to be intended as a measure of the favorability of the molding condition for assessing the coating performance. In conclusion, a coating that has a broader range of influence on the flow is preferable. A deeper analysis of the pressure data has to be carried out to better explore the phenomena involved in this effect.

9.2.3 Pressure drop evolution during the cavity filling

The experimental setup allows for the study of the master curve, performing the mean of the sensed pressure for each time step. At the same time, the trend of the standard deviation is proposed (cf. subsection 6.2.1). The mean of the standard deviation throughout the cycle is calculated to give an understanding of the variability of the curves and never exceeds 6 bar for all the tested conditions.

The high repeatability of the experimental setup allows for the study of the pressure drop evolution along with the cavity filling. Figure 9.6 and Figure 9.7 report the pressure signals for the DLC and

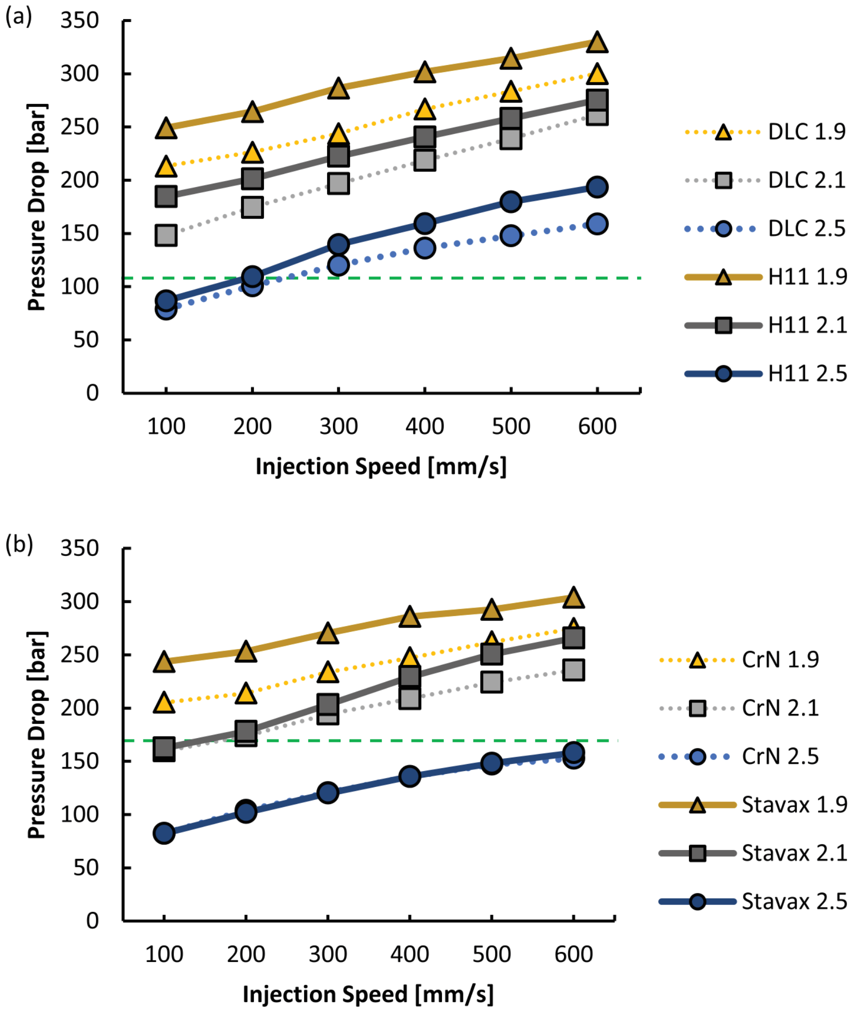

Figure 9.5: Pressure drop results for (a) the H11 and (b) the Stavax substrate in the uncoated and coated setup. The results are proposed at the three considered thicknesses (in mm on the key names). The dashed green line marks the threshold pressure for the coating effect. The maximum standard deviation is 7 bar.

the CrN coating against the uncoated setup, respectively. Each figure presents three plots for the three analyzed cavity thicknesses. The solid lines represent the uncoated inserts, the dotted ones represent the coated ones. The signals are truncated as the polymer starts to exit the mold (i.e. at the end of the filling phase cf. subsection 6.2.1). Therefore, the difference between the solid and dotted lines at the truncation point is the pressure drop difference. The stabilized flow pressure does not present different trends between coated and uncoated solutions and it is not the object of this discussion.

The vast majority of the pressure curves relative to uncoated inserts present a kick (i.e. a discontinuity from the linear behavior) in correspondence with a certain pressure. This pressure level seems to be steel and thickness dependent. The H11 steel presents a kick for almost all the tested conditions, a linear behavior of the solid line is visible only for the low injection speeds at 2.5 mm cavity thickness (cf. Figure 9.6 (c)).

The Stavax steel has a linear behavior for thickness 2.5 mm (cf. Figure 9.7 (c)) and for the low injection speeds at thickness 2.1 mm (cf. Figure 9.7 (b)). By comparing the results with the ones presented in Figure 9.5 it can be concluded that the presence of the kick always corresponds to the existence of a pressure drop difference between the inserts.

When the mold is coated the pressure never shows a kick. Both the steels present the kick phenomenology, but it never occurs for the coated solutions. Therefore, it can be noted that the beneficial effect of the coatings is the ability to inhibit kick formation.

9.2.4 Skin layer formation effect on pressure

The kick (i.e. the increase in the pressure gradient) can be regarded as a sudden change in the flow conditions inside the mold cavity. Similar changes of a pressure trend can be found when, during flows into regular channels, the flow section rapidly reduces. The cavity section object of the study has a constant section. However, the reducing-section analogy can help an interpretation of the phenomena. When a hot polymer melt flowing into a cold cavity touches the mold wall it freezes forming the so-called skin layer (cf. subsection 2.1.1).

The skin layer formation depends on the local temperature of the outer polymer layer (i.e. polymer contact temperature). This temperature is difficult to measure and predict. It depends on the temperature of the melt, of the mold, and on the thermal flow between the polymer and the mold. In particular, the polymer contact temperature is correlated to the balance between heat convection from the injected polymer and heat conduction through the mold. The understanding of the evolution of the contact temperature puts the basis for the comprehension of the skin formation phenomena. Indeed,

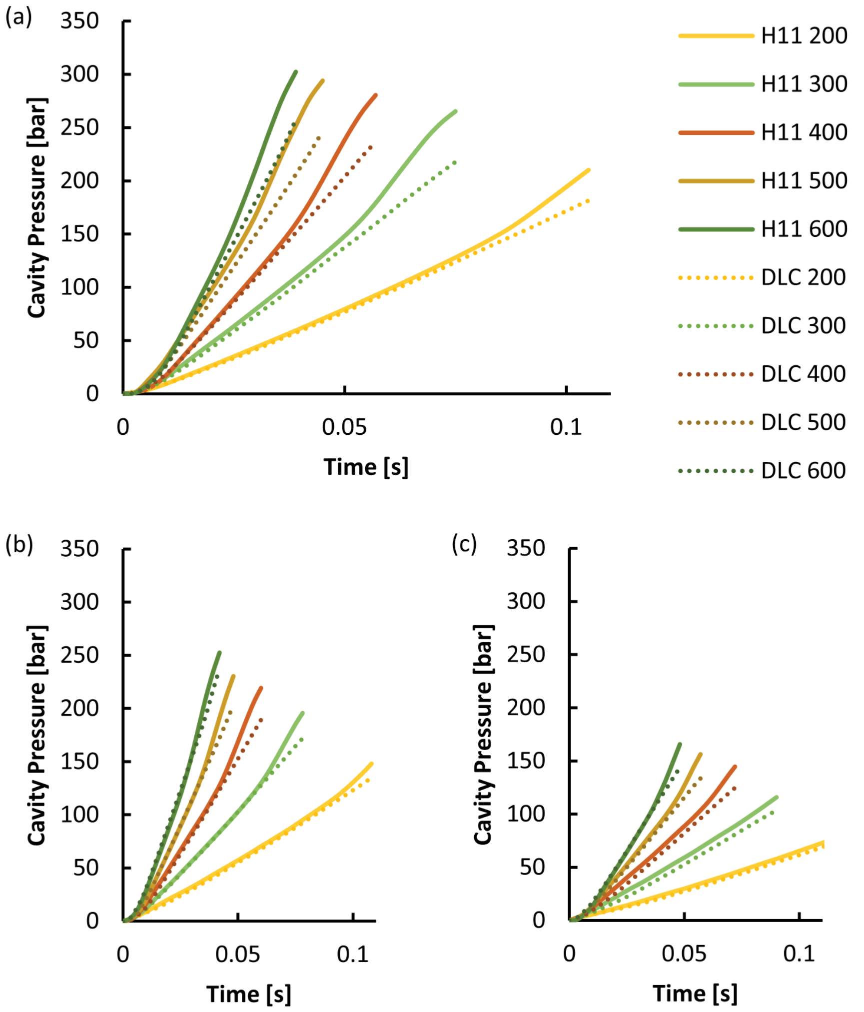

Figure 9.6: Cavity pressure signals of the filling experiments using the H11 and H11 DLC coated inserts. The solid lines refer to the uncoated insert, the dotted lines refer to the coated insert. The pressure curves report only the cavity filling phase, the free flow is omitted for clarity. The results are divided by means of the cavity thickness: (a) 1.9 mm, (b) 2.1 mm, and (c) 2.5 mm.

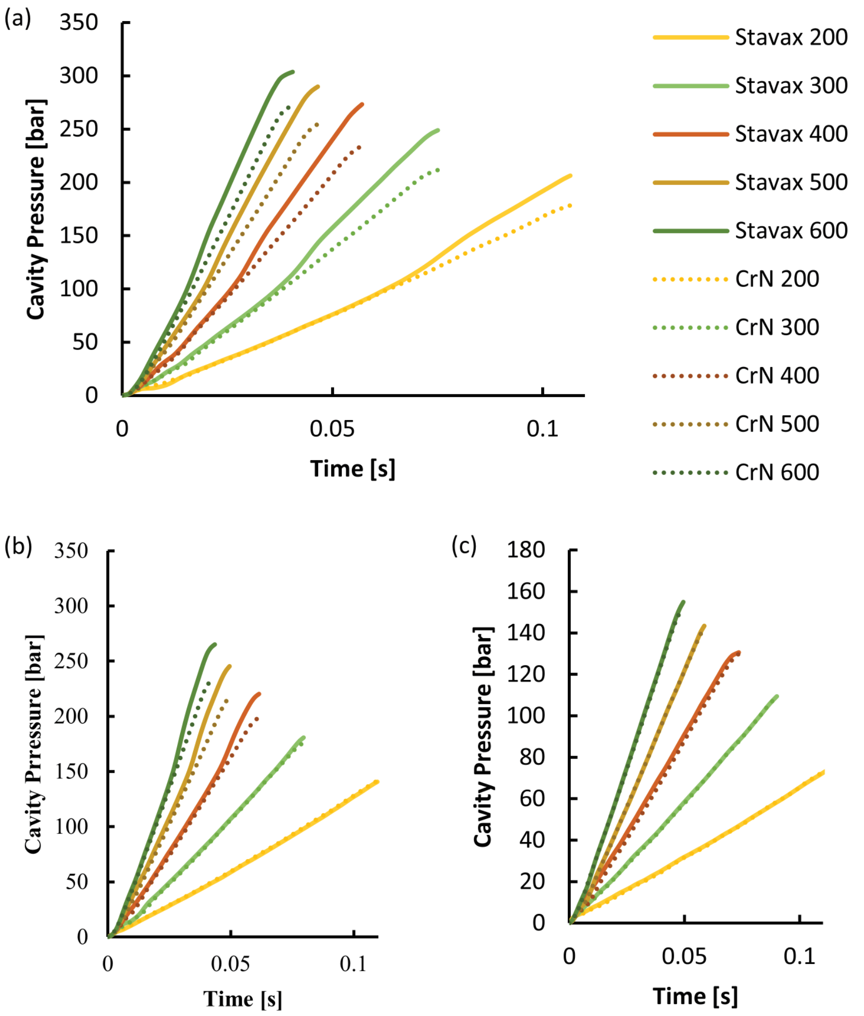

Figure 9.7: Cavity pressure signals of the filling experiments using the CrN and Stavax CrN coated inserts. The solid lines refer to the uncoated insert, the dotted lines refer to the coated insert. The pressure curves report only the cavity filling phase, the free flow is omitted for clarity. The results are divided by means of the cavity thickness: (a) 1.9 mm, (b) 2.1 mm, and (c) 2.5 mm.

in commercial injection molding simulation environments, the skin thickness is predicted as the temperature drops lower than a certain threshold.

The section constriction may be interpreted as a sudden increase in skin layer thickness (cf. Figure 9.8). In this study, the semi-crystalline PET used for the experiments is pushed under shear into a cold cavity. Therefore, skin formation is surely accompanied by crystallization phenomena. Considering the typical non-isothermal shearing conditions of the injection molding process, shear-induced crystallization and thermal crystallization occur simultaneously. The crystals layer formation occurs after a certain time, which can be regarded as incubation time. The incubation time is schematized in Figure 9.8 as an offset between the skin and the crystal layer positions. The effect of the incubation time is also visible on the obtained pressure curves, where the first part of the linear trend of the pressure is equal between the coated and uncoated inserts. After a certain time, thermal and shear-induced crystallization starts. Indeed, from the results, it is possible to detect the consequences on the kick position of both the aforementioned crystallization processes.

- The shear-induced crystallization depends on the shear stress and the strain accumulated by the polymer (cf. subsection 2.4.2). The kick is indeed shifting back for increasing shear rates. This effect can be seen by comparing the master curves taken at the same thickness in Figure 9.7 for CrN and in Figure 9.6 for DLC. By increasing the injection speed, the polymer melt shear rate grows, and the time the kick occurs shifts backward.
- The thermal crystallization effect can be seen by comparing the master curves obtained at different thicknesses. As the thickness increases, the heat introduced by convection by the polymer inside the cavity increases. Therefore, the polymer close to the mold wall is subjected to minor cooling. Indeed, the kick shifts to higher injection times when increasing the mold cavity thickness, until no kicks are present in the master curve at all. Low local temperatures of the polymer can trigger crystallization phenomena that locally increase enormously the viscosity. The temperature has been individuated as a major cause of the reduction of crystallization induction times. The coating acts as an insulator avoiding the temperature drop of the polymer and subsequently increasing the crystallization induction times. The crystallization effect of pressure is then avoided when a coated inset is present.

The effect of the coating presence can therefore be linked to a delay of thermal flow between the melt and the mold. Higher contact temperatures inhibit the fast crystals nucleation and shift the kick to longer injection times.

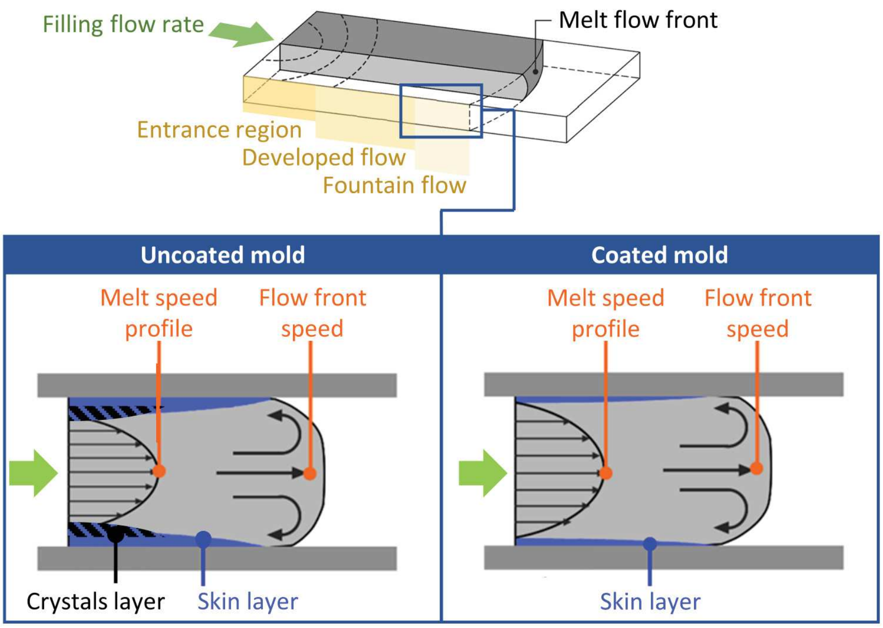

Figure 9.8: Scheme of the polymer melt flow in an injection mold cavity. The interpretation of the crystal layer formation is schematized, introducing an offset between the skin and the crystal layer to include the effect of the incubation time.

10 HIERARCHICAL TEXTURING EFFECTS ON FILLING FLOW

The second approach named in this work to modify the filling flow during injection molding operations is surface texturing. As discussed in section 2.3, mold surface morphology modification can interfere with the interactions between the mold and the polymer macromolecules that come are exposed to the cavity surface.

In this work, the effect of hierarchical mold textures obtained through ultrafast laser texturing on filling flow is studied exploiting a semi-crystalline PET (cf. subsection 6.4.4). The mold structures are in the micro and nanoscale. The polymer flow is studied exploiting an open-flow cavity mold.

10.1 EXPERIMENTAL APPROACH

The most promising textures obtained through ultrafast laser irradiation in the process parameters optimization work (cf. chapter 8) were machined onto mold inserts to perform injection molding experiments. A DoE for the injection molding experiments was set to study the effect of different mold surfaces textures on the pressure drop of the polymer melt in the cavity. Two nanostructured patterns, a microstructure, and the hierarchical structures have been obtained by the combination of the two pattern levels (cf. section 8.6).

Globally, 6 mold inserts were exploited for the study (nanostructured IR and GR, microstructured, hierarchically structured with nanostructure IR and GR, and a smooth setup for comparison). The ripples and the microstructures are both aligned to the direction of the polymer melt flow in the cavity. The injection molding experiments were carried out at typical industrial processing conditions varying the injection flow rate (from 200 to 600 mm/s) and cavity thickness (1.5 and 1.0 mm) in order to study different flow regimes. The experimental DoE comprised four factors: the presence of microstructures and nanostructures, the injection speed, and the cavity thickness, for 2 x 3 x 3 x 2 levels, respectively (cf. Table 10.1).

The injection molding experiments were carried out at a melt and mold temperature of 300 °C and 15 °C, respectively. The effects of the mold textures were studied by analyzing the whole pressure signal obtained with the sensor. The molding cycle was stabilized performing 20 cycles before the first data collection and sampling one pressure curve every three injections. For each molding condition, 10 cycles were collected. From the signals obtained by these repeated

Factor	Level 1	Level 2	Level 3	Unit
Microstructure	Yes	No		
Nanostructure	GR	IR	No	
Thickness	1.45	1		mm
Injection Speed	200	400	600	mm/s

Table 10.1: Mold inserts textures and injection molding parameters for the experimental DoE.

measures, it was possible to create a master curve, computing the arithmetical mean (cf. subsection 6.2.1) to study the repeatability of the experiment.

10.2 INJECTION MOLDING RESULTS

The injection molding experimental results indicate that the polymer flow in the open slit die is sensible to the mold surface morphology. The results of the molding experiments were analyzed in terms of resulting pressure drop using the analysis of variance (ANOVA). The pressure drop is defined as the pressure sensed at the sensor location when the polymer starts to flow out of the mold, which is the point of separation between the filling flow of the cavity and the free flow out of the mold (cf. subsection 6.2.1).

In Table 10.2 the results for the single factors and the second-order interactions are reported. The ANOVA test is performed on the cavity pressure drop results. In this work, a confidence level of 5 % was selected. All factors or interactions below the 5 % level of confidence were eliminated. All the single factors have statistically significant interaction with the selected response variable. However, the nanostructure presence P-value is much higher than the others. In addition to that, the interactions of the nanostructure presence with the injection molding parameters (i.e. cavity thickness and injection velocity) are not statistically significative. Therefore, the nanostructure presence does not have a major influence on the pressure results. It is interesting to note that the interaction between the nanostructure and the microstructure factors is statistically significative. This statistical consideration is linked to the combined effect of the two factors, that is the effect of having a hierarchical texture.

From the main effects plot presented in Figure 10.1, it is possible to note that the cavity thickness strongly outperforms the other factors. This was an expected result, as the cavity thickness diminished by about 30%. A more in-depth analysis of the results was carried out by dividing the DoE into two sets of experiments. The first is the

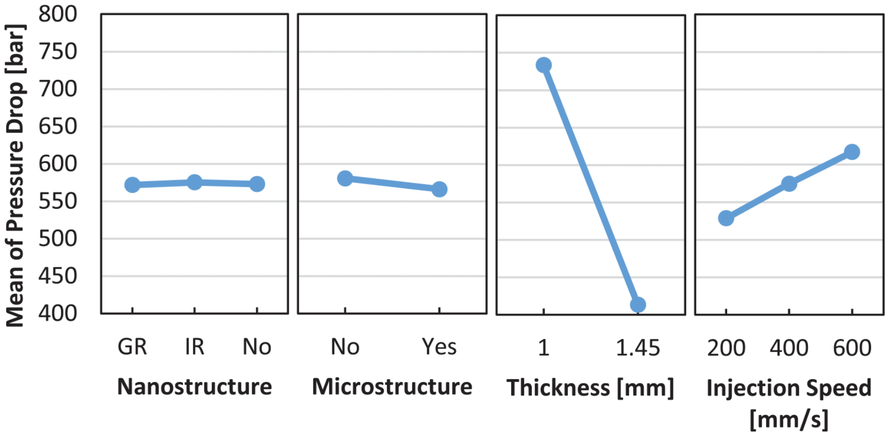

Figure 10.1: Main effects plot for the DoE factors.

set of experiments carried out at 1.45 mm thickness, the latter was carried out at 1.00 mm cavity thickness.

10.2.0.1 *1.45 mm cavity thickness*

The ANOVA tests were applied to the 1.45 mm thickness subgroup of experiments. The results are reported in Table 10.3. The test was carried out using the same approach as the global one. The results readily show that the only significant factor for the mold texture is the microstructure presence. Moreover, the microstructure and nanostructure interaction does not result statistically significative. From a processing perspective, the results mean that the presence of nanostructures is not sensed by the polymer melt flowing inside the cavity.

Figure 10.2 reports the main effects plot for the factors injection speed and microstructure presence. The effect of the injection speed is obvious. The microstructure presence induces a reduction of the pressure drop. The pressure results of the smooth and microstructured solutions are reported in Figure 10.3. The plot reports the percentage of pressure drop reduction linked to the microstructures' presence. The maximum pressure drop reduction is 2.6 % at 200 mm/s injection speed.

10.2.0.2 *1.00 mm cavity thickness*

The ANOVA tests were also applied to the 1.00 mm subgroup of experiments. The results are reported in Table 10.4. The test was carried out using the same approach as the others. At this low thickness, the nanostructure presence is a statistically significative factor. Moreover, the interaction for microstructure and nanostructure results statistically significative, highlighting the importance of the hierarchical tex-

Source	Adj SS	Adj MS	F-Value	P-Value
Microstructure	1919	1919	189	0.0000
Nanostructure	74	37	4	0.0420
Thickness	923727	923727	90969	0.0000
Injection Speed	46659	23330	2298	0.0000
Microstructure * Nanostructure	267	133	13	0.0000
Microstructure * Thickness	434	434	43	0.0000
Nanostructure * Thickness	322	161	16	0.0000
Thickness * Injection Speed	528	264	26	0.0000

Table 10.2: ANOVA results for the experimental DoE.

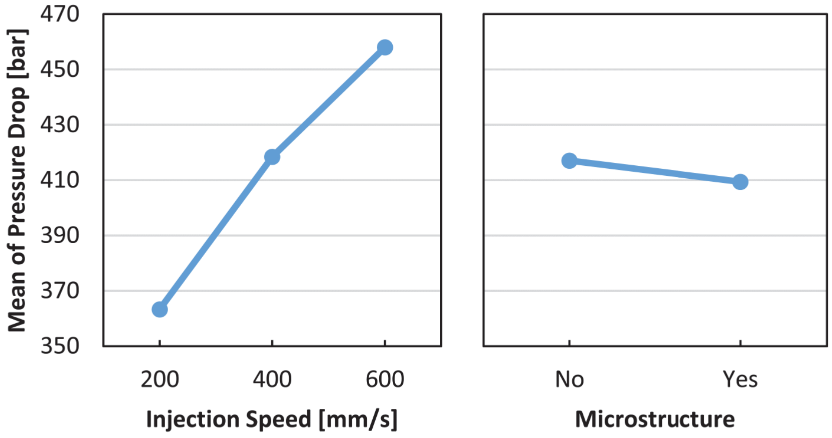

Figure 10.2: Main effects plot for the factors at thickness 1.45 mm.

Source	Adj SS	Adj MS	F-Value	P-Value
Microstructure	264,1	264,1	17,98	0,001
Injection Speed	27156,6	13578,3	924,09	0,000

Table 10.3: ANOVA results for the experimental DoE.

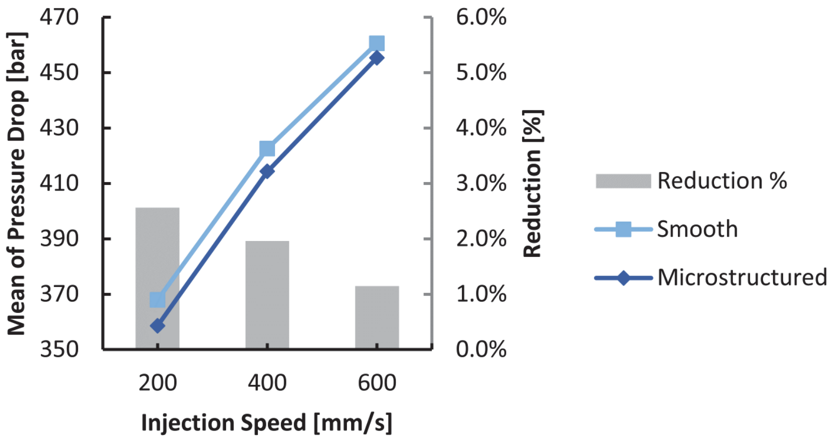

Figure 10.3: Pressure drop results plot at thickness 1.45 mm. The maximum standard deviation is 2 bar. The percentual decrease of the pressure drop is reposted as grey bars.

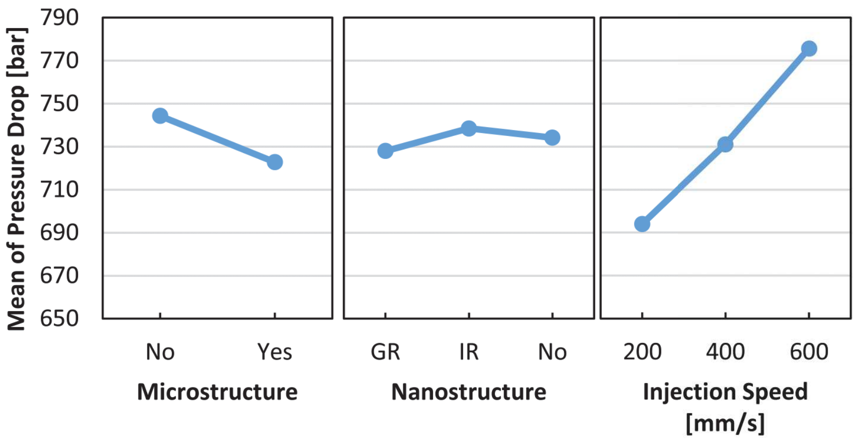

Figure 10.4: Main effects plot for the factors at thickness 1.00 mm.

ture. Therefore, at low thickness, the micro and nano morphology of the mold induce effects of the polymer flow.

Figure 10.4 reports the main effects plot for the factors injection speed, microstructure, and nanostructure presence. The effect of the injection speed is obvious. The microstructure presence induces again a reduction of the pressure drop. The GR nanostructure is effective in facilitating the polymer flow in the cavity. The IR nanotexture does not show flow improvements, the improvements seem to be mainly linked to the presence of the microstructure. The pressure results of the smooth and microstructured solutions are reported in Figure 10.5. The bar plot reports the percentage of pressure drop reduction linked to the microstructures and nanostructures presence. The maximum pressure drop reduction is 4.2 % at 400 and 600 mm/s injection speed.

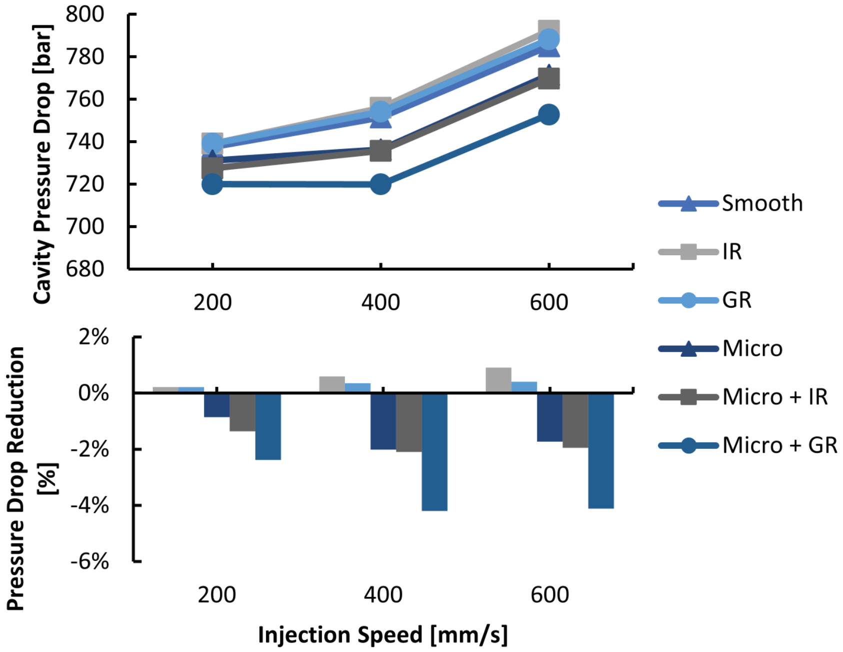

Figure 10.5: Pressure drop results plot at thickness 1.00 mm. The maximum standard deviation is 3 bar. The percentual decrease of the pressure drop with respect to the smooth insert is reported in the bottom bars plot.

Source	Adj SS	Adj MS	F-Value	P-Value
Microstructure	2089	2089	223	0.000
Nanostructure	336	168	18	0.000
Injection Speed	20031	10015	1071	0.000
Microstructure * Nanostructure	251	126	13	0.001

Table 10.4: ANOVA results for the experimental DoE.

10.2.1 Effects of laser-induced texture on polymer flow

The effects of the mold surface texture on the polymer flow are more visible for severe flow conditions (i.e. with low cavity thickness and high flow rate). The results show that the hierarchical texture that exhibits the larger difference between the micro- and the nano-periodicity produces the lowest cavity pressure drop. The best performing texture is the one presenting the higher difference between the periodicities of the two patterns (i.e. the Micro+GR), showing a cavity pressure drop reduction of 4.2 %. The microstructure has an effect on flow, showing a reduction of 2.0 % at 1.00 mm thickness and 2.6 % at 1.45 mm thickness. Therefore, at low thickness, the presence of the GR nanotexture further improves the texture impact. The result is consistent with the improved effect of hierarchical structures with respect to the single-pattern ones.

The experimental observations are consistent with the phenomenology of the polymer wall slip. As polymer melt flowing over solid boundaries exceeds a certain wall shear stress threshold it violates the classical no-slip boundary condition of fluid mechanics. The phenomenon is called wall slip and it is characterized by three slip regimes: (i) weak slip (occurs at low shear stresses) (ii) stick-slip regime and (iii) strong slip regime (cf. section 2.3). This last regime is characterized by large slip speeds that modify the speed profile into a near plug flow profile, macroscopically affecting the polymer flow resistance into the injection mold cavities. The surface texture promotes wall slip lowering the strong slip wall shear stress threshold. A smooth surface offers more attachment points to the melt than a hierarchical one. The fewer are the chains that are linked to the mold (i.e. have an absorbing atom in the mold) the less are the interactions between the mold and the polymer. The results suggest that the surface is functionalized through LIPSS in the sense that it has fewer interactions with the melt, promoting slip.

Part V

MOLD SURFACE REPLICATION

11 PART FUNCTIONALIZATION BY TEXTURE REPLICATION

Polymers are materials characterized by very different properties that can be tailored for many applications. Surface functionalization has emerged as a solution to the needs of various stakeholders. Functional surfaces find application as self-cleaning parts, scaffolds, tissues, optical parts, and anti-icing parts, in friction reduction, and in the engineering of injection mold surfaces section 4.4. All these applications generated an increasing demand to develop reliable and cost-effective mass manufacturing technologies for polymer surface replication.

Surface functionalization can be achieved by tailoring the surface chemistry or the surface topography. In this work, the morphology of the mold surface is textured to achieve functionalization of the plastic part through texturing. The replication of textured mold surfaces is challenging since the injected molten polymer tends to solidify quickly touching the cold mold, hindering the filling of the structures, especially when those are on the micro- or nanoscale. Replication is influenced by process parameters and mold design (cf. chapter 3).

This work focuses on the study of a process chain for manufacturing functional submicron-structured plastic parts through injection molding. Different mold surface textures are obtained on steel using a femtosecond laser source. The mold surface-induced patterns are then replicated by microinjection molding of different thermoplastic resins. Texture design, laser processing, and the wettability of parts are studied to optimize the manufacturing process as well as the functionality of the parts.

11.1 EXPERIMENTAL APPROACH

The proposed process chain accomplishes the plastic part functionalization through three fundamental steps.

1. Mold and texture design.

2. Mold preparation.

3. Ultrafast laser texturing of the mold cavity inserts.

4. Replication of the mold surface through micro injection molding.

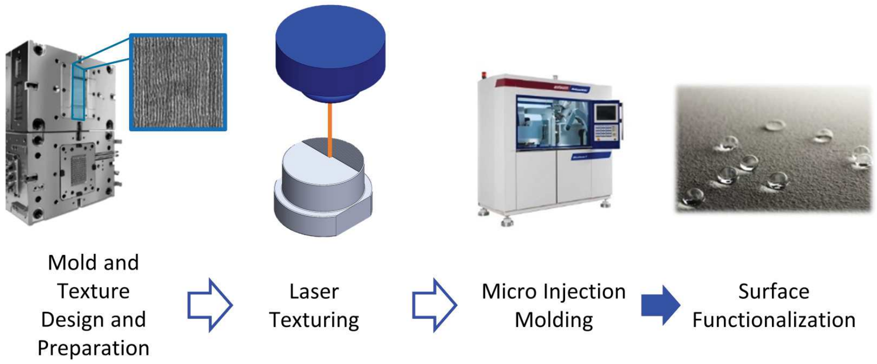

Figure 11.1: Schematics of the process chain exploited to functionalize plastic parts.

The process chain (cf. Figure 11.1) was validated by characterizing the micro injection molding process capability of replicating different mold patterns. The process performance was evaluated considering the functionality of the manufactured plastic parts. The experimental approach followed a three-step scheme.

- Creation of 4 different surface textures on mold inserts by ultrafast laser texturing.
- Formulation and execution of a DoE for the microinjection molding experiments.
- Characterization of the obtained plastic parts by means of the wetting performance.

The DoE comprised the polymer material and the mold temperature as factors. The design has 2x9 levels (cf. Table 11.1). The obtained plastic parts replicated texture was characterized using AFM and the part functionality was characterized through water contact angle measurement (i.e. wetting characterization).

Several injection molding parameters were kept constant along with the experiments. In Table 11.2 the melt temperature, back and switch over pressure, injection speed, packing time, and cooling time are summarized for the two polymers object of the study. The cooling time varied between 10 s (used only for 40°C mold temperature) and 100 s depending on the mold temperature. Variotherm injection molding was carried out at highest mold temperatures to allow for part ejection.

11.2 MOLD INSERTS TEXTURES

The mold insert textures are characterized by patterns presenting different pitches. The induction of different periodicities was carried

Factor	Polymer	Mold Temperature
Unit		*C*
Level 1	PS	40
Level 2	PMMA	50
Level 3		60
Level 4		70
Level 5		80
Level 6		90
Level 7		100
Level 8		110
Level 9		120

Table 11.1: Polymers and injection molding parameters for the experimental DoE.

Parameter	Unit	PS	PMMA
Melt temperature	°C	235	255
Back pressure	MPa	5	2
Switch-over pressure	MPa	80	82
Injection speed	mm/s	110	110
Packing pressure	MPa	45	50
Cooling time	s	10	10

Table 11.2: Polymers and injection molding parameters for the experimental DoE.

Insert	**Tilt angle**	$\gamma\ \Lambda_{High}$	$\gamma\ \Lambda_{Low}$	**Regularity**
A	0	6	3	90%
B	10	6	2	82%
C	20	7	4	74%
D	30	9	4	69%
Unit	*deg*	*deg*	*deg*	

Table 11.3: Regularity and dispersion angle results for the ultrafast laser induced patterns on the four inserts of the study.

out by changing the inclination of the laser beam over with respect to the normal to the insert surface (i.e. Beam Inclination Angle – BIA). The SEM micrographs of the four textures are reported in Figure 11.2. The texture periodicities were found through 2D FFT of the SEM micrograph (cf. section 7.2). The patterns obtained at BIA higher than 0 degrees show a double pitch. The values of the spatial pitches are reported below the SEM micrographs in Figure 11.2.

The pitches (Λ) measured through the SEM image processing closely follow the theoretical formulation [178].

$$\Lambda_{Low,High} = \frac{\epsilon \cdot \lambda}{1 \pm sin(BIA)} \tag{11.1}$$

Where λ is the laser beam wavelength and ϵ is the loss factor to account for the reduction of the spatial LIPSS pitch with respect to the laser wavelength [163]. In Figure 11.3, the experimental spatial pitches are compared to the predicted ones.

11.2.1 Pattern quality

The pattern regularity and homogeneity were evaluated through the 2D FFT for the four textures (cf. section 7.2). Table 11.3 reports the results of the consistency of the ripple pitch perpendicularly to the ripple direction (i.e. regularity) and the presence of ripple bifurcation along the ripple direction, measured through the dispersion angle γ.

It can be observed that pattern regularity decreases as the BIA increases. This can be related to the interference phenomena occurring on the surface during the short pulse irradiation durations, and the formation of irregular intermediary ripples in-between the primary periodic structures. This trend has also been confirmed by the dispersion angle increase along with the increase in BIA.

11.2.2 AFM results

The AFM analysis allowed a quantitative characterization of the inserts’ topographies; in particular, the aspect ratio of the induced rip-

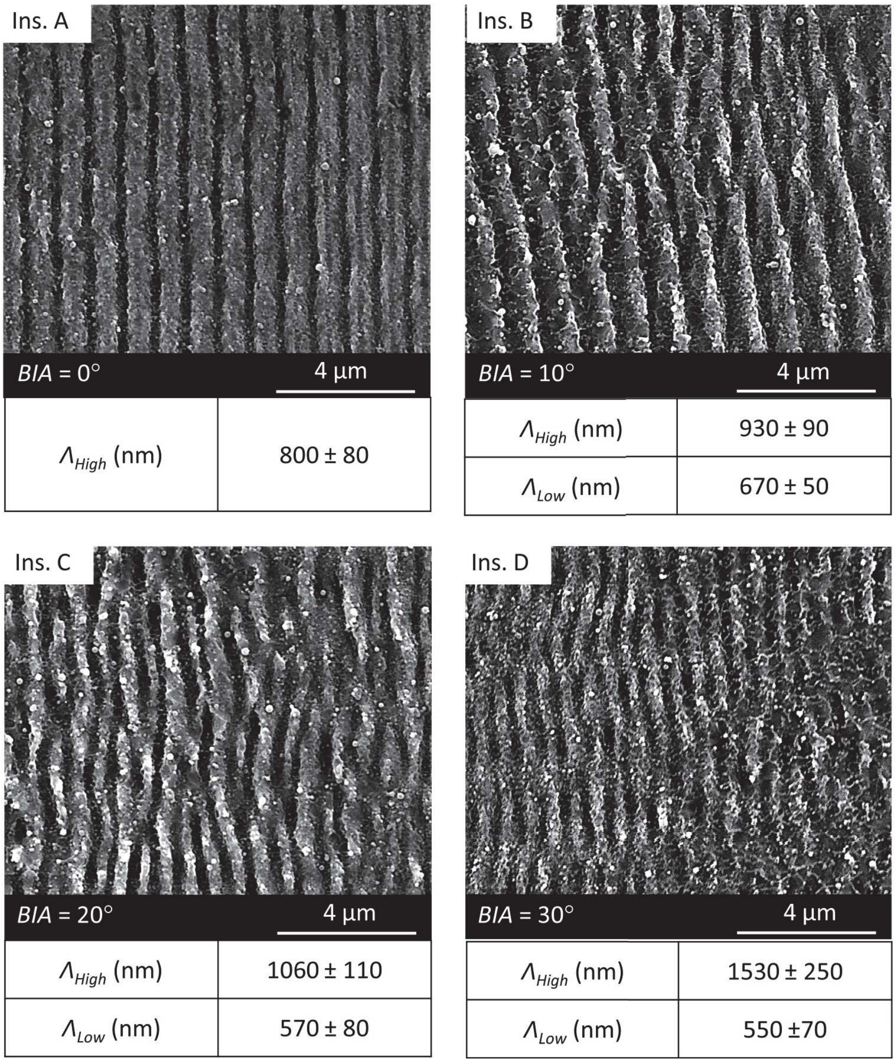

Ins. A

Λ_{High} (nm)	800 ± 80

Ins. B

Λ_{High} (nm)	930 ± 90
Λ_{Low} (nm)	670 ± 50

Ins. C

Λ_{High} (nm)	1060 ± 110
Λ_{Low} (nm)	570 ± 80

Ins. D

Λ_{High} (nm)	1530 ± 250
Λ_{Low} (nm)	550 ±70

Figure 11.2: SEM micrographs of the four mold inserts of the study. Below the pictures the figure reports the spatial pitches of the LIPSS.

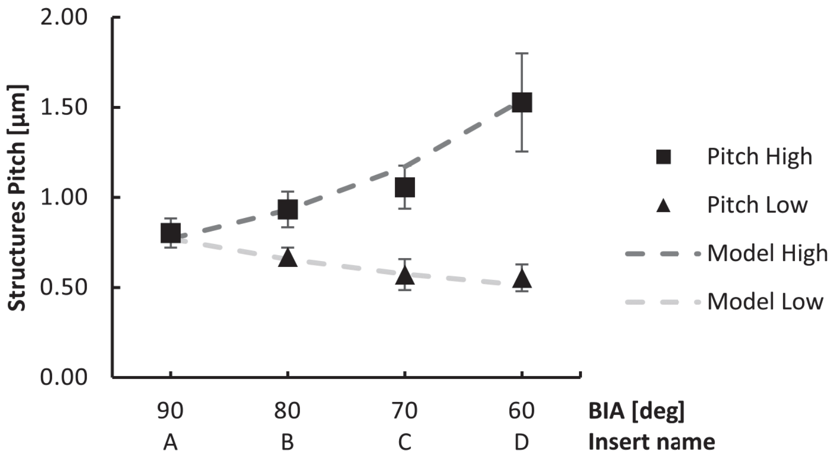

Figure 11.3: Comparison between the measured and predicted spatial pitches. The lines (i.e. model high and low) refer to the equation solutions, the dots are the experimental values.

Insert	BIA	Aspect Ratio
A	0	0.31
B	10	0.46
C	20	0.46
D	30	0.15
Unit	*deg*	

Table 11.4: Regularity and dispersion angle results for the ultrafast laser induced patterns on the four inserts of the study.

ples has been evaluated. Since the surface structures sizes are not linked to any tooling size, an areal parameter was exploited to estimate the structure's height. The Abbot-Finestone curve has been evaluated for each 10x10 μm acquired topography (cf. section 7.3).

The core height (Sk) was calculated to estimate the height of the structures and the aspect ratios. The obtained aspect ratios are reported in Table 11.4. The insert B is the one that presents a higher aspect ratio value. Aspect ratio is one of the most important parameters affecting the replication effectiveness of the mold structures. High aspect ratios lead to replication issues chapter 3. To thoughtfully characterize the micro injection molding process replication capabilities, the insert showing the higher aspect ratio (i.e. insert B) was exploited for the experiments.

11.3 REPLICATED PARTS TEXTURES

The SEM analysis of the replicated plastic parts was carried out with the aim of qualitatively assessing the replication homogeneity along

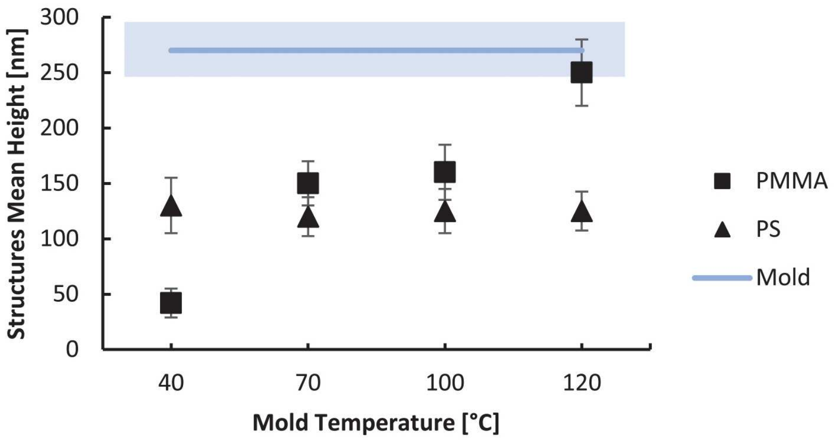

Figure 11.4: Replicated structure heights for PMMA and PS parts. The blue line and shadow area represent the mold structure height and standard deviation, respectively.

the insert surface. The SEM micrographs show the absence of significant defects and that the LIPSS are replicated homogeneously over the entire insert area.

The replicated plastic topographies were characterized on 10x10 μm areas. The obtained point clouds were processed using the Abbott-Finestone curves method to obtain the core height (Sk). Figure 11.4 shows the achieved polymer structures height with respect to the mold structures height. The plot shows the replication variation for the two polymers at increasing mold temperatures. The PMMA exhibit higher replication fidelity than the PS. Moreover, the effect of mold temperature was analyzed, indicating that, as expected, higher mold temperatures lead to higher replications.

11.3.1 Mold temperature effect

The effect of mold temperature was different for the two resins. When molding PMMA, the effect of increasing mold surface temperature was more significant than for PS. This could be related to the temperature dependency of PMMA polymer melt viscosity. In fact, as the hot melt touches the cold mold, it quickly cools down and its viscosity increases significantly. The rise in viscosity depends on the polymer/mold thermal boundary and polymer properties. Figure 11.5 compares the Newtonian viscosity for the two polymers as a function of temperature. The behavior of the two polymers intersects around 210 °C, which is below both melt temperatures. Thus, during molding, PMMA has a higher melt viscosity than PS. The replication phenomena for PMMA starts with a lower melt viscosity and, as the polymer cools down in contact with the mold, increases more rapidly

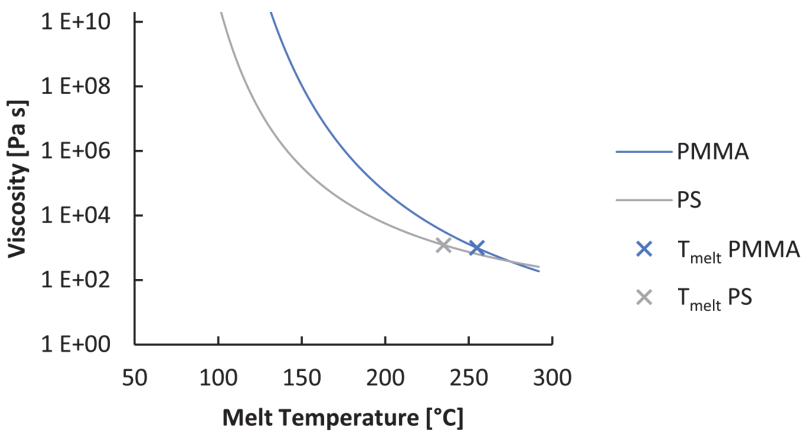

Figure 11.5: Zero shear viscosity dependance on temperature for PMMA and PS. The viscosity at the melt temperatures used in the injection molding experiments are marked.

its viscosity. This explains the smaller replication obtained when using PMMA at low mold temperatures and the higher sensitivity to an increase of mold temperature.

11.4 FUNCTIONALIZATION RESULTS

The analysis of the contact angles indicates that the wetting properties of plastic parts were affected by the replicated sub-micron structures. Due to the anisotropy of the textured surface, the drop has an ellipsoidal shape. To account for this effect, the contact angle along with two directions (cf. section 7.4) was measured. The results reported in Figure 11.6 show that the parallel angle assumed higher values than the perpendicular one, indicating that water drops spread easier along the ripples. The maximum water contact angle increase was about 20% for PMMA and 17% for PS with respect to the smooth part.

The two polymers showed different wetting properties as a function of the mold temperature. Indeed, molding PMMA at a higher temperature substantially improved the functionalization of the surface (cf. Figure 11.6 (b)). In particular, the most significant contact angle increase (i.e., 17%) was observed when increasing the temperature from 60 to 70 °C. This allowed the identification of a threshold value above which increasing the mold temperature did not yield significant variations in part functionality. Conversely, the wetting properties of the PS molded part did not indicate any substantial effect of the mold temperature in the investigated range (cf. Figure 11.6 (a)).

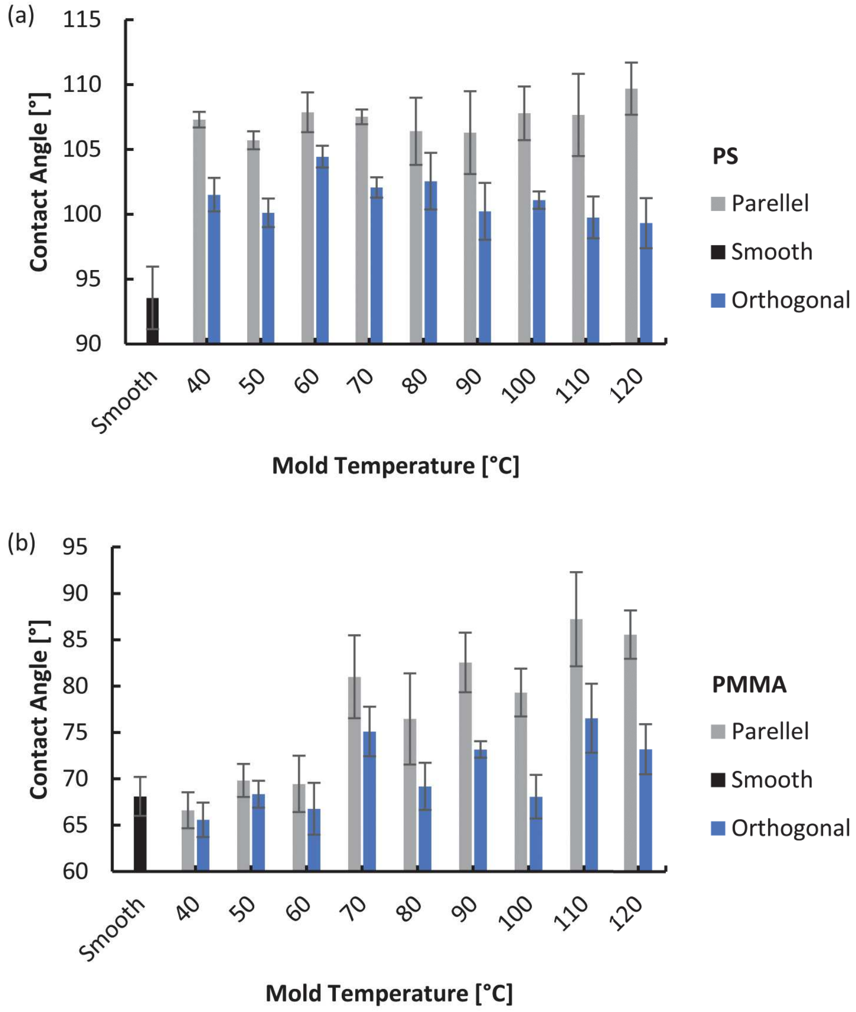

Figure 11.6: Conact angle measurements results for (a) PS and (b) PMMA. The results are repored for both the parallel and orthogonal configurations, with respect to the LIPSS direction (cf. section 7.4).

11.4.1 Replication and functionalization results comparison

The plot in Figure 11.7 compares the polymer replication grade of submicron structures and the functionalization grade. The comparison is carried out by calculating two performance evaluators.

- The replication degree expresses the ratio between the height of the structures on the polymer part and the depth of the mold structures.
- The functionalization degree describes the contact angle gain for the textured plastic parts with respect to the smooth ones as a percentage.

For parts molded with PS, the degree of functionalization and replication follows the same trend, showing similar results for all tested mold temperature values (cf. Figure 11.7 (a)). Conversely, when molding PMMA at low mold temperature, the higher melt viscosity leads to lower replication. In this condition, water droplets have similar behavior as when they were deposited onto a smooth surface. The results are de facto showing that the surface was not yet functionalized (cf. Figure 11.7 (b)). As the mold temperature increases, the replication grade increases, and the surface becomes more hydrophobic. The further increase of mold temperature beneath the glass temperature (T_g) of the polymers leads to an increase in replication accuracy that is not followed by the wetting properties of the surface.

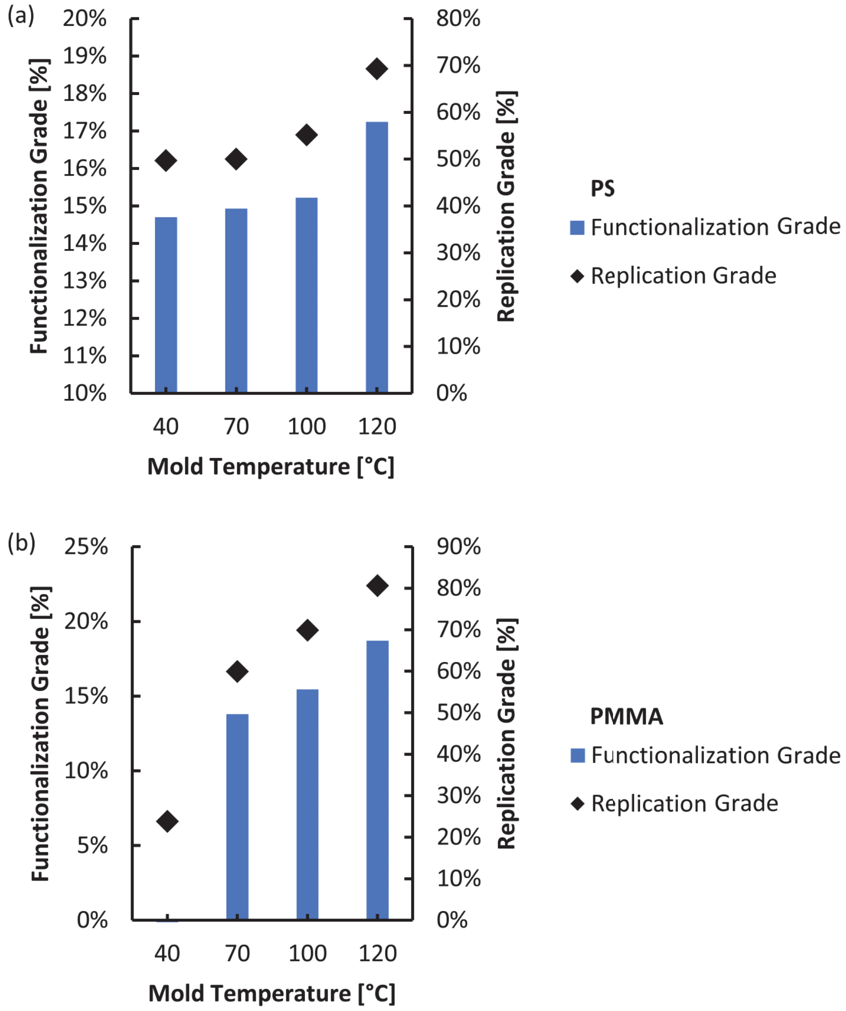

Figure 11.7: Replication and functionalization degree comparison for the two studied polymers: (a) PS and (b) PMMA.

12 MOLD PROPERTIES EFFECT ON REPLICATION

As it was experimentally demonstrated (cf. chapter 11), the replication of submicron surface structures by microinjection molding is a crucial factor in achieving advanced functionalities in mass-produced plastic products. One of the most promising sectors for the applications of functionalized devices is the medical industry. A range of synthetic bio-based polymers has been developed for the production of temporary scaffolds for regenerative medicine and tissue engineering. Among the different biocompatible and resorbable polymers, polylactic acid (PLA) and its copolymers are the most widely utilized.

Microinjection molding is one of the most cost-effective technologies for the production of submicron-structured scaffolds (cf. section 3.1). The mold structure's replication fidelity depends on polymer, process, and mold properties. Several process variation to the conventional microinjection molding process has been proposed in order to obtain the desired replication degree (cf. chapter 3).

This experimental work focuses on the study of the replication fidelity of laser-induced submicron texture onto different biopolymers. The polymer, mold, and process properties were changed throughout the experiments. The molded texture was coated to change the chemical properties of the mold. The thermal effects during replication were experimentally studied over different mold temperatures.

12.1 EXPERIMENTAL APPROACH

The study of the mold properties' effect on the replication of different biopolymers was carried out using the microinjection molding setup described in subsection 6.2.2. The experimental campaign considers variations of mold surface properties, mold temperature, and polymer properties. A general full factorial Design of the Experiment plan was designed to define the injection molding experimental tests. The two considered biopolymers are benchmarked with a commercial PP. A deep characterization of the polymer, of the morphological properties of mold and part textures, and of the wetting properties of the polymer on the Al_2O_3 coated and uncoated mold.

- Polymer characterization comprises rheological and thermal characterization through differential scanning calorimetry (DSC) and a capillary rheometer, respectively.

Factor	Units	Level 1	Level 2	Level 3	Level 4
Polymer		PP	PBAT/PLA	PLA	
Mold Temperature	°C	30	60	90	120
Mold Surface	Uncoated	Al_2O_3 coated			

Table 12.1: Mold inserts and injection molding parameters for the experimental DoE.

- Table 12.1 shows the 3 factors and 3x4x2 levels selected for the injection molding DOE plan. Ten cycles were performed before collecting the first part to ensure the stability of the process. For each molding condition, five samples were collected for topography characterization, one every five cycles.

- Beyond the uncoated and coated mold insert textures, three parts were considered for each injection molding DOE run for topography characterization.

- Polymer melts were poured onto smooth uncoated and Al_2O_3 coated inserts to characterize the wetting properties of the polymer onto the mold.

Several injection molding parameters were kept constant along with the experiments. In Table 12.2 the melt temperature, injection speed, holding pressure, packing time, and cooling time are summarized for each studied polymer. The cooling time varied between 10 s and 60 s depending on the mold temperature. Variotherm injection molding was carried out at the highest mold temperatures to allow for part ejection.

12.2 CHARACTERIZATION OF THE MOLD INSERTS

The mold inserts of the mold designed for replication studies (cf. subsection 6.2.2) were characterized by SEM and AFM. The LIPSS are homogeneous and do not present significant defects (cf. Figure 12.1). The coated insert does not exhibit any difference from the uncoated one, confirming the deposition quality of the ALD process.

From the acquired SEM micrographs, the pitch distance between consecutive ripples and the homogeneity of the pattern were evaluated. The periodicity is 930 nm, with a standard deviation of 30 nm. The regularity (R) is 82% and the dispersion angle (γ) is 6 deg.

Parameter	**Unit**	**PP**	**PLA**	**PBAT / PLA**
Melt Temperature	°C	230	220	220
Injection Speed	mm/s	150	150	150
Holding Presssure	bar	260	260	260
Packing Time / s	s	10	10	10
Cooling Time / s	s		From 10 s to 60 s	

Table 12.2: Polymer-dependent injection molding parameters for the experimental DoE.

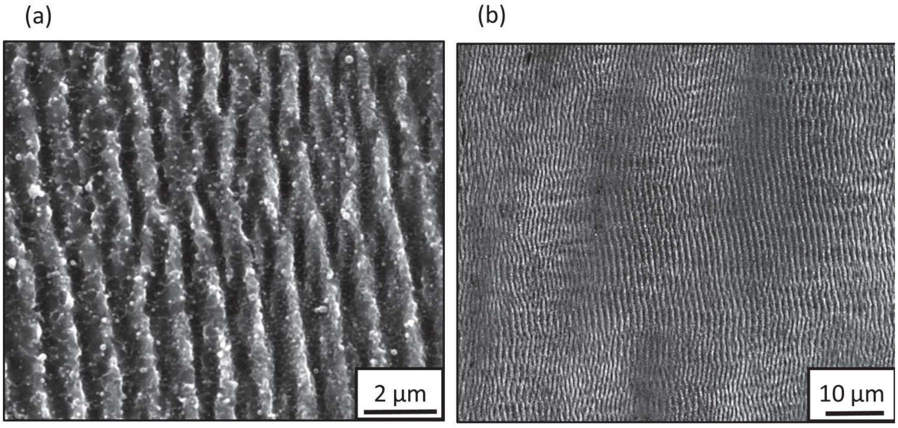

Figure 12.1: SEM micrographs of the textured surfaces on the steel mold insert at (a) 24000X and (b) 4000X.

Supplier, Grade	**Material**	**Melting Temperature**	**Crystallization Onset Temperature**	**Shear Rate Threshold**
Baseline, Pro-fax 702	Isotactic PP	169	116	150
Natureworks, NW3052D	PLA	156	118	5
Biofed, BF MV GP1025	PBAT/PLA blend	172	118	10
Unit		C	C	s^{-1}

Table 12.3: Characterized thermal properties for the selected polymers.

12.2.1 AFM characterization

Quantitative characterization of the inserts' topography was carried out through AFM measurements. In particular, the acquired point clouds were exploited to evaluate the height of the structures. The AFM measurements showed comparable dimensions on the uncoated and coated inserts. The average depth of the ripples was 250 nm, with a standard deviation of 30 nm. therefore, the LIPSS mold topographies are characterized by an aspect ratio of about 0.5.

12.3 BIOPOLYMERS CHARACTERIZATION

The thermal and rheological properties of the selected resins were deeply characterized to study the polymer properties' influence on replication.

12.3.1 DSC characterization

Table 12.3 reports the melting and crystallization temperatures for the different polymers, as observed from heat flow peaks in the DSC curves (Figure 12.2) [179]. By fitting two straight lines on the DSC curve, one before (i.e. at higher temperatures) the crystallization peak and the second after (i.e. at lower temperatures) the peak onset. The no-flow temperature (NFT), that is the temperature at which a molten polymer that is driven by a pressure gradient ceases to flow due to the increase of its viscosity, was determined at the intersection of the two lines [180].

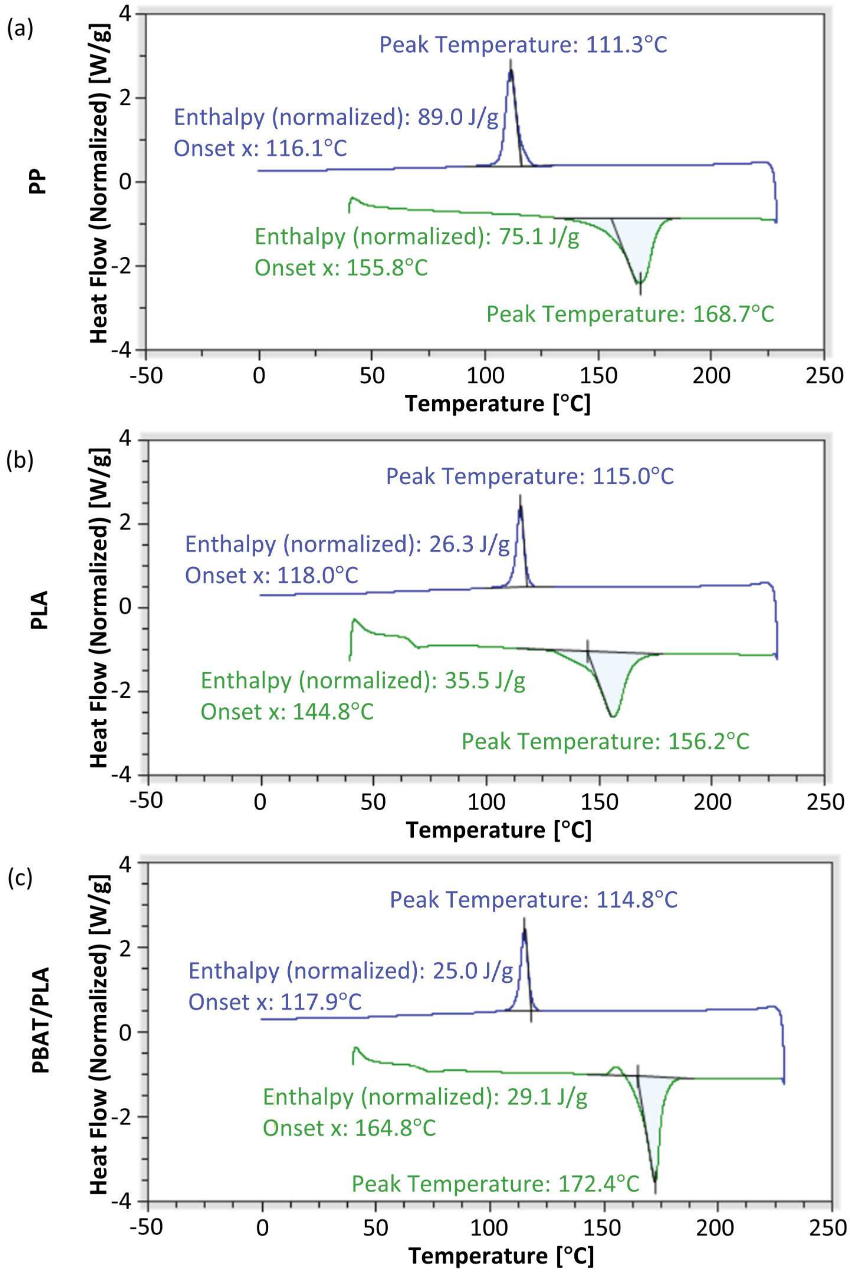

Figure 12.2: Line fitting of the melting and crystallization peak onset for (a) PP, (b) PLA, and (c) PBAT/PLA.

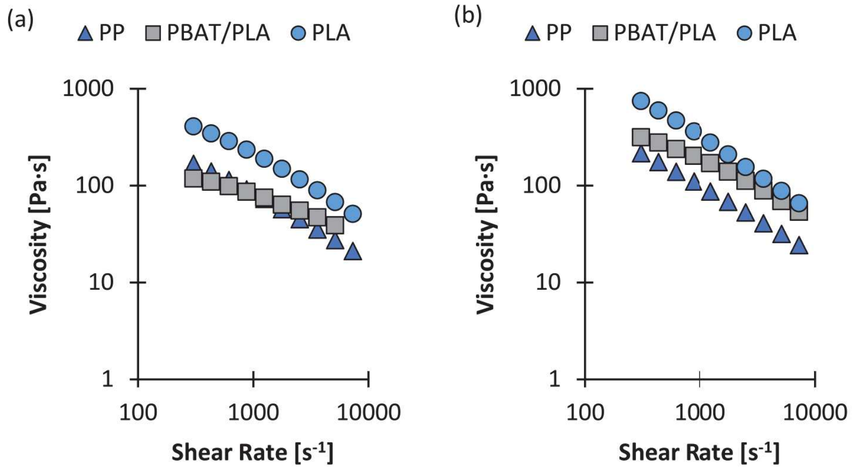

Figure 12.3: Shear-thinning behavior of the selected polymers at (a) 200°C and (b) 180°C.

12.3.2 Rheological characterization

The rheological properties of the selected resins were examined through a capillary rheometer. The effect of shear rate and the temperature was tested to obtain the experimental data to fit the Cross-WLF model subsection 6.4.1. The bio-based polymers have been engineered by the producers to be a *green* alternative to polypropylene. In consequence, it may be expected that the rheological properties do not differ much from the ones of PP. Figure 12.3 show that the biopolymer properties have similar behavior to the benchmark PP.

12.3.3 Polymer melt wetting characterization

The wetting properties for the different polymers are reported in Table 12.4. The tests were performed on smooth uncoated and Al_2O_3 coated samples subsection 6.4.3 at the injection molding melt temperature. The samples and the injection mold inserts share the same steel. The results indicate that, compared to PP, the bio-based polymers have reduced interaction with both the uncoated and coated mold surface. Moreover, the effect of the coating on the contact angle is more significant for the bio-based polymers.

12.4 INJECTION MOLDING REPLICATION RESULTS

The results of the AFM topographical characterization (cf. section 7.3) were analyzed using the analysis of variance (ANOVA). A significance level of 5% was selected, eliminating the factors and the interactions that have a lower confidence level. The DOE plan (cf. Table 12.1)

Substrate	Polymer	Contact Angle	Unit
Uncoated	PP	10	deg
	PBAT/PLA	105	deg
	PLA	90	deg
Al_2O_3	PP	11	deg
	PBAT/PLA	98	deg
	PLA	105	deg

Table 12.4: Contact angle for the polymer melts measured over the uncoated and Al_2O_3 coated mold surface. The maximum standard deviation of the measurements was smaller than 2°.

Source	Adj SS	Adj MS	F-Value	P-Value
Polymers	13011	6506	25.27	0.000
Mold Temperature	38682	12894	50.08	0.000
Polymers * Mold Temperature	6092	1015	3.94	0.002

Table 12.5: ANOVA results for the experimental DoE.

was initially evaluated considering the obtained p-values, reported in Table 12.5. The selected response variable is Sk, resulting from the Abbott-Finestone curve associated with the surface topography.

The mold temperature, the polymer type, and their interaction are significant factors, while the mold surface properties and their interactions have been eliminated. Therefore, the effect of the mold coating on replication is confounded. In Figure 12.4 the main effects plot for the polymer type and the mold temperature are proposed. The effect of the mold temperature is obvious. The PBAT/PLA blend shows a higher overall replication height with respect to the other two resins.

The interaction plot showed in Figure 12.5 further clarifies how the PBAT/PLA blend outperforms the other two resins in replicating the mold structures. It is interesting to note that at 120 °C mold temperature, the three resins reach substantially the same level of replication. At this temperature, the polymers essentially reach the complete replication of the mold micro and nanostructures.

The completeness of discussion, on Figure 12.6 the whole experimental Sk results are proposed. The effects of the two significant factors are clearly visible from the plot. As expected from the statistical analysis, the comparison of the results obtained with and without the coating does not reveal any interesting trend. Again, the three resins achieve the same Sk height at the higher mold temperature.

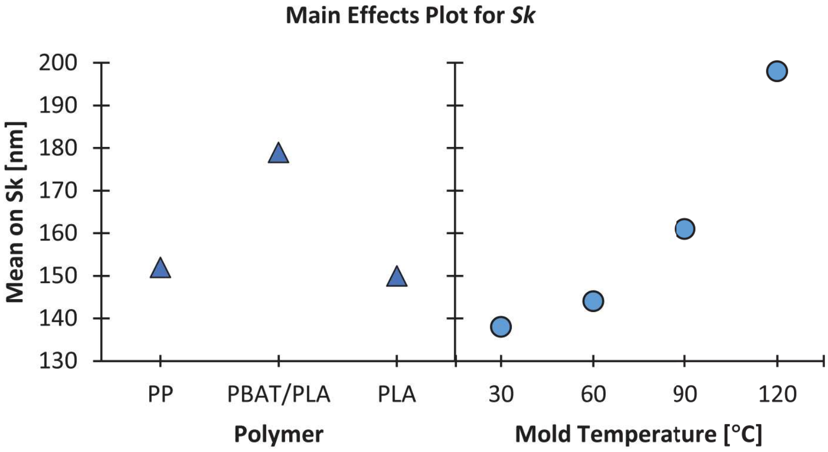

Figure 12.4: Main effect plots for the DOE plan considering Sk as the response variable.

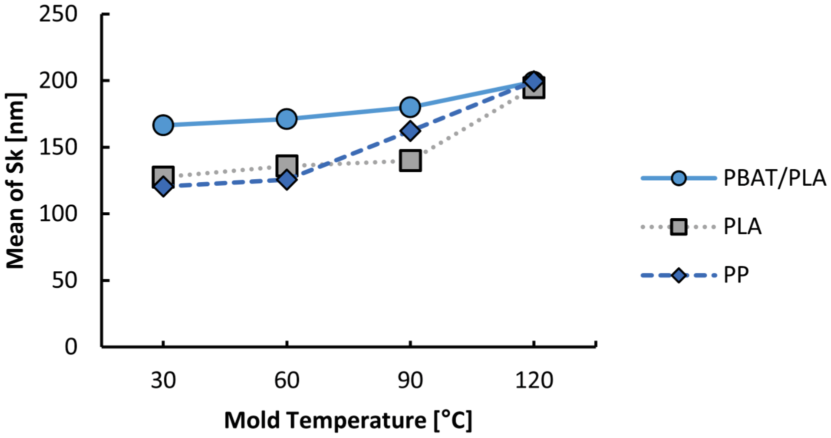

Figure 12.5: Interaction plot for the mold temperature and resin type factors.

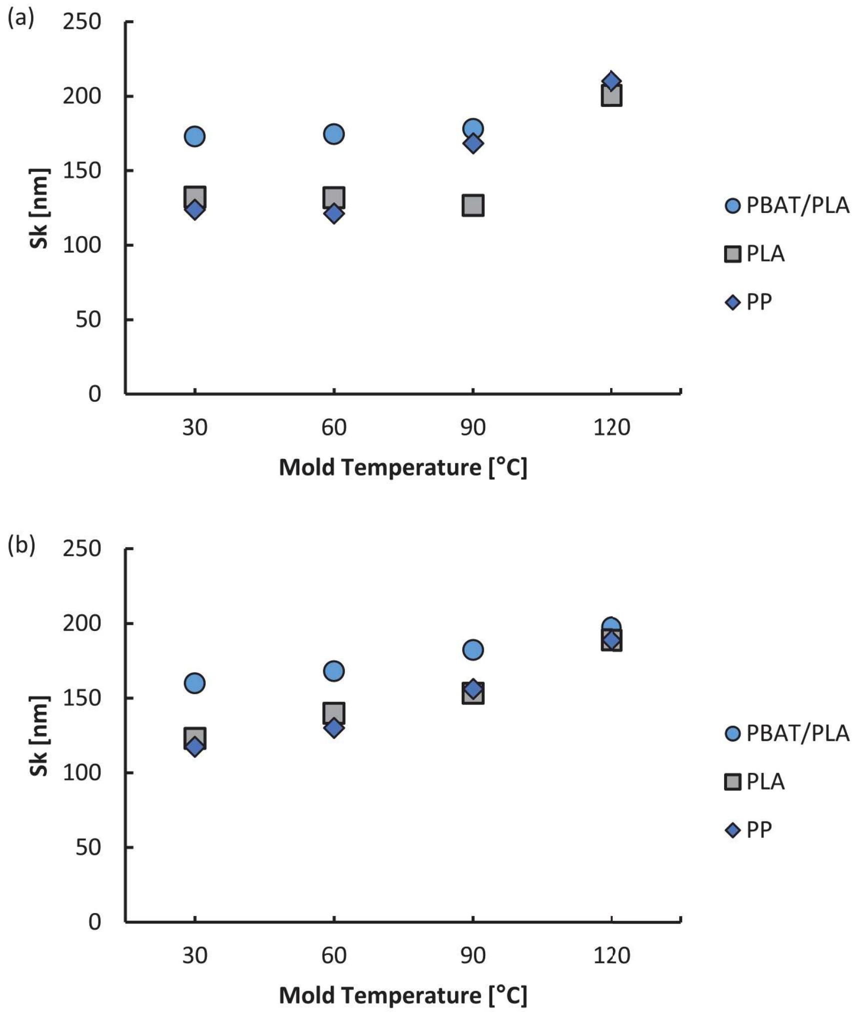

Figure 12.6: Experimental results of the biopolymers replication at the selected mold temperatures for the (a) uncoated and (b) Al_2O_3 coated texture. The structure height is evaluated as the core height Sk.

Part VI

MODELING

13 MODELING OF THE FILLING FLOW

In the micro and thin-wall injection molding process, the polymer flow is inherently transient, and it is characterized by a free surface moving through a narrow cavity. The filling melt experiences a deeply non-isothermal shearing flow. At the polymer/mold interface, the temperature profile is characterized by a marked discontinuity due to the very different temperature values. The thermal phenomena between the cold mold and the hot polymer melt are complex and depend on mold material properties and process characteristics.

Injection molding simulation models use the Heat Transfer Coefficient (HTC – cf. subsection 2.1.2) to model this discontinuity and predict the heat transfer rate. The reliability of the temperature and pressure profiles in the cavity relies on the accuracy of this value. Typically, in simulation environments, the HTC value ranges between 2000 and 5000 W/(m^2°C).

The accurate description of the thermal phenomena occurring at the mold wall and of the effects of ceramic mold coatings can open new possibilities, improving the design phase, the performance of the mold in its operating life, and the performance of the produced plastic (e.g. reducing the material intensity of the part cf. chapter 2).

13.1 MODELING APPROACH

The objective of the work is to get an accurate filling flow description through the identification of a value of HTC that fits the numerical model to the experimental values. The thermal modeling of the polymer mold interface will be carried out in uncoated and coated conditions. The obtained HTC value can be used to get more accurate predictions of the mold coating effect on applications-related part geometries. Indeed, the experimental results collected using a simple cavity geometry can be translated through simulation onto more complex geometries. The case study considered in this work is a filter case for water treatment.

The effect of the mold coating is captured through an inverse analysis to numerically estimate the thickness reduction achievable for the case study. The experimental data exploited to calibrate the numerical model are described in chapter 9. Autodesk Moldflow, a commercial simulation software, was exploited for numerical injection molding simulations. The modeling approach followed a series of numeric and optimization steps.

- Preliminary numerical simulations were carried out to evaluate the range of HTC that allowed the modeling of the range of the experimentally collected pressure drops. All the process parameters, geometry, and material properties, and characteristics were kept constant, with the only exemptions of the HTC value and the injection flow rate.

- To reduce the computational time, an Artificial Neural Network (ANN) was created to replace the numerical model (direct model). The inputs for the ANN were created by performing numerical simulations changing the HTC with small steps (i.e. 100 W/(m^2°C)). The same procedure was carried out for the different injection velocities involved in the experimental study.

- The training of the ANN was carried out using the Levenberg-Marquardt backpropagation for all the simulation runs performed with the direct numerical model.

- The ANN was then exploited to reproduce the results of the direct simulation model locally. The inverse analysis was performed using the ANN to continuously changing the HTC input and quickly evaluating the error between the experimental and calculated pressure drop values. A genetic optimization algorithm (MOGA-II) was exploited to automatically minimize the pressure error between the experimental pressure values and the numerical predictions over the six considered injection velocities.

- The optimization algorithm outputs are uncoated and coated HTC values.

- The case study part was designed with a nominal wall thickness of 4 mm (cf. Figure 13.1). Numerical simulations are carried out to individuate the best set of process parameters for molding the plastic filter with PET. The aim of the optimization was to get the lowest injection pressure to completely fill the whole part.

- The last step consists of estimating the thickness reduction allowed by the mold coating. The simulations were performed with decreasing part thickness on the coated and uncoated cases. For each geometry, the optimization of the process parameters was carried out. The thickness reduction is ultimately evaluated as the difference between the coated and uncoated simulations showing the same maximum injection pressure.

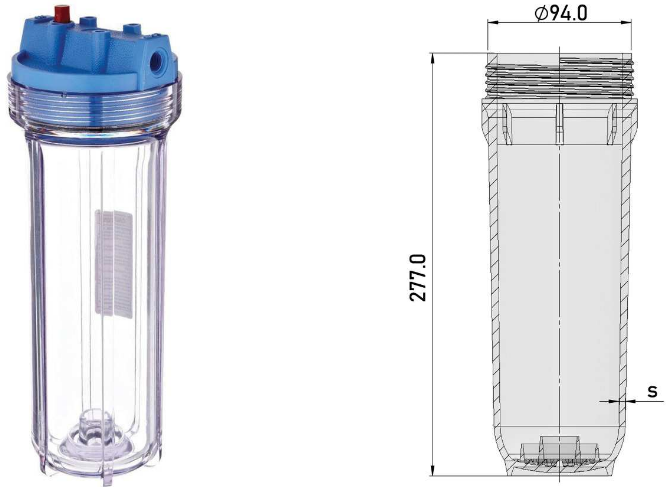

Figure 13.1: PET filter used as a case study for the numerical estimation of thickness reduction yielded by the mold coating.

13.2 CALIBRATION OF THE HEAT TRANSFER

Injection molding simulations were performed using a 3D mesh to discretize the part (cf. Figure 13.2). The elements have a global edge length of 0.8 mm and an average aspect ratio of 4.65, resulting in a total of about 35000 tetrahedral elements. The simulations were run using the polymer flow rate to control filling.

The simulation results were compared to the experimental ones obtaining the pressure results predicted by the simulation at the node that has the same location as the pressure sensor in the mold cavity (cf. Figure 13.2). The pressure drop has been individuated as the maximum pressure sensed by the node during cavity filling.

The experimental campaign and the model results are compared in Figure 13.3. The model was calibrated with the DLC coating since it yielded the highest pressure drop reduction with respect to the uncoated solution. The resulting HTC values are 5600 W/(m^2°C) and 1400 W/(m^2°C) for the uncoated and coated surfaces, respectively.

13.3 THICKNESS REDUCTION MODELING

The effect of the change in HTC on the plastic part design has been evaluated using an application-related plastic part. The part is characterized by a relatively long flow length (cf. Figure 13.1). The starting design is currently produced and has a nominal wall thickness of 4 mm. The thickness value has been selected to guarantee a proper flow until the very end of fill, which is located at about 314 mm from the injection location. The end of fill corresponds with the tread, which has to be accurately molded.

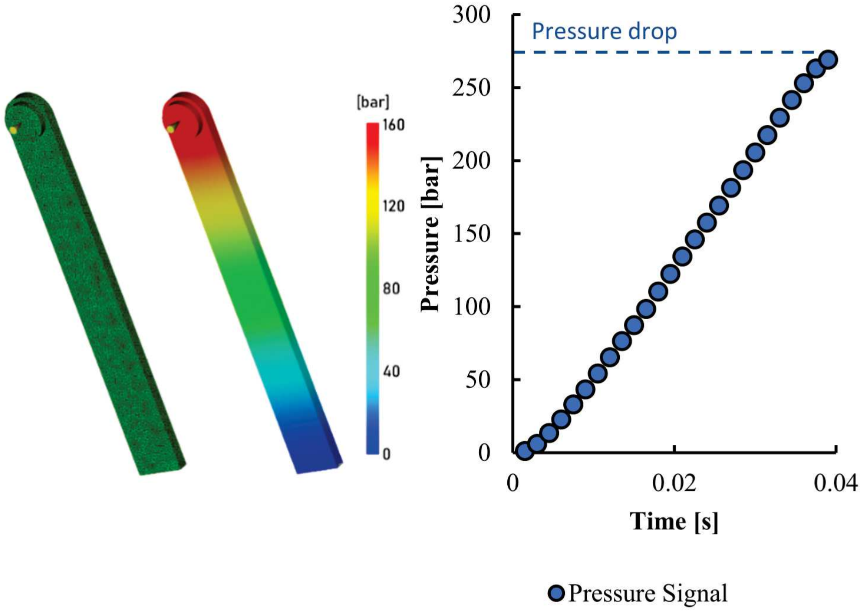

Figure 13.2: Form left to right: cavity mesh, polymer pressure at the end of fill, and pressure evolution within filling measured at the pressure sensor location.

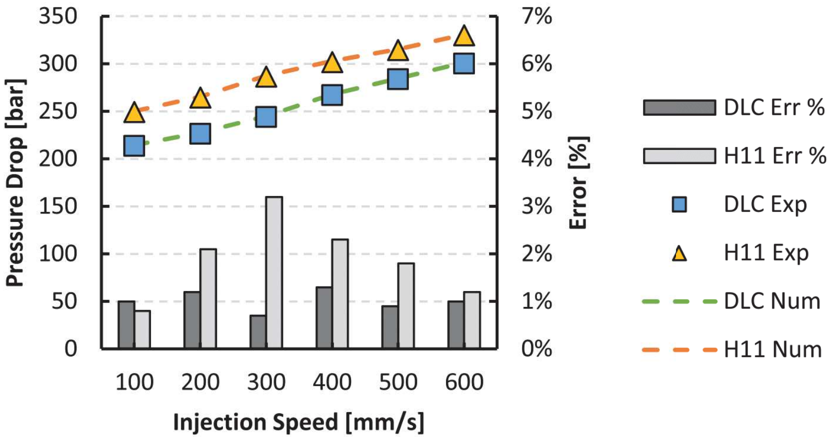

Figure 13.3: Results at 1.9 mm thickness and comparison with the numerical model results. The errors against the experimental data are reported as gray bars.

The HTC values calibrated using the ANN and optimization algorithm were exploited to run the Moldflow simulations and reproduced the polymer flow inside the case study cavity. The part geometry was modeled in the numeric environment using a 3D mesh, with an edge length of 2 mm and a maximum aspect ratio of 6.3 (cf. Figure 13.4 (a)). To study the effects of the coating on the thickness reduction, parts with thickness varying from the actual 4 mm to 3 mm were designed. The intermediate steps for the part designs were set to 0.2 mm, for a total of 6 different designs. All the other geometrical characteristics were kept constant.

The processing conditions for the numerical model were kept constant through all the mold designs and the mold surface forms. The only exception is the filling flow rate, which has been exploited as the leading parameter for the filling phase. The flow rates were optimized for each filter geometry and molding condition. This allows for the effective comparison of the performances of the coating at the best, and so desirable, processing conditions.

The output value of the numerical simulation has been individuated as the maximum injection pressure, at the gate location. Figure 13.4 (b) and (c) clearly show the effect of the mold coating onto the cavity pressure distribution. The pressure and injection flow rates optimized for each part thickness and mold surface are reported in Table 13.1. The effect of the mold coating has been interpreted as the delaying of the skin layer formation. In Figure 13.6 the typical dependence of the injection pressure on the flow rate is plotted. The optimal flow rate is found in the correspondence of the minimum injection pressure. At lower flow rates, the injection pressure rises as a result of the flow section constriction due to skin formation. At flow rates higher than the optimal one, the injection pressure rises as a result of the larger amount of shear experienced by the melt. In Figure 13.5 the contributions of the skin formation (i.e. flow section reduction) and of the shear are plotted. The contribution of the shear has a quasi-hyperbolic behavior against the flow rate. The shear contribution is here represented with a linear behavior. The dashed lines represent the total injection pressure needed to fill the cavity, which is the sum of the two contributions. By delaying the skin formation, the coating delays the skin formation, shifting leftward the thermal curve. Therefore, the dashed line minimum shifts leftward and downward. The scheme is presented assuming that the shear curve is the same, which corresponds to the fact that the cavity geometry is the same. The presented scheme illustrates the effects that have arisen from the results in Table 13.1. The optimal injection pressures and flow rates for the coated solution always show lower values for both variables.

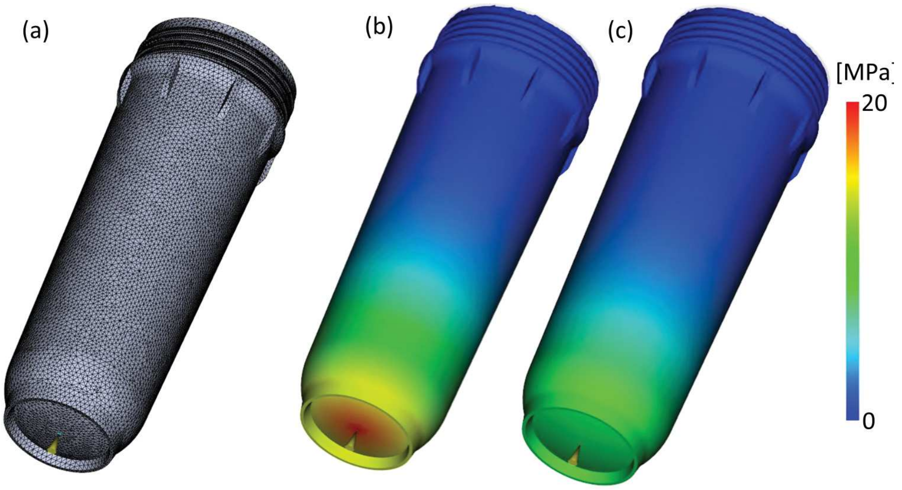

Figure 13.4: Mesh for the filter cavity at 4 mm nominal wall thickness (a) and gate placement and pressure distribution at the end of filling for the 4 mm thick uncoated (b) and coated (c) mold.

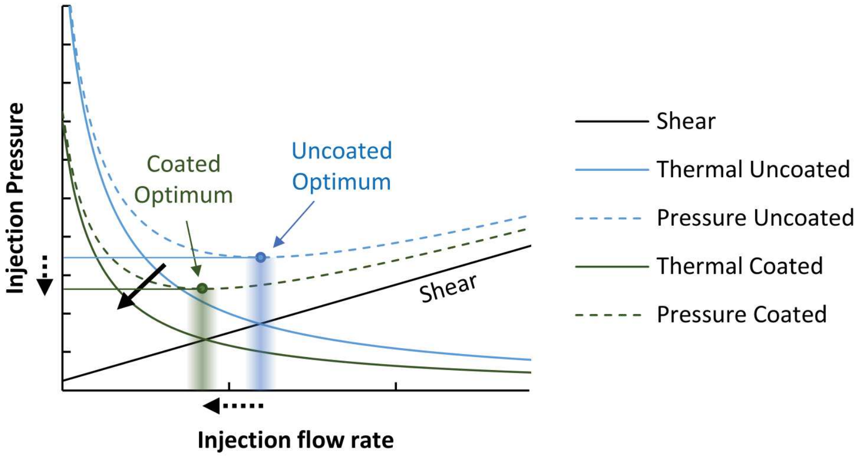

Figure 13.5: Scheme representing the thermal and shear contributions to the injection pressure for an injection mold cavity. The scheme for the uncoated solution is plotted in blue, the one for the coated solution in in green.

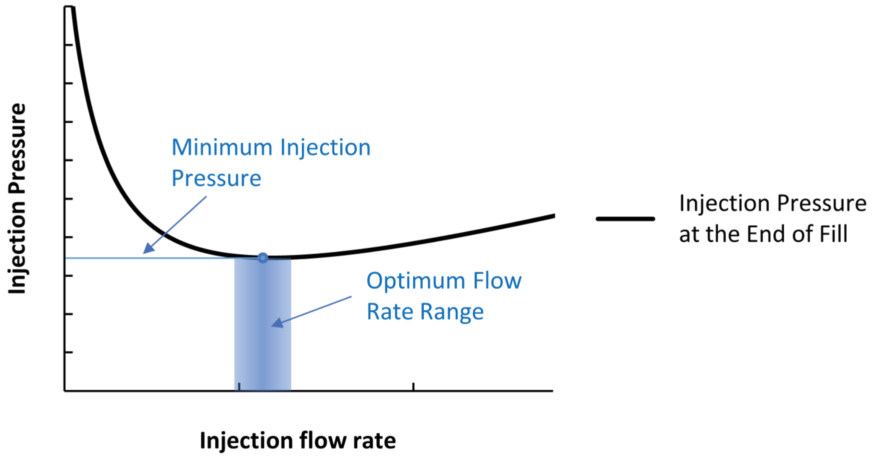

Figure 13.6: Typical dependence of the injection pressure on the flow rate and selection of the optimal rate value.

	Uncoated		DLC	
Part thickness *mm*	Optimal flow rate cm^3/s	Injection pressure *MPa*	Optimal flow rate cm^3/s	Injection pressure *MPa*
4.0	153.3	20.1	120.8	11.5
3.8	175.6	25.6	124.4	14.3
3.6	193.9	32.8	129.5	18.2
3.4	203.0	42.0	138.6	23.7
3.2	214.4	51.8	151.0	31.3
3.0	230.8	61.6	157.1	40.5

Table 13.1: Optimized injection pressure and flow rates as a function of the part nominal thickness and the mold surface conditions.

Parameter	Uncoated	Coated	Unit
a	19400	18100	MPa
b	-1.14	-1.27	mm^{-1}
R^2	0.995	0.998	

Table 13.2: Data-fitted coefficient values for the unocated and coated mold setup. The R^2 values are reported to assess the goodness of fit.

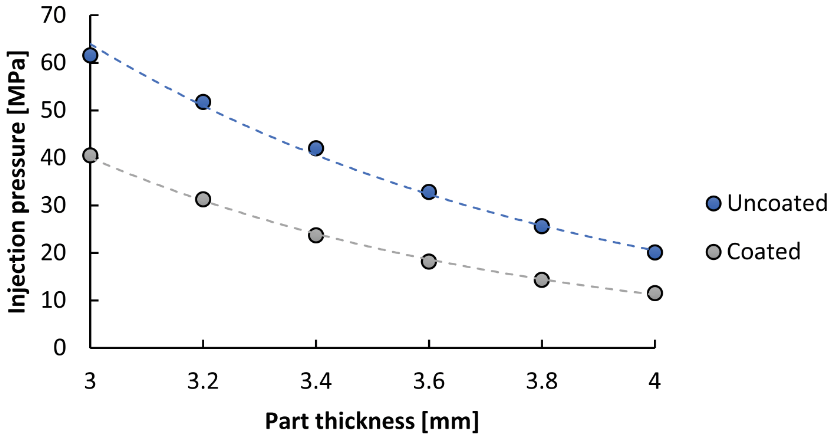

Figure 13.7: Injection pressure for the different considered part geometries and exponential data fitting (i.e. dashed lines) of the coated and uncoated trends.

13.3.1 Reduced thickness design

Figure 13.7 compares the numerical results for the different part geometries in terms of injection pressure. The trends for the uncoated and coated surfaces have been fitted using an exponential equation. The best fits follow the equation:

$$P_{inj} = a \cdot e^{b \cdot t} \tag{13.1}$$

Where t is the part nominal thickness and the a and b values are data fitted coefficient and have the scores presented in Table 13.2. The thickness of the coated-processed part can be found by inverting and solving the equation relative to the coated mold using the injection pressure required for the original 4 mm thick design. Hence, the potential part thickness reduction yielded by the presence of the mold coating is 0.46 mm. Such thickness reduction corresponds to reducing by 8% the material consumption.

14 MODELING OF REPLICATION

Microinjection molding is one of the most cost-effective processes for the replication of microstructures on plastic parts (cf. chapter 3). The surface structure's replication capabilities depend on a wide range of factors that belong to the polymer properties, processing conditions, and mold characteristics. When considering micro- and nano-scale polymer replication, the flow of the melt is characterized by the onset of scaling issues that are still hindering the modeling efforts. Commercial software can not reach sufficiently thin mesh sizes to model the polymer flow into mold microstructures. In the literature, analytical models have been developed to predict the flow behavior and the replication quality in microinjection molding (cf. section 3.4).

Overall, the proposed models well predict the polymer flow behavior but also present some limitations for the analysis of submicron-scale systems. Current polymer micro-scale replication models lack accuracy, and they do not provide a comprehensive description of polymer/mold interface interactions. This chapter describes the development of a comprehensive multiscale model for the prediction of the replication of mold surface submicron structures, which can be integrated into commercial software to implement new tools for the assessment of the effectiveness of replication for microstructures. The model has been validated using the experimental results presented in chapter 12.

14.1 MODELING APPROACH

The multi-scale model approaches the technological phenomena dividing the macro-flow to the micro-flow. The macro model is exploited to model the polymer flow in the cavity until it approaches the entrance of the microfeatures. Then, the novel analytical model predicts the polymer flow inside the microcavities. The multiscale approach allows the separation of the phenomena that control the filling of the mold cavity and the submicron features, overcoming the limitations of the commercial numerical model.

- The macro flow in the mold cavity is modeled through a numerical model. Commercial software (Moldex3D) is used to analyze the macro polymer behavior. The simulation results are exploited to determine the boundary conditions for the filling of the submicron structures. Hence, the macro numerical model serves as an input data generator for the micro model. In particular, the temperature, pressure, and velocity field data of the polymer in the region close to the mold surface have been extracted as a function of time from the simulation results. Hence, not only the state of the polymer next to the mold surface has been considered, but also the time-dependent behavior of the thermal and kinematic properties.

- A novel analytical micro model for the study of the micro-replication is developed in this work. The novel analytical model studies the replication of the mold micro-topography considering geometrical parameters, polymer rheology, and thermal behavior, and mold surface energy. The governing physical phenomenon exploited for the replication modeling is the compression of the air trapped inside the microcavities. The here proposed analytical model newly considers the air trapped in the microcavities and its behavior during polymer filling. The time-dependent inputs from the numerical model are processed to describe the cinematic of the entering flow inside the microcavities.

14.1.1 Numerical macro model

The part geometry is imported and discretized using a three-dimensional Boundary Layer Mesh (BLM) approach (cf. Figure 14.1). The BLM approach allows for the seeding of a high density of nodes close to the mold surface, increasing the accuracy of the numerical prediction at the polymer/mold interface, which is the region of the part responsible for surface texture replication. Hence, the vast majority of the nodes are placed in the interest regions, and a low node density is present in the middle of the part, diminishing the computational time. The boundary regions were discretized with ten layers of prisms, while the core was filled using tetrahedral elements. A global seeding length of 0.3 mm was used to discretize the surface, thus creating about 250,000 elements.

The rheological and thermal properties of the polymers were characterized according to the capillary and DSC experiments reported in section 12.3. The material properties were implemented using the Cross-WLF model coefficients fitted on the experimental testing data. A material database was created for each one of the selected polymers.

The process parameters in the numerical model were set in agreement with the experimental tests (cf. section 12.1). The injection speed defines the filling control, and the pressure at the injection location establishes the velocity/pressure switchover. The mold assembly was redesigned in the simulation environment to closely reflect the real geometries. Particular attention was posed to the heating and cooling system design. By using the *transient cooling* module of

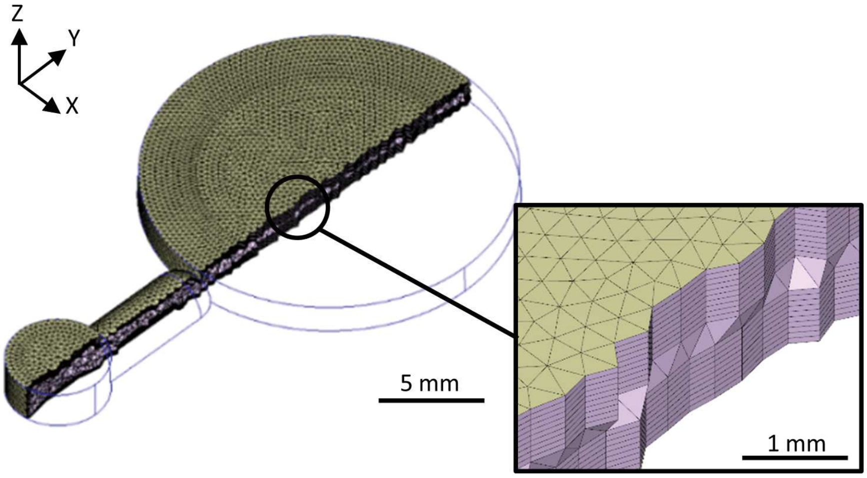

Figure 14.1: Cavity mesh for the part designed to study the replication. At the bottom right of the figure, an example of a BLM mesh with 10 surface layers is reported.

the code, it was possible to model the rapid heat cycle molding process for the high mold temperatures, allowing the match to the real processing conditions.

The numerical simulation was analyzed to determine the boundary conditions for the micro-scale analytical model. The results were probed at three different locations (cf. Figure 14.2) defined to match the position at which the topographies were acquired using AFM, as described in section 7.3. For each simulation run, it was considered the pressure of the polymer in the cavity (p_c) as a function of location and time, the temperature of the polymer in contact with the mold (T_c), and the polymer velocity along a direction orthogonal to the cavity surface (v_z). The data were evaluated as a function of time, using 25 time steps for both the filling and packing phases. Overall, more than 9,000 values were recorded for each simulation run.

14.1.2 Micro topography description

The quantitative analysis of the AFM acquired point clouds was carried out from the Abbott-Firestone curves according to standard DS/EN ISO 25178-2 [177]. For each topography, obtained either from the mold surface of the replicated part texture, the core surface roughness Sk was determined from the linear representation of the material ratio curve that describes the increase of the material portion of the surface with increasing roughness depth (cf. section 12.4).

The relatively high replication height reached during the experimental campaign necessitates an accurate description of the mold texture at the very bottom of the valleys. Hence, the description of the core height using the Sk value has been updated to better model the

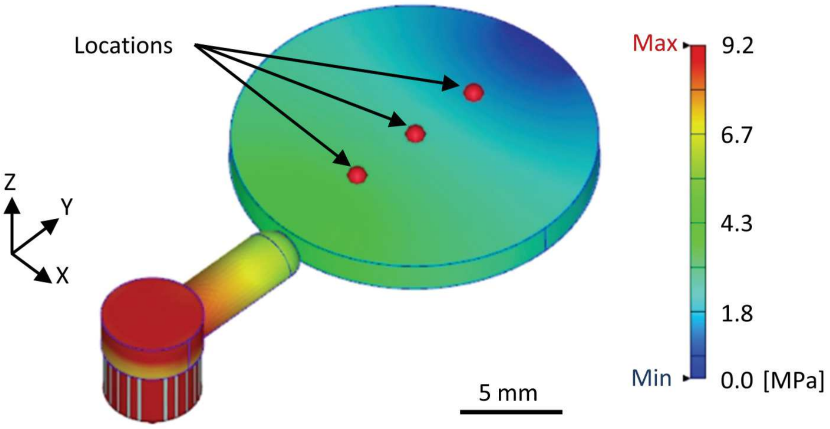

Figure 14.2: Cavity pressure results at the end of fill and locations for the probes along the cavity.

behavior of the topography at the very bottom of the valley. Figure 14.3 shows an example of the Abbott-Firestone curve derived from an AFM data point cloud. The dashed black curve resulted from the AFM measurements is processed following the standard descriptions and the *Equivalent Straight Curve* is derived. The *Equivalent Straight Curve* defines the value of the core height (*Sk*). The projection of the two tails of the *Equivalent Straight Curve* into the Abbott-Finestone curve individuate the points marked as 1 and 2 in the figure. The points define the (Smc1; Smr1) and the (Smr2; Smc2) coordinates. The line that intersects those two points has been selected as the line representing the mold topography and it has been named *Equivalent Height Curve*. The equation describing the *Equivalent Height Curve* is

$$Smc = \frac{Smc2 - Smc1}{Smr2 - Smr1} \cdot Smr + Smc2 \tag{14.1}$$

Where Smc and Smr are the dependent and independent variables for the line. The height (H) is individuated as the total range of the *Equivalent Height Curve*.

For modeling purposes, the description of the surface topography has been further simplified. The *Equivalent Height Curve* has been reduced at a one-parameter equation.

$$Smc = H \cdot Smr \tag{14.2}$$

Where H is

$$H = \frac{Smc1 - Smc2}{Smr2 - Smr1} \tag{14.3}$$

The simplified version of the *Equivalent Height Curve* has the advantage of being easy to use in the analytical model and preserves the

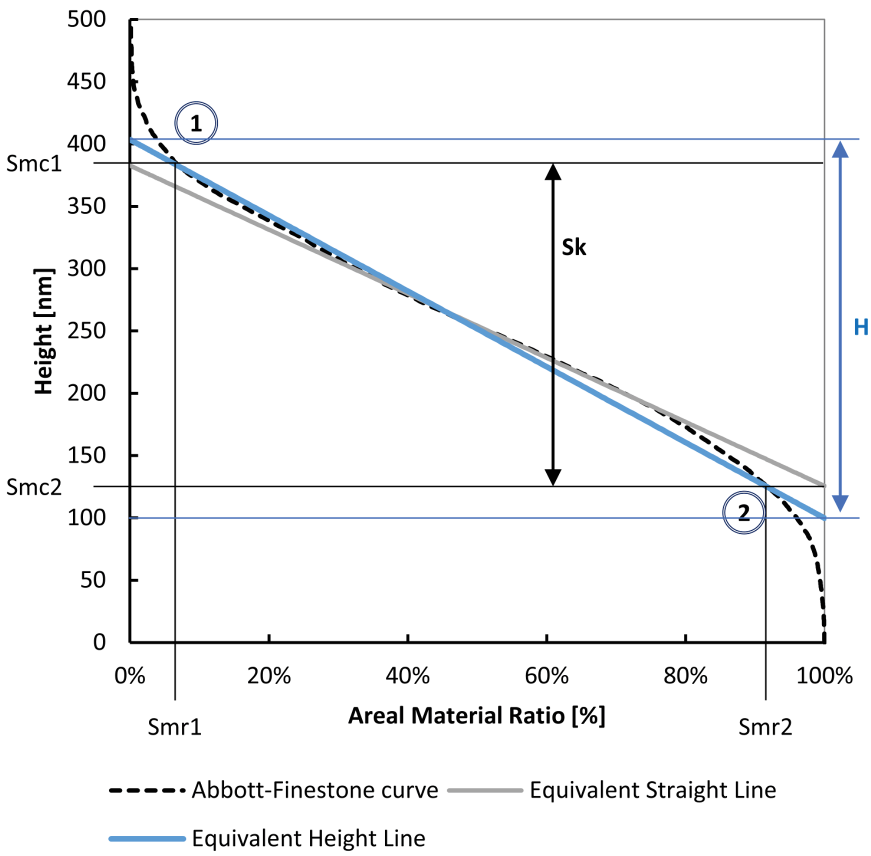

Figure 14.3: Schematics for the derivation of the *Equivalent Straight Curve* and the *Equivalent Height Curve*. The extrapolation of Sk and H are shown on the plot.

same topographical information of the *Equivalent Height Curve*. In the model, the output parameter H takes different names accordingly to the surface is refers. The height of the mold structures is called H_m, and the height of the replicated polymer structures is called H_p.

The pitch of the surface structures (w) has been characterized through the 2D fast Fourier transform of the SEM micrograph of the micropattern (cf. section 7.2). As it can be expected, no difference in pitch was found between the mold and replicated pitches, thus a single w value is considered in the model.

14.1.3 Polymer thermal properties description

The polymer thermal and rheological properties were experimentally characterized (cf. section 12.3). The deep properties study allows for the feeding of both the numerical and the analytical part of the multi-scale model.

- The DSC results were exploited to characterize the No-Flow Temperature (NFT), which has been implemented both in the numerical and analytical model.
- The rheological characterization served to the fitting of the Cross-WLF model, which describes both the macro and the micro polymer flow.
- The wetting properties study has been carried out to feed the analytical model. According to the literature, the surface wetting interactions have been considered only on the microscale.

14.1.3.1 Sensitivity of the melt viscosity to temperature

The replication of micro and nanostructured surfaces by microinjection molding is characterized by the high-cooling rates, which hinders replication and limits the capabilities of the process. Indeed, as the polymer melt touches the cold mold, it starts cooling down until it reaches the NFT. The consistent increase in viscosity at the NFT triggers hesitation phenomena in the microcavities.

Current commercial numerical models for injection molding simulation use the NFT to define the thickness of the skin layer, overcoming the inaccuracies of the rheological models and data in the low-temperature regions [181]. Approaching the NFT, the increase of the viscosity can be modeled by the derivation of the Cross-WLF model, as suggested by Mannella et al. [182]. The derivative of the rheological model represents the sensitivity of melt viscosity to temperature for increasing shear rates. During the filling flow, as the shear rate decreases and the melt cools down, the viscosity increase becomes more significant until the polymer cannot flow any further.

The DSC results were considered in relation to the experimentally fitted Cross-WLF model to study the resins' viscosity sensitivity to temperature. The derivation of the viscosity with respect to temperature was carried out. An example of the resulting curves is presented in Figure 14.4. The derivatives are plotted at different temperatures: the lighter the color, the higher the temperature (in °C). The curves show a twist region, in which the temperature influence of the viscosity sensitivity changes. At shear rates above the twist region, the increase in flow temperature leads to lower viscosity sensitivity to temperature. Contrarily, below the twist region, the flow temperature has the opposite effect.

Figure 14.5 shows the derivative of viscosity to temperature as a function of the shear rate, as calculated at the NFT. The plot shows, for each resin, the sensitivity of polymer viscosity to temperature changes ($d\eta/dT$) for decreasing shear rate. The trend is flat for the high shear rate region, indicating constant sensitivity of viscosity to temperature changes. In this region, the shear-thinning behavior prevails, and the polymer melt is not freezing. As the shear rate de-

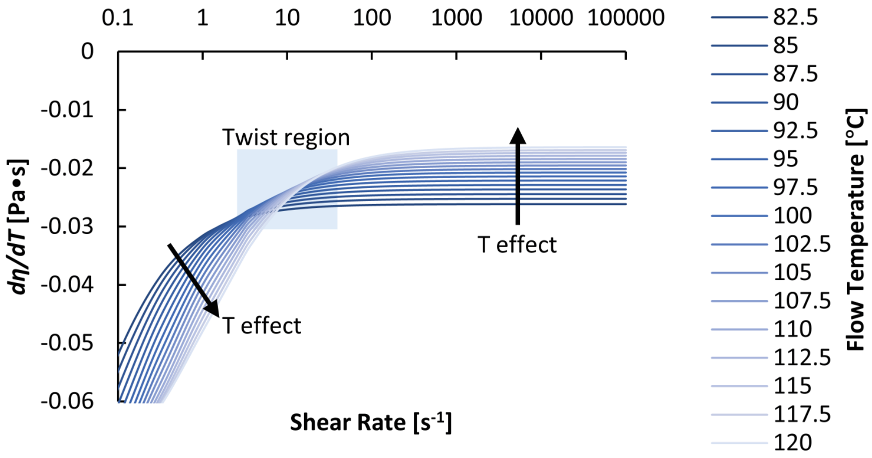

Figure 14.4: Example of derivatives of the viscosity (modeled through the Cross-WLF model) to temperature. The derivatives are plotted as a function of the shear rate and of the flow temperature. Lighter curve color matches with higher flow temperature. The twist region and the different flow temperature effect are highlighted in the plot.

Material	Shear Rate Threshold
Isotactic PP	150
PLA	5
PBAT/PLA blend	10
Unit	s^{-1}

Table 14.1: Shear rate thresholds for the selected resins.

creases, the melt viscosity gets increasingly sensitive to temperature changes, thus cooling has a significant effect. The threshold value for the shear rate ($\dot{\gamma}_t$) was identified for each polymer as the point of the curves at which the viscosity derivative starts decreasing. The threshold values determined for each polymer are reported in Table 14.1.

14.1.4 Analytical model description

During molding, air is trapped in the mold topography by the advancing flow of polymer melt, and an equilibrium is established between the compressed air pressure and that of the replicating polymer. The replicated height of submicron features on a molded plastic part (H_p) is evaluated by balancing the pressure of the trapped air and the polymer pressure (cf. Figure 14.6).

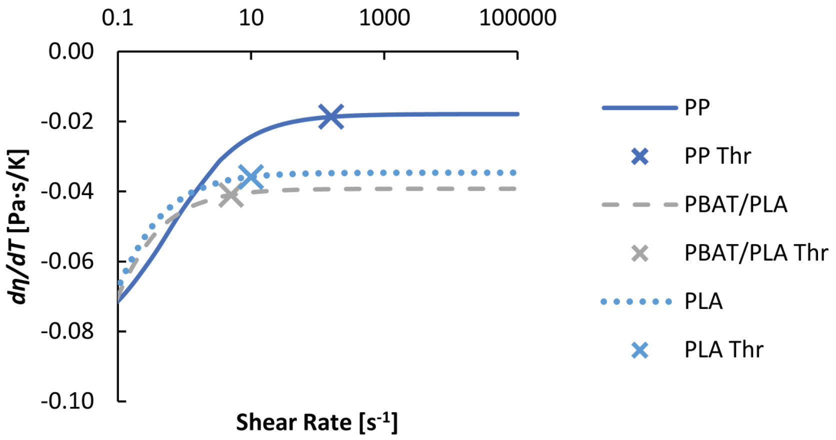

Figure 14.5: Sensitivity of viscosity to temperature changes for the three selected resins plotted at the NFT. The shear rate thresholds for each polymer is highlighted along each curve.

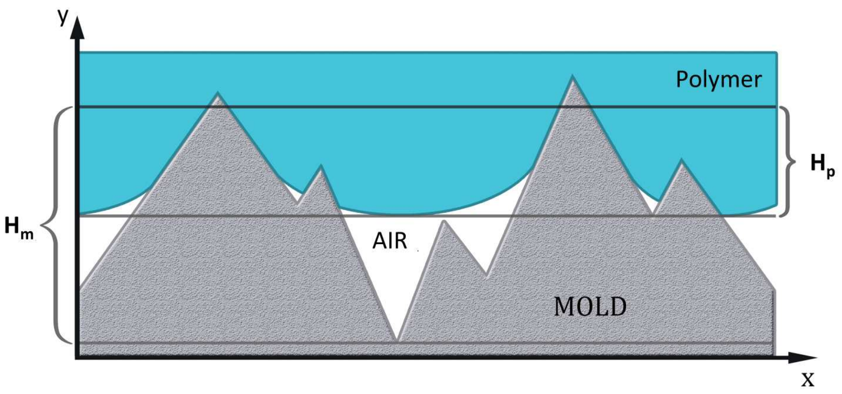

Figure 14.6: Schematics of polymer replication of mold surface topography.

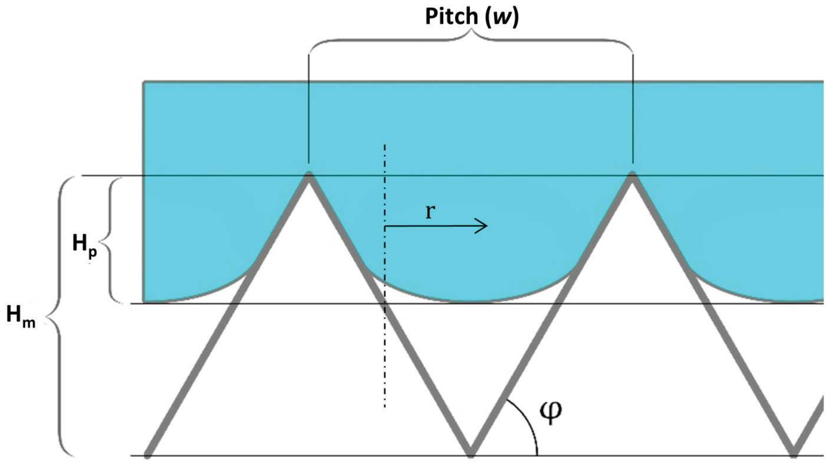

Figure 14.7: Schematics representation of a generic submicron feature and indication of the main geometrical parameters.

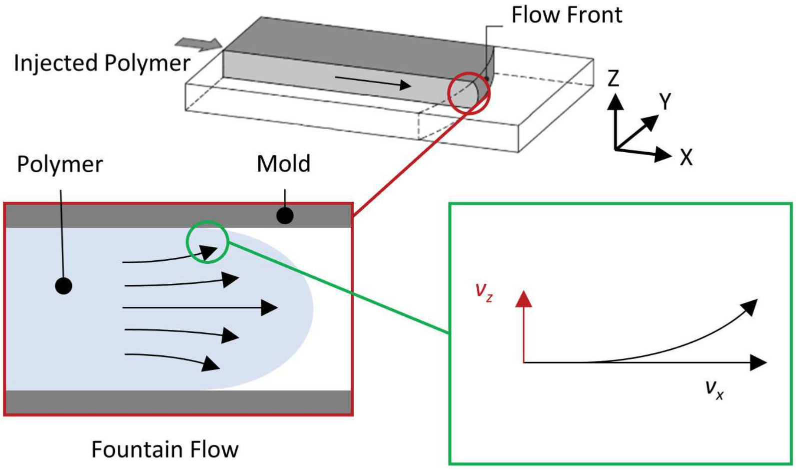

Figure 14.8: v_z as a component of the velocity distribution of the polymer fountain flow in the cavity.

14.1.4.1 Combined gas law

The combined gas law can be used to compare the air conditions before and after the injection molding cycle:

$$\frac{p_a \cdot V_0}{T_m} = \frac{p \cdot V}{T_c} \tag{14.4}$$

where p_a is the atmospheric pressure, T_m is the mold temperature, and T_c is the contact temperature between the melt and the mold. With geometrical considerations, the volume of the air trapped at the end of fill (V) and the volume within the crests and valleys in the mold topography (V_0) can be related to the height of the mold topography (H_m) and the replicated polymer height (H_p). Figure 14.7 presents the schematics of the mold texture and replicating polymer.

$$\frac{V_0}{V} = \frac{(H_m)^2}{(H_m - H_p)^2} \tag{14.5}$$

where the depth of the valleys in the mold topography (H_m), is calculated from the topographical analysis. The height of the replicated polymer surface structures (H_p) is the unknown parameter for the model, which is compared to the part topographies for validation. The simplified texture representation of Figure 14.7 indicates the structure's main geometrical parameters. The volume defined by the texture (V_0) is calculated considering the cavity volume defined from the top of the feature to its bottom. The mold structures are assumed as bidimensional, i.e. the ripples are assumed straight and parallel along their direction. The volume of the air that remains trapped in the feature (V) is calculated from the height reached by the replicating polymer to the bottom of the features Equation 14.5.

The air pressure during mold filling and packing (p) is balanced by the local polymer pressure in the cavity (p_c), adjusted as follows:

$$p = p_c - (p_a - p_\gamma + p_\eta) \tag{14.6}$$

where p_γ is the capillarity pressure, and p_η is the viscous pressure drop.

14.1.4.2 Capillary pressure

The capillarity pressure (p_γ) can be calculated considering the polymer surface tension (γ_l), the contact angle between the molten polymer and the mold surface (θ), the aspect ratio (m), and the pitch distance of the surface structures (w).

$$p_\gamma = \frac{2 \cdot \gamma_l \cdot cos(\theta)}{r} \tag{14.7}$$

where r (cf. Figure 14.7) represents half of the distance between consecutive features at the polymer replication depth. The r distance is calculated as:

$$r = (H_m - H_p) \cdot cot(\phi) \tag{14.8}$$

Where ϕ is the wall angle of the surface structures, which can be calculated from the structures aspect ratio m.

$$\phi = tan^{-1}(m) = tan^{-1}\left(\frac{H_m}{w/2}\right) \tag{14.9}$$

14.1.4.3 *Viscous pressure drop*

The viscous pressure drop (p_η) is given by:

$$P_\eta = \frac{\eta \cdot \dot{\gamma}}{cos(\phi)} \cdot ln\left(\frac{H_m}{H_m - H_p}\right) \tag{14.10}$$

where η is the polymer viscosity described by the Cross-WLF model and $\dot{\gamma}$ is the shear rate of the polymer filling the submicron feature.

$$\dot{\gamma} = \frac{2(2 + n^{-1}) \cdot v_z}{(H_m - H_p) \cdot (2/m)} \tag{14.11}$$

where n is the power-law index in the Cross viscosity model, and v_z is the speed of the polymer at the mold surface along the direction of the feature filling (cf. Figure 14.8).

14.1.5 Analytical model stream

For each combination of experimental parameters, the polymer pressure evolution in the mold cavity (p_c), the melt temperature (T_m), and the velocity of the melt (v_z) in the direction of the feature filling (i.e. orthogonally to the cavity wall) are imported from the numerical simulation of the injection molding process. These variables were calculated during the injection and packing phase as a function of the injection time feeding the equation that derives from Equation 14.5 and Equation 14.4.

$$\frac{p \cdot T_m}{p_a \cdot T_c} = \frac{(H_m)^2}{(H_m - H_p)^2} \tag{14.12}$$

In Figure 14.9 a flow chart representation of the proposed analytical model is shown.

14.1.5.1 *Virtual replication height*

In step 1, an iterative procedure was used to solve Equation 14.12 (cf. Figure 14.9). The result of the iterative process is the 'virtual' replication grade ($H_{p,virtual}$, Step 2, cf. Figure 14.9). The model evaluates the replication for each time step, considering the variation of the boundary conditions of the polymer melt at the entrance of the micro valleys during filling and packing.

The *virtual* grade of replication obtained at step 2 was then adjusted to consider the hesitation phenomena that affect the polymer flow into the submicron surface features. As the replicating polymer melts are reaching the NFT, it eventually hesitates in the microcavities because of the quick raise of its viscosity. The thresholds found as a result of the thermal and rheological characterization and analysis of the resins were implemented to better model the hesitation phenomena.

From the replication calculated without any hesitation consideration ($H_{p,virtual}$), two conditions were implemented in the model to correct the value of the time-dependent replicated height.

14.1.5.2 Step 3

In step 3 (cf. Figure 14.9) the polymer flow hesitates if the shear rate ($\dot{\gamma}$) of the polymer melt flowing into the surface features is lower than a given threshold value ($\dot{\gamma}_{threshold}$). The threshold value for the shear rate defines the limit flow conditions below which the polymer is more sensitive to the temperature-driven steep rise of the melt viscosity. Indeed, when flowing into the surface features, the shear-thinning behavior counteracts the rapid cooling. However, this happens only for shear rate values that are above the threshold. As suggested by Kennedy and Zheng [183], semi-crystalline polymers can flow below the crystallization temperature upon high-rate cooling.

14.1.5.3 Step 4

In step 4 (cf. Figure 14.9) the polymer hesitates if the temperature of the melt in contact with the mold surface is smaller than the NFT. Indeed, as the polymer/mold contact temperature is below the NFT, the flow ceases because of the solidification of the polymer melt. Moreover, Brulez et al. [184] observe that low injection velocities increase the influence of mold temperature on microstructure replication.

14.1.5.4 Replication grade calculation

The evaluation of these conditions of steps 3 and 4 allows for the correction of the replication depth, which is lower than the *virtual* value predicted in step 2 ($H_{p,virtual}$) because the latter did not consider any hesitation effect. The two conditions are tested as a function of time throughout the filling and the packing of the mold cavity. The predicted replication as a function of time $H_p(t)$ still conserves the time dependence, thus considering the evolution of the boundary conditions in the macro-cavity.

The final predicted replication H_p (Step 5, cf. Figure 14.9) is calculated as the maximum structure height achieved by the polymer over time. The replication grade is finally evaluated as the ratio between the predicted polymer replication (H_p) and the actual height of the mold structures (H_m).

$$R_{\%} = \frac{H_p}{H_m} \cdot 100\% \qquad (14.13)$$

14.2 MODEL VALIDATION

The analytical model was validated against replication data measured at different experimental conditions for the tested polymers (cf. section 12.4). The height of the submicron structures in the mold topography (H_m) and that of the LIPSS on molded parts ($H_{p,exp}$), was evaluated using Sk. From the experimental values of the Abbott-Finestone curve, the values of $H_{p,exp}$ were calculated.

$$H_{p,exp} = \frac{Sk}{S_{mr2} - S_{mr1}} \qquad (14.14)$$

The experimental replication grade $R_{exp\%}$ is calculated using the experimental results for the different polymers.

$$R_{exp\%} = \frac{H_{p,exp}}{H_m} \cdot 100\% \qquad (14.15)$$

Figure 14.10 reports the comparison between the experimental values and the model prediction and the errors for each combination of the considered parameters. The error ϵ between calculated and experimental results summarizes the model efficacy and quality. Moreover, the experimental standard deviation (σ) for the AFM measurements are reported.

The comparison between the reported ϵ and σ values shows how the model can accurately predict the polymer replication capabilities at different process conditions. Indeed, the model deviation ϵ is within or close to the standard deviation (cf. Figure 14.10 (a)). The model results are accurate also when considering the replication of the coated structures (cf. Figure 14.10 (b)).

In Table 14.2 the deviations of all the polymer and mold temperature combinations for the uncoated mold are reported. The column and row average values have been calculated to study the polymer and temperature effect on the experimental and analytical results. The analytical deviations always get values lower than 10%, confirming the accuracy of the proposed model for all the polymer and mold temperature combinations. The overall average deviation is ϵ = 4.6%, slightly lower than the overall experimental deviation, which is σ = 5.4%.

In Table 14.3 the deviations of all the polymer and mold temperature combinations for the coated mold are reported. Similar conclusions can be withdrawn. However, the PLA polymer shows for the

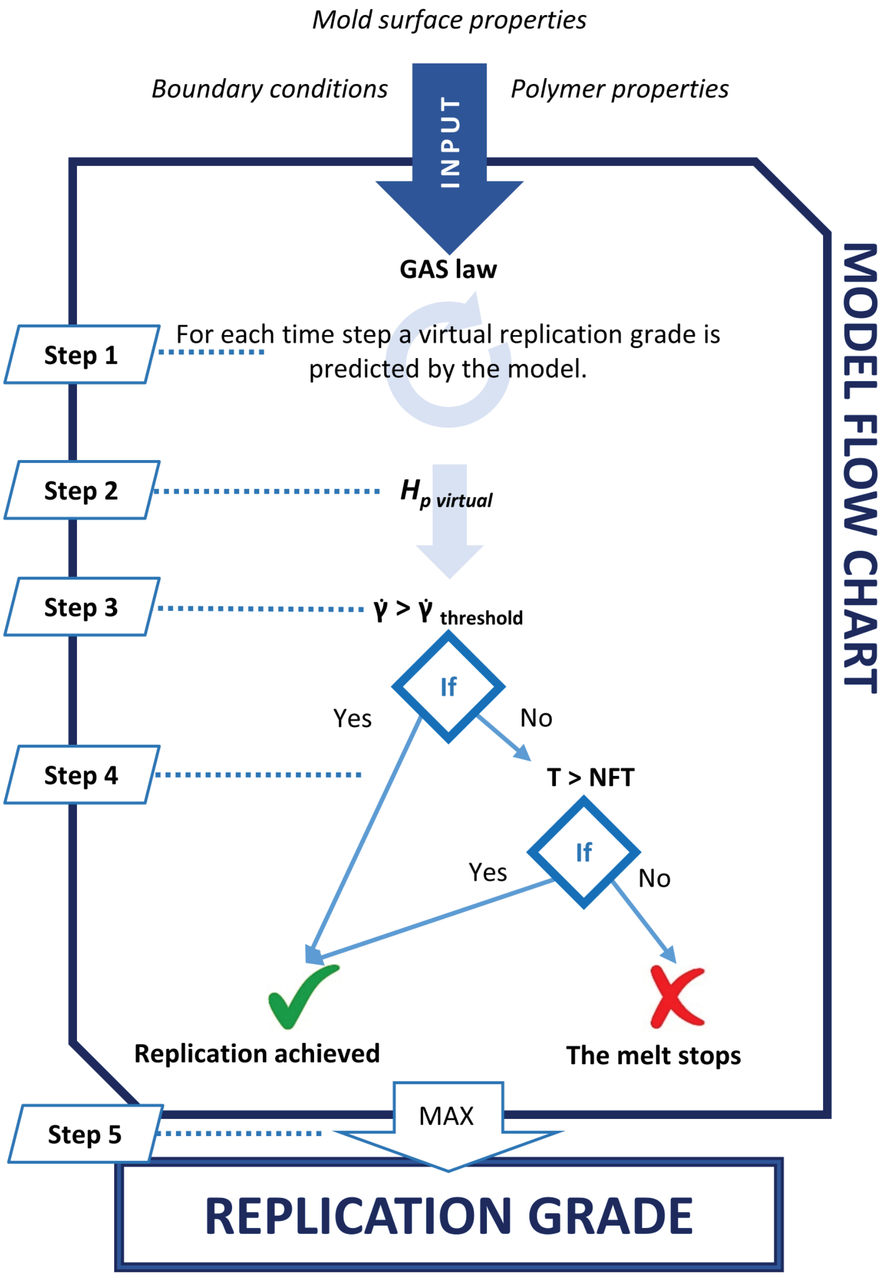

Figure 14.9: Flow chart for the micro surface structures replication model developed in this work.

Mold Temperature [°C]	**PBAT/PLA**	**PLA**	**PP**	**Row Average**
		σ		
30	6.0%	4.3%	4.9%	*5.1%*
60	8.0%	7.0%	5.1%	*6.7%*
90	5.0%	8.7%	2.9%	*5.5%*
120	5.5%	2.3%	5.2%	*4.3%*
Column Average	*6.1%*	*5.6%*	*4.5%*	***5.4%***
		ϵ		
30	2.6%	8.1%	2.9%	*4.5%*
60	1.1%	0.5%	8.1%	*3.2%*
90	8.6%	7.8%	3.6%	*6.7%*
120	6.4%	3.4%	2.6%	*4.1%*
Column Average	*4.7%*	*4.9%*	*4.3%*	***4.6%***

Table 14.2: σ and ϵ deviation values for the polymer and mold temperature combinations for the uncoated mold. The average value at constant mold temperature and for the same polymer are calculated. The bold entry at the bottom right of the sub tables reports the overall deviation value.

coated setup analytical deviations that exceed 10%. This result may be linked to inaccuracies during the experimental characterization of the PLA molten drop over the coated mold.

14.3 MICROSCALE MODEL SENSITIVITY

The replication results obtained through the analytical model show variations with respect to polymer, mold surface properties, and mold temperature, thus demonstrating that the model is able to capture the effect of these processing variables. Moreover, the model considers the dynamics of the replication, analyzing the flow in the submicron structures for several time steps and considering the evolution of the properties of the melt and of the physical quantities.

The effect of the selected variables on the values of the viscous pressure drop and capillarity pressure were evaluated using a DoE approach. The sensitivity of the model to the different factors was analyzed at the time step in which the polymer achieves the maximum replication grade. Moreover, the effect of the replication kinetics has been evaluated.

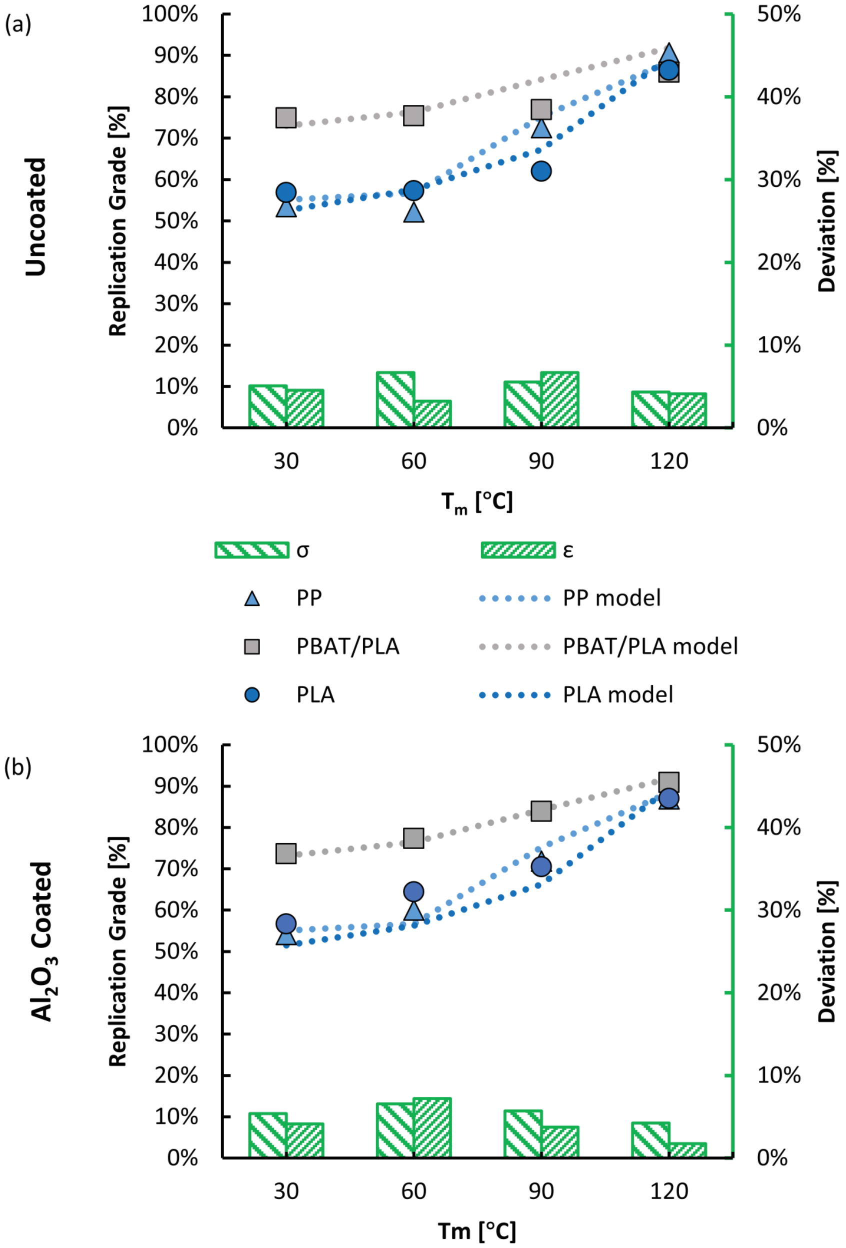

Figure 14.10: Comparison plots for the model validation. Experimental points are shown as bullets, model predictions are shown as dotted lines. The secondary axis presents the experimental standard deviation (σ) and the model deviation to the experimental values (ϵ). The validation is presented for the uncoated (a) and coated (b) molds.

Mold Temperature [°C]	PBAT/PLA	PLA	PP	Row Average
		σ		
30	6.2%	5.0%	4.9%	*5.4%*
60	6.7%	6.0%	7.0%	*6.6%*
90	6.3%	7.4%	3.4%	*5.7%*
120	4.3%	3.5%	4.9%	*4.2%*
Column Average	*5.9%*	*5.5%*	*5.1%*	***5.5%***
		ϵ		
30	0.6%	10.0%	1.8%	*4.1%*
60	1.2%	14.6%	5.8%	*7.2%*
90	0.4%	6.4%	4.5%	*3.8%*
120	1.0%	2.6%	1.7%	*1.8%*
Column Average	*0.8%*	*8.4%*	*3.4%*	***4.2%***

Table 14.3: σ and ϵ deviation values for the polymer and mold temperature combinations for the Al_2O_3 coated mold. The average value at constant mold temperature and for the same polymer are calculated. The bold entry at the bottom right of the sub tables repots the overall deviation value.

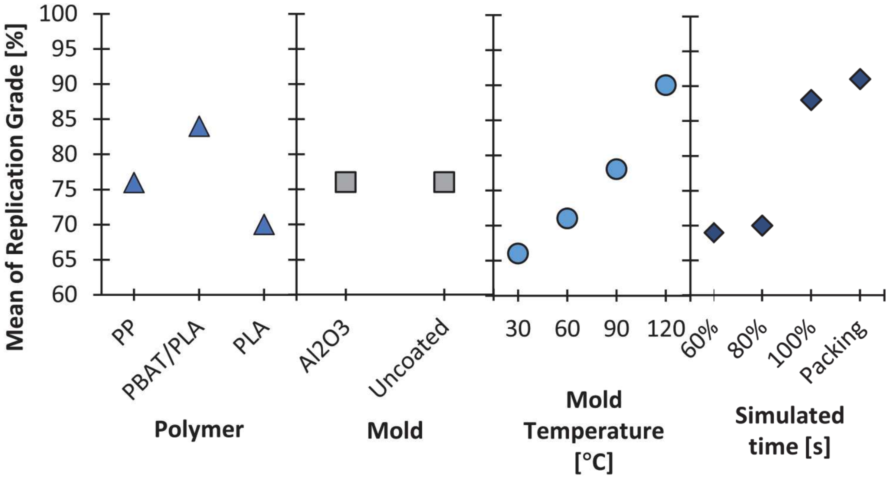

Figure 14.11: Main effects plot for the replication grade. The simulated time is considered as a factor, to study the effect of the polymer flow kinetics.

14.3.1 Main effect of the selected parameters

The model sensitivity was first analyzed considering the effect of the different selected parameters on the predicted replication grade (cf. Figure 14.11). The trends for the main effect plots are similar to those observed for the experimental data (cf. section 12.4). This confirms the efficacy of the model in capturing the micro-scale flow for the different polymers, mold surface properties, and mold temperatures. The model also shows the negligible effect of the mold coating. The time when the replication occurs has a strong effect on the replication grade. When the process allows for a long time for replication (i.e. the polymer flow in the microcavities stops after a long time) higher replication grades are obtained.

14.3.2 Pressure balance in the microcavities

Table 14.4 and Table 14.5 report the cavity pressure (p_c) and the relative contributions of viscosity (p_η) and capillarity (p_γ) to the air pressure (p) for the uncoated and coated molds, respectively. The contributions were extracted at the end of the replication process, that is when the polymer achieves the maximum replication. From both the tables, it can be highlighted that the viscous pressure drop is generally higher than the capillarity pressure. The only exeption is the PP at high mold temperature, which show higher capillary pressure than the viscous one (cf. Figure 14.12). However, it can be concluded that the polymer replication phenomena are mainly viscosity-driven. In accordance with the well-known effect of mold temperature on replication, the viscous pressure drop strongly decreases with increasing mold temperatures. Through the model results, it is possible to ob-

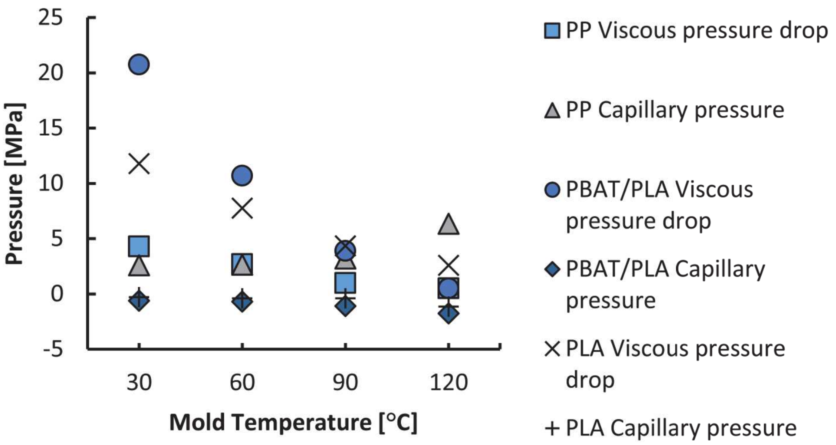

Figure 14.12: Viscous and capillary pressure contributions for the selected polymers at the considered mold temperatures.

serve that the negligible effect of the mold coating is explained by the relatively high effect of the viscous pressure drop, which reduces the sensitivity to capillarity.

The ANOVA analysis shows that the effect of mold surface wettability is significant in the analytical model for the capillarity pressure when considering the biopolymers. The interaction plot (cf. Figure 14.13 (a)) shows the dependence of the capillary pressure on the mold surface properties. Higher contact angles (cf. section 12.3) lead to negative capillarity pressure, thus counteracting the filling of the submicron cavities. The Al2O3 coatings decreased the contact angle for PBAT/PLA, thus increasing the capillarity pressure and leading to higher wettability. Conversely, the trend is opposite for the PLA, thus leading to lower wettability and lower pressure. The significantly lower contact angles observed with PP resulted in a negligible effect of the capillarity pressure.

Figure 14.13 (b) reports the trends of the capillary pressure at different mold temperatures. The PP capillary pressure increase is due to its better wetting properties, and the consequent decrease of the liquid tension. Conversely, for the biopolymers, the capillarity pressure decreases for increasing temperature.

14.3.3 Replication kinetics effect

Figure 14.14 reports information on the replication grade with respect to the time step at which replication occurs. The time step is reported as a percentage of the filling time. The interaction plot includes the mold temperature factor to clearly show the kinetics of replication. The main effect of the time step is increasing the replication grade. At low mold temperatures, the complete replication takes place earlier

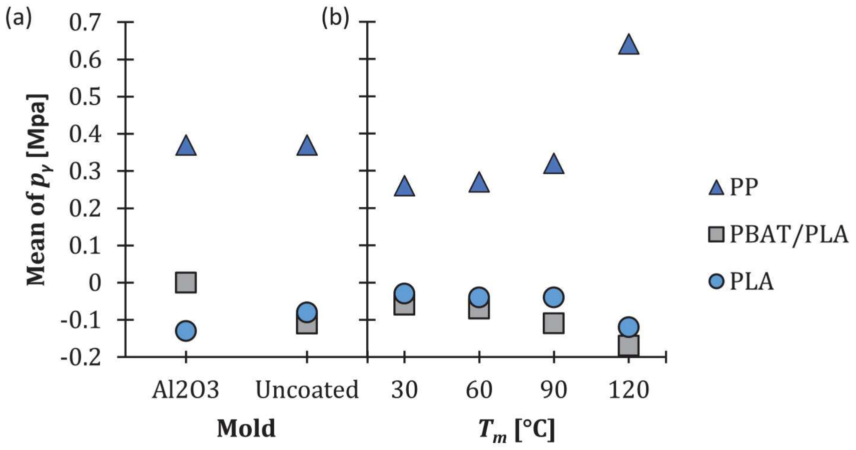

Figure 14.13: Interaction plots for the capillary pressure at the maximum replication height. The dependence of the capillary pressure is showed with respect to the mold surface properties (a) and the mold temperature (b).

Mold Temperature °C	p_c MPa	p_η MPa	p_γ MPa	p MPa
		Polymer: PP		
30	14.8	4.3	2.6	12.1
60	14	2.7	2.6	13
90	19.8	1	3.2	21
120	74.6	0.5	6.3	79.4
		Polymer: PBAT/PLA		
30	40.8	20.8	-0.4	18.5
60	40.4	10.7	-0.5	28.1
90	67.6	3.9	-0.8	61.9
120	161.7	0.5	-1.3	158.9
		Polymer: PLA		
30	18.9	11.6	-0.6	5.7
60	18.7	7.6	-0.8	9.3
90	18.1	4.3	-0.8	12
120	98.5	2.6	-2.3	92.5

Table 14.4: Cavity pressure and contribution on the pressure balance of the viscous, capillarity, and air pressure for the uncoated mold.

Mold Temperature °C	p_c MPa	p_η MPa	p_γ MPa	p MPa
		Polymer: PP		
30	14.8	4.3	2.6	12.2
60	14	2.7	2.7	13
90	19.8	1	3.2	21.1
120	74.6	0.5	6.4	79.5
		Polymer: PBAT/PLA		
30	40.8	20.7	-0.8	18.3
60	40.4	10.7	-0.9	27.8
90	67.6	3.9	-1.4	61.3
120	161.7	0.5	-2.2	158
		Polymer: PLA		
30	18.9	12	0	5.9
60	18.7	7.9	0	9.8
90	18.1	4.4	0	12.7
120	98.5	2.6	0	94.8

Table 14.5: Cavity pressure and contribution on the pressure balance of the viscous, capillarity, and air pressure for the Al_2O_3 coated mold.

in the process. The plot also demonstrates that the relation between the mold temperature and the time at maximum replication is tight. In fact, the effect of the high mold temperatures is the delay of the polymer viscosity increase and skin formation, giving more time for the polymer flow during micro cavity filling.

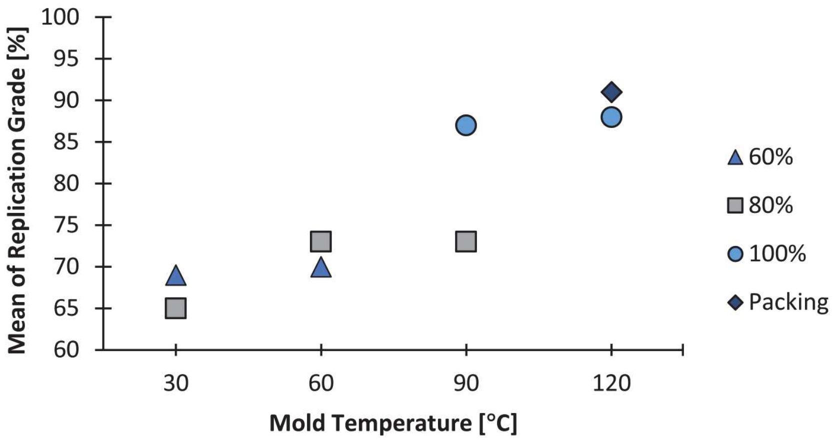

Figure 14.14: Interaction plot to illustrate the influence of the mold temperature and the replication kinetics on the replication grade. The time step is presented as a percentage of the filling time.

Part VII

CONCLUSIONS

15 CONCLUSIONS

This work focuses on the study of mold surface modifications for the improvement of the polymer flow for injection molding and microinjection molding applications. The effects of the surface modifications were investigated through experimental campaigns and numerical and analytical models were proposed for a deep description of the physical mechanisms occurring in the injection mold cavity. Through the experimental investigations, the mold surface was modified introducing (i) micro and nano surface topographies, (ii) modified chemical and thermal interface properties, and (iii) the combination of the two, obtaining a simultaneous modification of the surface morphology and chemical properties.

The effects of the proposed surface modifications were considered in relation to different aspects of the polymer flow inside the injection mold cavity. The interactions between the surface modification and the ability of the polymer melt to fill the mold cavity and the phenomena occurring during micro and nanostructure replication have been examined during the work. The general goals that were fixed approaching the design of the surface were the reduction of the pressure drop yielded by the polymer to fill the cavity and the functionalization of replicated plastic surfaces through optimized replication fidelity of the mold surface.

The research experimental investigations mainly focus on the modification of the mold surface morphology and on injection molding tests to explore the effects of the modified surfaces on the filling phase of the process. Ultrafast laser systems have been exploited to induce superficial micro and nanostructures on the mold surfaces. Several mold surface morphology modifications were examined during the study. Surface characterization techniques were regularly exploited to characterize the mold and the replicated micro and nanostructures. Moreover, the functionality of the surfaces was characterized. Different monitoring instrumentations were implemented in the considered injection molding setups allowing the control of the most important physical properties during the process. The obtained characterization and experimental data were finally exploited to feed and validate the models proposed in the work.

ULTRAFAST LASER TEXTURING

The experimental investigations using the ultrafast laser texturing technology have been carried out focusing on injection molding applications. Laser-Induced Surface Structures are currently a hot topic in the literature, and this work converges quickly on surface textures designed for injection molding. The experimental investigations were carried out to create hierarchical textures onto mold steel.

The structuring process was optimized in terms of structure geometry and regularity. Characterization of the capabilities of the two considered wavelengths (i.e. infrared and green) was carried out. The hierarchical structuring process was divided into three steps, to improve process control and ultimately the structure regularity and geometry. The first step involves the creation of the microstructure. The green laser beam was selected and the laser and scanning parameters were optimized using a DoE approach. The second step objective was eliminating the presence of burrs and recasts after the first micro structuring step. Surface polishing was optimized using green laser light, exploiting a high pulse repetition rate and fast scanning speeds. The third step focuses on the creation of Laser-Induced Surface Structures over the already machined microstructures. The green and red lights were exploited to achieve about half a micron and about one-micron pitch periodical and regular ripples, respectively. The pitch of the ripples closely follows the size of the laser incident wavelength.

The obtained textures were deeply characterized in terms of structure regularity and homogeneity. As a result of the laser capabilities and obtained structure characterization an analytical tool to predict the energy distribution over the treated surface has been developed. The tool has shown high affinity with the achieved surface structures' presence and regularity. The tool can help the process design phase for the selection of the energetical laser intensities and of the cinematic aspects.

CAVITY FILLING

The characterization of the effects of the mold surface modifications onto the filling behavior of the plastic melt investigates the effects of the thermal and morphological boundary conditions on flow resistance. The modifications of the thermal and of the morphological boundary conditions were experimentally evaluated separately, to isolate the peculiarities of each treatment. The experimental tests were carried out using an open-flow cavity varying the shear conditions using different cavity thicknesses and flow rates. The selected resin is a semi-crystalline PET, widely used in industrial applications.

The thermal boundary conditions' effect on filling was characterized using two different mold insert steel types in the coated and uncoated setup. A full factorial DoE was set to varying the mold insert properties and the flow conditions. The whole pressure signal during filling was analyzed to study the developing flow phenomena. The results show that the coating has a beneficial effect on filling flow, reducing the pressure drop inside the cavity. When comparing the two tested coatings (DLC and CrN), the DLC one shows a wider effect on pressure reduction. Moreover, the analysis of the pressure signal along the cavity filling shows that the flow pressure evolution has a discontinuity that can be linked to the onset of crystallization. The effect is present only for the uncoated conditions. The presence of a ceramic mold coating is beneficial since it is able to eliminate the discontinuity effect by insulating the flowing polymer from the cold mold. A numerical model was calibrated to account for the effect of the DLC coating. The calibrated model was exploited in a case study to minimize the material intensity of a plastic part by reducing the thickness. The model results show that the coating can allow a part volume reduction of 8%.

The mold surface morphology was optimized to achieve regular micro and nano textures and study the effects of the modified surface on the filling flow of polymer melts in non-isothermal conditions. A full factorial DoE was set to discern between the effects of the different nanostructures, the microstructure, and the combination of the two (i.e. hierarchical structures). The injection molding results show that the hierarchical structures improve the filling flow with a 4.2% lower cavity pressure drop at low thickness. The nanotexture has a minor effect with respect to the micro-texture. By combining the two texture hierarchies, the effect on flow increases, showing the lowest pressure drops (that was obtained with the hierarchical texture that presents the higher pitch difference). The texture effect can be related to a reduction of the polymer-mold interactions, favoring the phenomenon of wall slip. This study proves that the modification of mold surface topography can control the polymer macro-flow only for very thin cavities (i.e. 1 mm thick). Moreover, the study proves that the hierarchical nature of the texture is beneficial. Starting from the results presented in this work, new developments through the optimization of the design of the hierarchical texture should be considered.

MOLD SURFACE REPLICATION

The replication of mold surface Laser-Induced Periodic Surface Structures by microinjection molding was investigated using a wide range of resins. The objective of accurately replicate the mold structures is to functionalize the plastic parts, inducing modified properties such as high-wetting and self-cleaning ones. The experimentations were divided into two works, the first have a broader approach and considers the whole process chain from the insert manufacturing to the part functionalization, the latter focuses on the study of the replication in the microinjection molding process.

The process chain proposed in this work consists of the fast fabrication of micro- and nano-structures on a steel surface using a femtosecond laser and their reproduction on plastic parts by microinjection molding. Mold inserts were engraved to obtain highly aligned and uniform LIPSS that were replicated using PS and PMMA. The replication accuracy of the textured surface and the achieved part functionality were studied as a function of the mold temperature. The results show that the replication accuracy is affected by the mold temperature, and in particular by the temperature dependence of melt viscosity. The wetting behavior results mostly follow the trends obtained for replication. When low replication is achieved, the part does not get functionalized. In contrast, once the part achieves functionalization, an increase in replication does not translate into an increase in the contact angle.

This work experimentally studies the replication quality of submicron-scale Laser-Induced Periodic Surface Structures by microinjection molding using different biopolymers (i.e. PLA, PBAT/PLA, and PP). The replication grade was studied varying the mold temperature and the chemical properties of the mold surface, modified using a thin layer of alumina. The experimental results show that texture replication is mainly affected by polymer selection and mold temperature. A deep characterization of the mold and plastic surfaces and of the exploited polymers was carried out. The obtained results were exploited to feed and validate a multi-scale model for polymer replication at the submicron scale. First, the numerical model analyzes the polymer behavior in the mold macro cavity and determines the boundary conditions for the filling of the submicron structures. Then, the replication of the mold topography is calculated considering topographical parameters, polymer rheology and thermal behavior, and the mold surface energy. The analytical model is sensitive to the variations of mold temperature and polymer selection, being accurate on replication prediction (the maximum error is 8%). The model results show that polymer replication is mainly viscosity-driven, which is generally higher than the capillarity pressure. Therefore, the effect of mold surface energy on replication is weak.

BIBLIOGRAPHY

[1] PlasticsEurope, Plastics – the Facts 2015, an Analysis of European plastics production, demand and waste data. Tech. rep., Brussels., **2015**.

[2] PlasticsEurope, Plastics – the Facts 2017, an Analysis of European plastics production, demand and waste data. Tech. rep., Brussels., **2017**.

[3] PlasticsEurope, Plastics – the Facts 2019, an Analysis of European plastics production, demand and waste data. Tech. rep., Brussels., **2019**.

[4] PlasticsEurope, Plastics – the Facts 2020, an Analysis of European plastics production, demand and waste data. Tech. rep., Brussels., **2020**.

[5] O. Ogorodnyk, K. Martinsen, *Procedia Cirp* **2018**, *67*, 380–385.

[6] C. Yang, X.-H. Yin, G.-M. Cheng, *Journal of Micromechanics and Microengineering* **2013**, *23*, 093001.

[7] J. Giboz, T. Copponnex, P. Mélé, *Journal of micromechanics and microengineering* **2007**, *17*, R96.

[8] B. Whiteside, M. Martyn, P. Coates, P. Allan, P. Hornsby, G Greenway, *Plastics rubber and composites* **2003**, *32*, 231–239.

[9] M. Song, Z. Liu, M. Wang, T. Yu, D. Zhao, *Journal of Materials Processing Technology* **2007**, *187*, 668–671.

[10] G Lucchetta, M Sorgato, S Carmignato, E Savio, *CIRP Annals* **2014**, *63*, 521–524.

[11] D. O. Kazmer, D. Masato, L. Piccolo, K. Puleo, J. Krantz, V. Venoor, A. Colon, J. Limkaichong, N. Dewar, D. Babin, et al., *Sustainability* **2021**, *13*, 8102.

[12] M. Heckele, W. Schomburg, *Journal of Micromechanics and Microengineering* **2003**, *14*, R1.

[13] K. Maghsoudi, R. Jafari, G. Momen, M. Farzaneh, *Materials today communications* **2017**, *13*, 126–143.

[14] L. Piccolo, K. Puleo, M. Sorgato, G. Lucchetta, D. Masato, *Materials & Design* **2021**, *198*, 109272.

[15] D. O. Kazmer, *Injection mold design engineering*, Carl Hanser Verlag GmbH Co KG, **2016**.

[16] G Gourmelon, *Retrieved from Global Plastic Production Rises Recycling Lags: http://www. worldwatch. org/global-plastic-productionrises-recycling-lags-0* **2015**.

[17] *United States Environmental Protection Agency* **2012**.

[18] G Lucchetta, P. Bariani, *CIRP annals* **2010**, *59*, 33–36.

[19] R Selden, *Journal of Injection Molding Technology* **2000**, *4*, 159.

[20] C. Gornik in Macromolecular Symposia, *Vol. 217*, Wiley Online Library, **2004**, pp. 365–374.

[21] H. A. Barnes, J. F. Hutton, K. Walters, *An introduction to rheology*, *Vol. 3*, Elsevier, **1989**.

[22] C. W. Macosko, *Measurements and Applications* **1994**.

[23] B Xu, K. Ooi, T. Wong, C. Liu, *Journal of Micromechanics and Microengineering* **1999**, *9*, 377.

[24] E. E. Rosenbaum, S. G. Hatzikiriakos, *AIChE journal* **1997**, *43*, 598–608.

[25] V Piotter, K Mueller, K Plewa, R Ruprecht, J Hausselt, *Microsystem Technologies* **2002**, *8*, 387–390.

[26] R. Surace, V. Bellantone, G. Trotta, I. Fassi, *Journal of Manufacturing Processes* **2017**, *28*, 351–361.

[27] N. Zhang, Q. Su, S. Y. Choi, M. D. Gilchrist, *Materials & Design* **2015**, *83*, 835–847.

[28] Q. Su, N. Zhang, M. D. Gilchrist, *Journal of Applied Polymer Science* **2016**, *133*.

[29] G. R. Berger, C. Steffel, W. Friesenbichler, *International Journal of Materials and Product Technology* **2016**, *52*, 193–211.

[30] L. Crema, M. Sorgato, G. Lucchetta, *International Journal of Heat and Mass Transfer* **2017**, *109*, 462–469.

[31] G. Lucchetta, D Masato, M Sorgato, L Crema, E Savio, *CIRP Annals* **2016**, *65*, 537–540.

[32] S.-C. Chen, Y. Chang, Y.-P. Chang, Y.-C. Chen, C.-Y. Tseng, *International Communications in Heat and Mass Transfer* **2009**, *36*, 1030–1035.

[33] S. G. Hatzikiriakos, *Progress in Polymer Science* **2012**, *37*, 624–643.

[34] S. G. Hatzikiriakos, K. B. Migler, *Polymer processing instabilities: control and understanding*, CRC Press, **2004**.

[35] F Brochard, P. De Gennes, *Langmuir* **1992**, *8*, 3033–3037.

[36] Y. M. Joshi, A. K. Lele, R. Mashelkar, *Journal of non-newtonian fluid mechanics* **2000**, *94*, 135–149.

[37] P. P. Drda, S.-Q. Wang, *Physical review letters* **1995**, *75*, 2698.

[38] M. Ansari, Y. W. Inn, A. M. Sukhadia, P. J. DesLauriers, S. G. Hatzikiriakos, *Journal of Rheology* **2013**, *57*, 927–948.

[39] D. A. Hill, *Journal of Rheology* **1998**, *42*, 581–601.

[40] S. Hatzikiriakos, C. Stewart, J. Dealy, *International Polymer Processing* **1993**, *8*, 30–35.

[41] E. Chatzigiannakis, M. Ebrahimi, S. G. Hatzikiriakos, *Journal of Rheology* **2017**, *61*, 731–739.

[42] V. Mhetar, L. Archer, *Macromolecules* **1998**, *31*, 8607–8616.

[43] T. Zhiltsova, M. Oliveira, J. Ferreira, *Journal of Materials Science* **2013**, *48*, 81–94.

[44] R.-D. Chien, W.-R. Jong, S.-C. Chen, *Journal of Micromechanics and Microengineering* **2005**, *15*, 1389.

[45] C.-S. Chen, S.-C. Chen, W.-L. Liaw, R.-D. Chien, *European Polymer Journal* **2008**, *44*, 1891–1898.

[46] M. Ebrahimi, V. K. Konaganti, S. Moradi, A. K. Doufas, S. G. Hatzikiriakos, *Soft matter* **2016**, *12*, 9759–9768.

[47] D. Masato, M. Sorgato, M. Babenko, B. Whiteside, G. Lucchetta, *Materials & Design* **2018**, *141*, 286–295.

[48] D. Masato, M. Sorgato, A. Batal, S. Dimov, G. Lucchetta, *Polymer Engineering & Science* **2019**, *59*, 1889–1896.

[49] E. Borzenko, O. Y. Frolov, G. Shrager, *Fluid Dynamics* **2014**, *49*, 37–45.

[50] S. Andjelić, R. C. Scogna, *Journal of Applied Polymer Science* **2015**, *132*.

[51] H Janeschitz-Kriegl, *Colloid and polymer science* **2003**, *281*, 1157–1171.

[52] R. Pantani, A. De Meo, V. Speranza, G. Titomanlio in AIP Conference Proceedings, *Vol. 1695*, AIP Publishing LLC, **2015**, p. 020065.

[53] J. van Meerveld, G. W. Peters, M. Hütter, *Rheologica Acta* **2004**, *44*, 119–134.

[54] R. H. Somani, B. S. Hsiao, A. Nogales, H. Fruitwala, S. Srinivas, A. H. Tsou, *Macromolecules* **2001**, *34*, 5902–5909.

[55] Y. Zhong, H. Fang, Y. Zhang, Z. Wang, J. Yang, Z. Wang, *ACS Sustainable Chemistry & Engineering* **2013**, *1*, 663–672.

[56] G. Kumaraswamy, J. A. Kornfield, F. Yeh, B. S. Hsiao, *Macromolecules* **2002**, *35*, 1762–1769.

[57] C. Duplay, B. Monasse, J.-M. Haudin, J.-L. Costa, *Polymer International* **1999**, *48*, 320–326.

[58] C. Duplay, B. Monasse, J.-M. Haudin, J.-L. Costa, *Journal of materials science* **2000**, *35*, 6093–6103.

[59] M. D'Haese, P. Van Puyvelde, F. Langouche, *Macromolecules* **2010**, *43*, 2933–2941.

[60] M. Farah, R. E. Bretas, *Journal of applied polymer science* **2004**, *91*, 3528–3541.

[61] M. Derakhshandeh, A. K. Doufas, S. G. Hatzikiriakos, *Rheologica Acta* **2014**, *53*, 519–535.

[62] L Scelsi, M. Mackley, H Klein, P. Olmsted, R. Graham, O. Harlen, T. McLeish, *Journal of rheology* **2009**, *53*, 859–876.

[63] A. Asti, L. Gioglio, *The International journal of artificial organs* **2014**, *37*, 187–205.

[64] B. Dhandayuthapani, Y. Yoshida, T. Maekawa, D. S. Kumar, *International journal of polymer science* **2011**, *2011*.

[65] J Bekesi, J. Kaakkunen, W Michaeli, F Klaiber, M Schoengart, J Ihlemann, P Simon, *Applied Physics A* **2010**, *99*, 691–695.

[66] Q. Xu, W. Zhang, C. Dong, T. S. Sreeprasad, Z. Xia, *Journal of the Royal Society Interface* **2016**, *13*, 20160300.

[67] C David, P Häberling, M Schnieper, J Söchtig, C Zschokke, *Microelectronic Engineering* **2002**, *61*, 435–440.

[68] P Zhang, F. Lv, *Energy* **2015**, *82*, 1068–1087.

[69] L. Oberli, D. Caruso, C. Hall, M. Fabretto, P. J. Murphy, D. Evans, *Advances in colloid and interface science* **2014**, *210*, 47–57.

[70] H. A. Abdel-Aal, *Surface Topography: Metrology and Properties* **2016**, *4*, 043001.

[71] C Gachot, A. Rosenkranz, S. Hsu, H. Costa, *Wear* **2017**, *372*, 21–41.

[72] M. Sorgato, F. Zanini, D. Masato, G. Lucchetta, *Journal of Applied Polymer Science* **2020**, *137*, 49280.

[73] M Sorgato, D Masato, G Lucchetta, L Orazi, *CIRP Annals* **2018**, *67*, 575–578.

[74] H. N. Hansen, R. Hocken, G. Tosello, *CIRP annals* **2011**, *60*, 695–714.

[75] F. Baruffi, M. Gülçür, M. Calaon, J.-M. Romano, P. Penchev, S. Dimov, B. Whiteside, G. Tosello, *Journal of Manufacturing Processes* **2019**, *47*, 367–381.

[76] W. Yu, S. Ruan, Z. Li, J. Gu, X. Wang, C. Shen, B. Chen, *The International Journal of Advanced Manufacturing Technology* **2019**, *103*, 2929–2940.

[77] C. Huang, *Journal of Micromechanics and Microengineering* **2007**, *17*, 1518.

[78] D. Masato, M. Sorgato, G. Lucchetta, *Materials & Design* **2016**, *95*, 219–224.

[79] S. B. Biancardo, H. J. Pranov, N. B. Larsen, *Advanced Materials* **2008**, *20*, 1825–1829.

[80] X Han, H Yokoi, *Polymer Engineering & Science* **2006**, *46*, 1590–1597.

[81] M. Yoshii, H. Kuramoto, K. Kato, *Polymer Engineering & Science* **1994**, *34*, 1211–1218.

[82] W.-B. Young, *Applied mathematical modelling* **2007**, *31*, 1798–1806.

[83] R Surace, G Trotta, V Bellantone, I Fassi, *The micro injection moulding process for polymeric components manufacturing*, Intechopen, **2012**.

[84] O Rötting, W Röpke, H Becker, C Gärtner, *Microsystem Technologies* **2002**, *8*, 32–36.

[85] Y.-C. Su, J. Shah, L. Lin, *Journal of Micromechanics and Microengineering* **2003**, *14*, 415.

[86] C. Griffiths, S. S. Dimov, S Scholz, G. Tosello, **2011**.

[87] Y.-K. Shen, C.-Y. Chang, Y.-S. Shen, S.-C. Hsu, M.-W. Wu, *International Communications in Heat and Mass Transfer* **2008**, *35*, 723–727.

[88] H.-Y. Lin, W.-B. Young, *Applied Mathematical Modelling* **2009**, *33*, 3746–3755.

[89] M. Sorgato, M. Babenko, G. Lucchetta, B. Whiteside, *The International Journal of Advanced Manufacturing Technology* **2017**, *88*, 547–555.

[90] M. Sorgato, D. Masato, G. Lucchetta, *Microsystem Technologies* **2017**, *23*, 2543–2552.

[91] M. Geoghegan, G. Krausch, *Progress in Polymer Science* **2003**, *28*, 261–302.

[92] C Sriropinyo, S. Yoon, J. Lee, J. Mead, C. Barry in Proc, **2005**, pp. 754–8.

[93] M. Matschuk, N. B. Larsen, *Journal of Micromechanics and Microengineering* **2012**, *23*, 025003.

[94] P. Mosaddegh, D. C. Angstadt, *Journal of Micromechanics and Microengineering* **2008**, *18*, 035036.

[95] D. Loaldi, L. Piccolo, E. Brown, G. Tosello, C. Shemelya, D. Masato, *Micromachines* **2020**, *11*, 509.

[96] C. Rytka, N. Opara, N. K. Andersen, P. M. Kristiansen, A. Neyer, *Macromolecular Materials and Engineering* **2016**, *301*, 597–609.

[97] J. Stormonth-Darling, R. Pedersen, C How, N Gadegaard, *Journal of Micromechanics and Microengineering* **2014**, *24*, 075019.

[98] R. H. Pedersen, Q. Xu, J. M. Stormonth-Darling, N. Gadegaard, *Macromolecular Materials and Engineering* **2015**, *300*, 172–180.

[99] H. Zhang, N. Zhang, W. Han, M. D. Gilchrist, F. Fang, *Precision Engineering* **2021**, *67*, 248–261.

[100] S. Kim, C.-S. Shiau, B. H. Kim, D. Yao, *Polymer-Plastics Technology and Engineering* **2007**, *46*, 1031–1037.

[101] D. Loaldi, D. Quagliotti, M. Calaon, P. Parenti, M. Annoni, G. Tosello, *Micromachines* **2018**, *9*, 653.

[102] K Metwally, T. Barriere, C Khan-Malek, *The International Journal of Advanced Manufacturing Technology* **2016**, *83*, 779–789.

[103] H.-S. Lee, Y.-G. Yoo, *International Journal of Precision Engineering and Manufacturing* **2012**, *13*, 2155–2161.

[104] Y. K. Shen, H. Chang, L. Hung in Key engineering materials, *Vol. 329*, Trans Tech Publ, **2007**, pp. 643–648.

[105] M Rohde, A. Derdouri, M. R. Kamal, *International Polymer Processing* **2009**, *24*, 288–297.

[106] H. Ito, H. Suzuki, *Journal of Solid Mechanics and Materials Engineering* **2009**, *3*, 320–327.

[107] M.-S. Huang, C.-F. Chung, *Journal of Applied Polymer Science* **2011**, *121*, 1151–1159.

[108] D. Masato, M. Sorgato, G. Lucchetta, *Microsystem Technologies* **2017**, *23*, 3661–3670.

[109] L. Yu, L. J. Lee, K. W. Koelling, *Polymer Engineering & Science* **2004**, *44*, 1866–1876.

[110] S.-W. Kim, L.-S. Turng, *Polymer engineering & science* **2006**, *46*, 1263–1274.

[111] D. Loaldi, F. Regi, F. Baruffi, M. Calaon, D. Quagliotti, Y. Zhang, G. Tosello, *Micromachines* **2020**, *11*, 614.

[112] D. Yao, B. Kim, *J. Manuf. Sci. Eng.* **2004**, *126*, 733–739.

[113] C. Rytka, J Lungershausen, P. Kristiansen, A Neyer, *Journal of Micromechanics and Microengineering* **2016**, *26*, 065018.

[114] A. Einstein, P. Ehrenfest, *Zeitschrift für Physik* **1923**, *19*, 301–306.

[115] F. M. Dickey, S. C. Holswade, et al., *Laser beam shaping*, Marcel Dekker New York, **2000**.

[116] P. Gregorčič, B. Šetina-Batič, M. Hočevar, *Applied Physics A* **2017**, *123*, 766.

[117] M Geiger, U Popp, U Engel, *CIRP Annals* **2002**, *51*, 231–234.

[118] J. Bonse, S. Höhm, S. V. Kirner, A. Rosenfeld, J. Krüger, *IEEE Journal of selected topics in quantum electronics* **2016**, *23*.

[119] X. Wang, H. Zheng, Y. Wan, W. Feng, Y. C. Lam, *Engineering* **2018**, *4*, 816–821.

[120] L Orazi, M Sorgato, L Piccolo, D Masato, G Lucchetta, *Lasers in Manufacturing and Materials Processing* **2020**, *7*, 207–221.

[121] A. Lasagni, D. Benke, T. Kunze, M. Bieda, S. Eckhardt, T. Roch, D. Langheinrich, J. Berger, *Journal of Laser Micro/Nanoengineering* **2015**, *10*.

[122] M Martínez-Calderon, A Rodríguez, A Dias, M Gómez-Aranzadi, S. Olazoila in Proceedings of the Lasers in Manufacturing Conference, Munich, Germany, **2015**, pp. 15–22.

[123] M. Camara, J. C. Rubio, A. Abrão, J. Davim, *Journal of Materials Science & Technology* **2012**, *28*, 673–685.

[124] A. Abdelrahman Elkaseer, S. Dimov, K. Popov, R. Minev, *Journal of Micro and Nano-Manufacturing* **2014**, *2*.

[125] R. Melentiev, F. Fang, *CIRP Journal of Manufacturing Science and technology* **2018**, *22*, 1–20.

[126] T. Wu, K. Cheng, *Micro-Cutting: Fundamentals and Applications* **2013**, 185–226.

[127] S. N. B. Oliaei, Y. Karpat, *The International Journal of Advanced Manufacturing Technology* **2016**, *84*, 1963–1980.

[128] K. Ho, S. Newman, *International Journal of Machine Tools and Manufacture* **2003**, *43*, 1287–1300.

[129] K. Rajurkar, G Levy, A Malshe, M. Sundaram, J McGeough, X Hu, R Resnick, A DeSilva, *CIRP annals* **2006**, *55*, 643–666.

[130] D. Patel, V. Jain, J Ramkumar, *Proceedings of the Institution of Mechanical Engineers Part B: Journal of Engineering Manufacture* **2018**, *232*, 941–964.

[131] U. Maradia, E Filisetti, M. Boccadoro, M. Roten, J.-M. Dutoit, S. Hengsberger, *Procedia CIRP* **2018**, *68*, 58–63.

[132] S. N. Bhavsar, S Aravindan, P. V. Rao, *Precision Engineering* **2014**, *38*, 168–173.

[133] Y Holovenko, M Antonov, L Kollo, I Hussainova, *Proceedings of the Institution of Mechanical Engineers Part J: Journal of Engineering Tribology* **2018**, *232*, 43–53.

[134] C. Wang, W. Zhang, Z. Zhao, Y. Wang, P. Gao, Y. Luo, X. Luo, *Micromachines* **2016**, *7*, 118.

[135] J. C. W. Lim, C. H. Wong, **2018**.

[136] J. Bonse, *Nanomaterials* **2020**, *10*, 1950.

[137] C. Barr, L. Wang, J. Coffey, F. Daver, *Journal of materials science* **2017**, *52*, 1221–1234.

[138] J. Yao, C. Zhang, H. Liu, Q. Dai, L. Wu, S. Lan, A. V. Gopal, V. A. Trofimov, T. M. Lysak, *Applied Surface Science* **2012**, *258*, 7625–7632.

[139] B. Dusser, Z Sagan, H. Soder, N. Faure, J.-P. Colombier, M. Jourlin, E. Audouard, *Optics express* **2010**, *18*, 2913–2924.

[140] H. Liu, Y. Wang, J. Huang, Z. Chen, G. Chen, Y. Lai, *Advanced Functional Materials* **2018**, *28*, 1707415.

[141] J. Vera, A.-C. Brulez, E. Contraires, M. Larochette, S. Valette, S. Benayoun, *Journal of Micromechanics and Microengineering* **2015**, *25*, 115027.

[142] L. Piccolo, M. Sorgato, A. Batal, S. Dimov, G. Lucchetta, D. Masato, *Micromachines* **2020**, *11*, 429.

[143] G Lucchetta, M Sorgato, E Zanchetta, G Brusatin, E Guidi, R Di Liddo, M. Conconi, *Express Polymer Letters* **2015**, *9*, 354–361.

[144] B. Saha, W. Q. Toh, E. Liu, S. B. Tor, D. E. Hardt, J. Lee, *Journal of Micromechanics and Microengineering* **2015**, *26*, 013002.

[145] R Surace, M Sorgato, V Bellantone, F Modica, G Lucchetta, I Fassi, *Journal of Manufacturing Processes* **2019**, *43*, 105–111.

[146] N. Ong, H. Zhang, Y. Lam, *Advances in Polymer Technology: Journal of the Polymer Processing Institute* **2008**, *27*, 89–97.

[147] N. S. Ong, H. L. Zhang, Y. C. Lam, *The International Journal of Advanced Manufacturing Technology* **2009**, *45*, 481.

[148] T. Sasaki, N. Koga, K. Shirai, Y. Kobayashi, A. Toyoshima, *Precision engineering* **2000**, *24*, 270–273.

[149] K. Delaney, G Bissacco, D Kennedy, *International Polymer Processing* **2012**, *27*, 77–90.

[150] M BIRNBAU, *Journal of Applied Physics* **1965**, *36*, 3688–3689.

[151] Á. Rodríguez-Rodríguez, E. Rebollar, M. Soccio, T. A. Ezquerra, D. R. Rueda, J. V. Garcia-Ramos, M. Castillejo, M.-C. Garcia-Gutierrez, *Macromolecules* **2015**, *48*, 4024–4031.

[152] B. Yilbas, S. S. Akhtar, C. Karatas, *Optics and Lasers in Engineering* **2010**, *48*, 740–749.

[153] N Yasumaru, K Miyazaki, J Kiuchi, *Applied Physics A* **2005**, *81*, 933–937.

[154] E. L. Gurevich, *Applied Surface Science* **2016**, *374*, 56–60.

[155] J. Cheng, C.-s. Liu, S. Shang, D. Liu, W. Perrie, G. Dearden, K. Watkins, *Optics & Laser Technology* **2013**, *46*, 88–102.

[156] N. M. Bulgakova, I. M. Bourakov, *Applied surface science* **2002**, *197*, 41–44.

[157] D. Perez, L. J. Lewis, *Physical review letters* **2002**, *89*, 255504.

[158] L. J. Lewis, D. Perez, *Applied Surface Science* **2009**, *255*, 5101–5106.

[159] J Ouyang, W Perrie, O. Allegre, T Heil, Y Jin, E Fearon, D Eckford, S. Edwardson, G Dearden, *Optics express* **2015**, *23*, 12562–12572.

[160] X. Li, Y. Guan, *Nanotechnology and Precision Engineering* **2020**, *3*, 105–125.

[161] G. D. Tsibidis, C. Fotakis, E. Stratakis, *Physical Review B* **2015**, *92*, 041405.

[162] E Stratakis, J. Bonse, J Heitz, J. Siegel, G. Tsibidis, E Skoulas, A Papadopoulos, A Mimidis, A.-C. Joel, P Comanns, et al., *Materials Science and Engineering: R: Reports* **2020**, *141*, 100562.

[163] A. M. Prokhorov, A. S. Svakhin, V. A. Sychugov, A. V. Tishchenko, A. Khakimov, *Soviet Journal of Quantum Electronics* **1983**, *13*, 568.

[164] C. Wang, H. Huo, M. Johnson, M. Shen, E. Mazur, *Nanotechnology* **2010**, *21*, 075304.

[165] Z. Kan, Q. Zhu, H. Ren, M. Shen, *Materials* **2019**, *12*, 2043.

[166] D. Zhang, K. Sugioka, *Opto-Electronic Advances* **2019**, *2*, 190002.

[167] M. Shen, J. E. Carey, C. H. Crouch, M. Kandyla, H. A. Stone, E. Mazur, *Nano letters* **2008**, *8*, 2087–2091.

[168] M. Shen, C. H. Crouch, J. E. Carey, E Mazur, *Applied Physics Letters* **2004**, *85*, 5694–5696.

[169] P. Bizi-Bandoki, S. Benayoun, S. Valette, B. Beaugiraud, E Audouard, *Applied Surface Science* **2011**, *257*, 5213–5218.

[170] G. Giannuzzi, C. Gaudiuso, R. Di Mundo, L. Mirenghi, F. Fraggelakis, R. Kling, P. M. Lugarà, A. Ancona, *Applied Surface Science* **2019**, *494*, 1055–1065.

[171] U. Hermens, M. Pothen, K. Winands, K. Arntz, F. Klocke, *Optics and Lasers in Engineering* **2018**, *101*, 44–50.

[172] J.-M. Romano, A. Garcia-Giron, P. Penchev, S. Dimov, *Applied Surface Science* **2018**, *440*, 162–169.

[173] A. Bogaerts, Z. Chen, *Spectrochimica Acta Part B: Atomic Spectroscopy* **2005**, *60*, 1280–1307.

[174] K. Ding, C. Wang, Y. Zheng, Z. Xie, Z. Luo, S. Man, B. Wu, et al., *Surface and Coatings Technology* **2019**, *367*, 244–251.

[175] M Martínez-Calderon, A Rodríguez, A Dias-Ponte, M. Morant-Miñana, M Gómez-Aranzadi, S. Olaizola, *Applied Surface Science* **2016**, *374*, 81–89.

[176] S. Razi, F. Ghasemi, *The European Physical Journal Plus* **2018**, *133*, 1–8.

[177] G. P. Specifications, *International Standard ISO* **2012**, 25178–2.

[178] C.-S. Chang, C.-K. Chung, J.-F. Lin, *Journal of Materials Processing Technology* **2020**, *277*, 116465.

[179] P. K. Kennedy, **2008**.

[180] D Astm, *Current edition approved Dec* **2003**, *1*, 66–72.

[181] Q.-H. Li, B. Li, *Applied Mathematical Modelling* **2016**, *40*, 7349–7367.

[182] G. Mannella, V La Carrubba, V. Brucato, W Zoetelief, G Haagh, *Journal of Applied Polymer Science* **2011**, *119*, 3382–3392.

[183] P. Kennedy, R. Zheng, *Flow analysis of injection molds*, Carl Hanser Verlag GmbH Co KG, **2013**.

[184] A.-C. Brulez, C. Boschard, M. Larochette, S. Benayoun, *Polymer Engineering & Science* **2020**, *60*, 2235–2247.

[185] M. Sorgato, D. Masato, L. Piccolo, G. Lucchetta, *CIRP Journal of Manufacturing Science and Technology* **2020**, *30*, 79–86.

[186] N. Bulgakova, V. Zhukov, A. Vorobyev, C. Guo, *Applied Physics A* **2008**, *92*, 883–889.

[187] M. D'Haese, B. Goderis, P. Van Puyvelde, *Macromolecular Materials and Engineering* **2011**, *296*, 603–616.